Synthesis and characterisation of direct and indirect hydrogen storage materials

James M. Hanlon BSc(Hons)

Submitted in fulfilment of the requirements for the Degree of Doctor of Philosophy

School of Chemistry
College of Physical Science
University of Glasgow

February 2013

Declaration

The content of this thesis is original work, except where reference is made to other authors. This work has not been submitted previously for any other degree or qualification in this or any other university.

James M. Hanlon

Abstract

The work in this thesis describes the synthesis and characterisation of direct and indirect hydrogen storage materials. The main experimental techniques used have been Powder X-ray Diffraction (PXD), Powder Neutron Diffraction (PND) and Temperature Programmed Desorption (TPD).

The Magnesium ammines, $Mg(NH_3)_6X_2$ (where X= Cl, Br, I) are interesting materials for use as an indirect H_2 storage material (by the splitting of NH_3) due to their high H_2 gravimetric capacities. These ammines have been synthesised at room temperature through the reaction of the starting salt with NH_3 and are cubic ($Fm\bar{3}m$). TPD investigations have revealed that the ammines deammoniate in a three step process, with the chloride ammine possessing the most favourable deammoniation temperatures. Ex-situ PND has been used to refine the structure and in-situ PND has been employed to study the deammoniation processes in more detail.

'*H_2 release*' systems have been examined as a potential solution for H_2 storage. $Mg(NH_3)_6Cl_2$ has been mixed with LiH or MgH_2 at room temperature and studied using TPD with the LiH system the most encouraging in terms of the H_2 release temperature. In-Situ PND has also been employed to understand the mechanism of H_2 release. The $Mg(OH)_2$ –LiH 'H_2 release' system has also been studied using both bulk starting materials and microstructured materials. Microplates of $Mg(OH)_2$ have been synthesised by a new MW (microwave) heating process in 6 mins. The employment of microstructured materials has reduced the onset reaction temperature from 147 ^oC in the bulk materials to 79^oC when the starting materials are mixed for 10 mins.

Acknowledgements

Firstly I would like to thank my supervisor Professor Duncan Gregory for all his help and support during my PhD and for giving me the opportunity to undertake this research. I would also like to thank past and present members of the Gregory Group, particularly Dr Tapas Mandal and Dr Robert Hughes for assistance and guidance in the lab. I would also like to thank Helen Kitchen for helping me with Refinements and Hazel Riordan for Raman measurements.

I would like to thank Dr Winfried Kockelmann at ISIS for assistance and support with the In-Situ Powder Neutron Diffraction experiments and also the Pressure and Furnace team for assistance with the experimental set-up. For the ex-situ Powder Neutron Diffraction experiments I would like to thank Dr Clemens Ritter at ILL for his assistance and support. For funding I would like to thank the ESPRC UKSHEC consortium.

Finally I would like to thank my parents for their support particularly during writing up.

List of Abbreviations

AFC	Alkaline Fuel Cell
DFT	Density Functional Theory
DAFC	Direct Ammonia Fuel Cell
DMFC	Direct Methanol Fuel Cell
DSC	Differential Scanning Calorimetry
DTA	Differential Thermal Analysis
FC	Fuel Cell
IR	Infra-Red Spectroscopy
LOHC	Liquid Organic Hydrogen Carrier
MCFC	Molten Carbonate Fuel Cell
MW	Microwave
MS	Mass Spectrometry
PAFC	Phosphoric Acid Fuel Cell
PEMFC	Proton Exchange Fuel Cell
PND	Powder Neutron Diffraction
PXD	Powder X-ray Diffraction
SEM	Scanning Electron Microscopy
SOFC	Solid Oxide Fuel Cell
TGA	Thermo Gravemetric Analysis
TPD	Thermal Programmed Desorption

Table of Contents

1. Introduction

One of the main challenges being faced in the 21st century is that of global warming and the finite amount of fossil fuels available for everyday use. At the present time, non-renewable fossil fuels (oil, gas and coal) accounts for 79.5% of the world's primary energy supply, with oil being the largest at 35%.[1] The production of CO_2 and other waste materials using fossil fuels has also contributed to global warming and the degradation of the ozone layer. A new and clean sustainable energy source must be found to address these issues.

One possible sustainable fuel is hydrogen. Less than 1% of hydrogen in the world is available as H_2 with the majority being available in H_2O. H_2 also has a large chemical energy per mass of 142 MJ kg^{-1} compared to 47 MJ kg^{-1} for liquid hydrocarbons.[2] H_2 is also a clean and renewable depending on the fuel. The production, storage and conversion of H_2 is known as the H_2 energy cycle (Figure 1.1).

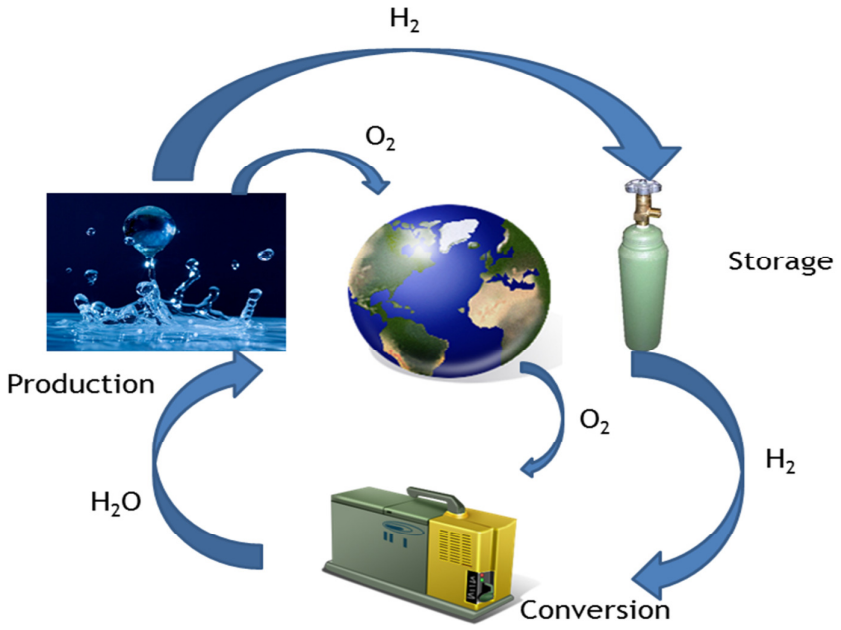

Figure 1.1: H_2 energy cycle. Adapted from Ref 3

For the production of H_2 a number of methods can be utilised. H_2 can be produced from electrolysis[4], artificial photosynthesis [5], hydrocarbons [6] and biomass.[7]

Another alternative H_2 source are indirect H_2 storage materials, such as Liquid Organic Hydrogen Carriers (LOHC)[8] and NH_3. LOHC are organic compounds, such as N-ethylcarbozole that can be loaded with H_2 which can then be used when required. NH_3 is a fuel that could be used as an indirect H_2 storage material (it can theoretically store 17.6 wt. % H_2) by cracking the NH_3 into N_2 and H_2 or *via* use in fuel cells. Toxicity and safety issues are still a major issue for NH_3 to be used as part of a green economy. The green economy can be defined as a low carbon economy, where the sustainable fuel used has a negligible environment impact in both production and use and at a reasonable cost.[9] Ammonia is also readily available, is cheap to produce and is produced by industry in large quantities by the Born Haber process.

For an H_2 or NH_3 economy to become a viable alternative to fossil fuels, the safe storage of H_2/NH_3 must be optimised. H_2 can be stored as a compressed gas, as liquid H_2 or in a solid state material.

H_2 storage as a compressed gas is the most common storage at the present time.[10] The hydrogen can be stored at pressures ranging from 200 bar to 800 bar. At 800 bar the volumetric density of the H_2 is 36 kg m^{-3}. [11] At a pressure of 700 bar, the mechanical energy content is 8 MJ Kg^{-1} and taking into account the compression, the ideal energy content for a compressed gas storage system is 10.2 MJ Kg^{-1} so working at high pressures should not be an issue.[12] An important step to increase this H_2 pressure is the design of the storage tanks to safely store H_2 at high pressures. Typically in a cylinder or tank used for compressed H_2 storage, the inner liner is a polymer that acts as a H_2 permeation barrier with a carbon resin covering the inner layer. There is also an outer shell to protect the cylinder from damage.[13] The drawback is the cost and weight of the compressed gas storage system. Public perception is also an issue regarding the safety of such a system although the HyFLEET : CUTE hydrogen powered buses use compressed H_2.[14] This project has been a success in regards to public perception with 68 % of the respondants to a survey into the HYFLEET project supporting the replacement of buses with H_2 powered buses and 76 % of the respondants would prefer to travel on the H_2 powered bus rather than a conventional bus.[15]

H_2 can also be stored as liquid hydrogen. Liquid hydrogen has a high mass density at low temperatures compared to the compressed gas which allows for

compact storage of H_2 in a vehicle.[16] There are however, major drawbacks to this method of storage. This system requires a large heat input as approximately 30% of the net energy is used for the liquefaction of H_2.[17] Another issue is that venting is required when the system is pressurised which results in the loss of H_2 which is known as boil-off gas. Boiling or evaporation of the gas would also occur during refilling. Another disadvantage is the insulation required for the liquid H_2 tanks. Taking these issues into account, current research into liquid H_2 storage has been limited.

Ammonia is presently stored in liquid form. The drawback to this is the high toxicity, the corrosive behaviour of NH_3, the strong odour associated with NH_3 and the safety considerations when transporting and handling NH_3.

Solid state storage is an alternative method of storing H_2, however there are a number of barriers that need to be overcome. The ideal material must be cheap, non-toxic and meet the demands required, in terms of storage capacity, cost, recyclability and weight. The targets commonly quoted for H_2 storage requirements are that of the US Department of Energy (US DOE).[18] These targets for 2015 include a H_2 gravimetric capacity of 9 wt. % H_2, low cost (less than 67 \$/kg H_2) and also a filling time from start to finish of less than 5 minutes. Hydrides (section 1.2) can meet the targets for gravimetric capacity, but kinetics and reversibility are a barrier. Meanwhile, metal-organic frameworks (MOFs) which are porous inorganic coordination polymers can meet the H_2 storage targets at -196 ^{o}C, but possess minimal H_2 storage at room temperature (section 1.2.1).

As well as meeting the US DOE targets, there are a number of other issues that must be overcome by solid state chemists if a successful solid state store is to be realised. These include the handling of materials given that many hydrides and other H_2 storage materials are sensitive to air and water in the atmosphere. This in turn, means that materials must be handled and synthesised via inert techniques.

The conversion of the H_2 to H_2O in the H_2 energy cycle occurs in fuel cells (section 1.1).

1.1 Fuel Cells (FC) Introduction

Fuel cells are used for producing electricity from a fuel via a chemical reaction with an oxidising agent. Fuel cells can be utilised for both stationary and mobile applications. Stationary applications can include electricity generation and for heating.[19] Mobile applications include vehicles and also as replacements for batteries in mobile phones, laptops and MP3 players.[20]

In a fuel cell there are three main components: the anode, the cathode and the electrolyte which is located between the anode and cathode. In a fuel cell, the fuel (containing H_2) is transferred to the anode with an oxidant (typically O_2 from the atmosphere) transferred to the cathode. The hydrogen from the fuel is oxidised to H^+ and an electron. The H^+ then travels through the electrolyte and the electron travels towards the cathode. The anion generated from the H_2 is used to create a current, which results in O^{2-} production by reduction of O_2. This O^{2-} then reacts with the H^+ to form H_2O which is released from the fuel cell. A fuel cell will produce electricity continually as long as there is a sufficient supply of both the fuel and the oxidant and there is no degradation to the cell. To speed up the time to produce the electricity a catalyst is commonly employed for the production of the cations and anions. The most common catalysts used are Pt, Pt alloys and Ni.[21,22] The materials used for the anode, cathode and electrolytes are discussed for each fuel cell in the following sections. A schematic of a H_2 powered fuel cell can be seen in Figure 1.2:

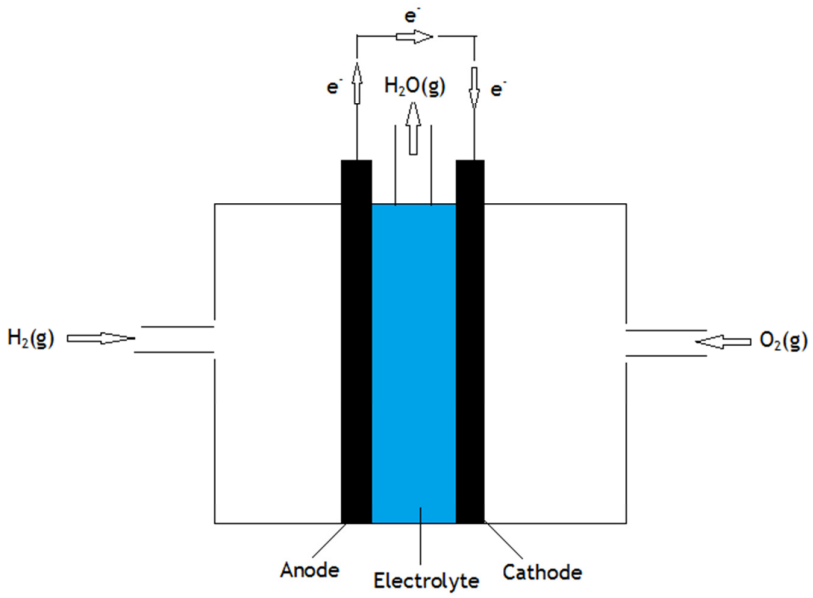

Figure 1.2: Schematic of a H_2 fuel cell

Fuel cells can be divided into two categories depending on their temperature of operation, either high temperature fuel cells or low temperature fuel cells.[23] High temperature fuel cells include solid oxide fuel cells (SOFC) and molten carbonate fuel cells (MCFC). Low temperature fuel cells include proton exchange membrane fuel cells (PEMFC), direct methanol fuel cells (DMFC), alkaline fuel cells (AFC) and phosphoric acid fuel cells (PAFC).

There are a number of sources of H_2 for use in fuel cells including hydrocarbons (such as from petrol and diesel) [24], biofuels and chemical intermediates such as methanol and ammonia.[19] The H_2 sources are associated with problematic contaminants that can lead to a shorter lifespan of the fuel cell which must be overcome. Sulfur is one contaminant that can poison the fuel cell although this is removed before the H_2 source is used in the fuel cell.[19] CO is another problematic contaminant which can be an impurity in the fuel, particularly in the low temperature fuel cells. Other problem contaminants can include other fuel impurities such as H_2S and air impurities such as CO_x and NO_x. These are discussed in more detail in Section 1.1.1. and 1.1.2.

1.1.1 High Temperature Fuel Cells

1.1.1.1 Solid Oxide Fuel Cells (SOFCs)

Solid oxide fuel cells require high temperatures, in the region of 500 ^{o}C to 1000 ^{o}C.[25] This high temperature means practical applications are limited however the temperature is an advantage in that the fuel cell is not poisoned by CO from fossil fuels as the cell can convert the CO to CO_2. A SOFC has a high efficiency of ~60% when the fuel is H_2. The main source of H_2 for a SOFC is from hydrocarbons. However, using hydrocarbons results in the production of CO_2 as the by-product from the fuel cell process. If the source of H_2 is either H_2 on its own or a clean energy fuel such as NH_3 (section 1.1.3) then the product of the fuel cell process will be H_2O.

The electrochemical reactions that occur in the SOFC are:

Cathode: $O_2\ (g) + 2e^- \rightarrow O^{2-}\ (s)$ (1.1)

Anode: $H_2\ (g) + O^{2-} \rightarrow H_2O + 2e^-$ (1.2)

$CO\ (g) + O^{2-} \rightarrow CO_2 + 2e^-$ (1.3)

The electricity is produced when the O^{2-} travel through the electrolyte to the anode.

Electrolytes that have been investigated for use in a SOFC include zirconia, [26] ceria [27] and perovskites.[28] Materials for use as cathodes that have been investigated include doped periovskites,[29] while for the anode, Ni/YSZ (yttria-stablised zirconia) has been extensively used.[25] The disadvantage of using Ni/YSZ is that it is susceptible to sulfur poisoning.[30]

1.1.1.2 Molten Carbonate Fuel Cells (MCFC)

The other high temperature fuel cell is the molten carbonate fuel cell. These also require high temperatures for operation (typically 600 ^{o}C-700 ^{o}C [31]). The electrolyte is commonly a mixture of both lithium carbonate and potassium carbonate impregnated in $LiAlO_2$.[31] The carbonate ions from the lithium or potassium carbonate are transferred through the electrolyte to the anode where

they react with the H_2 fuel from the fuel source (commonly hydrocarbons) to produce H_2O, CO_2 and $2e^-$. The electrons produced travel to the cathode to produce electricity. The anode is usually NiO mixed with various oxides, including CoO and LiO.[32,33] The cathode materials used include NiO and $LiFeO_2$.[34] The catalyst used in a MCFC is nickel due to its activity and also due to its low cost when compared to other metal catalysts such as Pt.[19] The advantages of this fuel cell is that it is not susceptible to CO poisoning and has efficiency comparable to an SOFC. The disadvantages are the cell is susceptible to sulfur poisoning, the time required to heat the fuel cell and the corrosive electrolyte used which has an effect on the lifespan of the iron metals.[31]

1.1.2 Low Temperature Fuel Cells

1.1.2.1 Proton Exchange Fuel Cells (PEMFC)

Proton exchange membrane fuel cells operate at temperatures of 50 ^oC – 100 ^oC.[19] The electrolyte used is Nafion, which is a conductive thin polymer membrane.[35] Nafion allows the flow of protons but not electrons. The material used for the anode and cathode is porous carbon. The catalyst used is Pt, although due to the cost, Pt alloys such as Pt/C catalysts are used.[21,36] The electrochemistry involved in a PEM fuel cell is as follows:

Anode: $2\ H_2 \rightarrow 4\ H^+ + 4\ e^-$ (1.4)

Cathode: $O_2 + 4\ H^+ + 4\ e^- \rightarrow 2\ H_2O$ (1.5)

The low temperature involved makes PEMFCs ideal for vehicle fuel cells due to the short time taken for the fuel cell to reach temperature, the high power density and the efficiency of 50-60%.[19] However, low temperature operation does have its drawbacks, including a short lifespan of the cell.[37] The Pt catalyst is susceptible to impurities in fuel, primarily CO. Unlike SOFCs, the fuel cell cannot convert the CO produced to CO_2. The fuel cell is also susceptible to other fuel impurities (CO_2, H_2S and NH_3), air contaminants (NO, SO,CO) and cations produced by corrosion of the fuel cell (Fe^{3+}, Cu^{3+}).[38] These issues mean that pure H_2 must be used for the fuel, which has led to the development of the direct methanol fuel cell (DMFC) and the direct ammonia fuel cell (section 1.1.3).

1.1.2.2 Direct Methanol Fuel Cell (DMFC)

The direct methanol fuel cell is based on the PEM fuel cell except the fuel source is methanol.[39] At the anode, the methanol is oxidised to CO_2 and H_2. At the cathode, the O_2 combines with the hydrogen from the anode to form water. Using methanol as a liquid fuel results in a faster filling time. The cell also has an efficiency of 30-40%.[19] The disadvantage of this fuel cell is that the low operating temperature of the cell (60 ^oC) requires a high loading of catalyst (Pt/alloy) to split the methanol to produce the H_2 for the fuel cell.[40]

1.1.2.3 Alkaline Fuel Cells (AFC)

Alkaline Fuel cells (AFC) are another class of low temperature fuel cell and was the first fuel cell developed. The most famous use of this fuel cell has been its use on the space shuttle.[41] The electrolyte consists of potassium hydroxide.[42]

The electrochemistry involved is described in equation 1.6 for the anode and equation 1.7 for the cathode. A schematic of the alkaline fuel cell can be seen in figure 1.3.

$$2\ H_2(g) + 4\ OH^-(aq) \rightarrow 4\ H_2O(g) + 4\ e^- \qquad (1.6)$$

$$O_2(g) + 2\ H_2O(l) + 4\ e^- \rightarrow 4\ OH^-(aq) \qquad (1.7)$$

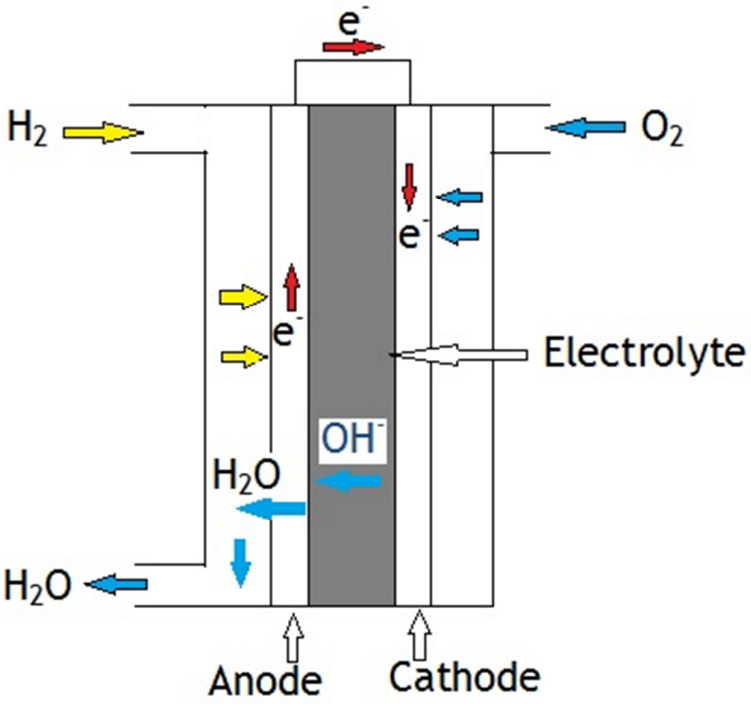

Figure 1.3: Schematic of an Alkaline Fuel Cell

As alkaline fuel cells (AFC) have similar operating temperatures to PEMFCs, they reach their operating temperature quickly. It has been suggested that the low power density of the AFC would stop them being used for large scale power applications, however ambient air AFC possess similar power densities to PEMFCs.[43] Fuel sources investigated for alkaline fuel cells include methanol and ethanol.[44,45]

1.1.2.4 Phosphoric Acid Fuel Cells (PAFC)

Phosphoric Acid Fuel Cells are fuel cells that are similar to PEMFCs. The electrolyte consists of phosphoric acid in a SiC matrix.[23] The catalyst used is Pt or Pt alloys.[46] The fuel cell operates between 150-200 ^{o}C and this increase in temperature allows some CO from fossil fuels being tolerated. The disadvantage of this fuel cell is the cost due to the catalyst needed and also the corrosive nature of the electrolyte.

1.1.3 Ammonia as a Fuel in Fuel Cells: Direct Ammonia Fuel Cells

Ammonia can be used as the source of H_2 for use in fuel cells. One of the major drawbacks of using NH_3 is the toxicity and safety issues presented by using NH_3. Ammonia could be stored in a solid state material such as NH_3 (such as the metal ammines- Section 1.6). These materials can then be heated to release NH_3 for use in a Direct Ammonia Fuel Cell (low temperature fuel cell) or a SOFC (high temperature fuel cell) as described in Section 1.1.5.

Direct Ammonia fuel cells (DAFC) were first reported in the 1960s with an operating temperature of 120 ^oC by Wynveen who concluded that '*Ammonia represents, in many ways, an ideal cell fuel'*.[47,] Simons *et al*. then developed a DAFC based on the direct alkaline fuel cell.[48] KOH(aq) was used as the electrolyte, graphite for the electrodes and Pt as the catalyst. NH_3 was split by electrochemical oxidation in the fuel cell. The optimised operating temperature was found to be between 60-140 ^oC.

In the NH_3 fuel cell, the NH_3 is oxidised at the anode, with oxygen being reduced at the cathode. The equation for this electrochemical reaction is: [49]

Anode : $2\ NH_3 + 6\ OH^- \rightarrow N_2 + 6\ H_2O + 6\ e^-$ $E^o = +0.40$ V (1.8)

Cathode: $O_2 + 2\ H_2O + 4\ e^- \rightarrow 4\ OH^-$ $E^o = +0.77$ V (1.9)

Overall: $4\ NH_3 + 3\ O_2 \rightarrow 2\ N_2 + 6\ H_2O$ $E^o = +1.17$ V (1.10)

One of the major issues for DAFC use is the oxidation of the NH_3 in the fuel cell and also the toxic nature of NH_3 both to humans and the environment. A concentration of NH_3 over 60 ppm in air can result in irritation to the eyes and lungs and at levels above 500 ppm can cause irreservible injuries to humans.[50] The most common metal used for the oxidation is Pt.[51] The effect of different metals on the oxidation of NH_3 has been studied, with Pt and Ir the most suitable catalysts for oxidation.[52]

For DAFCs to be successful the optimum anode/cathode and electrolyte must be found and also, crucially a solid state ammonia storage material which stores a high wt. % of NH_3 while minimising any toxicity issues to both the catalyst and the environment.

1.1.4 Ammonia in PEM fuel Cells (PEMFCs)

Using NH_3 directly in a PEM fuel cell in which the NH_3 is oxidised in the fuel cell results in poisoning and efficiency issues. Exposing a PEM fuel cell to an H_2(g) flow containing 10 ppm NH_3 can result in a significant loss in the cell performance over 24 hrs.[53] The loss of performance in the fuel cell is due to NH_3 poisoning of the catalyst and the cathode and anode where ammonium was observed. Exposing the fuel cell to a H_2 flow with 1 ppm NH_3 over a period of 7 days also results in a significant loss of cell performance due to NH_3 poisoning of the fuel cell.[53] The authors suggest that improving the fuel cell tolerance to NH_3 could be improved by designing new cathode catalyst materials which would increase the rate of oxidation of NH_3 in the fuel cell.

If NH_3 is to be used in a PEM fuel cell, then the present approach would be to split the NH_3 to N_2 and H_2 outside of the fuel cell at elevated temperatures (>500 ^oC using a Ni-Pt/Al_2O_3 catalyst) and then using the obtained H_2 as the fuel.[54]

1.1.5 Ammonia in Solid Oxide fuel cells (SOFCs)

Ammonia has been greatly studied as the possible fuel of choice for Solid Oxide Fuel Cells (SOFC).[55,56,57] As discussed in section 1.1.1 the disadvantage of a SOFC is the high temperature required for operation. Thermal decomposition of the ammonia (via a catalyst, for example Ni) occurs at the anode to produce hydrogen. This hydrogen is transferred to the cathode through the electrolyte where H_2O is produced:

Anode:

$$2\ NH_3 \rightarrow N_2 + 3\ H_2 \qquad (1.11)$$

$$H_2 \rightarrow 2\ H^+ + 2\ e^- \qquad (1.12)$$

Cathode:

$$2\ H + \tfrac{1}{2}\ O_2 + 2e^- \rightarrow H_2O \qquad (1.13)$$

Overall:

$$2\ NH_3 + ½\ O_2 \rightarrow N_2 + H_2O + 2\ H_2 \qquad (1.14)$$

Ma *et al.*[58] have designed a SOFC fuel cell, with NH_3 as the fuel. The anode consists of $BaCe_{0.8}Gd_{0.2}O_{2.9}$ (BCGO) and NiO while the cathode is $La_{0.5}Sr_{0.5}CoO_{3-\delta}$ (LSCO) and BCGO based. The electrolyte is a BCGO film. The NH_3 was fed directly into the anode. At 700 ^oC the cell operated at 0.985 V with a power density of 355 mW cm^{-2} which is comparable to a power density of 371 mW cm^{-2} when H_2 was used as the fuel. Fornier *et al.*[59] using yttria stabilized zirconia (YSZ) as the electrolyte with a NiO-YSZ cermet (a cermet is a composite material composed of ceramic and metallic materials) as the anode found that at 800 ^oC using NH_3 instead of H_2 as the fuel source resulted in an improved conductivity of 11 mW cm^{-2}. The authors conclude this is due to the choice of nickel cermet for the anode which acts as a catalyst for NH_3 decomposition at a high efficiency.

When different fuels were compared (NH_3, N_2H_4 and H_2) [60] in an SOFC at high temperatures, NH_3 delivered the same performance as H_2. However, at low temperature H_2 had a better performance than NH_3. This was due to the poor activity of the $BaZr_{0.1}Ce_{0.7}Y_{0.2}O_{3-\delta}$ (BZCY) and NiO anode for the decomposition of NH_3 (using Ni as the catalyst), which resulted in decreased amount of fuel available to the fuel cell.

For fuel cells involving NH_3, a solid state store of NH_3 is required, especially for safety and toxicity issues related to NH_3.

1.2 Hydrogen Storage

There are two types of solid state hydrogen storage systems. These are divided according to the way that the hydrogen binds to the material: physical storage and chemical storage. In physical storage (physisorption - which refers to an adsorption process in which the involved forces are intermolecular and don't involve a significant change in the electronic orbital patterns of the involved species [61]) the forces of attraction between the hydrogen molecules and the host originate mainly from weak van der Waals interactions, thereby restricting any

significant hydrogen adsorption to that at low temperatures and/or at high pressures. High storage capacities have been seen at temperatures of -196 ^{o}C under a pressure of H_2, but this is often significantly decreased to very low or negligible storage capacities at room temperature.

The other type of solid state hydrogen storage material is one that interacts with H_2 by chemical storage.[62] This involves the chemical binding of H_2 to the storage material. Chemisorption, is an adsorption process which involves the same valance forces which are found in the formation of chemical compounds [61], which is a surface process, is the initial step of the adsorption of H_2. During chemisorption, the molecular H_2 is dissociated to atomic H_2 on the surface. Chemisorption is an exothermic process. The next step of chemical storage of H_2 involves the absorption of H into the bulk material and the formation of a chemical bond.[63] This can result in high gravimetric H_2 storage capacities at higher temperatures, but for reversible H_2 storage to occur an elevated temperature is typically required to break the hydride bonds in the bulk.

1.2.1 MOF's and Carbons as H_2 storage materials (Physical Storage)

A number of materials that store H_2 by physical storage methods (physisorption) have been studied, including zeolites, covalent organic frameworks (COFs) and polymers of intrinsic microporosity (PIMs).[64,65,66] The most promising physical storage material are Metal Organic Frameworks (MOFs) while carbon based materials have been extensively researched.

MOFs came to prominence as a potential H_2 storage material when Yaghi *et al*. synthesised MOF-5.[67] This MOF was found to store 4.5 wt. % H_2 at -196 ^{o}C and 20 bar, although H_2 uptake decreased to 1.0 wt. % at room temperature. A number of MOFs have since been synthesised with encouraging H_2 uptake, including MIL101 that can store 6.1 wt. % H_2 at 196 ^{o}C and NOTT-122 that can store 7.01 wt. % H_2 at -196 ^{o}C.[68,69]

At the present time, the heat of adsorption and also the wt. % of H_2 storage for MOFs are greater at -196 ^{o}C than at room temperature by a large degree. Palomino *et al*. suggests that for effective hydrogen delivery at room

temperature at pressures the H_2 adsorption enthalpy needs to be between 22 - 25 kJ/mol^{-1}.[70] MOF-177 at -196 ^oC in a comparative study with its room temperature properties absorbed 1.5 wt. % H_2 at -196 ^oC but this decreased to 0.6 wt. % H_2 at room temperature. The heat of adsorption at room temperature was 5.8 kJ/mol l^{-1}.[71] MIL-101 has a heat of adsorption of 9.3 kJ/mol l^{-1} at -196 ^oC storing 6.1 wt. % H_2 but is reduced to 0.39 wt. % at room temperature.[68] No heat of adsorption data is given at room temperature but it can be assumed that the value is significantly less at room temperature than at -196 ^oC.

A number of strategies to improve the H_2 binding enthalpy have been investigated including exposure of metal sites [72,73] and hydrogen spillover.[74,75]

The exposure of metal sites involves removing a ligand from the framework, which leads to the metal site being exposed for H_2 binding. An example of this, was the DUT-9 MOF designed by Gedrich *et al*. that had exposed Ni sites. This MOF was prepared by the solvothermal synthesis and the ligands in the MOF (DMF/DEF) and also water can then be removed to create open metal sites. By having open metal sites in the MOF, this increased the wt. % H_2 adsorbed from 1.1 wt. % at -196 ^oC and 1 bar to 4.99 wt. % at -196 ^oC and 45 bar.[76] No data regarding the heat of adsorption of this MOF is given by the authors.

Hydrogen spillover involves the dissociation of H_2 onto a metal surface. The hydrogen is then spilled over from the metal surface to the porous material with the aid of a catalyst.[77] For the secondary H_2 spillover close contact ('bridge building') is required between the two participating materials in turn due to the energy involved in the process to occur. In this process the H_2 is dissociated at the catalyst and is then diffused onto the MOF with the help of a carbon bridge as illustrated in Figure 1.4

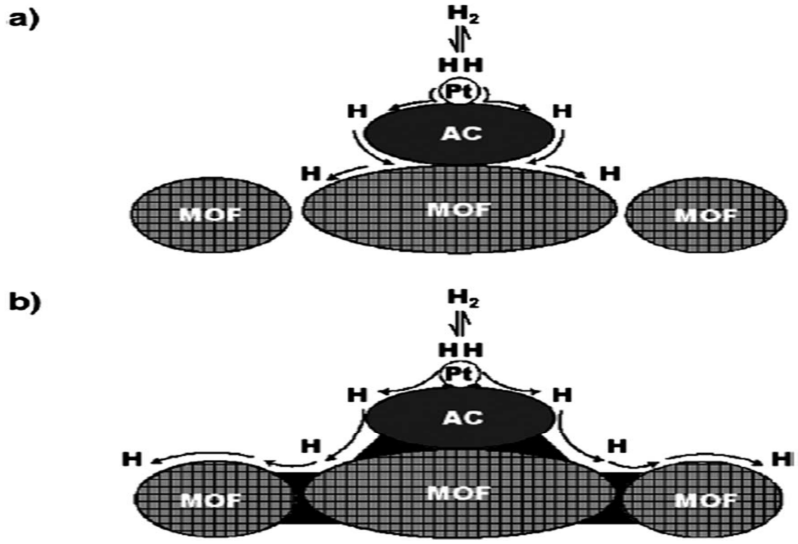

Figure 1.4: (a) The primary spillover of atomic H_2 from the Pt metal to the activated carbon support with a small degree of spillover to the MOF while (b) illustrates the primary and secondary spillover to the MOF by using carbon bridges. Reproduced with permission from Y. Li and R. T. Yang, *J. Am. Chem.Soc*, 2006, 1**28**, 8136. Copyright 2006 American Chemical Society.

H_2 spillover has been used to improve the H_2 storage of MIL-101 from 0.19 wt. % H_2 to 0.35 wt. % H_2 at room temperature with the aid of a Pd catalyst.[78] No heat of adsorption data for hydrogen spillover is supplied by the authors.

Carbon has been the subject of investigation for hydrogen storage materials for a number of years.[79,80] Carbon came to prominence as a H_2 storage material when Chambers *et al*.[81] reported that a GNF (graphite nanofibre) herringbone absorbed 67.55 % wt. H_2 at a pressure of 121.6 atm at 25 ^{o}C. These results have not been able to be independently verified, and the high gravimetric densities of these results have been suggested due to experimental error. Dillon *et al*. [82] reported single wall carbon nanotubes (SWCNTs) could gravimetrically store 5-10 wt. % H_2 at room temperature although this has not been reported since. Carbon has been of great interest as a possible hydrogen storage material due to their high surface area, high porosity and cost. Carbon nanostructures, [83] graphene, [84,85] activated carbon,[86] carbon aerogels [87] and fullerenes [88] have been investigated. As per other physisorption materials, the heat of adsorption at room temperature needs to be improved, as appreciable H_2 uptakes in carbon materials typically occurs at -196 ^{o}C. A number of strategies have been

investigated including doping with metal ions and hydrogen spillover.[89,90] It is worth noting that, Guay *et al*. [91] concluded that carbon nanotubes would not be able to meet the 2010 US DOE gravimetric hydrogen storage of 6 wt. % H_2 but might be used in combination with other H_2 storage materials to meet this target.

1.2.1 Hydrides as H_2 storage materials

1.2.1.1 Metal hydrides

MgH_2 has attracted the most interest of the metal hydrides for H_2 storage applications as it can gravimetrically store 7.66 wt. % H_2.[92] MgH_2 decomposes to Mg with the release of H_2 at temperatures above 300 ^oC.[93] The drawback of MgH_2 being used as a H_2 storage material is the slow rate of hydride formation from Mg and the slow rate of hydride dehydrogenation.[94]

A number of strategies have been employed to improve the kinetics of formation and decomposition of MgH_2 which include ball milling and the use of catalysts and additives.[95] Ball milling MgH_2 for 70 hours results in decomposition temperatures as low as 274 ^oC.[96] Adding a catalyst, such as Pd has been shown to decrease the desorption temperature by 123 ^oC.[97]

Another metal hydride, LiH (cubic *Fm3m* structure), can theoretically store 12.7 wt. % H_2 but its high decomposition temperature (680 ^oC) makes it unsuitable on its own. LiH is commonly used as a component of a H_2 storage system with complex hydrides such as $NaNH_2$ and $LiNH_2$.[98]

1.2.1.2 Complex hydrides

Other complex hydrides, apart from the nitrides, amides and imides have been investigated as H_2 storage materials.[99] Amongst these complex hydrides are the borohydrides.

$LiBH_4$ which is the most encouraging borohydride in terms of H_2 storage (18 wt. % H_2) decomposes in two steps:[100]

$$2\ LiBH_4 \rightarrow 2\ LiBH_2 + 2\ H_2 \qquad (1.15)$$

$2\ LiBH_2 + 2\ H_2 \rightarrow 2\ LiH + 2\ B + 3\ H_2$ (1.16)

$LiBH_4$ which can store 18 wt. % H_2 decomposes according to equations 1.15 and 1.16. H_2 release from $LiBH_4$ commences at 280 ^oC, with LiH and boron the products at 500 ^oC.[101] Reversibility is an issue for $LiBH_4$ as per other complex hydrides. For bulk $LiBH_4$ to rehydride a pressure of 850 bar H_2 with a temperature of 600 ^oC is required.[102] Nanostructuring approaches have been employed to improve the hydrogenation/dehydrogenation of $LiBH_4$ (section 1.3.2) and additives have been added, such as SiO_2 which have improved the desorption by 75 ^oC.[103]

A number of complex hydrides have been investigated for H_2 storage and these are summarised in Table 1.1 although these also suffer from unfavourable hydrogenation/dehydrogenation temperatures as per $LiBH_4$:

Table 1.1: Complex hydrides for H_2 storage

Compound	% wt.H_2 storage	Dehydrogenation Temp (^{o} C)	Ref
$CaBH_4$	11.6	350-390	104
$MgBH_4$	14.9	285-550	105
$NaAlH_4$	5.5	200-270	106
$Mg(AlH_4)_2$	9.3	110-400	107
$LiAlH_4$	10.5	150-400	108

1.2.2 Nitrides, Imides and Amides

Lithium nitride, Li_3N is one of the most promising chemical storage materials.[109] The interaction between lithium nitride and hydrogen was first reported in 1910 when Dafert and Miklauz synthesised an "Li_3NH_4" compound from Li_3N and hydrogen.[110]

Li_3N can theoretically store 10.4 wt. % H_2 by the following two step mechanism demonstrated by Chen *et al.* in 2002 (although only 9.3 wt. % H_2 was stored experimentally at that time):[111]

$Li_3N + 2\ H_2 \rightarrow Li_2NH + LiH + H_2$ (1.17)

$Li_2NH + LiH + H_2 \leftarrow\rightarrow LiNH_2 + 2\ LiH$ (1.18)

The second step of this reaction ($Li_2NH \rightarrow LiNH_2$) is reversible at temperatures above 320 ^oC at 10^5 mbar and can theoretically store 6.5 wt. % H_2. The second step of this reaction has been investigated by David *et al*. using synchrotron XRD.[112] The structural transformation occurs through a non-stoichiometric process involving intermediate anti-fluorite, type Li-N-H structures.

Above 300 ^oC, $LiNH_2$ decomposes to Li_2NH with the release of NH_3. However when the amide is mixed with LiH it can produce H_2 at 150 ^oC with the formation of Li_2NH, Li rich imide and Li_3N depending on the ratios of the starting material.[113] The Li rich imide ($Li_{2.2}\ NH_{0.8}$) is formed when a ratio of 1:2 is used for the amide and hydride. It has been proposed that the decomposition of $LiNH_2$ is controlled by diffusion of NH_3 through the Li_2NH layer.[114] The reaction of lithium amide with lithium hydride has also been proposed as a 2 step process, with the first process being the rate determining step:[115,116]

$2\ LiNH_2 \rightarrow Li_2NH + NH_3$ (1.19)

$NH_3 + LiH \rightarrow LiNH_2 + H_2$ (1.20)

Magnesium Amide, $Mg(NH_2)_2$, which can theoretically store 7.1 wt. %H_2 is another candidate H_2 storage material. When heated, magnesium amide decomposes to Mg_3N_2 with the release of NH_3. However, when reacted with MgH_2,[117] the system can evolve H_2, theoretically storing 4.88 wt. %:

$Mg(NH_2)_2 + MgH_2 \rightarrow 2\ MgNH + 2\ H_2$ (1.21)

$Mg(NH_2)_2$ can be used as part of a Li-Mg-N hydrogen storage system. The reactions with LiH proceeds as follows:

$Mg(NH_2)_2 + 2\ LiH \rightarrow Li_2Mg(NH)_2 + 2\ H_2$ 5.6 wt. % H_2 [118] (1.22)

$3\ Mg(NH_2)_2 + 8\ LiH \rightarrow Mg_3N_2 + 4\ Li_2NH + 8\ H_2$ 7 wt. % H_2 [119] (1.23)

$3\ Mg(NH_2)_2 + 12\ LiH \rightarrow Mg_3N_2 + 4\ Li_3N + 12\ H_2$ 9.1 wt. % H_2 [119] (1.24)

1.2.2.2 Structure of Nitrides, Imides and Amides

Li_3N is also the only known stable alkali metal nitride. Lithium nitride has three forms: α-Li_3N, ß-Li_3N and γ-Li_3N. The alpha phase typically exists at room temperature and pure α phase Li_3N can be synthesised from the reaction of Li metal in molten Na under N_2 gas at high temperatures.[120] The beta phase can be prepared from the alpha phase under moderate pressure and temperature (4.2 k Bar at 25 °C).[121] The gamma phase transforms from the ß phase at pressures between 350-450 kBar.[122]

Li_3N possesses a hexagonal structure. This was first discovered by Zintl *et al.* [123] and a subsequent single X-ray crystallography experiment by Rabenau showed that Li_3N crystallises in the *P6/mmm* space group.[124] Using Powder Neutron Diffraction (PND), Gregory *et al.* have shown there are nearly 3% Li vacancies in Li_3N.[120]

The nitrogen atom in Li_3N is connected to eight Li atoms in a hexagonal bipyramidal geometry (Figure 1.5). The layers are connected by a further Li atom in the third dimension.

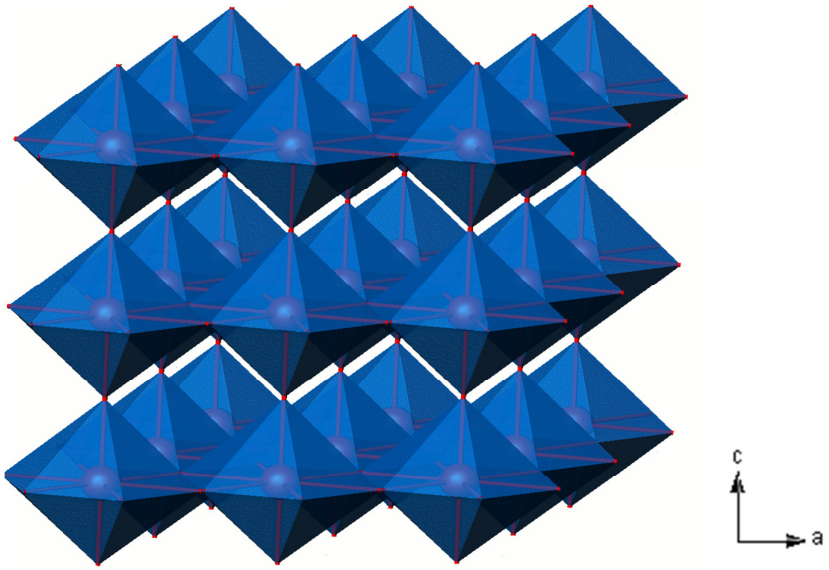

Figure 1.5: Polyhedral representation of the Li_3N structure. The Li atoms are at the vertices and N at the centre of each hexagonal bipyramid.

Lithium amide ($LiNH_2$) can be synthesised through the reaction of Li metal and NH_3 at 400 °C.[125] The structure of $LiNH_2$ (Figure 1.6) was first studied by X-ray diffraction [126] and crystallises in the orthorhombic system (*I4/m*). Neutron diffraction subsequently confirmed this structure.[127] The nitrogen in $LiNH_2$ is in a distorted, close packed arrangement. It was also found that the cations occupied tetrahedral interstices. PND experiments have been carried out, with the N-H distance being 0.986(10) Å and 0.942(13) Å [128] and for $LiND_2$ the N-D distance in the amide group was found to be 0.967(5) Å and 0.978(6) Å.[129]

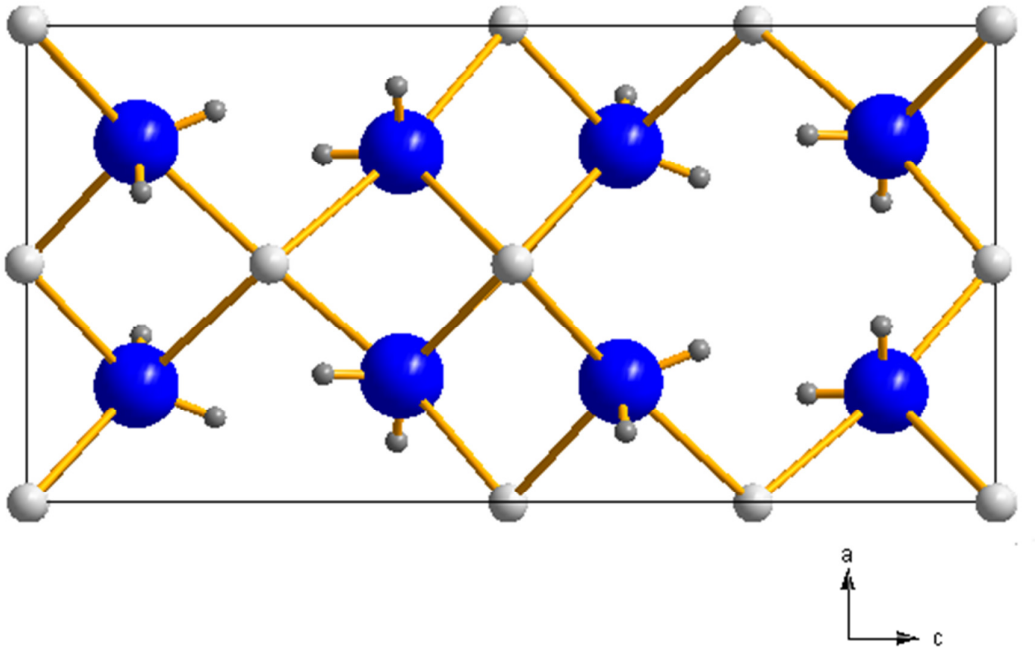

Figure 1.6: Structure of $LiNH_2$ (Blue spheres- Nitrogen, White spheres- Lithium, Grey spheres- Hydrogen)

Lithium imide (Li_2NH) is formed through the decomposition of lithium amide:

$$2LiNH_2 \rightarrow Li_2NH + NH_3 \qquad (1.25)$$

Li_2NH was first investigated in 1951 and was found to have the cubic, anti-fluorite structure ($Fm\bar{3}m$).[126] However, subsequent investigations have found another possible structure, the $F\bar{4}3m$ cubic structure.[130] Using X-ray synchrotron, Noritake *et al*. proposed the $Fm\bar{3}m$ model at room temperature.[131] The $Fm\bar{3}m$ structure (Figure 1.7) consists of the hydrogen occupying the 48h Wyckoff site around the nitrogen. The unit cell constant is 5.0742(2) Å with the N-H bonding

being 0.80(16) Å. Further investigations are required to determine the effect of the different structures have for storage as only DSC measurements have been performed on one structure (see Page 21).

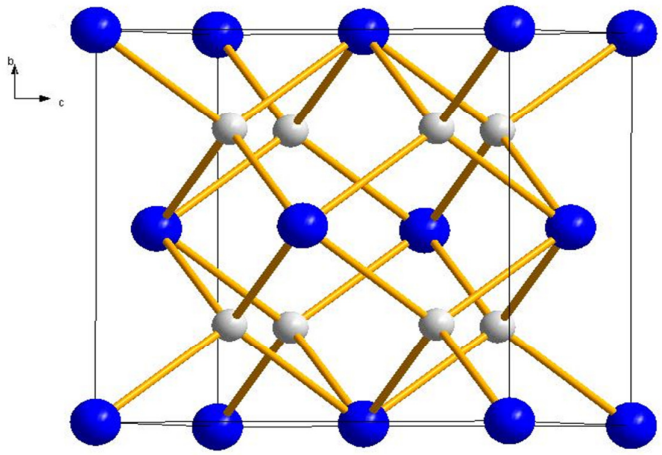

Figure 1.7: (a) Structure of Li_2NH ($Fm\bar{3}m$)- White spheres represent lithium and the blue spheres represent nitrogen. Hydrogen has been omitted for clarity.

Using PND, Ohoyama *et al.*[132] found at room temperature, that the $F\bar{4}3m$ structure is favoured over the $Fm\bar{3}m$ structure. In the favoured structure the hydrogen is located at the 16e Wyckoff site. In this model, four hydrogen positions with an occupancy of ¼ surround the nitrogen atom. The N-H distance is 0.82(6) Å with a unit cell of 5.0769(1) Å. However, Balogh *et al.*[133] have suggested that the low temperature structure is a different disordered cubic structure (*Fd3m*). In this structure, the Li partially occupies the 32e Wyckoff site compared to the Li occupying the 4c and 4d Wyckoff sites in the previous model. The nitrogen in this model are close-packed and slightly distorted with the D(H) in fully occupied sites (32e Wyckoff site) and a N-D bond length of 0.977 Å (no error measurement was reported). The unit cell has lattice parameters of 10.08728(18) Å at -173 °C and 10.1268(10) Å at 27 °C.

Balogh *et al.* have studied Li_2NH at 127 °C and concluded the structure is that of the cubic, anti-fluorite structure as seen previously at room temperature.[133] In this structure, the D(H) partly occupies the 192l Wyckoff site.

Using Li_2ND, a phase transformation was seen at 77 °C by Differential Scanning Calorimetry (DSC) measurements. This phase transformation was previously

reported by Forman.[134] At this point, the ordered structure changes to the disordered, anti-fluorite structure ($Fm\bar{3}m$). During PND experiments, Balogh *et al*. found that there were more reflections at the temperature points before the phase transition at -173 °C, -73 °C and 27 °C which indicated a more ordered structure at these temperatures.

Magnesium Amide ($Mg(NH_2)_2$) can be synthesised from the reaction of Mg with NH_3 at 300 °C.[135] Initial PND studies [136] showed that magnesium amide crystallises in the tetragonal $I4_1/acd$ space group. Further PND investigations confirmed this structure.[137] $Mg(NH_2)_2$ consists of two crystallographic distant (NH_2^-) groups connected to the Mg atom. The bonding interactions of the N-H in the two (NH_2^-) ligands have been found to be slightly different. A two step decomposition mechanism has been proposed for $Mg(NH_2)_2$ with the product of the decomposition process being MgNH and NH_3 being released.[138]

1.3 Microstructuring and Nanostructuring

Microstructuring and Nanostructuring refer to a method of reducing the particle size of a bulk material which in turn leads to an increase in the surface area. As the surface area increases, the amount of reactant atoms on the surface also increases. This, in turn should lead to an increased reactivity.

Microstructuring refers to structure sizes in the micron scale, so microstructured materials can vary, for example from 0.1 μm in size to 100 μm in size.

The idea of reducing the particle size of materials (i.e. nanostructuring) came to the fore in December 1959, when Richard Feynman presented his talk entitled "Plenty of Room at the Bottom".[139] During this presentation, he presented the idea of "*making, manipulating, visualising and controlling things on the small scale*" and that atoms could be arranged however we wanted. However, Robert Heinlein's '*Waldo*' short story in 1942 discussed the idea of nanostructuring, although James Clerk Maxwell nearly one hundred years previously had first introduced the idea.[140] "Nano" refers to the 10^{-9} scale with nanomaterials being a few nano metres in size.[141]

The microstructuring and nanostructuring of materials came to prominence with the synthesis of carbon nanotubes by Iijima in 1991.[142] Since this, a number of materials including metal carbides and oxide nanowires have been synthesised and their properties examined.[143] Reducing the particle size of these materials has resulted in improved performance, particularly for TiO_2 when used as a catalyst.[144]

Micro materials and nano materials can also possess different chemical properties than that of its equivalent bulk materials with gold being an example. Nanoparticles of gold results are chemically active while in its bulk material, gold is inert. This has allowed gold to be used in catalysis.[145]

1.3.1 Microstructuring and Nanostructuring in H_2 Storage Materials

Tailoring hydrogen storage materials, particularly complex hydrides, to meet US DOE targets represents a major effect in current H_2 storage research. Microstructuring or nanostructuring these materials is one method to tailor these materials to improve (a) the kinetics of H_2 uptake/release and (b) reversibility of H_2 storage.[3,146]

A number of strategies to reduce the particle size of H_2 storage materials have been employed in the literature. Due to the air sensitive nature of many hydride materials, common nanostructuring techniques, such as hydrothermal /solvothermal synthesis, templating and sol-gel synthesis cannot be employed as easily as for air stable materials.

The most common method for reducing the particle size for H_2 storage materials has been ball milling. Li-Mg-N-H systems, [147,148] $LiBH_4$ [149] and $LiAlH_4$[150] are amongst the materials that have been ball milled, and from this it has been seen that dehydrogenation kinetics are improved in the resulting milled hydrides. The drawback to ball milling can be uneven size distributions and agglomeration of particles in the sample.

A number of other strategies have been employed for the synthesis of nanostructured hydrogen storage materials. Nanoconfinement of hydrides has recently been employed.[151] This process involves the confinement of the nano-

sized hydride in a porous scaffold host. Nanoconfinement can improve the thermodynamics as the hydride thermodynamic stability is influenced by the surface area and the thermodynamics can also be improved by altering the surface of the scaffold host.[152] The kinetics of H_2 adsorption/desorption can also be improved due to the shorter distances involved and larger surface area.[153] $NaBH_4$ has been nanoconfined in a carbon aerogel with a pore size of 13 nm.[154] This resulted in a reduction of the dehydrogenation temperature from 230 ^oC in the bulk material to 140 ^oC in the confined material. Ammonia borane has also been nanoconfined in porous polystyrene fibres which results in dehydrogenation commencing at 85 ^oC which is an improvement of 15-20 ^oC for the bulk material.[155]

Li_2NH nanospheres have been produced by a metal plasma experiment, using the Kirkendall effect.[156] The Kirkendall effect is as a result of the comparative diffusion migrations among different atomic species which leads to a difference in the diffusions of the components of the reaction. This effect commonly leads to porosity in the component that has the lower melting point in the diffusion couple. [157] Due to the larger surface area, these nanospheres absorbed 6 wt. % H_2 at 200 ^oC and desorbed H_2 at a temperature of 179 ^oC which is a temperature of 115 ^oC lower than for the bulk material. Li_3N nanofibres can also improve H_2 absorption kinetics by a factor of three compared to the bulk material.[158]

1.4 '*Hydrogen Release Systems*'

One alternative solution to the hydrogen storage problem is that of a '*one shot*' hydrogen release system. These systems are typically non-reversible under normal operating conditions as described in Section 1.1.
One possible H_2 release system studied is $NaBH_4$ with water (known as the 'Millennium cell') [159]:

$$NaBH_4 + 2\ H_2O \rightarrow NaBO_2 + 4\ H_2 \quad (H_2 \text{ release} = 6.6 \text{ wt. \% } H_2) \qquad (1.26)$$

This system is encouraging both in terms of the wt. % of H_2 released and the temperature of H_2 release. This system has been proposed to be used as a H_2 storage system in vehicles. The system would work as follows: the components of the system, $NaBH_4$ (in solution) would be delivered to the service station.

The user would then fill up their vehicle with the new fuel and also dispose of their used fuel, which would be $NaBO_2$. The $NaBO_2$ would then be regenerated 'offsite' to produce the borohydride and the cycle repeated. The H_2 would be released from the $NaBH_4$ solution via the use of a catalyst in the fuel cell when heated to a temperature of 60-80 ^oC. The fuel could be in disposable cartridges. This would result in the user switching cartridges when refilling, resulting in quick refuelling times.

Solid state '*hydrogen release systems*' have also been investigated. These typically consist of two components, for example a hydroxide and hydride (Figure 1.8). The two components are mixed together and then heated with H_2 being released. The end products are the oxides of the hydride and hydroxide. When a solid state H_2 release system is compared with the $NaBH_4$ and H_2O system there are a number of differences. The regeneration of materials of the solid state system is accomplished by a carbothermic process. This process is energy intensive so would need to be greatly improved.[160] For $NaBH_4$ regeneration, a one pot electrolytic cell recycling has been proposed, resulting in the synthesis of the borohydride from the borate using H_2 and electricity.[161] In terms of safety considerations, the solid state system would be a safer system in terms of handling and storing due to the use of disposable cartridges.

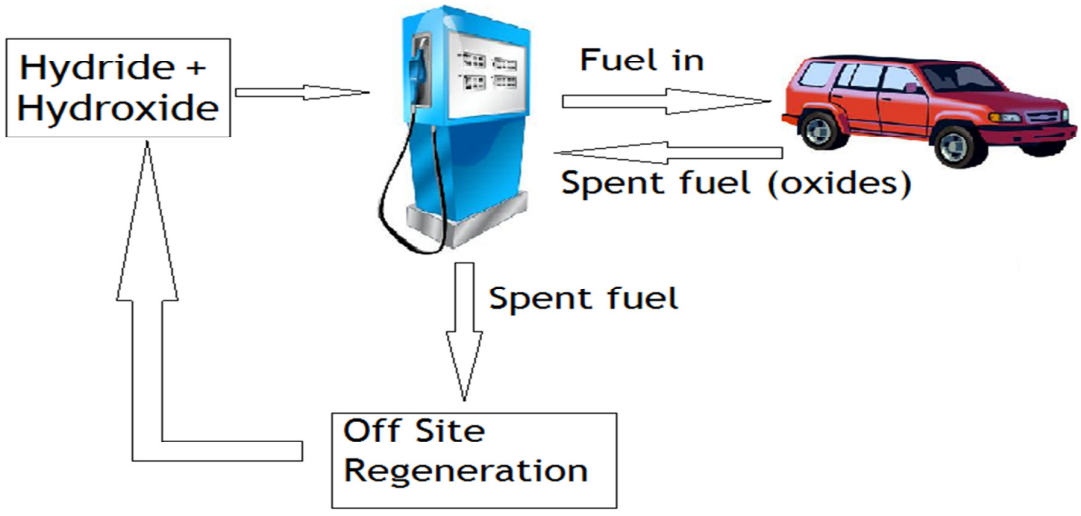

Figure 1.8: Proposed H_2 release system chain when the fuel source is hydrides with hydroxides. The off-site regeneration is described below in terms of the LiOH/LiH system.

Lu *et al.*[160] have investigated the LiOH or $LiOH.H_2O$ and LiH solid state system:

$LiOH + LiH \rightarrow Li_2O + H_2$ (H_2 release = 6.3 wt. % H_2) (1.27)

$LiOH.H_2O + 3\ LiH \rightarrow 2\ Li_2O + 3\ H_2$ (H_2 release = 8.8 wt. % H_2) (1.28)

The authors proposed that the reactants could be regenerated 'off site' as per the Millennium cell. The spent fuel, Li_2O would be regenerated by reacting with H_2O to produce LiOH (with a further reaction with H_2O to produce $LiOH.H_2O$). The LiOH would also be reacted with Mg (produced by the carbothermic reduction of MgO) to produce LiH.

Drozd *et al.* [162] investigated the $NaBH_4$ and $Mg(OH)_2$ H_2 release system which can theoretically release 5.2 wt. % H_2. They proposed that for H_2 release to occur, the $Mg(OH)_2$ first decomposed to MgO with the H_2O vapour reacting with the borohydride, to release the H_2:

$Mg(OH)_2 \rightarrow MgO + H_2O$ (1.29)

$NaBH_4 + 2\ H_2O \rightarrow NaBO_2 + 4\ H_2$ (1.30)

Particle size was found to be an important factor in determining the onset temperature of H_2 release and also on the percentage of H_2 release. Hand mixing (by mortar and pestle) released 54 wt. % of the theoretical H_2 content at 289 ^oC, while ball milling the reactants for 30 minutes led to 93 wt. % of the theoretical H_2 content being released at 286 ^oC.

$Mg(OH)_2$ and MgH_2 (theoretically releasing 4.5 wt. % H_2) system have also been investigated as a hydrogen release system.[163] Three H_2 desorption steps were seen at 150 ^oC, 350 ^oC and 450 ^oC on the Mass Spectrometry data.

1.4.1 Hydroxides: $Mg(OH)_2$ and LiOH

As hydroxides are typically used as a component of a H_2 release system, then the structure should be understood.

1.4.1.1 $Mg(OH)_2$ – Structure and Dehydrogenation

Nanostructured $Mg(OH)_2$ can be synthesised by a variety of methods involving reactant magnesium and water sources.[164,165, 166] There are many examples of the synthesis of nanostructured $Mg(OH)_2$, as $Mg(OH)_2$ is used as precursor for nanostructured MgO. $Mg(OH)_2$ crystallises in the hexagonal $P\bar{3}m1$ space group with lattice parameters of a= 3.15(1) Å and c= 4.80(2) Å.[167]

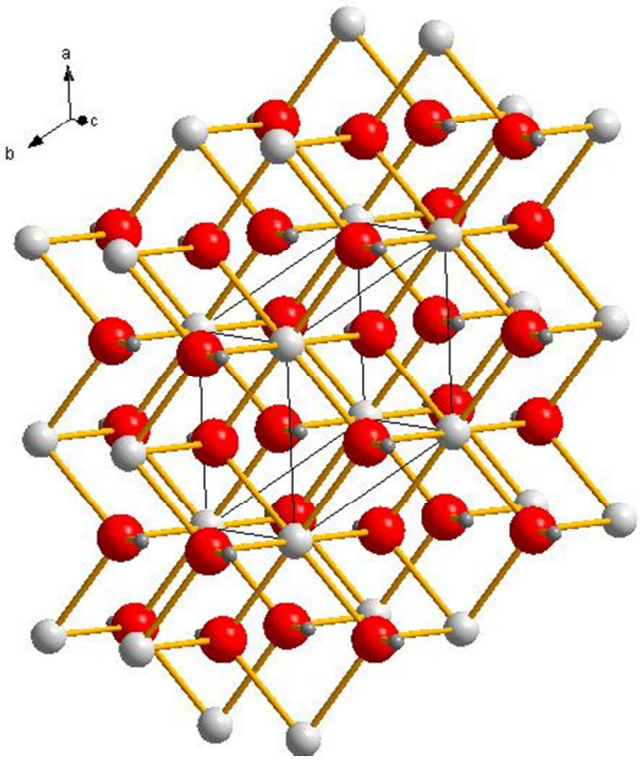

Figure 1.9: Structure of $Mg(OH)_2$. Red spheres are oxygen with the grey spheres representing hydrogen and the white spheres representing magnesium.

$Mg(OH)_2$ dehydrates when heated (≥350 ^oC + for bulk, typically 280 ^oC-330 ^oC for nanostructured $Mg(OH)_2$ [168]) to MgO and H_2O:

$$Mg(OH)_2 \rightarrow MgO + H_2O \qquad \Delta H = 98.4\ kJmol^{-1}\ H_2O\ [163] \qquad (1.31)$$

$Mg(OH)_2$ can indirectly store 4.83 wt% H_2. Due to its light weight, low cost and ease of synthesis, $Mg(OH)_2$ is an ideal material for a H_2 release system. $Mg(OH)_2$ could also be used as a precursor for the synthesis of a variety of magnesium based materials, as demonstrated for MgO.

1.4.1.2 LiOH- Structure and Dehydrogenation

LiOH crystallises in the tetragonal *P4/nmm* space group,[169] while the hydrated hydroxide, $LiOH.H_2O$ crystallises in the monoclinic *C2/m* space group (Figure 1.10).[170]

Perhaps due to the air sensitive nature of LiOH, which readily absorbs CO_2, no successful synthesis of nanostructured LiOH has been reported.

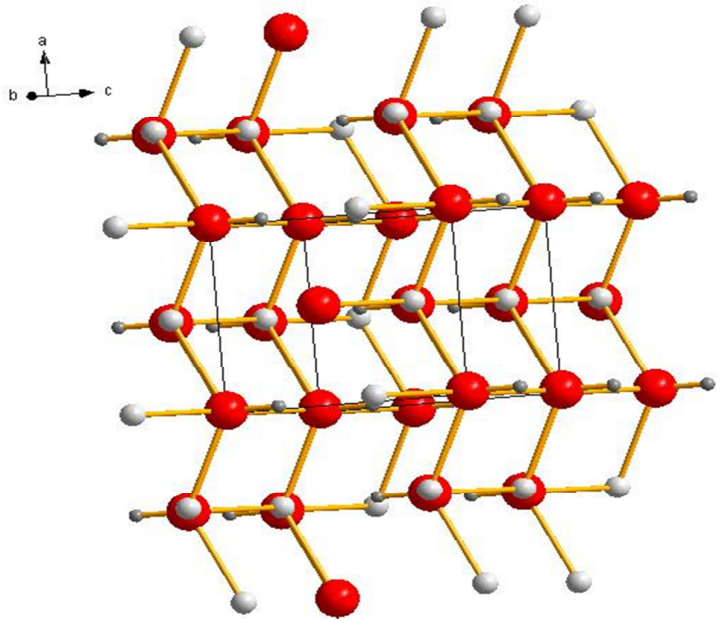

Figure 1.10: Structure of LiOH. The white spheres represent lithium, the red spheres represent oxygen and the grey spheres represent hydrogen

As per $Mg(OH)_2$, LiOH dehydrates to its corresponding oxide with the loss of water:

$$2LiOH \rightarrow Li_2O + H_2O \qquad \Delta H = 45.6\ kJ/mol^{-1} \qquad (1.32)$$

LiOH can indirectly store 4.2 wt% H_2, while the hydrated form, $LiOH.H_2O$ can indirectly store 7.2 wt. % H_2.

Due to the air sensitive nature of LiOH, which readily absorbs CO_2, synthesis of nanostructured LiOH is difficult to achieve.

1.5 Ammonia Storage

Ammonia has been used extensively for decades, particularly in the agricultural industry. Ammonia is cheap to produce and is produced in tonnes by industry *via* the Born Haber process.[171] The Born Haber process is an energy intensive process that requires an elevated temperature of 450 ^{o}C with a pressure of 2026 bar and the use of a catalyst to optimise the yield with the rate determining step being the dissociation of N_2 to N atoms which are chemisorbed onto the catalyst.[172] The limitation of the Born Haber process is that at low temperatures and pressure the yield of NH_3 produced would be commercially unviable and also the catalyst used must be high purity to minimise catalytic poisoning. [172] Ammonia can be, and is presently, transported in liquid form (it can be liquified at room temperature at a pressure of 10 atm) although this is associated with relatively high cost and demands important safety considerations. The main issues with transporting liquid ammonia arises from its high toxicity, its high flammability, its corrosive nature and also its unpleasant strong odour.[173]

One potential solution to this transport issue is to use a solid state material that is able to store ammonia in sufficient quantities with favourable uptake/release NH_3 kinetics.

Ammonia has been proposed previously as an energy vector in a green economy.[174,175,176] Ammonia can also be used as a source of H_2. For direct fuel cell use, the issues concerning the use of liquid NH_3 in fuel cells (in terms of safety) could be overcome by employing solid state storage. Hence, a solid state ammonia storage material could provide an attractive alternative in the transport of NH_3 and also as a source of H_2 for fuel cells.

1.6 Metal Ammines Introduction

Dihalide Metal ammines have the formula $M(NH_3)_nX_2$ where M= metal (Li, Na, Mg, Ca and transition metals such as Mn), X= halide (typically Cl, Br, I, F) and n= 1-8 molecules of NH_3. Research on the metal ammines began in the 1950s-70s mainly on transition metal ammines.[177,178,179] Until recently, there was limited research on the ammines (mainly structural investigations of selected compounds). Since, Christensen *et al.*[180] published studies on $Mg(NH_3)_6Cl_2$ in 2008

there has been a renewed interest in these compounds. This has led to the publications discussing other metal ammines including non-halides such as $LiBH_4.NH_3$ and $MgBH_4.NH_3$.[181,182]

1.6.1 Metal ammines Structure

The structure of one of the most promising potential NH_3 storage compounds, the hexaammine $Mg(NH_3)_6Cl_2$ was first derived by Olovsson as being a K_2PtCl_6 cubic structure.[183]

Subsequent DFT calculations refined the cubic (*Fm$\bar{3}$m)* structure with a lattice parameter of 10.1899(4) Å.[184] The magnesium is bonded to nitrogen with the halogen (chloride) situated at the corners of the unit cell as seen for the other hexaammines (Figure 1.11).

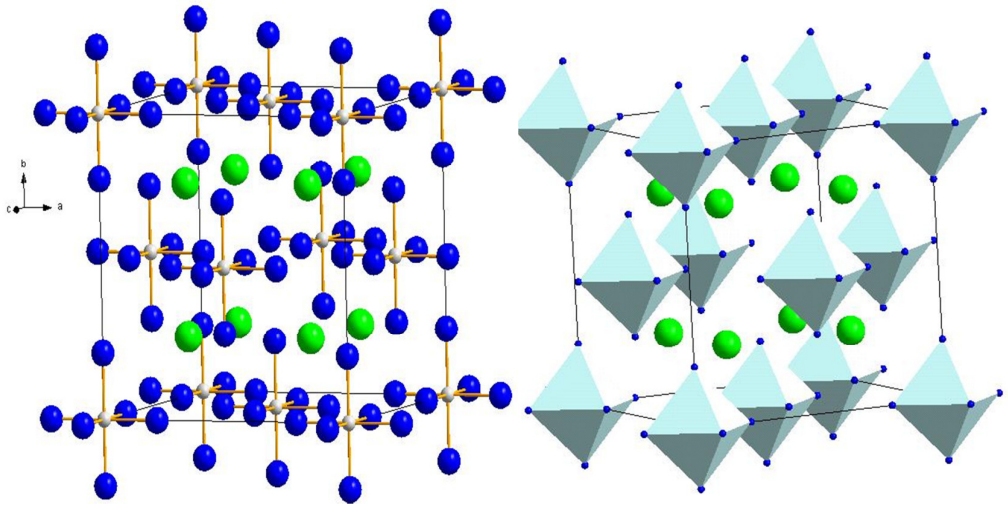

Figure 1.11: Structure of $Mg(NH_3)_6Cl_2$ and its polyhedral representation . The white spheres represent Mg, the green spheres represent chlorine and the blue spheres represent nitrogen. H atoms have been omitted for clarity.

The bonding of the hexaammines is unusual. It might be assumed that the metal-halogen bond in MX_2) remains intact following ammoniation (due to the low temperatures associated with the synthesis). However, this is not the case. The Mg-Cl bond is broken with Mg-N bonds forming and the halogen "free" in the unit cell, effectively acting as a counter anion to the complex cation $M(NH_3)_n^{2+}$.

Other known hexaammine, include those of the transition metals such as $Mn(NH_3)_6Cl_2$, $Fe(NH_3)_6Cl_2$, $Fe(NH_3)_6Br_2$ [185] and $Mn(NH_3)_6I_2$.[186] These all crystallise in the cubic *Fm$\bar{3}$m* space group and can be considered to be isostructural to each other. Commonly, only PXD (Powder X-ray Diffraction) and Single Crystal X-ray diffraction has been performed to elicit the structure of the hexaammines. For an accurate position of the hydrogens in the unit cell further PND (Powder Neutron Diffraction) is required.

Work by Sørby *et al*. used PND data coupled with molecular dynamics (MD) simulations to refine the structure of the $Mg(NH_3)_6Cl_2$ hexaammine.[187] The position of the nitrogen was modified from the 24e Wyckoff site to the 96j Wyckoff site which is now partly occupied. Further, in the modified structural model, deuterium (hydrogen) partially occupies two 96-fold positions. These changes were prompted by MD simulations which showed that the nitrogen is displaced from its average position. Hence, the ND_3 unit is more disordered than previously found and the model is in good agreement with the geometry of free ND_3. A summary of the original and newer disordered crystallographic models for the structure of $Mg(NH_3)_6Cl_2.6NH_3$ are presented in Tables 1.2 and 1.3:

Table 1.2: Crystallographic data for the original model of $Mg(NH_3)_6Cl_2$

Crystal System:			Cubic		
Space Group:			*Fm$\bar{3}$m* (225)		
Unit cell dimensions:			10.199(1) Å		
Atom	Wyckoff	x	y	z	Occupancy
Mg	4a	0	0	0	1
Cl	8c	¼	¼	¼	1
N	24e	0	0	0.2195(3)	1
D1	96k	0.0654(2)	0.0654(2)	0.2498(4)	$^3/_4$

Table 1.3: Structural model for $Mg(NH_3)_6Cl_2$ with disordered NH_3

Crystal System:		**Cubic**			
Space Group:		*Fm$\bar{3}$m* (225)			
Unit cell dimensions:		10.199(2) Å			
Atom	Wyckoff	x	y	z	Occupancy
Mg	4a	0	0	0	1
Cl	8c	¼	¼	¼	1
N	96j	0	0.021(1)	0.2161(3)	¼
D1	96k	0.0739(3)	0.0739(3)	0.2427(5)	½
D2	96j	0	0.0690(8)	0.2670(9)	¼

The structure of the magnesium chloride ammines, where n= 5,4,3 are not yet known. These ammines have not yet been successfully synthesised, isolated and characterised.

A number of the diammines ($M(NH_3)_2X_2$, M= Mg, X= Cl, Br,I) have been successfully synthesised and characterised.[188] The diammines are orthorhombic and depending on the halide they typically crystallise in the C*mmm* (no 65) or P*bam* (no 55) space groups.

$Mg(NH_3)_2Cl_2$ crystallises in the orthorhombic *Cmmm* space group (Figure 1.12) with lattice parameters of *a*= 8.180(2) Å, *b*= 8.2067(2) Å and *c*= 3.7550(1) Å. $Mg(NH_3)_2Cl_2$ is isostructural (has the same structure) with other diammines, $Cd(NH_3)_2Cl_2$[189] and $Fe(NH_3)_2Cl_2$.[190] $Mg(NH_3)_2Br_2$ (Figure 1.12) with lattice parameters of a= 5.944(2) Å, b= 11.876(3) Å and c= 3.983(1) Å and $Mg(NH_3)_2I_2$ form orthorhombic *Pbam* structures and are isostructural to each other. The nitrogen in the bromide (and the iodide) structure is located at the 4g Wyckoff site compared to the 4i site for the chloride structure and the hydrogen in the bromide is located at the 8i Wyckoff site compared to the 16r Wyckoff site in the chloride structure. These were originally synthesised *via* an autoclave reaction of magnesium and the corresponding ammonium halide.[188]

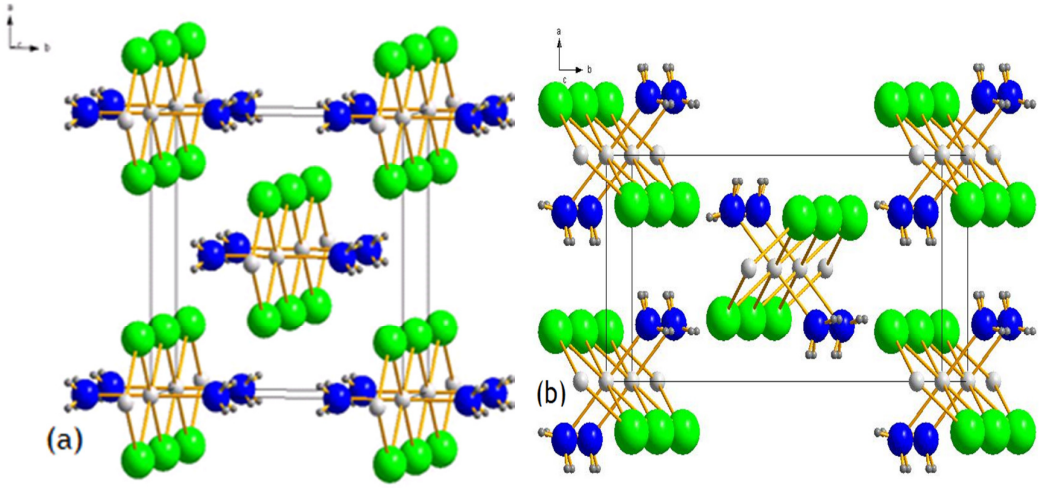

Figure 1.12: Structure of (a) $Mg(NH_3)_2Cl_2$ and (b) $Mg(NH_3)_2Br_2$ ((White spheres represent magnesium, green spheres represent chlorine/bromine, the blue spheres represent nitrogen and the grey spheres represent hydrogen)

The monoammines of the halides ($M(NH_3)X_2$, M=metal, X= Cl, Br,I) are the least studied of the halide monoammines. The only reported structures are that of $Ni(NH_3)Cl_2$, $Ni(NH_3)Br_2$, $Cu(NH_3)Cl_2$ and the aluminium monoammines which have the formula $Al(NH_3)X_3$.

The Ni compounds crystallise in the monoclinic *C*2/*m* space group. $Ni(NH_3)Cl_2$ (Figure 1.14) has lattice parameters of *a*= 14.8976(3) Å, *b*= 3.56251(6) Å and *c*= 13.9229(3) Å while isostuctural $Ni(NH_3)Br_2$ has lattice parameters of *a*= 15.5764(1) Å, *b*= 3.74346(3) Å and *c*= 14.4224(1) Å.[191]

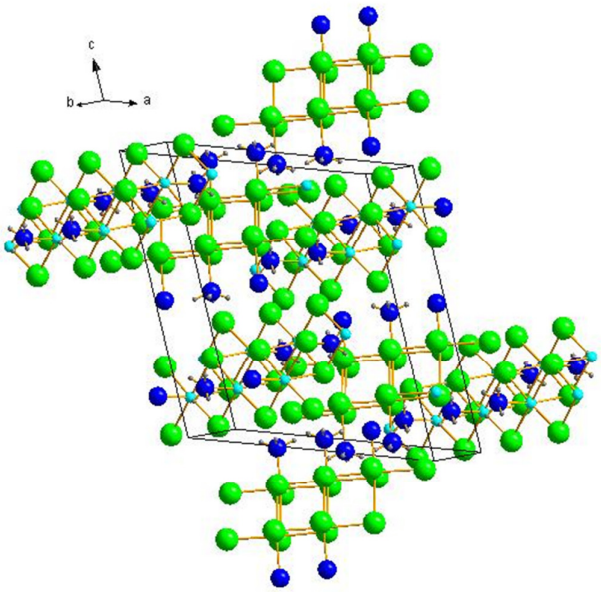

Figure 1.13: Structure of the monoammine, $Ni(NH_3)Cl_2$. The light blue spheres represent Nickel, green spheres represent chlorine, the dark blue spheres represent nitrogen and the grey spheres represent hydrogen

No monoammine structure has been reported for $Mg(NH_3)X_2$ where X= Cl, Br,I although it has been suggested that these compounds are isostructural to $Ni(NH_3)Cl_2$ and $Ni(NH_3)Br$.[191] The structure of $Cu(NH_3)Cl_2$ has been reported as cubic (space group $I2_13$).[192] The aluminium monoammines, $Al(NH_3)X_3$, where X= Cl, Br, I are isostructural to each other and crystallise in the orthorhombic P*bca* space group.[193,194]

1.6.2 Ammines as Ammonia Stores

Metal ammines are ideal solid state stores for NH_3 for use in both fuel cells and also for transport of NH_3. The metal ammines possess favourable gravimetric and volumetric NH_3 storage capacities and favourable kinetics (in terms of both NH_3 onset and release temperatures). Once full NH_3 desorption occurs, in principle MX_2 should be the end product. The deammoniated halide is readily reammoniated and cycled. A number of ammines have been synthesised and some of these are summarised in Table 1.4 in terms of their NH_3 capacity and desorption temperatures:

Table 1.4: Gravimetric capacities of metal ammines and their NH_3 decomposition temperatures

Metal ammine	NH_3 gravimetric Capacity (wt. %)	NH_3 desorption temperatures (^{o} C)	Ref
$Mg(NH_3)_2BH_4$	49.8	125-400	182
$Ca(NH_3)_8Cl_2$	55.1	52-302	180
$Al(NH_3)_6(BH_4)_3$	70.9	60-180	195
$Fe(NH_3)_6Br_2$	32.1	72-316	196
$Ni(NH_3)_6Cl_2$	44.0	167-427	180
$Ni(NH_3)_6Br_2$	31.9	90-260	197
$Mg(NH_3)_6Cl_2$	51.7	77-327	198
$Mg(NH_3)_6Br_2$	35.7	201-403	180
$Mg(NH_3)_6I_2$	26.9	265-439	180
$Mn(NH_3)_6Cl_2$	44.8	30-317	199
$Mn(NH_3)_6Br_2$	32.3	30-312	199

The volumetric capacities for the hydrogen storage for $Mg(NH_3)_6Cl_2$ has been reported as 0.115 Kg/L, 0.119 Kg/L for $Ni(NH_3)_6Cl_2$ and 0.112 Kg/L for $Mn(NH_3)_6Cl_2$.[180] For the majority of metal ammines in the literature, no deammoniation properties are reported. It is important that these are investigated if the metal ammines are to be considered for the solid state storage of NH_3.

1.6.3 Ammines- Indirect H_2 storage material

Ammines, as a source of ammonia, could be used as an H_2 storage material as ammonia itself is effectively a hydrogen carrier. For the splitting of NH_3 to N_2 and H_2 then, a catalyst is required. Amongst the ammines (Table 1.5), $Mg(NH_3)_6Cl_2$ can indirectly store 9.7 wt. % H_2 while $Ca(NH_3)_8Cl_2$ can indirectly store 8.5 wt. % H_2.

Table 1.5: Metal ammines that can be used for H_2 storage

Ammine	Gravimetric H_2 capacity (wt. %)	H_2 release temp range (^{o} C)	Ref
$Mg(NH_3)_6Cl_2$	9.1	*	180
$LiBH_4.^4/_3NH_3$	18.0	135-250	200
$Ca(NH_3)_8Cl_2$	11.8	*	180
$Mg(NH_3)_2BH_4$	16.0	125-400	184
$Al(NH_3)_6.3BH_4$	11.8	60-139 (7 hours)	195

*- H_2 release only temperatures are not known

The borohydride ammines process of release of H_2 is different to that of the dihalide ammines. In the borohydride ammines there is a stronger ability to promote coordination between the metal ion and NH_3 which maximises the H_2 release. The reason that H_2 release is more favourable than NH_3 release is that the lone pair atoms of the nitrogen are strongly attracted to the metal ions and the closer-packed $\{BH_4\}^-$ and NH_3 promotes the formation of N-H-H-B bonds with the release of H_2 and the stabilisation of NH_3.[195] The drawback of this process is the reaction is not reversible. A catalyst has been used to aid in the decomposition of lithium borohydride ammine, $LiBH_4(NH_3)_{4/3}$ where by using Co nanoparticles the material released 17.8 wt. % H_2 between 135 ^{o}C and 250 ^{o}C.[201]

For the metal dihalide ammines, splitting of NH_3 into N_2 and H_2 an appropriate catalyst is required. The catalysts typically used are ruthenium catalysts [202,203] and Ni-Pt catalysts [204] although the drawback with these catalysis are the high temperatures (>500 ^{o}C) associated with the cracking of the NH_3. There has recently been a renewed interest in catalysts that can split NH_3 at low temperature with the focus on transition metals, such as Fe nanoparticles [205] and Nickel.[206]

The proposed cycle for using metal ammines as a direct NH_3 or as an indirect H_2 store can be seen in Figure 1.14:

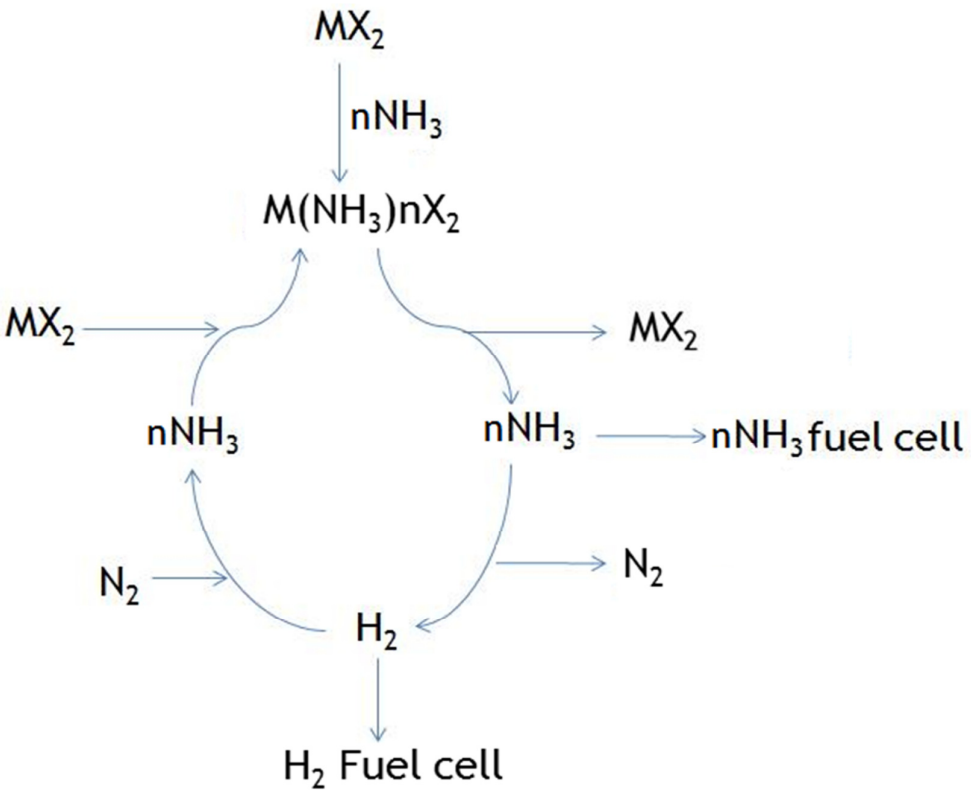

Figure 1.14: Metal ammines as indirect H_2 storage materials. Adapted from Ref 180

1.6.4 Ammines as a Component of a H_2 release system

Ammines can also be used as an integral component of a H_2 release system (section 1.4) with a hydride. Using the ammine with a hydride is similar to the H_2 release in the borohydride ammines. In an ammine-hydride system the ammine is the source of NH_3 and the hydride is the acceptor of the NH_3 to form an amide, so that H_2 release is maximised while minimising NH_3 release.

$Mg(NH_3)_6Cl_2$ has been studied in such a release system with LiH: [207]

$Mg(NH_3)_6Cl_2 + 6\ LiH \rightarrow MgCl_2 + 6\ LiNH_2 + 6\ H_2$ (H_2 release = 4.9 wt. % H_2) (1.32)

To minimise NH_3 release during mixing, $Mg(NH_3)_6Cl_2$ and LiH were ball milled at -40 °C. Another ammine, $LiBH_4.NH_3$ has been investigated as a H_2 release system with LiH, with H_2 release commencing at 60 °C.[208]

1.7 Scope of This Work

The research presented in this thesis covers the investigation of hydroxide and ammine hydrogen release systems and ammonia storage materials ($M(NH_3)_nX_2$ M= Mg, X= Cl, Br, I, n= 1-6).

The aim for the hydrogen release system study was to investigate the dehydrogenation behaviour of candidate materials, $Mg(NH_3)_6Cl_2$ + LiH, $Mg(NH_3)_6Cl_2$ +MgH_2 and LiH+ $Mg(OH)_2$. Using thermal programmed desorption (Thermo Gravemetric Analysis (TGA)- Differential Thermal Analysis (DTA) and Mass Spectrometry (MS)) measurements, the onset temperature of H_2 release was measured along with the weight loss and compared to that of the theoretical storage capacity. In the case of the systems involving $Mg(OH)_2$ particularly, the storage performance was studied as a function of morphology and particle size. The release systems involving $Mg(NH_3)_6Cl_2$ were also investigated using in-situ PND to understand the mechanisms involved in dehydrogenation. An understanding of the mechanisms would then present opportunities to modify the system to improve the kinetics of the systems further. For the hydroxide-hydride system, morphology of the samples was of great interest, as reducing the particle size should improve the kinetics of hydrogenation/dehydrogenation. Scanning Electron Microscopy (SEM) was employed to define the success of this approach as this allowed the morphology and sizes of the reactants and products to be studied.

The aim of the ammonia storage materials work was to synthesise the ammines, $M(NH_3)_nX_2$ (M=Mg, X=Cl, Br, I, n=6), structurally characterise them and investigate their deammoniation processes. The mechanistic detail of the deammonation processes of the ammines is unknown and the processes are crucial for optimising these materials.

1.8 References

[1] A. W. C van den Berg and C. O. Areán, *ChemComm*, 2008, **6**, 668.

[2] L. Schlapbach and A. Züttel, *Nature*, 2001, **414**, 353.

[3] J. M. Hanlon, H. Reardon, N. T-Ruiz and D. H. Gregory, *Aus. J. Chem*, 2012, **65**, 656.

[4] O. Khaselev and J. A. Turner, *Science*, 1998, **280**, 425.

[5] J. Barber, *Chem. Soc. Rev.,* 2009, **38**, 185.

[6] G. A .Deluga, J. R. Salge, L. D. Schmidt and X. E. Verykios, *Science*, 2004, **303**, 993.

[7] G. W. Huber, S. Iborra and A. Corma, *Chem. Rev.*, 2006, **106**, 4044.

[8] D. Teichmann, W. Arch, P. Wasserschield and R. Freymann, *Energy Environ. Sci.*, 2011, **4**, 2767.

[9] A. Midilli, I. Dincer and M. Ay, *J. Energy Policy*, **34**, 3623.

[10] B. Sorensen, *Hydrogen and Fuel Cells- Emerging Technologies and Applications 2nd Edn.*, Elsevier, 2012.

[11] A. Züttel, *Naturwissenschafen*, 2004, **91**, 157.

[12] U. Eberle, M. Felderhoff and F. Schüth. *Angew. Chem. Int. Ed.,* 2009, **48**, 6608.

[13] Q. Li, *DOE Hydrogen Program Annual Report*, 2009, **778**.

[14] HyFLEET : CUTE hydrogen powered buses accessed on 28th Feb 2012 at: http://www.global-hydrogen-bus-platform.com

[15] Hyfleet : Cute Final Public Report accessed on 7th Jan 2013 at: http://www.global-hydrogen-bus-platform.com/InformationCentre/Downloads

[16] S.M. Aceves, G. D. Berry, J. Frias and F. E. Loza, *Int. J. Hydrogen Energy*, 2006, **31**, 2274.

[17] US DOE, Liquid Hydrogen Tanks accessed on 28th Feb 2012 at: http://www1.eere.energy.gov/hydrogenandfuelcells/delivery/current_technology.html

[18] US DOE targets accessed on 28th Feb 2012 at:

http://www1.eere.energy.gov/hydrogenandfuelcells/storage/current_technology.html.

[19] S. Basu, *Recent Trends in Fuel Cells Science and Technology*, Springer Publishing, 2007.

[20] N. Rees and R. Compton*, Energy Environ. Sci.,* 2011, **4**, 1255.

[21] H. A. Gaasteiger, S. S. Kocha, B. Sompalli and F. T. Wagner*, Appl. Catal. B.*, 2005, **56**, 9.

[22] E. Antolini, J. R. C. Salgado and E. R. Gonzalez, *Appl. Catal. B.*, 2006, **63**, 137.

[23] D. Shekhawat, J. J. Spivey and D. A. Berry, *Fuel Cells*, Elsevier Publishing, 2011.

[24] C. Y. Wang, *Chem. Rev.,* 2004, **104**, 4727.

[25] A. J. Jacobson, *Chem. Mater.*, 2010, **22**, 660.

[26] N. Q. Minch, *J. Am. Ceram. Soc.*, 1993, **76**, 563.

[27] B. C. H. Steele, *Solid State Ionics*, 2000, **129**, 95.

[28] Z. Zhong, *Solid State Ionics*, 2007, **178**, 213.

[29] S. P. Jiang, *J. Mater. Sci.*, 2008, **43**, 6799.

[30] Y. Matsuzaki and I. Yasuda, *Solid State Ionics*, 2000, **132**, 261.

[31] A. L. Dicks, *Curr. Opin. Solid State Mater. Sci.*, 2004, **8**, 379.

[32] T. Fukui, S. Ohara, H. Okawa, M. Nati and K. Nogi, *J. Eur. Ceram. Soc.,* 2003, **23**, 2835.

[33] M. J. Escudero, T. Rodrigo, J. Soler and L. Daza, *J. Power Sources*, 2003, **18**, 23.

[34] R. C. Makkus, K. Hemmes and J. H. W. de Wit, *J. Electrochem. Soc.*, 1994, **141**, 3429.

[35] T. E. Springer, T. A. Zawodzinski and S. Gottesfeld, *J. Electochem. Soc.*, 1991, **138**, 2334.

[36] M. J. Larsen and E. M. Skou, *J. Power Sources*, 2012, **202**, 35.

[37] W. Schmittinger and A. Vahidi, *J. Power Sources*, 2008, **180**, 1.

[38] X. Cheng, Z. Shi, N. Glass, L. Zhang, J. Zhang, D. Song, Z-S Liu, H. Wang and J. Shen, *J. Power Sources*, 2007, **165**, 739.

[39] A. S. Aricò, S. Srinivasan and V. Antonucci, *Fuel Cells*, 2001, **1**, 133.

[40] H. Liu, C. Sung, L. Zhang,J. Zhang, H. Wang and D. P. Wilkinson, *J. Power Sources*, 2006, **155**, 95.

[41] NASA Fuel Cells: *A Better Energy Source for Earth and Space*, accessed on 1st March 2012 at: http://www.nasa.gov/centers/glenn/technology/fuel_cells.html

[42] M. Schulze and E. Gűlzow, *J. Power Sources*, 2004, **127**, 252.

[43] G. F. McLean, T. Niet, S. P-Richard, N. Djilali, *Int. J. Hydrogen Energy*, 2002, **27**, 507

[44] J. R. Varcoe and R. C. T. Slade, *Fuel Cells*, 2005, **5**, 187.

[45] E. Antolini and E. R. Gonzalez, *J. Power Sources*, 2010, **195**, 3431.

[46] H. Chunzhi, H. K. Kunz and J. M. Fenton, *J. Electrochem. Soc.*, 1997, **144**, 970.

[47] R. A. Wynveen, *Prepr.- Am. Chem. Soc., Div.Pet.Chem.*, 1961, **6**, 49.

[48] E. J. Simons, E .J. Cairns and D.J. Surd, *J. Electrochem. Soc.,* 1969, **116**, 556.

[49] N. Rees and R. Compton*, Energy Environ. Sci.,* 2011, **4**, 1255.

[50] R. A. Michaels, *Environ. Health Perspect.*, 1999, **107**, 617.

[51] F. J. Vidal-Iglesias, N, Garcia-Araez, V. Montiel, J. M. Feliu and A. Aldaz, *Electrochem. Commun.*, 2003, **5**, 22.

[52] A. C. A. De Vooys, M .T. M. Koper, R. A. Van Saten and J. A. R. Van Veen, *J. Electroanal. Chem.*, 2001, **506**, 127.

[53] R. Halseid, P. J. S. Vie and R. Tunold, *J. Power Sources*, 2006, **154**, 343.

[54] A. S. Chellappa, C. M. Fischer and W. J. Thomson, *Appl. Catal. A*, 2002, **227**, 231.d

[55] M. Ni, M. K. H. Leung and D.Y.C. Leung, *Int. J. Energy Res.*, 2009, **33**, 943.

[56] A. Wojcik, H. Middleton, I. Damopoulos and J. Van Herle, *J.Power Sources*, 2003, *118*, 342.

[57] S. Farhad and F. Hamdullahpur, *J. Power Sources*, 2010, **195**, 3084.

[58] Q. Ma, R. Peng, Y. Lin, J. Gao and G. Meng, *J. Power Sources*, 2006, **161**, 95.

[59] G. G. M. Fournier, I. W. Cumming and K. Hellgardt, *J. Power Sources*, 2006, **162**, 198.

[60] Y. Lin, R. Ran, Y. Guo, W. Zhou, R. Cai, J. Wang and Z. Shao, *Int. J. Hydrogen Energy*, 2010, **35**, 2637.

[61] IUPAC definations accessed at: http://old.iupac.org/reports/2001/colloid_2001/manual_of_s_and_t/node16.html on 4 th Feb 2013

[62] L. Schalpbach and A. Zűttel, *Nature*, 2001, **414**, 353.

[63] T. K. Mandal and D. H. Gregory*, Annu. Rep. Prog. Chem., Sect. A: Inorg. Chem.*, 2009, **105**, 21.

[64] J. Weikamp, M. Fritz and S. Ernst, *Int. J. Hydrogen Energy*, 1995, **20**, 967.

[65] S. S. Han, H. Furukawa, O. M. Yaghi and W.A. Goddard, *J. Am. Chem. Soc.*,2008, **130**, 11580.

[66] N. B. McKeown and P.M. Budd, *Chem. Soc. Rev.*, 2006, **35**, 675.

[67] N. L. Rosi, J. Eckert, M. Eddaoudi, D. T. Vodak, J. Kim, M. O. Keeffe and O. M. Yaghi, *Science*, 2003, **300**, 1127.

[68] M. Latroche, S. Surble, C. Serre, C. Mellot-Draznieks, P. L. Llewellyn, J.-H. Lee, J.-S. Chang, S .H. Jhung and G. Ferey, *Angew. Chem. Int. Ed*., 2006, **45**, 8227.

[69] Y. Yan, I. Telepeni, S. Yang, X. Lin, W. Kockelmann, A. Dailly, A. J. Blake, W. Lewis, G. S. Walker, D. R. Allan, S. A. Barnett, N. R. Champness and M. Schröder, *J. Am. Chem. Soc.*, 2010, **132**, 4092.

[70] C. O. Areán, S. Chaven, C. P. Cabello, E. Garrone and G. T. Palomino, *ChemPhysChem*., 2010, **11**, 3237.

[71] Y. Lang and R. T. Yang, *Langmuir*, 2007, **23**, 12937.

[72] R. C. Lochan, R. Z. Khaliullin and M. H. Gordon, *Inorg. Chem*., 2008, **47**, 4032.

[73] K. Gedrich, I. Senkovska, N. Klein, U. Stoeck, A. Henschel, M. R. Lohe, I. A. Baburin, U. Mueller and S. Kaskel, *Angew. Chem. Int. Ed,* 2010, **49**, 8489.

[74] S. McWhorter, C. Read, G. Ordaz, and N. Stetson, *Curr. Opin. Solid State Mater. Sci*., 2011, **15**, 29.

[75] Y. Li and R. T. Yang, *J. Am. Chem. Soc.,* 2006, **128**, 8136.

[76] K. Gedrich, I. Senkovska, N. Klein, U. Stoeck, A. Henschel, M. R. Lohe, I.A. Baburin, U. Mueller, and S. Kaskel, *Angew. Chem. Inter. Ed*., 2010, **49**, 8489.

[77] L. Wang and R. T. Yang, *Energy Environ. Sci*., 2008, **1**, 268.

[78] C. Zlotea, R. Campesi, F. Cuevas, E. Leroy, P. Dibandjo, C. Volkringer, T. Loiseau, G. Ferey and M. Latroche, *J. Am. Chem. Soc*., 2010, **132**, 2991.

[79] R. Strobel, J. Garche, P. T. Moseley, L. Jorissen and G. Wolf, *J. Power Sources*, 2006, **159**, 781.

[80] X. Hu, M. Fan, B. F. Towler, M. Radosz, and D .A. Bell, *Hydrogen Adsorption and Storage*, Elsevier Publishing, 2011.

[81] A. Chambers, C. Park, R.T.K. Baker and N.M. Rodriguez, *J.Phys.Chem.B*, 1998, **102**, 22

[82] A. C. Dillon, K. M. Jones, T. A. Bekkedahl, C. H. Klang, D. S. Bethune and M. J. Heben, *Nature*, 1997, **386**, 377.

[83] Y. Yürüm, A. Taralp, and T. N. Veziroglu, *Int. J. Hydrogen Energy*, 2009, **34**, 3784.

[84] G. Srinivas, Y. Zhu, R. Piner, N. Skipper, M. Ellerby and R. Ruoff, *Carbon*, 2010, **48**, 630.

[85] M. Pumera, *Energy Environ. Sci.,* 2011, **4**, 668.

[86] H. Wan, Q. Gao and J. Hu, *J. Am. Chem. Soc*., 2009, **131**, 7016.

[87] J. Biener, M. Stadermann, M. Suss, M. A. Worsley, M. M. Biener, K. A. Rose and T. F. Baumann, *Energy Environ. Sci.,* 2011, **4**, 656.

[88] G. Seifert and J. Schulte, *Phys. Lett. A.,* 1994, **188**, 364.

[89] I. Cabria, M. J. Lopez and J. A. Alonso, *J. Chem. Phys*., 2005, **123**, 204721.

[90] K. Y. Lin, W. T. Tsai and J. K. Chang, *Int. J. Hydrogen Energy,* 2010, **35**, 7555.

[91] P. Guay, B. L. Stansfield and A. Rochefort, *Carbon*, 2004, **42**, 2187.

[92] K. F. Aguey-Zinsou and J. R. Ares-Fernandez, *Energy. Environ. Sci*., 2010, **3**, 526.

[93] W. W. Grochala and P. P. Edwards, *Chem. Rev.,* 2004, **104**, 1283.

[94] C. P. Chen, B. H Liu, Z. P Li, J. Wu and Q. D. Wang, *Z. Phys. Chem.,* 1993, **181**, 259.

[95] B. Sakintuna, F. Lamari-Darkrim and M. Hirscher, *Int. J. Hydrogen Energy*, 2007, **32**, 1121.

[96] K. F. Aguey-Zinsou, J. R. Ares-Fernandez, T. Klassen and R. Bormann, *Int. J. Hydrogen Energy*, 2007, **32**, 2400.

[97] F. Zeppelin, H. Reule and M. Hirscher, *J. Alloys. Cmpd*., 2002, **330**, 723.

[98] W. Osborn, T. Markmaitree and L. Shaw, *Nanotechnology*, 2009, **20**, 204028.

[99] S. Orimo, Y. Nakamori, J. R. Eliseo, A. Züttel and C. M. Jensen, *Chem. Rev*., 2007, **107**, 4111.

[100] A. Züttel, A. Borgschulte and S. Orimo, *Scripta Mater*., 2007, **56**, 823.

[101] D. S. Stasinevich and G. A. Egorenko, *Russ. J. Inorg. Chem*., 1968, **13**, 341.

[102] P. Mauron, F. Buchter, O. Friederichs, A. Remhof, M. Bielmann, C. N. Zwicky, A. Züttel, *J. Phys. Chem. B* 2008, **112**, 906

[103] A. Züttel, S. Renstch, P. Fischer, P. Wenger, P. Sudan, P. Mauran and C. Emmenegger. *J. Alloys Compd*., 2003, **356**, 515.

[104] E. Ronnebro and E. H. Majzoub, *J. Phys. Chem. B*., 2007, **111**, 12045.

[105] G. L. Soloveichik. Y. Gao, J. Rijssenbeek, M. Andrus, S. Kniajanski, R. C. Bowman Jnr, S-J Hwang and J-C Zhao*, Int. J. Hydrogen Energy*, 2009, **34**, 916.

[106] B. Bogdanovic´ and M. Shwickardi, *J. Alloys Compd*. 1997, **1**, 253.

[107] M. Fitchner, O. Fuhr and O. Kircher, *J. Alloys Compd.,* 2003, **356**, 418.

[108] D. S. Easton, J. H. Schneibel and S. A. Speakman, *J. Alloys Compd*., 2005, **398**, 245.

[109] D. H. Gregory, *J. Mater. Chem*, 2008, **18**, 2321.

[110] F. W Dafert and R. Miklauz, *Monatsh. Chem*, 1910, **31**, 981.

[111] P. Chen, Z. Xiong, J. Luo, J. Lin and K . L. Tan, *Nature*, 2002, **420**, 302.

[112] W. I. F. David, M. O. Jones, D. H. Gregory, C. M. Jewell, S .R. Johnson and P. P. Edwards, *J. Am. Chem. Soc*., 2007, **129**, 1594.

[113] P. Chen, Z. Xiong, J. Luo, J. Lin and K. L. Tan, *J. Phys. Chem. B*, 2003, **107**, 10967.

[114] T. Markmaitree, R. Ren and L.L. Shaw, *J. Phys. Chem. B*, 2006, **110**, 20710.

[115] Y. Hu and E. Ruckenstein, *J. Phys. Chem. A*., 2003, **107**, 9737.

[116] T. Ichikawa, N. Hanada, S. Isobe, H. Leng and H. Fujii, *J. Phys. Chem. B*., 2004,**108**, 7887.

[117] J. Hu, Z. Xiong, G. Wu, P. Chen, K. Murata and K. Sakata, *J. Power Sources*, 2006, **159**, 120.

[118] Z. T. Xiong, G. T. Wu, J. J. Hu and P. Chen, *Adv. Mater*, 2004, **16**, 1522.

[119] Y. Nakamoori, G, Kitahara, K. Miwa, N. Ohba, T. Noritake, S. Towata and S. Orimo, *J. Alloys Compd.,* 2005, **402**, 396.

[120] D. H. Gregory, P. M. O'Meara, A. G. Gordon, J. P. Hodges, S. Short and J. D. Jorgensen, *Chem. Mater*., 2002, **14**, 2063.

[121] M. Mali, J. Roos and D. Binkmann, *Phys. Rev. B*, 1987, **36**, 3888.

[122] A. Lazicki, B. Maddox, W. J. Evans. C. S. Yoo, A. K. McMahan, W. E. Pickett, R. T. Scalettar, M. Y. Hu, *Phys. Rev. Lett*., 2005, **95**, 166503.

[123] E. Zintl and G. Brauer, *Z. Elektrochem*., 1935, **41**, 102.

[124] A. Rabenau and H. Schulz, *J. Less-Common Met.*, 1976, **50**, 155.

[125] A. W. Titherley, *J. Chem. Soc. Trans.*, 1894, **65**, 504.

[126] V. R. Juza and K.Z. Opp, *Z. Anorg. Allg. Chem.*, 1951, **266**, 325.

[127] H. Jacobs and R.Z. Jura, *Z. Anorg. Allg. Chem*, 1972, **391**, 271.

[128] J. B. Yang, X. D. Zhou, Q. Cui, W. J. James and W. B. Yelon, *Appl. Phys. Lett.*, 2006, **8**, 41914.

[129] M. H. Sørby, Y. Nakamura, H. W. Brinks, T. Ichikawa, S. Hino, H. Fujii and B. C. Hauback, *J. Alloys Compd.*, 2007, **428**, 297.

[130] K. Ohoyama, Y. Nakomori, S. Orimo and K. Yamada, J. Phys. Soc. Jpn., 2005, 393, 264.

[131] T. Noritake, H. Nozaki, M. Aoki, S. Towata, G. Kitahara, Y. Nakamori and S. Orimo, *J. Alloys Compd.,* 2005, **393**, 264.

[132] K. Ohoyama, Y. Nakamori, S. Orimo and K. Yamada, *J. Phys. Soc. Jpn.*, 2005, **74**, 483.

[133] M. P. Balogh, C. Y. Jonwa, J. F. Herbst, L. G. Hector Jr and M. Kundrat, *J. Alloys Compd.,* 2006, 420, 326

[134] R. Forman, *J. Chem. Phys.*, 1971, **55**, 1987.

[135] J. Hu, G. Wu, Y. Liu, Z. Xiong, P. Chen, K. Murata, K. Sakata and G. Wolf, *J. Phys. Chem. B*, 2006, **110**, 14688.

[136] H. Jacobs, *Z. Anorg. Allg. Chem.*,1971, 382, 97.

[137] M. H. Sørby, Y. Nakamura, H. W. Brinks, T. Ichikawa, S. Hino, H. Fujii and B. C. Hauback, *J. Alloys Compd.*, 2007, **428**, 297.

[138] Y. Song and R. Yang, *Int. J. Hydrogen Energy*, 2009, **34**, 3778.

[139] R. Feynman, *Caltech Engineering and Science*, 1960, **23**, 26.

[140] J. Ramsden, *Nanotechnology: An Introduction,* Elsevier Publishing, Oxford, 2011.

[141] C. Suryanarayana, *Adv. Eng. Mater.*, 2005, **7**, 983.

[142] S. Iijima, *Nature*, 1991, **354**, 56.

[143] C. N. R. Rao, F. L. Deepak, G. Gundiah and A. Govindaraj, *Prog. Solid State Chem.*, 2003, **31**. 5.

[144] J.M. Macak, H. Tsuchiya, A. Ghicov, K. Yasuda, R. Hahn, S. Bauer and P. Schmuki, *Curr. Opinin. Mater. Sci.*, 2007, **11**, 3.

[145] M. Haruta and M. Date, *Appl. Catal. A.*, 2001, **222**, 427.

[146] H. Reardon, J.M. Hanlon, R. W. Hughes, A.G-Jopek, T. K. Mandal and D. H. Gregory, *Energy Environ. Sci.,* 2012, **5**, 5951.

[147] F. E. Pinkerton, *J. Alloys Compd.,* 2005, **400**, 76.

[148] R. R. Shahi, T. P. Yadav, M .A. Shaz and O. N. Srivastava, *Int. J. Hydrogen Energy*, 2008, **33**, 6188.

[149] B. J. Zhang, B. H. Liu and Z. P. Li, *J. Alloys Compd.*, 2011, **509,** 751.

[150] M. Fichtner, P. Canton, O. Kircher and A. Lèon, *J. Alloys Compd.*, 2005, **404,** 732.

[151] P. E. de Jongh and P.Adelhelm, *ChemUSChem*, 2010, **3**, 1332.

[152] R. D. Stephens, A. F. Gross, S. L. Van Atta, J. J. Vago and F. E. Pinkerton, *Nanotechnology*, 2009, **20**, 204018.

[153] J. J. Vago, *Curr. Opin. Mater. Sci.*, 2011, **15**, 52.

[154] M. Fichtner, Z. Z-Karger, J. Hu, A. Roth and P. Weider, *Nanotechnology*, 2009, **20**, 204029.

[155] Z. Kurban, A. Lovell, S. M. Bennington, D. W. K. Jenkins, K. R. Ryan, M. O. Jones, N. T. Skipper and W. I. F. David, *J. Phys .Chem. C*, 2010, **114**, 21201.

[156] L. Xie, J. Zheng, X. Liu, Y. Li and X. Li, *Chem Mater.*, 2008, **20**, 282.

[157] B. Liu and H. C. Zeng, *J. Am. Chem. Soc.*, 2004, **126**, 16744.

[158] D. H. Gregory, International Patent WO2004057070.

[159] U.S. Department of Energy, Office of Basic Energy Science: Basic Research Needs for the Hydrogen Economy, Report of BES Workshop on Hydrogen Production, Storage and Use, Argonne National Laboratory, May 13-15 2003.

[160] J. Lu, Z. Z Fang and H. Y. Song, *J. Power Sources*, 2007, **172**, 853.

[161] US DOE Annual Report 2007, http://www.hydrogen.energy.gov/pdfs/progress07/iv_b_2_moreno.pdf, accessed 20th March 2012

[162] V. Drozd, S. Saxena, S. V. Garimella, A. Durygin, *Int. J. Hydrogen Energy*, 2007, **32**, 3370.

[163] F. Leardini, J. R. Ares, J. Bodega, J.F. Fernandez, I. J. Ferrer and C. Sanchez, *Phys. Chem .Chem. Phys.*, 2010, **12**, 572.

[164] D. Jin, X. Gu, X. Yu, G. Ding, H. Zhu and K. Yao, *Mater. Chem. Phys.*, 2008, **112**, 962.

[165] L. Zhuo, J. Ge, L. Cao and B. Tang, *Cryst. Growth Des.*, 2009, **9**, 1.

[166] G. Zou, R. Liu, W.Chen and Z. Xu, *Mater. Res. Bull.,* 2007, **42**, 1153.

[167] L. Desgranges, G. Calvarin and G. Chevrier, *Acta Crystallogr.B.,* 1996, **52**, 82.

[168] Y. Ding, G. Zhang, H. Wu, B. Hai, L. Wang and Y. Qian, *Chem. Mater.*, 2001, **13**, 435.

[169] L. S. Mair, *Acta. Crystallogr. B.*, 1978, **34**, 542.

[170] L. Ojamaee, K. Hermansson, C. Pisani, M. Causa and C. Roetti, *Acta Crystallogr. B.*, 1994, **50**, 268.

[171] R. Schlögl, *Angew. Chem. Int. Ed.,* 2003, **42**, 2004.

[172] C. E. Housecroft and A. G. Sharpe, *Inorganic Chemistry 1st Edn*, Prentice Hall, 2001.

[173] http://www.cdc.gov/niosh/idlh/766417.html, accessed 25 th November 2011.

[174] L. Green Jnr, *Int. J. Hydrogen Energy*, 1982, **7**, 335.

[175] C. H. Christensen, T. Johannessen, R. Z. Sørensen and J. K. Nørkev, *Catal.Today*, 2006, **111**, 140.

[176] C. Zamfirescu and I. Dincer, *Fuel Process.Technol.,* 2009, **90**, 729.

[177] J .P. Smith and W. W. Wendlandt, *J. Inorg .Nucl. Chem.*, 1964, **26**, 1157.

[178] P. J. Hendea, *Spectrochimica Acta*, 1967, **23A**, 1275.

[179] G. W. Watt and D .R. Foerster, *J. Inorg. Nucl. Chem*, 1959,**11**, 253.

[180] R. Z. Sorensen, J. S. Hummelshoj, A. Klerke, J. B. Reves, T. Vegge, J. K. Norskov and C. H. Christensen, *J. Am. Chem. Soc*, 2008, **130**, 8660.

[181] S. R. Johnson, W .I .F. David, D. M. Royse, M. Sommariva, C. Y. Tang, F. P. A. Fabbiani, M. O Jones and P. P. Edwards, *Asian J. Chem*., 2009, **6**, 849.

[182] G. Soloveichik. J-H Her, P. W. Stephens, Y. Gao, J. Rijssenbeek, M. Andrus and J-C Zhao, *Inorg. Chem.,* 2008, **47**, 4290.

[183] I. Olovsson, *Acta Cryst*., 1965, **18**, 889.

[184] I. C. Hwang, T. Drews and K. Seppalt, *J. Am. Chem. Soc*., 2000, **122**, 8486.

[185] R. Essmen, G. Kreiner, A. Neimenn, D. Rechenbach, A. Schmeiding, T. Sichla, U. Zachwieja, *Z. Anorg. Allg. Chem*., 1996, **622**, 1161.

[186] H. Jacobs, J. Bock and C. Stuve, *J. Less Common Met*., 1987, **134**, 207.

[187] M. H. Sørby, O. M. Løvvik, M. Tsuboto, T. Ichikawa, Y. Kojima and B. C. Hauback, *Phys. Chem. Chem. Phys.,* 2011, **13**, 7644.

[188] A. Leinweber, M.W. Fredriszik and H.Jacobs, *J. Solid. State. Chem.,* 1999, **147**, 229.

[189] C. H. MacGillavry and J .M. Bijvoet, *Z. Kristallogr. Kristallgeom. Kristallphys. Kristallchem*., 1936, **94**, 231.

[190] S. Bremm and G. Meyer, *Z. anorg. allg. Chem*, 2003, **629**, 1875.

[191] A. Leineweber, H. Jacobs and H. Ehrenberg, *Z. anorg. allg. Chem,* 2000, **626**, 2146.

[192] G. Margraf, J. W. Bats, M. Bolte, H. W. Lerner and M. Wagner, *ChemComm*., 2003, **8**, 956.

[193] K. N. Semenenko, E. B. Lobkovskii, V. B. Polyakova, I. I. Korobov and O. V. Kravchenko, *Koordinats Khim*., 1978, **4**, 1649.

[194] H. Jacobs and F. O. Schroeder, *Z. anorg. allg. Chem*., 2002, **628**, 327.

[195] Y. Guo, X. Yu, W. Sun, D. Sun and W. Yang, *Angew.Chem.Int.Ed*., 2011, **50**, 1087.

[196] M. Grant, M.Sci. Thesis, University of Glasgow, 2010.

[197] K. Rejitha, T. Ichikawa and S. Mathew, *J. Therm. Anal. Calorim.,* 2011, **103**, 515.

[198] C. H. Christensen, R. Z. Sørensen, T. Johannessen, U. J. Quaade, T. D. Elmøe, R. Køhler and J. K. Nørskov, *J. Mater. Chem.,* 2005, **15**, 4106.

[199] H. Reardon, J. M. Hanlon, M. Grant, I. Fullbrook and D. H. Gregory, *Crystals*, 2012, **2**, 123.

[200] S. Appari, V. M. Janardhana, S. Jayanti, L. Maier, S. Tischer and O. Deutschmann, *Chem. Eng. Sci.,* 2011, **66**, 5184.

[201] X. Zheng, G. Wu, W. Li, Z. Xiong, T. He, J. Gou, H. Chen and P. Chen, *Energy Environ. Sci*., 2011, **4**, 3593.

[202] W. R-Pilecka, D. Szmigiel, Z. Kowalczyk, S. Jodzis and J. Zielinski, *J. Catal*., 2003, **218**, 465.

[203] P. F. Ng, L. Li, S. Wang, Z. Zhu, G. Lu and Z. Yan, *Environ. Sci. Technol.,* 2007,**41**,3758.

[204] A. S. Chellappa, C. M. Fisher, W. J. Thomson, *Appl. Catal. A. Gen.,* 2002, **227**, 231.

[205] A-H. Liu, J-J Nitz, M. Comotti, C. Weidenthaler, K. Schlichte, C. W. Lehmann, O. Terasaki and F. Schrűth*, J. Am .Chem. Soc*., 2010, **132**, 14152.

[206] S. Appari, V. M. Janardhana, S. Jayanti, L. Maier, S. Tischer and O. Deutschmann, *Chem. Eng. Sci.,* 2011, **66**, 5184.

[207] M. Tsuboto, S. Hino, H. Fujii, C. Oomatsu, M. Yamana, T. Ichikawa and Y. Kojima, *Int. J. Hydrogen Energy*, 2010, **35**, 2058.

[208] Y. H. Guo, W .W. Sun, Z. P. Guo, H. K. Liu, D. L. Sun and X. B. Yu, *J. Phys. Chem. C*., 2010, **114**, 12823.

2. Experimental

During this project, a wide variety of synthetic techniques to prepare nanostructured hydrogen storage materials, hydrogen release systems and metal ammines have been used.

A wide variety of characterisation techniques have also been used, including Powder X-ray Diffraction (PXD), Powder Neutron Diffraction (PND), TPD (Temperature Programmed Desorption) and Scanning Electron Microscopy (SEM).

The aim of this chapter is to describe the synthetic and characterisation techniques used throughout the project.

2.1 Air Sensitive Handling Techniques

As the majority of the samples used during this project are air sensitive (either pyrophoric or degrade in air), then they must be handled and stored in an inert atmosphere.

During this project, two different glove boxes (N_2(g) or Ar(g) recirculating) were used, either manufactured by Saffron Scientific or mBraun (UniLab). The operation of the Saffron and mBraun glove boxes is the same. Two gas atmospheres are available for the Saffron glove boxes. Ar(g) is used for the preparation and cleaning of Li metal using a molten Na pool while the N_2(g) recirculating glove boxes are used for all other sample preparation, handling and storage. The N_2(g) is supplied to the glove boxes via an N_2 generator in the lab (99-99.9% purity), while Ar(g) is supplied to the glove boxes by a gas cylinder (99.9% purity).

The atmosphere of the glove box is kept clean by the recirculating of inert gas (Ar or N_2 depending on the box) using an internal recirculating pump. For weighing manipulations, the recirculating pump can be switched off for minimal periods.

Excess moisture/oxygen is removed from the glove box by molecular sieves/catalysts at the side of the box. The molecular sieves remove the water

from the inert gas, while the catalyst removes the oxygen from the gas. These are regenerated at regular periods. The molecular sieve is regenerated by heating under vacuum with liquid N_2 used to collect the water. The catalyst is regenerated by heating under a flow of H_2/N_2(g) (1:9) under vacuum overnight to remove the oxygen that is absorbed to the water. The catalyst is then heated under vacuum to remove the water by-product. The levels of moisture and oxygen are indicated by their respective sensors at the left hand side of the glove box and should typically be in the 0-5 ppm region for oxygen and 0-30 ppm for water. The layout of the Saffron glove box can be seen in Figure 2.1. The user panel consists of the gas and vacuum valves, moisture/oxygen sensors and user controls.

The transfer of samples into and out of the Saffron glove boxes is via a transfer port at the side of the glove box in order to preserve the inert atmosphere of the glove box. The transfer port is kept under vacuum when not in use. To transfer samples and equipment to the glove box, the transfer port is filled with the relevant gas (either N_2(g) or Ar(g)) until atmospheric pressure is achieved. The items required to be transferred into the glove box are then placed in the transfer port. The transfer port is then evacuated using an Edwards Rotary Vane (RV) pump and gas is introduced until the pressure gauge reaches zero. This process is performed three times in total. After the third cycle, the contents of the port can be transferred to the glove box. For removing items from the glovebox the items are also transferred via the transfer port.

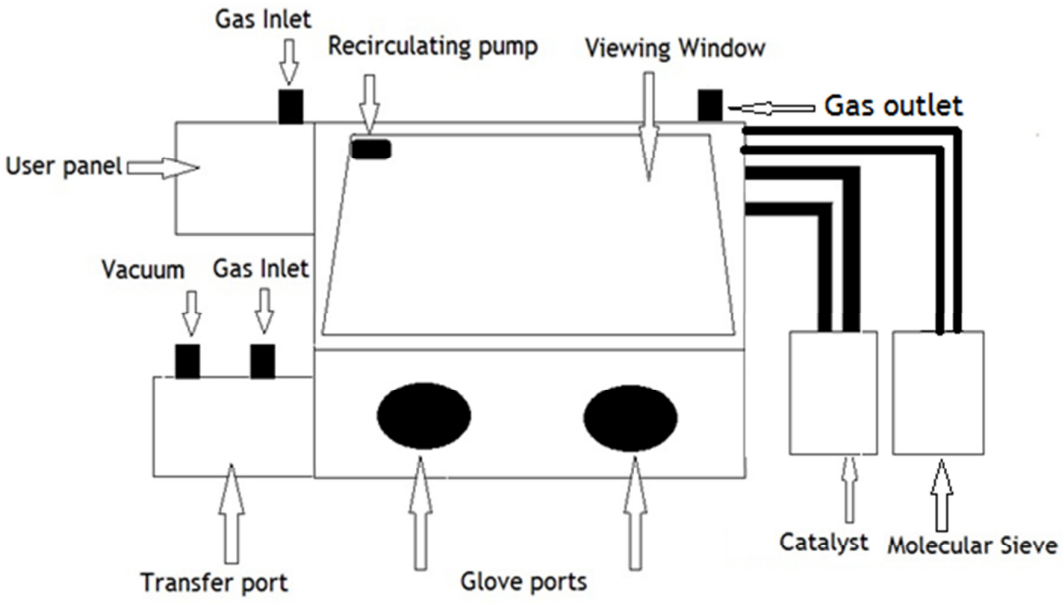

Figure 2.1: Schematic of the Saffron recirculating glove box

The Braun UniLab glove box works on the same principal as that of the Saffron glove box. The inert gas for this glove box is Ar(g). The molecular sieve and catalysts are contained internally and are regenerated using a N_2/H_2 gas mixture. The moisture and oxygen levels for this glove box are both <0.1ppm.

2.2 Preparation of Materials

2.2.1 Hydrothermal Synthesis for Preparation of $Mg(OH)_2$

Microstructured $Mg(OH)_2$ was prepared by hydrothermal synthesis. Hydrothermal synthesis (Figure 2.2) is a technique for the synthesis of crystalline materials from the bulk precursors under high pressure in an aqueous media at temperatures lower than that of traditional solid state reactions.[1] The reactants are normally a powder (metal reactant) and water that dissolves the powder. The reactants are heated under pressure in a sealed autoclave to a temperature above their boiling point, usually in an oven and a chemical reaction between the reactants occurs to form the product. Hydrothermal synthesis takes advantage of the increased solubility and reactivity of the metal reactant at higher temperatures without the solvent reaching its critical point.[2]

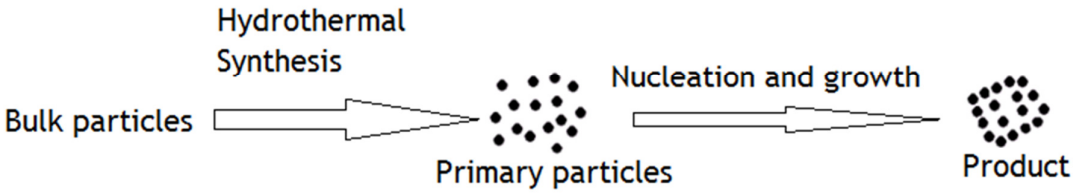

Figure 2.2: Hydrothermal synthesis of materials. Adapted from Ref 3. The primary particles refer to particles of the product ($Mg(OH)_2$).

For hydrothermal synthesis, the relevant reactants (normally a powder and water) are placed in a teflon-lined cup and sealed in a stainless steel vessel for heating. The cup and vessel are referred to as an autoclave (Figure 2.3).

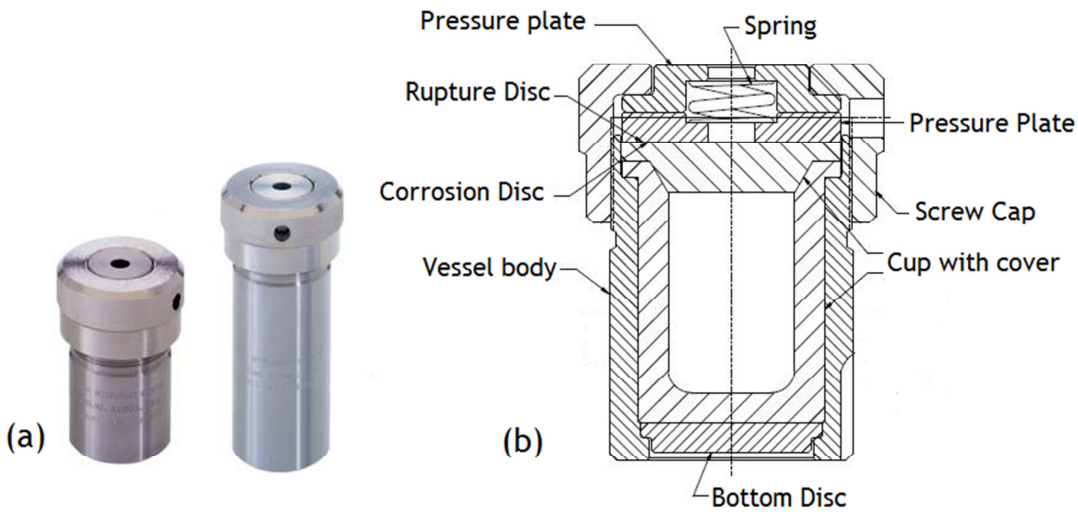

Figure 2.3: Set- up of the autoclave used for hydrothermal synthesis (a) is the fully set-up autoclave (b) is the schematic of the autoclave. Adapted From Ref [4]

When an autoclave is used, there are limits in the volume of the solvent and the heating temperature for safety reasons. The volume of solvent in the autoclave must not exceed 70% of the total volume of the autoclave. The reason for this is that during heating the volume will expand (at 250 ^{o}C a water based solution will expand by 25%) and if there is insufficient space in the autoclave to accommodate the increased vapour, the increased pressure generated would cause the autoclave to rupture.[4] The vessel also has a temperature limit and if it is heated above the temperature limit then the vessel can be damaged as the

vapour pressure increases exponentially with temperature which can lead to rupture. Heating above the temperature limit will also damage the material of the vessel (PTFE for the cup). The temperature limits are 250 ^{o}C for a normal vessel and 275 ^{o}C for a high strength vessel.[4] The materials used in the autoclave must also be carefully chosen, as if the reactions are highly exothermic or if the intermediate and final products are unstable then this could also damage the autoclave.

2.2.2.1 Microwave (MW) based Hydrothermal Synthesis

Microwave hydrothermal synthesis preparation has been used for the preparation of $Mg(OH)_2$. The autoclaves used for MW synthesis are Teflon-lined vessels making them suitable for use in microwaves (Figure 2.4).[5] The body parts of the autoclave are made of a high strength polymer which also acts as an insulator for the sample cup to prevent overheating. If there is overpressure in the autoclave, excess pressure is released through an adjustable Teflon screw at the top of the autoclave which works in conjunction with the o-ring seal on the sample cup.[6] The autoclaves can be heated to 250 ^{o}C and have a pressure limit of 1200 psi. MW heating is described in Section 2.2.3.

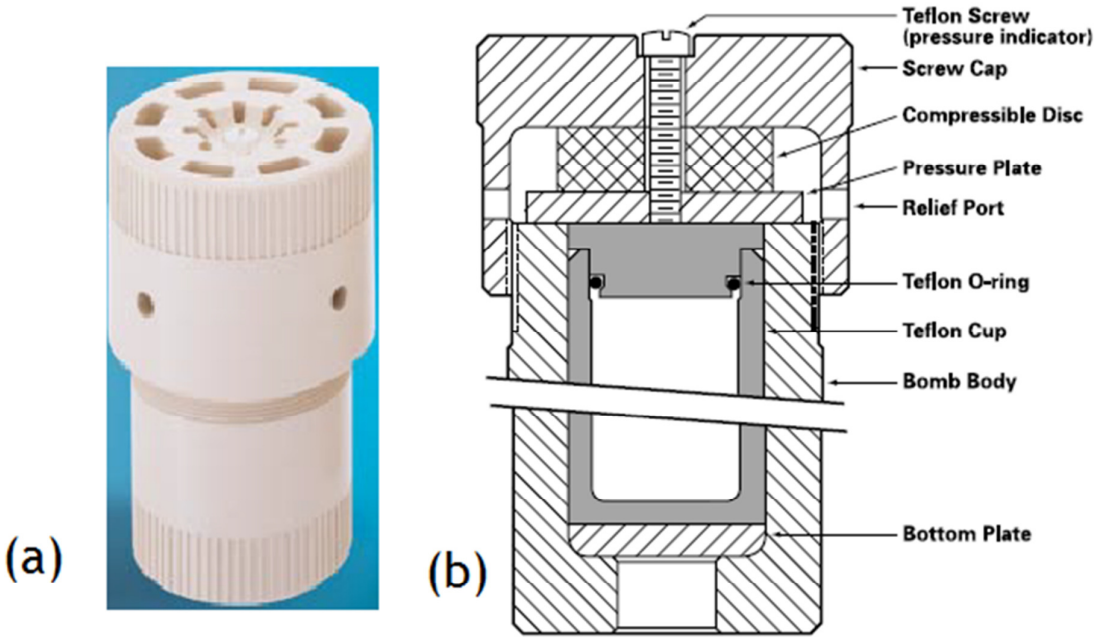

Figure 2.4: MW autoclave used for hydrothermal synthesis (a) is the fully set-up autoclave (b) schematic of the autoclave [4]

2.2.3 Microwave Heating

Microwave heating (MW) allows reaction times to be decreased from hours or days to a matter of minutes. Microwaves are part of the electromagnetic spectrum (Figure 2.5) and lie between radio waves and infrared radiation.

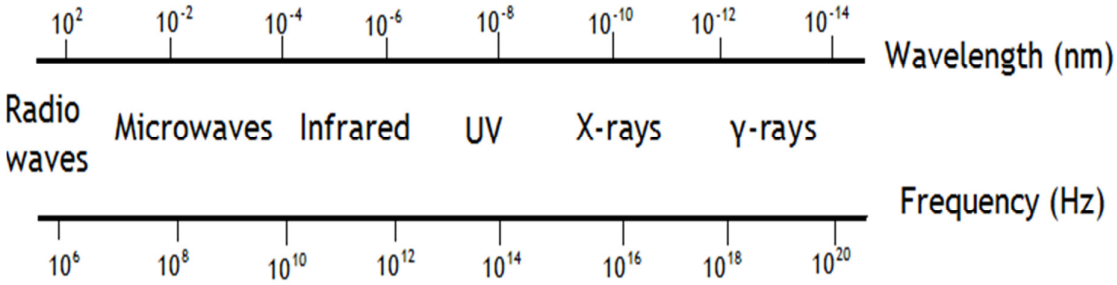

Figure 2.5: The electromagnetic spectrum

Only the frequencies at 900 MHz and 2.45 GHz are used for MW heating, as the rest of the MW spectrum is used for communication purposes. A domestic microwave oven (DMO) uses a frequency of 2.45 GHz for heating. In a DMO, the magnetron produces the microwaves.

Microwaves can interact with materials in a number of ways but there are three main ways.[7] If the material is a conductor, then the microwaves will be absorbed by the material. If the material is dielectric, then the microwaves will also be absorbed by the material, so heat will be generated. Dielectric heating is of interest for the synthesis of materials in a microwave.[7] If the material is an insulator, then no heat will be generated as the material is transparent to microwaves.

Microwave adsorption can occur via two main mechanisms. These are dielectric heating (dipole rotation in liquids) or ionic conduction.[8]

2.2.3.1 Microwave Heating in Liquids

In liquids, molecular rotation occurs when polar molecules (such as water) in a material have an electrical dipole moment, which involves the molecules continually aligning themselves in the electromagnetic field. When the field alternates the molecules will then change their direction. This results in the rotating molecules either pushing, pulling or colliding with other molecule. This results in energy distribution to other molecules in the material.[8] The energy is transferred rapidly resulting in an increased temperature of the reaction mixture and can also result in a more uniformed distribution if heating in the mixture. Microwave heating in liquids has been used for the hydrothermal synthesis including oxides and zeolites.[9,10]

2.2.3.2 Microwave Heating In Solids

In the MW heating of solids for dielectric heating to occur one of the materials involved in the synthesis needs to be a MW absorber able to couple to the MW frequency.[9] If the material is unable to couple to microwaves at this frequency, then a susceptor such as SiC can be used to aid coupling. In solid state MW heating, the dipoles are formed by charge separation. The equation given for the ability of a material to convert electromagnetic radiation to heat energy in solids at a given frequency is: [11]

$$\varepsilon'' / \varepsilon' = \tan \delta \qquad (2.1)$$

where ε“ = dielectric loss, ε’ = dielectric constant and δ = dissipation factor

The coupling is of the material to microwaves is dependent on the dielectric constant. The dielectric properties of a material are dependent on the chemical and physical composition of the material and also the conductivity of the material.

2.2.4 Preparation of $Mg(OH)_2$

Nanostructured $Mg(OH)_2$ was prepared by two methods. The first method was developed by Ding *et al.*[12] using a conventional oven. A stoichiometric amount of Mg powder (Alfa Aeser 98%) and 15 ml of a solution of ethylenediamine (Acros, 99%) and deionised water (typically in a 8:1 ratio) were placed in a 23 ml Teflon-lined autoclave (Parr). The autoclave was then heated in an oven at 180 ^oC for 20 hours. The obtained precipitate was then washed using deionised water and ethanol, centrifuged and then dried. Ethylenediamine was used as it acts as a template for the final product. The ethylenediamine binds to the Mg forming a Mg^{2+} complex. The OH^- from the H_2O weakens the Mg-ethylenediamine bonds. The OH- starts replacing the ethylenediamine, forming Mg-OH bonds. This process continues until $Mg(OH)_2$ is formed.[13]

The second method of synthesis was a MW preparation based on the experiment procedure carried out by Yu *et al.*[14] using conventional heating. For this, the authors heated 0.4 g of MgO (Sigma, 98%) with 16 ml H_2O in a 20 ml teflon-lined autoclave at 160 ^oC for 24 hours. In the MW synthesis used here, 0.4 g of MgO and 16 ml of H_2O were placed in a 23 ml teflon-lined microwave autoclave. This was then heated in a domestic microwave oven for four minutes. The obtained white sample was washed in water and allowed to dry in air at room temperature. This synthesis has also been successfully scaled up using a 45 ml teflon-lined autoclave to produce 1 g of $Mg(OH)_2$.

2.2.5 Preparation of LiOH

LiOH was prepared in a similar manner as the $Mg(OH)_2$ prep was prepared above using Mg powder and ethlylenediamine. Li metal was used as the source of Li, instead of Li powder. The Li metal (Alfa, 99.9%) was cleaned by the following procedure:

A molten Na pool was heated inside a Saffron Ar(g) recirculating glove box. The Na pool was used to preserve the inert atmosphere of the glove box as any oxygen present in then glove box would react with the Na. This meant that the

Li metal could be cleaned in an inert atmosphere and any possible problems with the atmosphere would be identified. The oxide layer in the Na pool, once molten was then skimmed off using a spoon leaving a shiny surface. If there was contamination of the glove box, the surface of the pool would dim indicating the presence of oxygen. A piece of Li metal was then cleaned using a file and an appropriate amount of the Li metal weighed and sealed in a glass vial for transport out of the glove box. The preparation of cleaned Li metal is the same method used in the preparation of α Li_3N.[15]

Outside the glove box, the Li metal was quickly placed in a 23 ml teflon-lined autoclave with an 8:1 solution of ethylenediamine and water and heated at 180 ^oC for 20 hours. Exposure to air of the cleaned Li metal was kept to a minimum.

A variety of drying techniques were investigated, as LiOH is sensitive to CO_2. The drying techniques involved were using a rotary evaporator to evaporate the liquid after heating to minimise air exposure during drying and also drying the obtained mixture after heating on a petri dish in a desiccator until the sample was dry.

2.2.6 Ball Milling

In order to reduce the particle size of bulk LiH and MgH_2, a Retsch PM100 planetary ball mill was used. The samples were loaded into the sample jar inside the glove box, along with ten grinding balls and sealed using the air sensitive clamp. The sample jar and the grinding balls used were either stainless steel or agate depending on the sample.

The jar was then placed on a sun wheel and clamped with a counterweight employed to prevent oscillations. The sun wheel acted as a counter rotating plate during ball milling as the sun wheel and the jar moved in different directions in a 1:2 ratio. The grinding balls were subjected to Coriolis forces which are superimposed rotational movements. The speed difference between the jar and the grinding balls provided an interaction between the frictional and impact forces, which resulted in a reduced particle size of the sample.

The ball milling time, speed and interval breaks are amongst the parameters that could be changed to achieve the desired particle size.

2.2.6.1 Ball milling of LiH

1 g of LiH (Sigma, 95%) was ball milled for four hours at 450 rpm with a 1 minute interval every 15 minutes using a stainless steel jar and grinding balls.

2.2.7 Synthesis of Metal Ammines

Metal Ammines ($M(NH_3)nX_2$), where M= Mg and X= Cl, Br, I n= 2,6 have been synthesised by a variety of techniques in the literature including:

1) Exposure of the starting salt to an atmosphere of NH_3 inside a glove bag [16]
2) Exposure of the starting salt to a known constant pressure of NH_3 for a period of time [17]
3) Reaction of MX_2 with the corresponding ammonium halide in an autoclave [18]

In this project, a technique based on preparation 1 has been used. The starting salt (MX_2) is loaded inside a glass tube and the tube sealed with a septum cap and parafilm. This preparation work is undertaken in a glove box, due to the hygroscopic nature of the starting materials. NH_3(g) (BOC, 99%) delivery to the tube is via syringes, one inlet (delivery of NH_3) and one outlet syringe for NH_3 to a water trap. A small NH_3 flow rate is used and the experiment typically ran overnight. For the synthesis of $Mg(ND_3)_6X_2$(where X= Cl, Br, I), ND_3(g) (Isotec, 99%) was used. A schematic of the set-up can be seen in Figure 2.6:

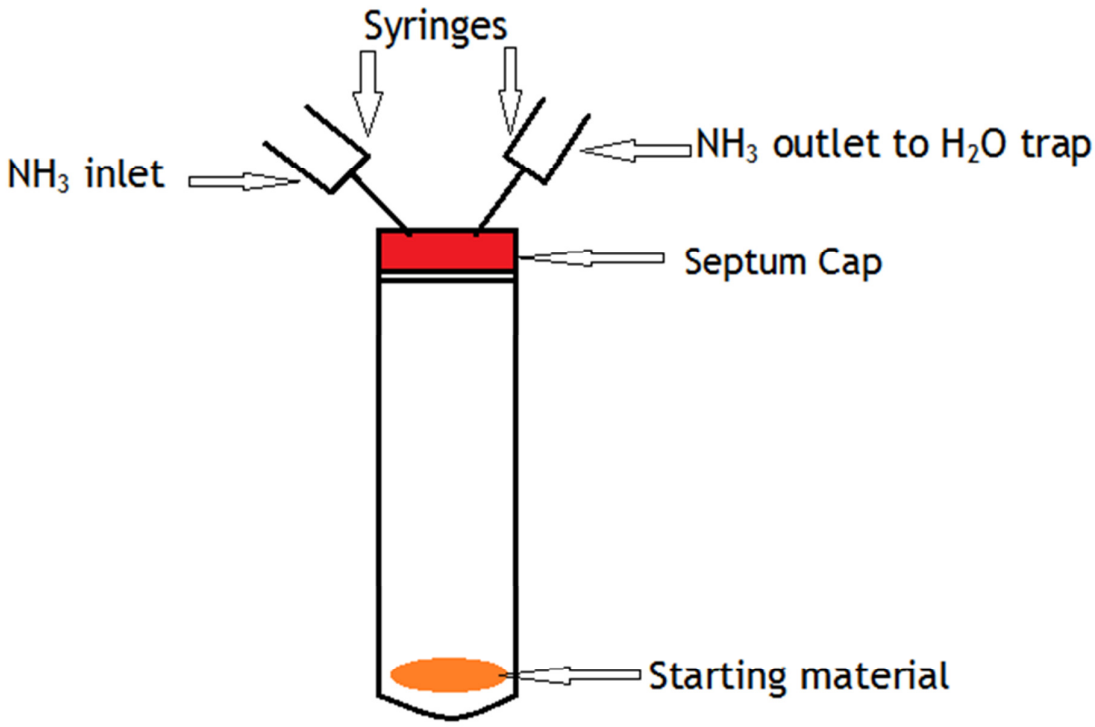

Figure 2.6: Experimental set- up for the synthesis of metal ammines

The obtained product would then be collected in a N_2(g) recirculating glove box.

2.3 Structural Characterisation Techniques

2.3.1 Powder X-ray Diffraction (PXD)

Powder X-ray diffraction (PXD) is a vital technique for chemists in determining the phase(s) present in a solid.[19] PXD is the prominent characterisation technique used in this thesis. Quick PXD scans can give information about the phase or phases present in a sample while longer PXD scans allow Rietveld refinement (Section 2.4) to be carried out for the sample to determine the crystal structure and quantative phase composition.

2.3.1.1 Background

For PXD to occur the sample must have a regular arrangement of atoms with long range positional order. A random orientation of crystallites is also required. Samples lacking long range order, such as liquids and amorphous solids do not produce Bragg peaks.

X-ray diffraction can be traced to 1913 when W.H. Bragg and W.L. Bragg derived the structure of NaCl and NaBr.[20,21] The structure of these two salts was determined from single crystals. From this, W.L. Bragg determined that a crystal is constructed from layers or planes to give a regular and repeating structure. Bragg also determined that crystals appeared to "reflect" X-rays at certain angles of incidence. These findings led to the fundamental equation of diffraction, the Bragg equation:

$$n\lambda = 2d\sin\Theta \qquad (2.2)$$

where n is an integer defined as the order of diffraction, λ is the wavelength of the X-ray, d is the perpendicular spacing between the planes in the lattice and Θ is the scattering angle

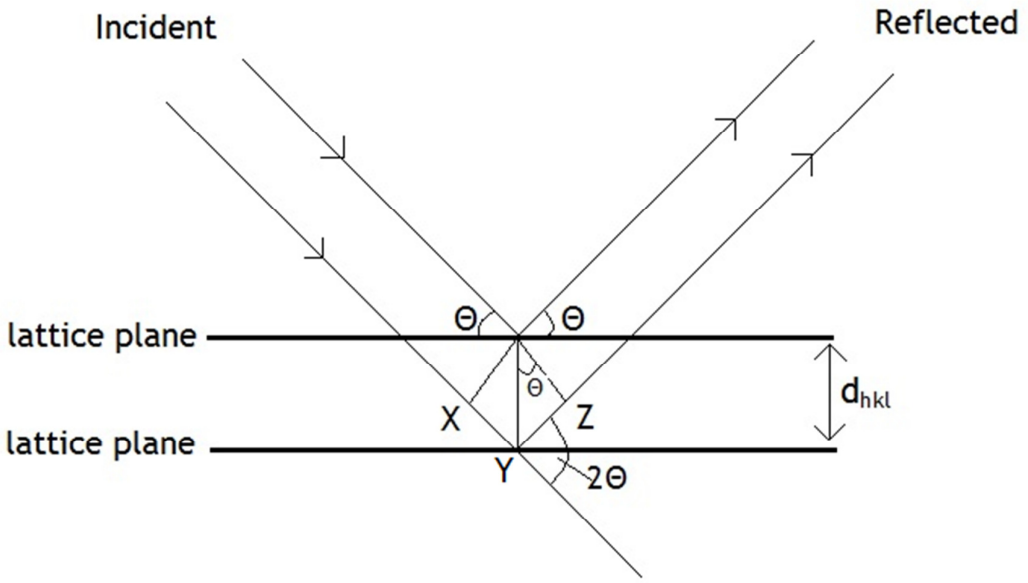

Figure 2.7: Schematic Illustration of the diffraction process

When the incident X-rays interact with the crystals, they can be either *in phase* or *out of phase*. For Bragg peaks with non-zero intensities to be produced, the X-rays must be *in phase*, which is also known as constructive interference. For the X-rays to be *in phase* then the n value in the Braggs Equation (equation 2.2) must be a whole number (positive integer).

As can be seen in Figure 2.7, there are two parallel incident X-rays, A and B. For the incident X-rays to be in phase, then beam B has further to travel than beam A. The difference in this distance between beam A and beam B is distance XYZ.

XYZ is directly related to the incident angle *Θ* and d_{hkl} (hkl is the miller indices) which is the interplanar spacing. The distance between d_{hkl} and *Θ* is given by:

$$XYZ = 2d\sin\Theta \tag{2.3}$$

For constructive interference (*in phase*) to occur then *XYZ* must equal a whole number of wavelengths. This gives rise to the equation:

$$XYZ = n\lambda \tag{2.4}$$

Braggs Law (equation 2.2) is then derived from combining equations 2.3 and 2.4. The distances between the planes are typically 2-3Å and so the crystal acts as a diffraction grating. For diffraction to occur the distance between the planes in a crystal must have similar wavelength as that of the incident X-rays.

In a crystal, the smallest repeating unit that has the full symmetry of the crystal lattice is the unit cell. The crystal lattice refers to the array of equivalent lattice points in a crystal related by translational symmetry. There are several possible unit cell geometries, which gives rise to the seven crystal systems:

Table 2.1: Seven Crystal Systems with unit cell parameters (*a*,*b*,*c* are the lengths of the unit cell, with *α*, *β* and *γ* being the angles in the unit cell)

Crystal System	Unit Cell Parameters
Triclinic	$a \neq b \neq c$, $\alpha \neq \beta \neq \gamma$
Monoclinic	$a \neq b \neq c$, $\alpha = \gamma = 90^o$, $\beta \neq 90^o$
Orthorhombic	$a \neq b \neq c$, $\alpha = \beta = \gamma = 90^o$
Trigonal (Rhombohedral)	$a = b = c$, $\alpha = \beta = \gamma \neq 90^o$
Hexagonal	$a = b \neq c$, $\alpha = \beta = 90^o$, $\gamma = 120^o$
Tetragonal	$a = b \neq c$, $\alpha = \beta = \gamma = 90^o$
Cubic	$a = b = c$, $\alpha = \beta = \gamma = 90^o$

Miller indices (*hkl*) are used for describing the orientation of a plane(s) in a lattice in relation to the unit cell. Miller indices are reciprocal positions where the plane cuts the a, b and c axes respectively. Miller indices (*hkl*) values can either be positive, negative or zero.

For each of the seven crystal systems, there is an equation for each system that can be used to determine, d_{hkl} :

Table 2.2: Interplanar distance between lattice planes (d_{hkl}) and their relationship to the crystal systems.

Crystal System	d_{hkl} Equation
Triclinic	$\frac{1}{d^2_{hkl}} = 1/V^2 \{h^2b^2c^2\sin^2\beta + k^2a^2c^2\sin^2\beta + l^2a^2\sin^2\beta + l^2a^2b^2\sin^2\gamma + 2hkabc^2(\cos\alpha\cos\beta-\cos\gamma) + 2kla^2bc(\cos\beta\cos\gamma-\cos\alpha) + 2hlab^2c(\cos\alpha\cos\gamma-\cos\beta)\}^{1/2}$ $V = abc(1-\cos^2\gamma-\cos^2\beta-\cos^2\gamma+2\cos\alpha\cos\beta\cos\gamma)^{1/2}$
Monoclinic	$\frac{1}{d^2_{hkl}} = \frac{1}{\sin^2\beta}\left(\frac{h^2}{a^2} + \frac{k^2\sin^2\beta}{b^2} + \frac{l^2}{c^2} + \frac{2hl\cos\beta}{ac}\right)$
Orthorhombic	$\frac{1}{d^2_{hkl}} = \frac{h^2}{a^2} + \frac{k^2}{b^2} + \frac{l^2}{c^2}$
Hexagonal/ Trigonal	$\frac{1}{d^2_{hkl}} = \frac{4}{3}\left(\frac{h^2+hk+k^2}{a^2}\right) + \frac{l^2}{c^2}$
Tetragonal	$\frac{1}{d^2_{hkl}} = \frac{h^2+k^2}{a^2} + \frac{l^2}{c^2}$
Cubic	$\frac{1}{d^2_{hkl}} = \frac{h^2+k^2+l^2}{a^2}$

The interplanar distance equations when combined with the Bragg equation can be used to index peaks and to determine the unit cell dimensions. If the crystal system is cubic, then combining the two relevant equations gives rise to the following equation:[22]

$$\frac{\sin^2\Theta}{(h^2 + k^2 + l^2)} = \frac{\sin^2\Theta}{S} = \frac{\lambda^2}{4a^2} \quad (2.5)$$

where $S = h^2 + k^2 + l^2$

Using known cubic systems and the 2Θ value that corresponds to the relevant Miller indexes, then indexing can be performed. The crystal lattice can be presumed as correct when $\sin^2\Theta/S$ values are constant. The lattice parameter (a) can then be calculated from the constant $\lambda^2/4a^2$. For other crystal systems a similar procedure is followed for indexing and the calculation of the unit cell dimensions.[22]

The Crysfire [23] suite (that contains the DICVOL [24] indexing program) software can be used for solving the crystal system of an unknown PXD scan and for indexing the pattern. If the crystal system is known and the lattice parameters need to be known, then the program CELL [25] can be used. In CELL, the following equation is minimised to extract the unit cell parameters and the symmetry by a least-squares method:

$$M = \sum_a W_n (sin_2\Theta_n^{obs} - sin2\Theta_n^{calc})^2 \quad (2.6)$$

where W_n is the weighting factor

There are limitations to PXD, particularly concerning materials containing light elements such as hydrogen. X-rays interact with the electrons in the sample and are then scattered. Heavier elements scatter more X-rays as there are more electrons present and this will lead to a greater intensity of the observed peaks. Lighter elements have less electrons, so the scattering is decreased and the intensity of the observed peaks is reduced. In the case of hydrogen, which has only one electron this is an issue as the peaks produced have poor intensities.

2.3.1.2 Preparation of PXD Samples

Before PXD analysis, samples are ground using a mortar and pestle to ensure a random distribution of crystallites. The random distribution of crystallites ensures that lattice planes are present in every orientation, so for each set of lattice planes some crystals will be orientated at Bragg's angle to give a

reflection from these planes. This can also lead to 'preferred orientation' which results in the increase of some intensities which are attributed to a particular direction. This can be overcome, in these cases by using Debye-Scherrer (capillary) measurements.

For air sensitive materials the samples were prepared by two methods: Capillary, for use with the Brucker D8 diffractometer and a bespoke Air Sensitive flat plate sample holder for use with the PANalytical X'pert Pro MPD powder diffractometer (Figure 2.8).[26] These are discussed in more detail below.

In this project, 0.5 mm and 0.7 mm silica glass capillaries were commonly used. Inside the glove box, the sample is placed in the capillary and the sample packed into the capillary by tapping. When there is sufficient sample (typically when the capillary is half full), the open end of the capillary is sealed using silica grease. This ensures the sample is not exposed to oxygen and moisture when transferring the capillary out of the glove box. Once the capillary is outside the glove box, it is then flame sealed. Flame sealing the capillary results in the preservation of the sample as it is not exposed to air and moisture. For the capillary to be run on the D8, the capillary is then placed on the goniometer with bees wax. This allows the capillary to be aligned (rotational and translation) so that the sample is centred in the X-ray beam and in an appropriate geometry for a transmission experiment.

The air sensitive flat plate sample holder used on the PANalytical X'pert diffractometer consists of two components: a back plate which is fixed to the goniometer of the diffractometer and an air sensitive cylinder (with polymer film) that covers the sample that is placed in the sample holder, which is a glass slide with an indent. The air sensitive holder minimises the exposure of the sample to air and moisture when performing a flat plate reflection experiment in Bragg-Brentano geometry (see page 63). The ground sample is placed in the indent of the slide. Ideally, the indent of the sample holder should be completely filled with powder sample, such that the sample is flat with the plane of the slide. The sample holder is then placed in the spigot. The air sensitive cylinder is then placed over the sample inside the glove box. The air sensitive sample holder is also attached to a clamp at all times to allow the air sensitive cylinder to be attached and also for transport of the sample.

Non-air sensitive samples were analysed using the flat plate on the X'pert. The samples were grounded using a pestle and mortar. The sample was then placed in the indent of a sample slide and smoothed.

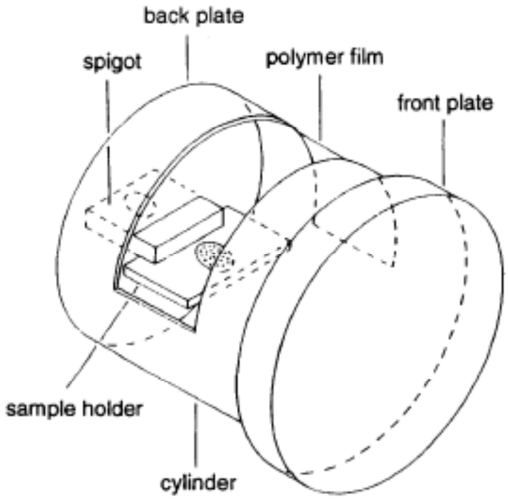

Figure 2.8: Schematic of the air sensitive sample holder. Reprinted from Ref 26 with permission from The Royal Society of Chemistry

2.3.1.3 Data Collection

Obtained samples were characterised by Powder X-Ray diffraction (PXD) using either a Brucker D8 Advance diffractometer in Debye-Scherrer (capillary) mode or a PANalytical X'pert Pro diffractometer in Bragg-Brentano reflection geometry.

The X-ray source in a laboratory PXD is typically a sealed tube or a rotating anode. The electrons are emitted by a heated tungsten filament by thermionic emission and are accelerated by high voltage and collide with a metal target typically Cu, and produce X-rays. At this stage, there are three wavelengths of X-rays, $K_{\alpha 1}$, $K_{\alpha 2}$ (produced from electrons dropping from the L shells) and K_{β} (produced from electrons dropping from the M shells) produced, with K_{α} ($K_{\alpha 1}$ and $K_{\alpha 2}$) the wavelength of choice as this is the most intense. In an atom, the innermost shell for electrons is the K-shell (which omits electrons when collision occurs) and this is surrounded by the L and M electron shells which replaces the emitted electrons from the K shell. The X-rays are then filtered through a slit to select the desired wavelength for diffraction.

The Debye-Scherrer configuration (Figure 2.9) uses a near parallel incident X-ray beam with a sufficient cross-section to irradiate the sample. Cones of diffracted beams are produced from the sample in accordance with Bragg's law and the arcs of the cones are then intercepted by the detector.

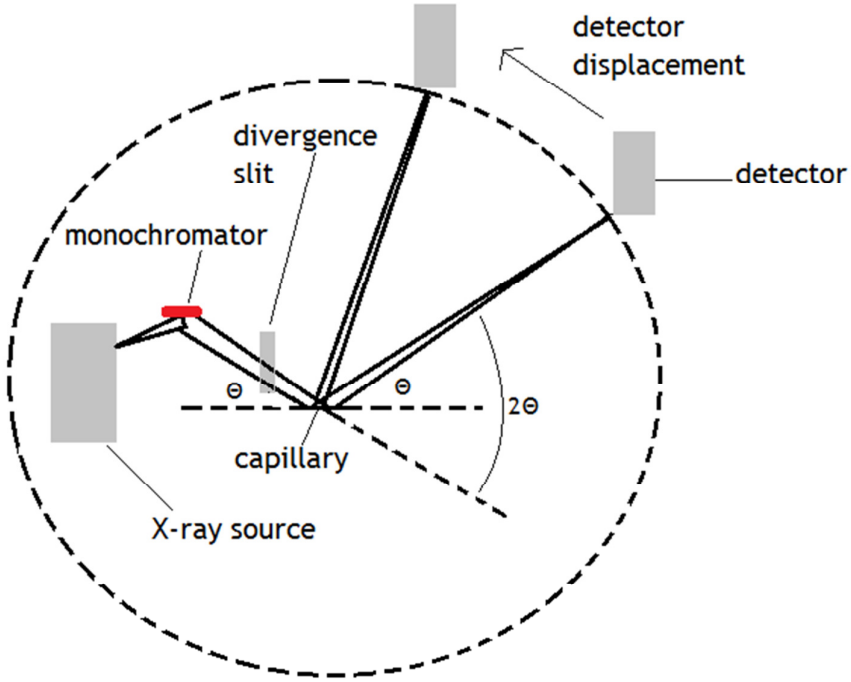

Figure 2.9: Debye-Scherrer geometry

The Brucker D8 uses Cu K_α radiation (λ = 1.5418 Å) with a monochromater slit and VANTEC detector. The operating power of the X-ray tube was 40 KV and 40 mA. PXD scans suitable for phase identification were obtained by scanning between 5^o-75^o for one hour with a step size of 1.3^o min^{-1}. The monochromator slit used was typically 1mm. PXD data suitable for Rietveld refinement (Section 2.4) were collected in capillary mode between $5 \leq 2\theta/^o \leq 105$ with a step size of $0.017^o/ 2\theta$ and a time per step of 0.12^o per minute. Run time was typically 12 hours using a monochromator slit of 0.6 mm.

For Bragg-Brentano geometry (Figure 2.10), samples were analysed using the PANalytical X'pert Pro diffractometer. In Bragg-Brentano configuration the sample is irridated using a standing X-ray source and a moving detector. The sample holder is placed on one axis and tilted by Θ with the detector at 2Θ. The diffractometer used Cu $K_{\alpha 1}$ radiation with the X-ray operating power being 40 KV

and 40 mA. The detector was a X'Celerator solid state detector. A monochromator slit of 10 mm was used and a slit size of 0.5 for the divergence and anti-scatter slit used. For phase identification, samples were typically run for 20-30 minutes between 5^{o}- 85^{o}. For Rietveld Refinement (Section 2.4), data was collected between 5^{o}-85^{o} for 12 hours with a step size of 0.0167 $^{0}/2\Theta$ and a time per step of 0.11^{o} per minute. The monochromator mask used was 10 mm.

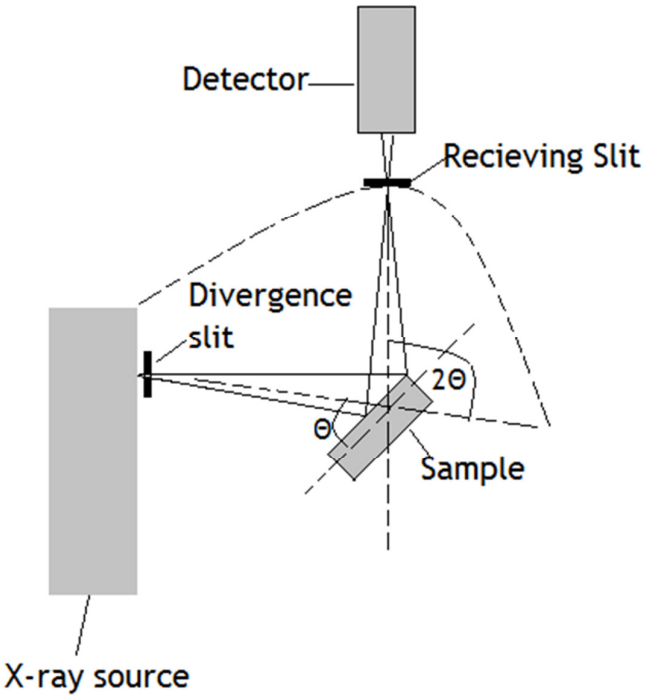

Figure 2.10: Bragg-Brentano geometry

2.3.1.4 Data Analysis

The D8 diffractometer produces PXRD patterns in a raw (*raw) data file. The PANalytical X'pert produces the PXRD pattern in a PANalytical format (*xdrml). This latter format can be converted to a raw data file by using the PowDLL convertor program.[27]

Data manipulation was carried out using the PowderCell program.[28] The obtained pattern was compared to calculated patterns in PowderCell using the crystal data from the Inorganic Crystal Structure database (ICSD).[29] The obtained pattern was also compared to known patterns in the International

Centre for Diffraction data Powder Diffraction File Database (ICDD PDF) using the PANalytical High Score Plus program.

Structure refinement was performed against X-ray data using the Rietveld method using the software GSAS [30] and EXPGUI.[31] (See Section 2.4)

2.3.2 Powder Neutron Diffraction (PND)

PND has been used in this thesis for characterisation purposes. In-situ PND studies of the deammoniation of the metal ammines (Chapter 4) and the H_2 release systems (Chapter 5) were carried out at the ISIS facility at the Rutherford Appleton Laboratory, Didcot. Ex-situ measurements at -269 ^oC and 25 ^oC were performed on the metal ammines at the ILL facility at Grenoble (Chapter 4).

2.3.2.1 Background

In X-ray diffraction, the X-rays are scattered by the electrons, so as an atom increases in atomic number, the scattering intensity increases. In neutron diffraction, neutrons interact directly with the nucleus and are scattered by the atomic nuclei. As neutrons are not scattered by electrons and not proportional to Z (mass) then lighter elements can now be detected in the sample. The scattering of each atom is dependent on the properties of the nucleus, for example Mg has a scattering length of 5.375 fm while deuterium has a scattering length of 6.674fm.

There are two different types of neutron source. The first is a nuclear reactor source, such as at the ILL in Grenoble. This uses a steady, continuous stream of neutrons produced by the fission process. The reactor produces 1.5 x 10^{15} neutrons per second per cm^2. [32] A monochromator (typically made of pyrolytic graphite, Cu or Si) is used which selects a beam of neutrons of a given wavelength.[33] The neutrons scattered by the sample are detected by the instrument detectors, and recorded as a function of the scattering angle that they were scattered. [34] The output is 2Θ along the x axis plotted against intensity (y axis).

The other type of neutron source is that of a spallation (pulsed) neutron source, such as at ISIS. To produce neutrons, the first step is the production of H^- ions at the start of an accelerator. To produce the H^- ions, $H_2(g)$ and caesium vapour is fed into a ring and ionised using electric discharge. The H^- ions are then accelerated by a Radio Frequency Quadruple accelerator (where they are also separated into two bunches) and then a linear accelerator. [35]

In the synchrotron ring, further acceleration occurs and the electrons are stripped away by a thin alumina foil, which leaves a beam of protons (~2.5×10^{13} protons). These protons are then accelerated and collide with a tungsten target.[36] The tungsten target is bombarded with the high energy protons, which in turn leads to the emission of neutrons from the target atom. Typically, each proton colliding with the target can produce around 15 neutrons. This process, called spallation produces an intense neutron pulse, so the neutrons are slowed down by moderators around the target (water, liquid methane and H_2 are used).[37] The neutrons are then directed to a wide variety of instruments, for neutron diffraction.

In a spallation source such as ISIS, the neutrons are produced in pulses with different wavelengths. In Time of Flight (ToF) neutron diffraction, the neutrons travel a known distance to the detector. The detectors are at fixed 2Θ angles. The arrival time of the neutrons are recorded, with the wavelength of the neutron being proportional to its ToF.

As neutrons have wavelengths [38] (a typical neutron at 273 K with a velocity of 2200 ms^{-1} has a wavelength of 1.8 Å), the de Broglie relationship can be used which relates the wavelength of a neutron with its velocity:

$$\lambda = h/mv \qquad (2.7)$$

Where h is the Planck constant, m is the mass and v is the velocity

The distance the neutrons travel for the primary flight path (moderator to the sample) is given by L_1, with a corresponding ToF, T_1 and for the secondary flight path (sample to detector) is given by L_2 and T_2. Hence equation 2.7 can be

rewritten with t_1,L_1, t_2 and L_2 and combined with the Bragg equation (equation 2.2) to give the following equation:[39]

$$\frac{h}{m}\frac{(t_1 + t_2)}{(L_1+L_2)} = 2d\sin\Theta \qquad (2.8)$$

This leads to $L_1 + L_2 = L$ and $t_1 + t_2 = t$ to give:

$$t = \frac{2dL}{h}(m/h)\sin\Theta \qquad (2.9)$$

As it can be assumed that the time of flight is therefore proportional to the wavelength, then the Θ and λ values can be used to calculate the d spacing.

2.3.2.2 In Situ PND on GEM

In situ PND for the metal ammines in Chapters 4 and 5 were collected on the GEM (General Materials) diffractometer at the ISIS facility at Didcot. [40,41] GEM is an ideal instrument for in situ measurements as GEM's detector array (7290 detectors in total) covers a large area (7,1270 m^2) and a wide range of scattering angles (from 1.2°-171.4°). The detectors on GEM (ZnS/^{6}Li detectors) are also stable, with a 0.1% change in efficiency over 24 hours.[41] GEM has a high count rate and also provides high resolution in reciprocal space which is ideal for powder diffraction. Results can be obtained from GEM in a matter of minutes (allowing changes to be seen immediately, i.e. structural changes), although for refineable data collection time is over a longer period. GEM consists of 6 detector banks (see Table 2.3), with Bank 6 achieving the highest resolution ($\Delta Q/Q$= 0.34%).

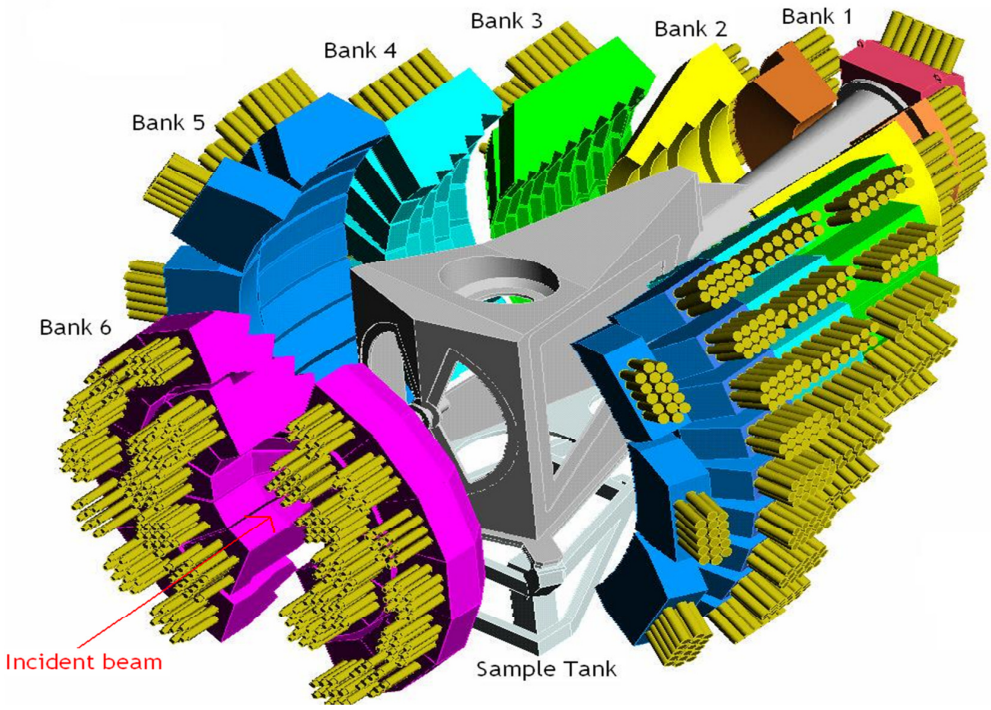

Figure 2.11: Schematic of GEM and its detector banks [42]

Table 2.3: Areas of coverage of the detector banks of GEM [41]

	2 theta/^{o}	d/Å
Bank 1	5.3-12.6	1.3-40
Bank 2	13.4-22.0	0.8-10
Bank 3	24.6-45.6	0.6-7
Bank 4	50-75	0.5-4
Bank 5	79-107	0.4-2.5
Bank 6	143-171	0.2-1.8

2.3.2.3 Sample Preparation on GEM

Due to the air-sensitive nature of the materials used for the GEM measurements, the samples were prepared in an MBraun glove box with an Ar(g) atmosphere at ISIS. Samples were loaded inside either 6 mm or 8 mm Vanadium cans with a Copper seal, with typically 1.5-2 g of sample loaded inside the can. The lid of the can consisted of an inlet/outlet connection which was capped to ensure the sample was not exposed to air/moisture. The cans were sealed and transferred outside the glove box, to be attached to a capillary stick for gas flow in an argon filled glove bag. The set-up that was employed can be seen in Figure 2.12:

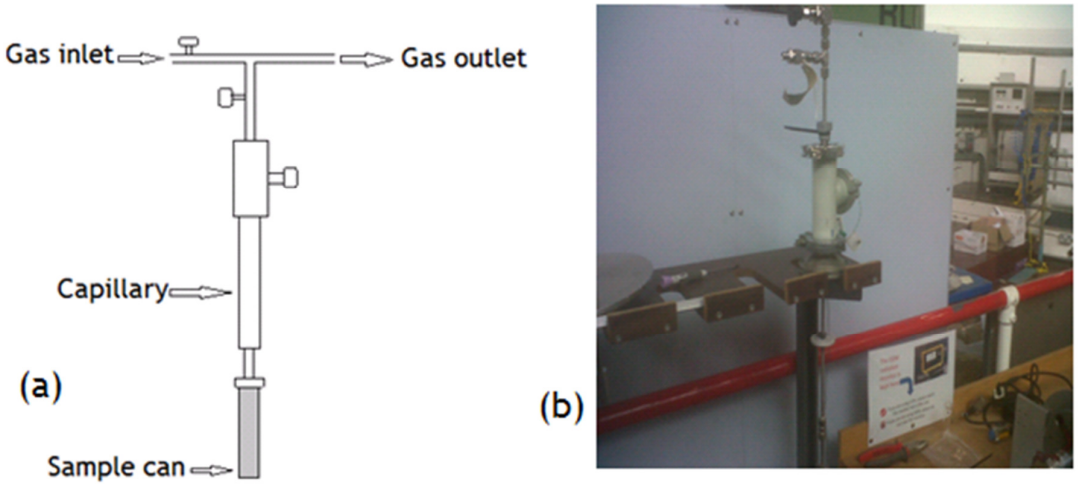

Figure 2.12: GEM set-up for In-situ PND experiments (a) is a schematic representation (b) the sample set-up prior to the neutron experiment

The set-up was then checked for leaks and was then loaded into a furnace (RAL-2) with a vanadium element and lowered into the neutron beam. Ar(g) was flowed across through the sample via the capillary with the gas outlet leading to a water trap.

2.3.2.4 Data Collection

Data were collected at each temperature point for a period of one to two hours depending on the sample quality.

Initial data analysis was carried out on Mantid, an ISIS neutron analysis program.[43] This initial data analysis allowed structural changes (such as the

change from the cubic hexaammine phase to the orthorhombic diammine phase) to be seen, with Bank 3 and Bank 4 providing the best information for sample changes.

The obtained neutron data were then converted into GSAS format (.gss) for Rietveld refinement (Section 2.4) using Mantid or GSAS.

All GEM measurements were performed with the help of Dr Winfried Kockelmann.

2.3.3 Ex-situ Powder Neutron Diffraction

Ex-situ PND experiments were carried out on the high resolution D2B diffractometer at the ILL laboratory in Grenoble.[44] D2B is characterised by its high take-off angle of 135° for the Ge monochromator to compensate for the loss of intensity with energy. D2B consists of 128 detectors at 1.25° intervals, meaning a complete scan of the sample can be undertaken in thirty minutes (25 steps of 0.05° for 2Θ). The optimum wavelength 1.594 Å was selected for the ex-situ measurements. A schematic of the layout of D2B can be seen in Figure 2.13

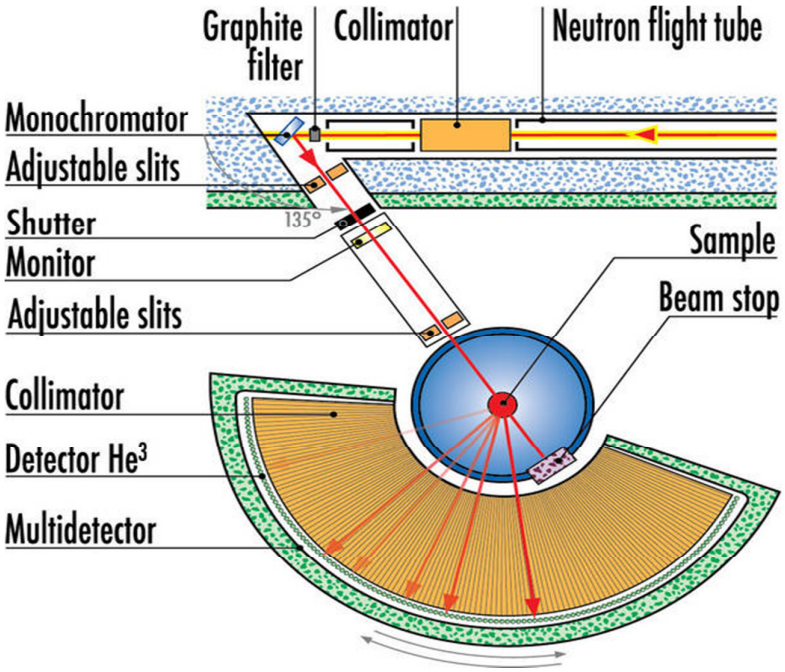

Figure 2.13: Schematic layout of the D2B diffractometer [45]

2.3.3.1 Sample Preparation

Due to the air-sensitive nature of the samples for the ILL experiments, the samples (~2 g) were loaded into large vanadium cans (>3 cm^3), with indium seals inside an N_2 (g) recirculating glove box (H_2O and O_2 <1 ppm).

2.3.3.2 Data Collection

Data for each sample were collected at room temperature (25 ^oC) and at -269.5 ^oC using the displex cryostat on D2B. The displex cryostat uses liquid He to cool the sample, with a temperature controller used to control the set point temperature required. Data were collected for each measurement for a period of 4-5 hours. The obtained data files were then converted to GSAS format for refinement purposes. All measurements at the ILL were performed with the help of Dr Clemens Ritter.

2.4 Rietveld Refinement

Rietveld refinement is a vital technique in the refinement of structural data in powder diffraction. The method was originally developed for constant wavelength neutron diffraction by H. M. Rietveld.[46,47] The technique has since been used for both time of flight neutron diffraction and for powder X-ray diffraction. In this project, Rietveld refinement has been used with both PXD and PND data (Chapters 4 and 5).

The Rietveld method was developed in response to the challenges faced by scientists when trying to extract structural information from a powdered sample. In single crystal diffraction, the structure factors are calculated from the measured intensities and can be extracted and solved using a variety of software packages, such as the WINGX package.[48] In PXD, this information has to be extracted from a one dimensional X-ray pattern. In powdered samples, particularly those that have complex structures and/or lower symmetry the degree of the reflection overlap could be to such a severe degree that the extraction of structural information is impossible. In response to this, Rietveld developed his refinement method.[49]

Rietveld Refinement is a least squares refinement method that refines the experimental pattern against a calculated pattern until the best fit is obtained. For analysing data in Rietveld Refinement as much crystal data should be known for the structure from as complete a model as possible. A good starting model is required as no attempt is made beforehand to match the observed intensities to Bragg reflections and there is no attempt made to resolve any overlapping intensities. Therefore, for solving unknown structures other methods must be used in conjunction with Rietveld Refinement.

Once a good starting model has been obtained, then the background parameters can first be obtained either manually or using a polynomial expression. Scale factors can also be introduced. The Bragg reflection positions can then be obtained by the variation of the lattice parameters and zero-point correction (sample displacement from the centre of the diffractometer). The peak shape parameters can then be refined. The atom positions can then be varied followed by the temperature factors of the atoms, which take into account the isotropic thermal motion of the atom. In some cases, the anisotropic temperature factors can then be refined. The final step is to allow all the refined parameters to vary until the refinement converges.

In a least squares refinement, S_y the residual function is minimised according to the equation 2.10:

$$S_y = \sum_i w_i \ (y_i - y_{ci})^2 \qquad (2.10)$$

where w_i is the weighting factor of $1/y_i$, y_i is the observed intensity at the i th step and y_{ci} is the calculated intensity at the *ith* step with *S* being the residual.

At any point i, its corresponding intensities are y_i. The intensity, y_{ci} is calculated from $|F_k|^2$ which are calculated from the structural factor (which is the contribution of the scattering amplitudes and phases of each atom), F by the summing of the calculated contributions from the neighbouring Bragg reflections along with the background:

$$y_{ci} = s \sum_k Lk \, |Fk|^2 \, \emptyset(2\theta_i - 2\theta_j) P_K A + y_{bi} \qquad (2.11)$$

where *s* is the scale factor, *K* are the Miller indices for a Bragg reflection, L_K contains the Lorentz, polarisation and multiplicity factors and ø is the reflection profile function, P_K is the preferred orientation factor, A is the absorption function, F_K is the structure factor for the *K th* Bragg reflection and y_{bi} is the background intensity at the i th step.

The Lorentz and polarisation factors depend on both instrument factors (geometry, detector, beam size) and sample factors (sample volume and geometry).

The background intensity can be obtained by three methods. These can be an operator-supplied Table of background intensities, an interpolation between operator selected points or a specified background function.

In GSAS, the background of a pattern can either be selected manually or fitted using one of the seven available background functions. Background Function 1 (Chebyschev polynomial) and background function 8 (Reciprocal Interpolation function) have been used for refinements in this thesis. The Chebyschev function is a polynomial of the first kind. Using the reciprocal interpolation function, the pattern is divided into equal 1/T (T= location) segments. This means that the intervals are concentrated into small d spacing regions, where background changes are more likely to occur.

At each point in the refinement, the observed intensities are compared with the calculated intensities. This means that it is vital that the calculated intensities correspond to the respective experimental Bragg reflections in terms of peak shape. The peak shape is generally governed by the instrument. The peak shape typically used for PXD and PND refinements is the Pseudo-Voigt peak shape function, which is a combination of the Gaussian and Lorentzian profile functions:

$$pV = \eta L + (1 - \eta)G \qquad (2.12)$$

where *pV* is the Pseudo-Voigt function, η is the mixing parameter, *L* is the Lorentzian function and *G* is the Gaussian function.

The mixing parameter, η can be refined as a linear function of 2Θ, with *NA* and *NB* both being refineable parameters:

$$\eta = NA + NB*(2\Theta_k) \quad (2.13)$$

The Gaussian profile function is given by the equation:

$$G = \frac{(4\ ln2)^{1/2}}{H_K \sqrt{\pi}} \quad exp\left(4\ ln2(2\Theta_i - 2\Theta_k)^2 / H^2_k\right) \quad (2.14)$$

The Lorentzian profile function is given by the equation:

$$L = \frac{2}{\pi H_K} \left/ 1+4\left(\frac{(2\Theta_i - 2\Theta_k)}{H^2_k}\right)^2\right. \quad (2.15)$$

In equations 2.14 and 2.15, $2\Theta_k$ is the calculated position for the *k th* Bragg reflection corrected for the counter zero-point with H_k being the full width at half maximum (FWHM) of the k th Bragg reflection.

The FWHM is given by the following equation:

$$H^2_K = (U\ tan^2\Theta + V\ tan\Theta + W)^{1/2} \quad (2.16)$$

where *U*, *V* and *W* being parameters that can be refined. These parameters are mostly refined from the sample, so any sample effects (i.e crystallite size) play a major role in the FWHM.

In order to determine if the 'best fit' has been obtained for a refinement (calculated intensities against the observed intensities) and thus if the proposed model is correct, then criteria of the fit must be measured. In Rietveld Refinement reliability factors, R, are used to determine if the 'best fit' has been obtained. The R values are defined as R_P (R profile), R_{exp} (R-expected and R_{wp} (R of the weighted profile).[50]

$$R_p = \frac{\sum_i (y_{i\,obs} - y_{i\,calc})}{\sum_i (y_{i\,calc})^2} \quad (2.17)$$

$$R_{wp} = \sqrt{\frac{\sum_I w_i \left[(y_{i\,obs} - y_{i\,calc}) \right]^2}{\sum_i \; w_i (y_{i\,calc})^2}} \quad (2.18)$$

$$R_{exp} = \sqrt{\left[\frac{(N-P+C)}{\sum_i^n w_i y^i (obs)^2} \right]^2} \quad (2.19)$$

Where *N* is the number of observations, *P* is the number of parameters and *C* is the number of constraints.

The R_{wp} factor (equation 2.18) is the most mathematically important of the index equations as the numerator, which is the residual, is the function being minimised. To calculate the goodness of fit, the chi-squared parameter X^2 is used and is calculated by the following equation:

$$X^2 = (R_{wp} / R_{exp})^2 \quad (2.20)$$

where R_{exp} is the R expected factor

The chi squared value should also be as close to 1 as possible, so the R_{wp} value should be as close as possible to the R_{exp} value. The quality of fit can be examined using an observed, calculated and difference (OCD) graphical plot of the profile fit.

Refinements using PND data in this thesis were performed using the GSAS and EXPGUI software.[30,31]

2.5 Raman Spectroscopy

Raman Spectroscopy has been carried out on the metal ammines in this project (Chapter 3) to elucidate information about the bonding characteristics.

2.5.1 Background

Raman spectroscopy dates back to 1928, when Sir Chandrasekhra Raman discovered the technique using sunlight as the source of light, a telescope as a collector and his eyes as the detector.[51] Raman spectroscopy is a form of vibrational spectroscopy, like Infra-Red (IR) spectroscopy. Raman spectroscopy can be used as a complimentary technique to IR and PXD to confirm structure and bonding and can also be used as a stand-alone characterisation technique. Raman spectroscopy probes the local bonding environment of a sample, thus information about bonding between the different elements in a sample can be elucidated. The use of Raman spectroscopy in hydrogen storage materials is beneficial in the characterisation of a number of materials due to the sensitivity of Raman spectroscopy to both crystalline and amorphous materials and also Raman allows a reaction to be followed by the changes of states (for example solid to liquid). Borohydrides and NH_3BH_3 are amongst the hydrogen storage materials that have been studied.[52]

Raman radiation involves the transitions between incident wavelengths. The sample in Raman spectroscopy is irradiated in the UV-region (V_o) of the electromagnetic spectrum (Figure 2.5) by a laser source, with the light (photons) being scattered in a perpendicular direction to that of the incident light. Raman is measured in the UV region so that both Raman scattering and excitation data can be obtained.

When the laser encounters a sample, Rayleigh scattering (elastic scattering) and Raman scattering (inelastic scattering) are produced. The latter consists of Stokes and anti-Stokes lines (Figure 2.14). When the photon collides with a molecule, the energy possessed by the photon promotes to a “virtual energy state” for a short period. The Rayleigh scattering is strong and is from an oscillating dipole that radiates light with the frequency v_o, the same frequency as that of the incident beam. The Stokes and anti-Stokes lines have a different

frequency to that of the incident beam. In Stokes lines, the photon is scattered at a lower energy. As the majority of the molecule population is in the ground state at room temperature, then the Stokes lines have a greater intensity than the anti-Stokes lines and are generally used for Raman measurements. The anti-Stokes lines occur when a small proportion of the molecule is in a higher vibrational state than the ground state, so the photon is scattered at a higher energy. The energy change of the photon is characteristic of the vibration of the molecule, so this allows different molecules to be identified.

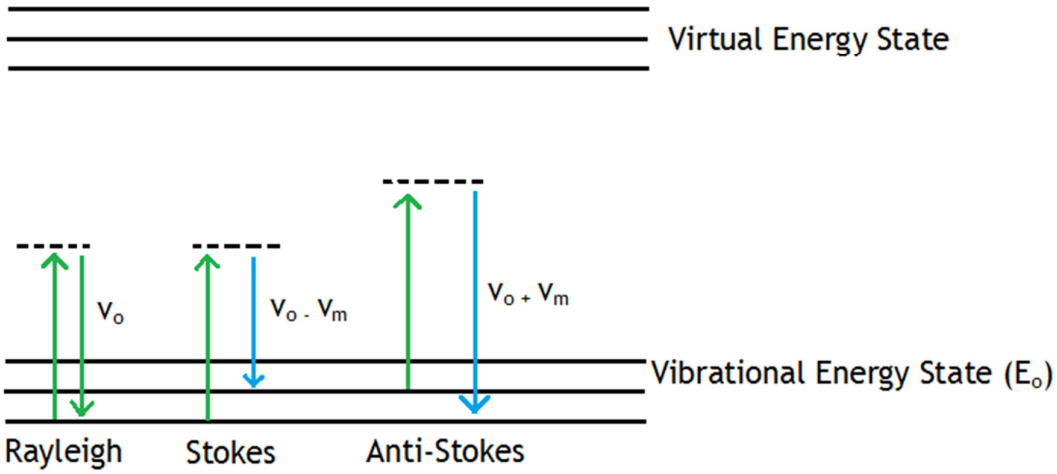

Figure 2.14: Rayleigh, Stokes and anti-Stokes scattering in Raman spectroscopy. V_o is the incident beam frequency and V_m is the vibrational frequency of the molecule

Raman Scattering can be explained by a series of equations.[51] The electric field strength of an electromagnetic wave fluctuates with time:

$$E = E_o \cos 2\pi \nu_o t \qquad (2.21)$$

Where E = electric field strength of the laser, t = time, E_o = vibrational amplitude and ν_o = laser frequency

When the molecule is exposed to the laser, distortion in the diatomic molecule occurs. This leads to an induced electric dipole moment (P)

$$P = aE = aE_o cos 2\pi v_o t \qquad (2.22)$$

where a = polarisibility (proportionally constant).

The a term also determines if a vibration is Raman active or Raman inactive as will be seen below. From the above equation, a molecule vibrating with a frequency can be defined as:

$$q = q_o cos 2\pi v_m t \qquad (2.23)$$

where q = displacement, v_m = vibrational frequency and q_o = vibrational amplitude.

Following on from this, if the vibration is of a small amplitude then α is a linear function of q, so the following equation is derived:

$$a = a_o + \left(\frac{\delta_a}{\delta_q}\right)_o q_o + \ldots. \qquad (2.24)$$

where a_o = polarisibility at an equilibrium position, δ_a / δ_q = rate of change of α and this is related to the rate of change in q at an equilibrium position

Combining these equations, the derived equation to explain Raman Scattering is as follows:

$$P = a_o E_o cos 2\pi v_o t + {}^1/_2 \left(\frac{\delta_a}{\delta_B}\right)_o q_o E_o \left\{cos\left[2\pi(v_o + v_m)\right] t\right\} \qquad (2.25)$$

The first term of this equation relates to the Rayleigh Scattering. The second term of this equation is that of Raman Scattering: the Stokes and anti-Stokes scattering. In the above equation, if δ_α / δ_q is zero, then the vibration will be

Raman inactive. Hence for the vibration to be Raman active then α must be non-zero. The units used in Raman are Raman Shift (cm^{-1}).

2.5.1.1 Sample Preparation

One of the major practical advantages of Raman over IR spectroscopy is that air sensitive samples can be measured in sealed silica glass capillaries. The preparation of the capillaries was as described in Section 2.3.3.

2.5.1.2 Measurement

The Raman spectrometer used was a Horibo Raman LabRAM HR. The experimental setup consisted of a Horibo-Jobin-Yvon HR confocal microscope and a Quantum Venus 532 laser at 150 mW excited with 532 nm light. Spectra were collected through a 50X objective lens in backscattering mode with a 600 mm^{-1} grating and Synapse CCD detector.[53] The software used for data collection/analysis was Horiba Lab Spec with Raman spectra manipulated using Origin.[54]

To obtain a Raman spectrum, the sample is first focused. The aperture size and number of collections was then selected. The laser was switched on and spectra collected. A broad range spectrum (~200 cm^{-1} – 4000 cm^{-1}) and a focussed spectrum between 3000 cm^{-1} -3500 cm^{-1} were typically obtained.

Raman measurements were carried out with the help of Hazel Reardon and Dr Robert W. Hughes.

2.6 Temperature Programmed Desorption (TPD) by Thermogravemetric Analysis (TGA)- Differential Thermal Analysis (DTA)- Mass Spectrometry (MS)

TPD measurements were carried for the deammoniation of the metal ammines (Chapter 3), for H_2 release in the ammine-hydride systems (Chapter 4) and for H_2 release in the hydroxide-hydride systems (Chapter 5). TPD measurements allowed the study of the deammoniation processes in the metal ammines with their related temperatures, while for H_2 release systems, TPD allowed the onset of H_2 release to be determined along with the total weight loss of the system.

2.6.1 Background

TPD conducted in this thesis consists of three components: Thermogravemetric analysis (TGA), Differential Thermal Analysis (DTA) and Mass Spectrometry (MS).

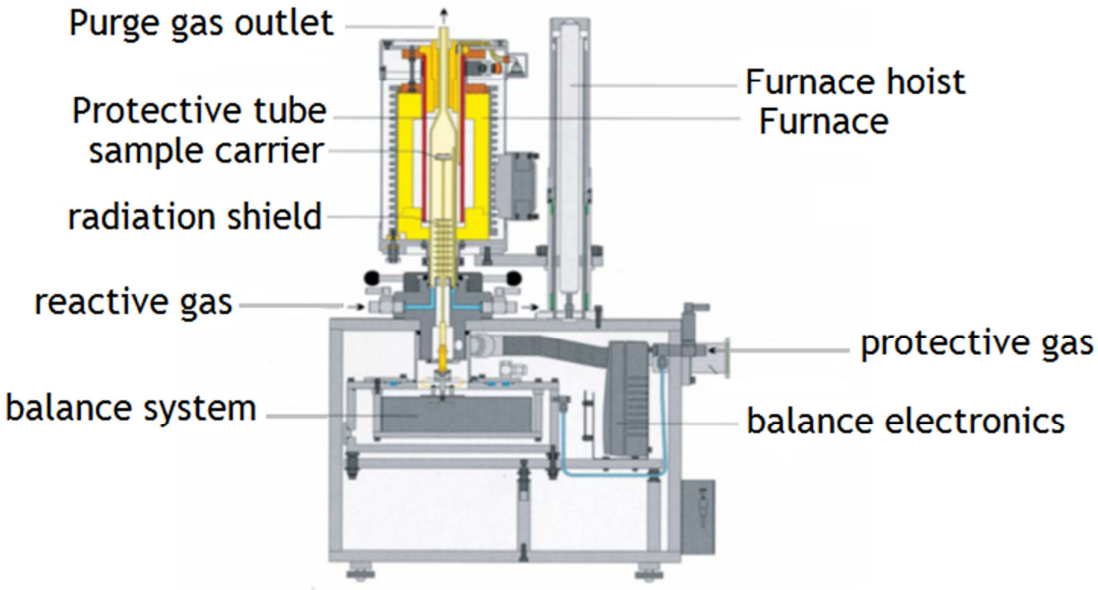

Figure 2.15: Schematic of the Netzsch STA409CD [55]

Measurements were performed using a Netzsch STA 409 analyser (Figure 2.15) which was interfaced to a Hiden HPR 20 Mass Spectrometer. As the samples required for TPD measurements were air sensitive, measurements were undertaken using an instrument located in a MBraun Ar(g) glove box (<0.1 ppm H_2O, <0.1 ppm O_2).

TGA is an important tool and can aid in determining the thermal stability of a material. In TGA, the sample is heated in a crucible which is typically alumina, platinum, nickel or stainless steel, with the weight loss of the sample recorded as a function of temperature.

Differential thermal analysis (DTA) is coupled to the TGA. DTA can be used to identify phase transition temperatures and also identify if a reaction or transition is either exothermic or endothermic. In DTA, the crucible containing the sample is heated under identical conditions as the reference crucible, which is an empty crucible (crucible depends on the sample crucible material, so if an alumina crucible is used for the sample then an empty alumina crucible is used for the reference). An empty crucible is used so that heat changes originating from the crucible can be taken into account, and that measured changes in the recorded thermal profile are attributed to the sample only. A schematic of the DTA arrangement is shown in Figure 2.16.

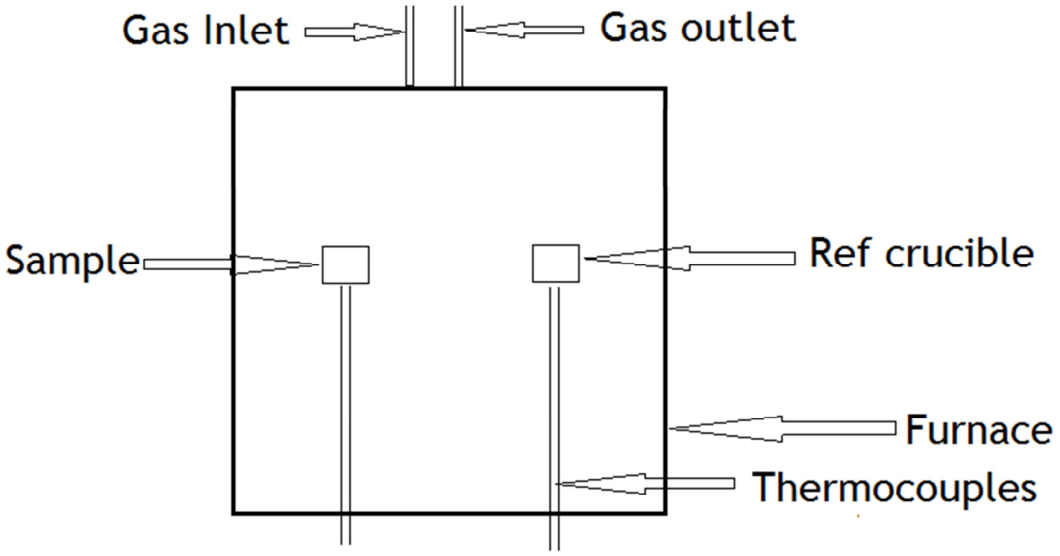

Figure 2.16: Schematic of the DTA arrangement

The STA is also coupled to a Mass spectrometer (Hiden Analytical HPR 20). This allows analysis of the gases evolved during heating and can be used in correspondence with TGA and DTA data to give a profile of the chemical changes involved during heating (such as dehydrogenation or deammoniation).

A mass spectrometer typically consists of three components: the ion source, the mass analyser and the mass detector. The first process in a mass spectrometer is the vaporisation of the sample at the ion source. This involves the ionisation of the sample by electrons, produced by the filament, to a cation with the loss of an electron (where M is the sample):

$$M + e^- \rightarrow M^+ + 2\ e^- \qquad (2.26)$$

The positive ion produced is referred to as the molecular ion, which gives the molecular mass of the material being measured. After the ionisation process, the ions are accelerated by an electric field (negatively charged accelerating slits) to the mass analyser, so that all the ions possess the same kinetic energy.

At the mass analyser, separation of the ions occurs in a curved tube according to their m/z ratio (m- mass, z= charge). During this process, the ions are deflected by an electromagnetic field. In this process, lighter atoms are deflected more than the heavier particles based on Newton's second law of motion, which states the acceleration produced by a force is directly proportional to the mass:

$$F = ma \qquad (2.27)$$

Where F= force applied, m= mass of the ion and a= acceleration of the ion

The detection of ions with different masses is achieved by varying the magnetic field used in the deflection process. After the selection of ions has occurred, the ions are focussed onto an ion collector where they are detected and also amplified. The mass spectrum is then recorded by the mass spectrometry software and analysis of the mass spectrum undertaken.

The Mass Spectrometer used in this project, the Hiden HPR20 is a quadrupole mass analyser. The quadrupole mass analyser (Figure 2.17) was developed by Wolfgang Paul.[56] In a quadrupole mass analyser there are four parallel quadrupole rods. These rods have a fixed DC (direct current) potential and alternating RF (radio frequency) factors, so that the ions produced by the ion source travel along the middle of the rods. Only ions with a particular m/z value (selected by the user) are stabilised and allowed to travel through to the mass

detector, due to changes in the electrical fields. The RF factor is changed to allow other ions with other particular m/z values to be detected by the mass detector in order to build up a spectrum.

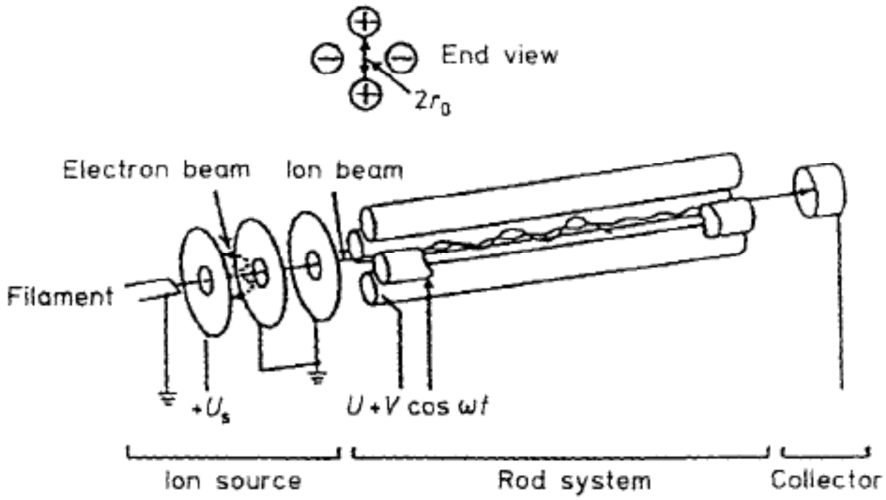

Figure 2.17: Quadrupole mass analyser developed by Wolfgang Paul. Reprinted with permission from Ref 56. Copyright 1990 John Wiley & Sons

2.6.1.1 Sample Preparation

Before a sample could be heated and analysed in a TG-DTA experiment, a correction file is needed. This involves heating an empty sample pan using the conditions required for the sample being studied. The correction file contains the information about the heating conditions for the sample and also the thermal profile of the sample pan. The Mass Spectrometry is also run during the correction file to mimic the conditions of the sample when heated. Ar(g) was the carrier gas used for all measurements during this project.

The first step for running the sample is to place an empty pan onto the TGA, and allowing the balance to stabilise to zero and the DTA value on the software to reach ~-1 mV. Once the balance is stabilised, the sample is added to the pan using a micro spatula. In a typical experiment, 30-40mg of sample is used. The balance/furnace (fig 2.16) is then closed, and the balance allowed to stabilise and the DTA value allowed to rest at ~-1mV. Once this is the case, the relevant correction file is selected and the sample is heated. Mass spectrometry data is also collected for the sample at the appropriate m/z values.

2.7 Electron Microscopy

Scanning Electron Microscopy (SEM) along with its complementary technique, Energy Dispersive X-ray Spectroscopy (EDX) has been used to determine the morphology, particle sizes and the elemental composition of samples respectively in this thesis.

2.7.1 Background

The electron source in an SEM (Figure 2.18) is typically an electron gun, which produces electrons thermionically. The gun consists of three sections: the filament (typically tungsten), a Wehnelt cylinder and an anode. The electrons are produced when a voltage is applied to the tungsten filament (100 um in diameter), which in turns leads to its heating. When a current is supplied, electrons escape from the tip of the filament. A negative potential is applied to the tungsten gun and the Wehnelt cylinder which results in the acceleration of the electrons towards the anode in the tungsten gun.[57] Through this process, a beam of high energy electrons is produced.

The beam of electrons is focussed by a condenser lens and then interacts with the sample. When the electrons interact with the sample, both secondary electrons (SE) and backscattered electrons (BSE) are produced along with Auger electrons, X-rays and cathodoluminesence.

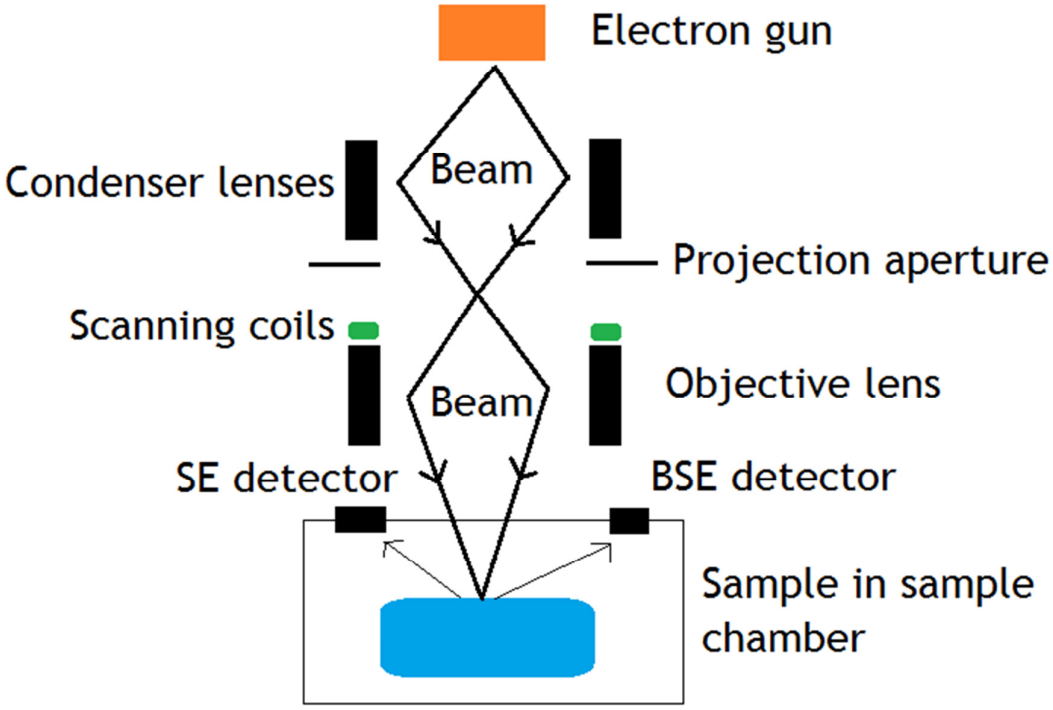

Figure 2.18: Schematic of an SEM. Only the backscattered electrons and secondary electrons when the beam interacts with the sample are shown for clarity.

Backscattered electrons are produced by the elastic collision of an incident electron with the sample at an angle of more than 90 °. Backscattering of electrons occurs through a wide variety of interactions between the incident electrons and the electrons in atoms of the sample. Energy is also transferred from the incident electrons to the atoms of the sample, with the energy loss dependent on the binding and excitation properties of the atoms.

During the ionisation of the atoms and the excitation of the incident electrons, secondary electrons are produced. Secondary electrons are produced by the ejection of electrons from the sample by the incident beam. The electrons produced are from near the surface of the sample and have a much lower energy than the backscattered electrons.

The incident electron beam is scanned across the surface of the sample and the backscattered and secondary electrons are detected by the detectors in the SEM to produce an image of the sample. The backscattered electrons provide

topographical information about the sample, while the secondary electrons provide the image contrast (due to more secondary electrons leaving the sample edges leading to increased brightness) and also topographical information of the sample.[58]

Auger electrons are also produced when the incident electron beam interacts with the sample. When an atom is ionised by the incident electrons, this results in an outer shell electron filling the inner shell electron vacancy caused by the ionisation. An excess of energy is produced which is transferred to another electron, called the Auger electron. Auger electrons, which have low energy are used in surface analysis as they are only emitted near the surface of the sample. Cathodoluminesence occurs when the excess energy produced by the interaction of the beam and the sample is released as photons. X-rays are also produced during the interaction of the beam and sample and are used for Energy Dispersive Spectroscopy (section 2.7.2).

2.7.2 Energy Dispersive X-ray Spectroscopy (EDX)

EDX is a complementary technique to SEM and is used for the measurement of the elemental composition of areas of the sample. EDX uses the X-rays produced by the interaction of the incident beam and the samples.

The X-rays are produced by the sample when an electron from the inner shell of the sample is emitted and an electron from the outer shell fills the vacancy. The excess energy is then released in the form of X-rays. The energy of the X-ray is characteristic of a particular element. The output in the EDX provides quantitative composition information for the sample.

The drawback of EDX is that the scattering of X-rays by light elements (section 2.2) is weak, so elements such as Li and H cannot be measured by this technique.

2.7.2.1 Sample Preparation for SEM/EDX

A small quantity of sample was placed on an aluminium stub with a carbon tab attached. For air sensitive samples, this was performed in the glove box and the sample placed in a sealed vial for transfer to the SEM.

If the samples were charging in the SEM (where good image contrast is not possible due to the brightness produced from the sample), the samples would be gold plated in an Ar(g) atmosphere before transfer to the SEM by a process called sputter coating. By sputter coating, a voltage is applied between the sample and the gold plate. This causes the argon to ionise and strike the gold plate causing some gold atoms to be ionised and become dislodged. These gold ions then form a uniform layer on the sample.[59] For air sensitive samples if gold plating was required, then exposure to air was kept to a minimum by the quick transfer to the Ar(g) atmosphere.

Once samples have been transferred to the microscope, the SEM was then placed under vacuum (10^{-5} -10^{-6} Pa) and the beam current set at 20-25 keV with a set working distance of 5 mm (for samples requiring EDX measurements) or 10 mm (for samples where only imaging was required).

High resolution SEM measurements were carried out either using a Hitachi S-4700, with a voltage of 5 keV and a working size of 12.5 mm in the School of Engineering by Dr Saleem Denholme or using a Zeiss Sigma SEM in the School of Geographical and Earth Sciences by Peter Chung.

2.7 References

[1] S. Somiya and R. Roy, *Bull. Mater. Sci.*, 2000, **23**, 453.

[2] B .L. Cushing, V. L. Kolesnichenko and C. J. O'Connor, *Chem. Rev.* , 2004, **9**, 3893.

[3] J. Yu, A. Xu, L. Zhang, R. Song, L. Wu, *J. Phys. Chem. B*, 2004, **108**, 64.

[4] Parr Acid Digestion Vessels Operating Instruction Manual

[5] Parr, US Patent No 4882128.

[6] Parr Sample Preparation Bombs Manual accessed on 22nd March 2012 at:

http://www.parrinst.com/wp-content/uploads/downloads/2011/06/4700MB_Parr_Sample-Preparation-Vessels-Literature.pdf

[7] K. J. Rao, B. Vaidhyanathan, M. Ganguli and P. A. Ramakrishnan, *Chem. Mater.*, 1999, **11**, 882.

[8] J. Zhao and W. Yan, *Modern Inorganic Synthetic Chemistry*, Elsevier Publishing, Amsterdam, 2011.

[9] J. J. Hassan, Z. Hassan and A. H. Hassan, *J. Alloys Compd.*, 2011, **509**, 6711.

[10] Z. W. Chen, S. Li and Y. S. Yan. *Chem. Mater.*, 2005, **17**, 2262.

[11] S. Caddick, *Tetrahedron*, 1995, **51**, 10403.

[12] Y. Ding, G. Zhang, H. Wu, B. Hai, L. Wang and Y. Qian, *Chem. Mater.*, 2001, **13**, 435.

[13] Y. Li, M. Sui, Y. Ding, G. Zhang, J. Zhuang and C. Wang, *Adv. Mater.*, 2000, **12**, 818.

[14] J. C. Yu, A. Xu, L. Zhang, R. Song and L. Wu, J. *Phys. Chem. B*, 2004, **108**, 64.

[15] D. H. Gregory, P. M. O'Meara, A. G. Gordon, J. P. Hodges and J. D. Jorgensen, *Chem. Mater.*, 2002, **14**, 2063.

[16] R. Z. Sorensen, J. S. Hummelshoj, A. Klerke, J. B. Reves, T. Vegge, J. K. Norskov and C. H. Christensen, *J .Am. Chem. Soc*, 2008, **130**, 8660.

[17] M. H. Sørby, O. M. Løvvik, M. Tsuboto, T. Ichikawa, Y. Kojima and B. C. Hauback, *Phys. Chem. Chem. Phys.,* 2011, **13**, 7644.

[18] A. Leineweber, M.W. Fredriszik and H.Jacobs, *J. Solid State Chem.,*1999, **147**, 229.

[19] V. K. Pecharsky and P. Y. Zavalij, *Fundamentals of Powder Diffraction and Structural Characterisation of Materials 2nd Ed.*, Springer Publishing, New York, 2009.

[20] W. L. Bragg, *Proceedings of the Royal Society of London Series A- Papers of a Mathematical and Physical Character*, 1913, **89**, 248.

[21] W. H. Bragg and W. L. Bragg, *Proceedings of the Royal Society of London Series A- Papers of a Mathematical and Physical Character*, 1913, **88**, 428.

[22] Y. Wasada, E. Matsubara and K. Shinoda, *X-ray Diffraction Crystallography*, Springer Publishing, 2011.

[23] R. Shirley, The CRYSFIRE System for Automatic Powder Indexing

[24] A. Boultif and D. Louër, *J. Appl. Crystallogr.*, 1991, **24**, 987.

[25] J. Laugier and B. Bochu, "CELREF Unit-Cell Refinement Software on a Multiphase System", Laboratoire des Materiaux et du Genie Physique Ecole Nationale Sup6rieure de Physique de Grenoble.

[26] M. G. Barker, M. J. Begley, P. P. Edwards, D. H. Gregory, S. E. Smith, *J. Chem. Soc. Dalton Trans.* 1996, 1.

[27] N. Kourkoumelis, *International Union of Crystallography, Commission on Powder diffraction*, 2005, **Newsletter 30**.

[28] G. Nolze and W. Kraus, *Powder Diffr.,* 1998, **13**, 256.

[29] A. Belsky, M. Hellenbrandt, V.L. Karen and P. Luksch, *Acta Crystallogr.*, 2002, **B58**, 364.

[30] A. C. Larson and R. B. von Dreele, The General Structure Analysis System, Los Alamos National Laboratories, Report LAUR 086–748, LANL, Los Alamos, NM, 2000

[31] B. H. Toby, *J. Appl. Crystallogr.,* 2001, **34**, 210.

[32] ILL Reactor Technical Characteristics, accessed on 27th March 2012 at:

http://www.ill.eu/reactor-environment-safety/high-flux-reactor/technical-characteristics/

[33] L. Liang, R. Rinaldi and H. Schober, *Neutron Applications in Earth, Energy and Environmental Sciences*, Springer Publishing, New York, 2009.

[34] A. C. Hannon, ISIS Neutron Course Training Manual.

[35] How ISIS works accessed on 27th March 2012 at: http://www.isis.stfc.ac.uk/about-isis/how-isis-works6313.html

[36] How ISIS works: In Depth accessed on 27th March 2012 at: http://www.isis.stfc.ac.uk/about-isis/how-isis-works---in-depth4371.html

[37] C. C. Wilson, *Single Crystal Neutron Diffraction from Molecular Materials*, World Scientific, London, 2000.

[38] D. P. Mitchell and P. N. Powers, *Phys. Rev.*, 1936, **50**, 486.

[39] R. I. Smith , ISIS Neutron Course Training Manual.

[40] W. G. Williams, R. M. Ibberson, P. Day and J. E. Enderby, *Physica B*, 1998, **234**, 241.

[41] A.C. Hannon, *Nucl. Instrum. Methods Phys. Res. A*, 2005, **551**, 81.

[42] GEM at ISIS Slides supplied by Dr W. Kockelmann, ISIS Facility, RAL, Didcot.

[43] Information about the Mantid program accessed on 27th March 2012 at: www.mantidproject.org

[44] E. Suard and A. Hewitt, *Neutron News*, 2001, **4**, 350.

[45] D2B Instrument at the ILL Grenoble accessed on 27th March 2012 at: http://www.ill.eu/instruments-support/instruments-groups/instruments/d2b/

[46] H. M. Rietveld, *Acta Crystallogr.,* 1967, **22**, 151.

[47] H. M. Rietveld, *J. Appl. Crystallogr*.. 1969, **2**, 65.

[48] L. J. Farrugia, *J. Appl. Crystallogr*.,1999, **32**, 837.

[49] R. A. Young, The Rietveld Method, IUCR- OUP publishing, Oxford, 1993.

[50] L. B. McClusker, R. B, Von Drelle, D. E. Cox, D. Louër and P. Scardi, *J. Appl. Cryst.*, 1999, **32**, 36.

[51] J. R. Ferraro, K. Nakamoto and C. W. Brown, *Introduction to Raman Spectroscopy 2nd Edn.,* Elsevier Publishing, 2003.

[52] D. Reed and D. Brook, *Curr. Opin. Solid State Mater. Sci.*, 2011, **15**, 62.

[53] H. Reardon, J. M. Hanlon, M. Grant, I. Fullbrook and D. H. Gregory, *Crystals*, 2012, **2**, 123.

[54] OriginLab software Information accessed on 27th March 2012 at: http://www.originlab.com/

[55] Netszch STA409 PC product brochure accessed on 27th March 2012 at: http://www.netzsch-thermal-analysis.com/download/STA409CD_e.0306_18.pdf

[56] W. Paul, *Angew. Chem. Int. Ed.,*1990, **29**, 739.

[57] W. Zhou and Z. L. Wang, Scanning Microscopy for Nanotechnology: Techniques and Applications, Springer Publishing New York, 2007.

[58] I. M. Watt, *The Principals and Practice of Electron Microscope- 2ND Edn.*, Cambridge University Press, Cambridge, 1997.

[59] J. Burgess, M. Marten and R. Taylor, *Under the Microscope: a hidden world revealed*, Cambridge University Press, Cambridge, 1990

3. Structural and TPD Deammoniation Investigations of the Magnesium Ammines, $Mg(NH_3)_6X_2$ (where X= Cl, Br, I)

3.1 Introduction

The magnesium ammines, $Mg(NH_3)_nX_2$ (X= Cl, Br,I) are prospective materials for both solid state ammonia storage and indirect H_2 storage. They possess high gravimetric capacities, especially the chloride adduct (Table 3.1).

Of the magnesium ammines, only $Mg(NH_3)_6Cl_2$ has been studied in any detail.[1,2] This is due to the high gravimetric capacity for both ammonia and hydrogen storage. The deammoniation of $Mg(NH_3)_6Cl_2$ occurs in three steps:

$$Mg(NH_3)_6Cl_2 \rightarrow Mg(NH_3)_2Cl_2 + 4\ NH_3 \quad (3.1)$$

$$Mg(NH_3)_2Cl_2 \rightarrow Mg(NH_3)Cl_2 + NH_3 \quad (3.2)$$

$$Mg(NH_3)Cl_2 \rightarrow MgCl_2 + NH_3 \quad (3.3)$$

The structure of $Mg(NH_3)_6Cl_2$ was calculated to be cubic ($Fm\bar{3}m$) by Density Functional Theory (DFT) methods. In the unit cell, the Mg is bonded to the nitrogen from NH_3. The chloride is not bonded to either the Mg or N and is "free" in the unit cell and is effectively acting as a counter anion to the complex cation $M(NH_3)_6^{2+}$. This structure has subsequently been refined by Powder Neutron Diffraction (PND) and molecular dynamic calculations (MD) using $Mg(ND_3)_6Cl_2$.[3] This proposed structure is discussed in Chapter 4.

The structure of $Mg(NH_3)_2Cl_2$ has been reported by Leineweber *et al.*[4,5] The structure derived from single X-ray crystallography and PND, is orthorhombic (*Cmmm*) with the nitrogen and chloride both bonded to the magnesium. The structure of $Mg(NH_3)Cl_2$ has been suggested to be isostructural with $Ni(NH_3)X_2$ (X= Cl, Br) which crystallise in the monoclinic *I2/m* space group.[6]

$Mg(NH_3)_6Br_2$ crystallises in the K_2PtCl_6 cubic structure.[7] The only published data concerning the deammoniation of $Mg(NH_3)_6Br_2$ has been the onset and end temperatures of deammoniation and the associated enthalpies of reactions.[8] No detailed data on its deammoniation mechanism are available. The structure of

$Mg(NH_3)_2Br_2$ has been studied by single X-ray crystallography and crystallises in the orthorhombic *Pbam* space group.[4]

Only the X-ray diffraction pattern of the magnesium iodide adduct, $Mg(NH_3)_6I_2$ has been reported. Its structure was proposed as cubic.[9] Its deammoniation properties have yet to be fully investigated. The diammine, $Mg(NH_3)_6I_2$ was found to be isostructural to $Mg(NH_3)_6I_2$ (*Pbam*).[4]

Table 3.1: Gravimetric ammonia and hydrogen capacities of the magnesium ammine adducts

Ammine	%wt. NH_3	%wt. H_2
$Mg(NH_3)_6Cl_2$	51.7	9.1
$Mg(NH_3)_2Cl_2$	13.2	4.6
$Mg(NH_3)_6Br_2$	35.7	6.3
$Mg(NH_3)_2Br_2$	10.4	3.7
$Mg(NH_3)_6I_2$	26.8	4.7
$Mg(NH_3)_2I_2$	10.9	1.9

The aims of this chapter have been to synthesise $Mg(NH_3)_6X_2$ (X= Cl, Br, I) and characterise their structure by PXD and subsequent refinement of the PXD data by the Rietveld method. The deammoniation of each of the hexammines have also been investigated by thermal programmed desorption (by TGA-DTA-MS) and the intermediates of the deammoniation ($Mg(NH_3)_2X_2$ and $Mg(NH_3)_6X_2$ isolated) and characterised. From this data, the deammoniation mechanism (and corresponding temperatures) have been elucidated.

3.2 Experimental

3.2.1 Synthesis of $Mg(NH_3)_6X_2$ where X= Cl, Br, I

The hexaammines were synthesised by the reaction of the starting salt MX_2 (X= Cl (Sigma, 98%), Br (Sigma, 98%), I (Alfa 99%, Sigma 98%)) under a flow of NH_3(BOC, 99%) overnight. Further investigations decreased this experimental time to a period of 1 – 2 hours.

Handling of the starting salt and product were performed in a N_2(g) recirculating glove box. The experimental set up used for the synthesis of the hexaammines is described in section 2.2.6.

3.2.2 Powder X-ray Diffraction (PXD) Experiments

Compounds were characterised by PXD, as described in section 2.3.1.2. For the hexaammines capillaries were prepared and data collected from 5 – 75 ^{o} with a step size of 1.3 ^{o} / min for 1 hr and 5 - 95 ^{o} with a step size of 0.14 ^{o}/min for refinement purposes using the Brucker D8. For the diammines and monoammines characterisation was performed using an air sensitive flat plate between 5-85 ^{o} for 20-30 mins for identification purposes and for 12 hours for refinement purposes using the PANalytical X'pert Pro.

3.2.3 Deammoniation of the ammines

Measurements of the deammoniation of the ammines were performed using a Netzsch STA 409 analyser which was interfaced to a Hiden HPR 20 Mass Spectrometer (section 2.6). Measurements were performed in an Ar(g) recirculating glove box, with 30-40 mg of samples typically used.

Samples were heated to 500 ^{o}C at a rate of 5 ^{o}C per min and held at 500 ^{o}C for two hours. Mass spec (m/z) data were collected for NH_3, N_2, H_2 and H_2O. The intermediates of the deammoniation (diammine and monoammine) were isolated by heating to the appropriate temperature.

3.2.4 Rietveld Refinement against PXD data

The synthesised ammines were refined using the GSAS program with the EXPGUI interface. [10,11] The background in the hexaammines was successfully fitted using background function 8, a reciprocal interpolation function. The backgrounds for the diammines were modelled using background function 1, a shifted Chebyschev function. This was then followed by refinement of cell parameters, atomic positions, profile coefficients, peak widths and temperature factors. Peak profiles were successfully modelled using function 2 in GSAS, a Simpson's integration of the Pseudo-Voight function.

3.2.5 Raman Measurements

Raman measurements were performed using a Horibo Raman LabRAM HR. The setup consisted of a Horibo- Jobin- Yvon HR confocal microscope and a Quantum Venus 532 laser at 150 mW excited with 532 nm light. Spectra were collected through a 50X objective lens in backscattering mode with a 600 g mm^{-1} grating and Synapse CCD detector.

Samples were loaded into silica capillaries inside the glove box and sealed using vacuum grease. The samples were flame sealed outside the glove box and data collection carried out as per section 2.5.1.2.

3.2.6 Summary of Reactions

Table 3.2: Summary of the Reactions presented in this Chapter

Reaction	Material	Conditions
1	$Mg(NH_3)_6Cl_2$	
2	$Mg(NH_3)_6Br_2$	
3	$Mg(NH_3)_6I_2$	
4	$Mg(NH_3)_6Cl_2$ (**1**)	Heated to 500 ^oC
5	$Mg(NH_3)_6Br_2$ **(2)**	Heated to 500 ^oC
6	$Mg(NH_3)_6I_2$ **(3)**	Heated to 500 ^oC
7	$Mg(NH_3)_2Cl_2$	Intermediate Study
8	$Mg(NH_3)Cl_2$	Intermediate Study
9	$Mg(NH_3)_2Br_2$	Intermediate Study
10	$Mg(NH_3)Br_2$	Intermediate Study
11	$Mg(NH_3)_2I_2$	Intermediate Study
12	$Mg(NH_3)I_2$	Intermediate Study

3.3 Results and Discussion

3.3.1 Preparation of $Mg(NH_3)_6X_2$, where X= Cl, Br, I

The synthesised $Mg(NH_3)_6Cl_2$ (sample **1**) was a fine, white powder while the starting material is a white powder. PXD analysis (Figure 3.1) using PowderCell confirmed that the cubic hexaammine had been formed (PDF no: 01-075-6756) with a small phase of NH_4Cl present. This impurity phase may be due to the flame sealing of the capillary. Initial indexing and cell parameter refinement was carried out using CELLREF with a lattice parameter of 10.1934(6) Å. A cell volume of 1059.16 (1) $Å^3$ was obtained.

Synthesised $Mg(NH_3)_6Br_2$ (sample **2**) was a fine, white powder. PXD analysis (Figure 3.1) was carried out on the sample. There is no structure for $Mg(NH_3)_6Br_2$ in the ICSD database so the High Score Plus database was used in the first instance to identify the product from a known powder pattern only. From the match generated, it was concluded that $Mg(NH_3)_6Br_2$ was isostructural to $Fe(NH_3)_6Br_2$ (PDF no: 01-085-2095) which like $Mg(NH_3)_6Cl_2$ is cubic (*Fm*$\bar{3}$*m*).[12] Substituting Fe with Mg in PowderCell allowed the match to be observed (Figure 3.2). An NH_4Br impurity phase was present in the longer PXD scans like the chloride. Initial cell parameter refinement was carried out using CELLREF to obtain a lattice parameter of 10.52(4) Å and a unit cell volume of 1162.6(5) $Å^3$.

Synthesised $Mg(NH_3)_6I_2$ (sample **3**) was a fine, white powder like its chloride and bromide equivalents, compared to the starting material MgI_2 which was light orange-brown in colour. PXD analysis (Figure 3.3) found that the sample is isostructural with $Mn(NH_3)_6I_2$ (PDF no 01-084-1377) which is cubic (*Fm*$\bar{3}$*m*) was carried out on the sample. There is a known pattern for $Mg(NH_3)_6I_2$ but this is an incomplete X-ray pattern.[13] Long PXD scans showed a NH_4I impurity phase as per seen for $Mg(NH_3)_6Cl_2$ and $Mg(NH_3)_6Br_2$. Initial cell parameter refinement was carried out using CELLREF, with a lattice parameter of a= 10.99(6) Å and a unit cell volume of 1328.5 (1) $Å^3$ obtained.

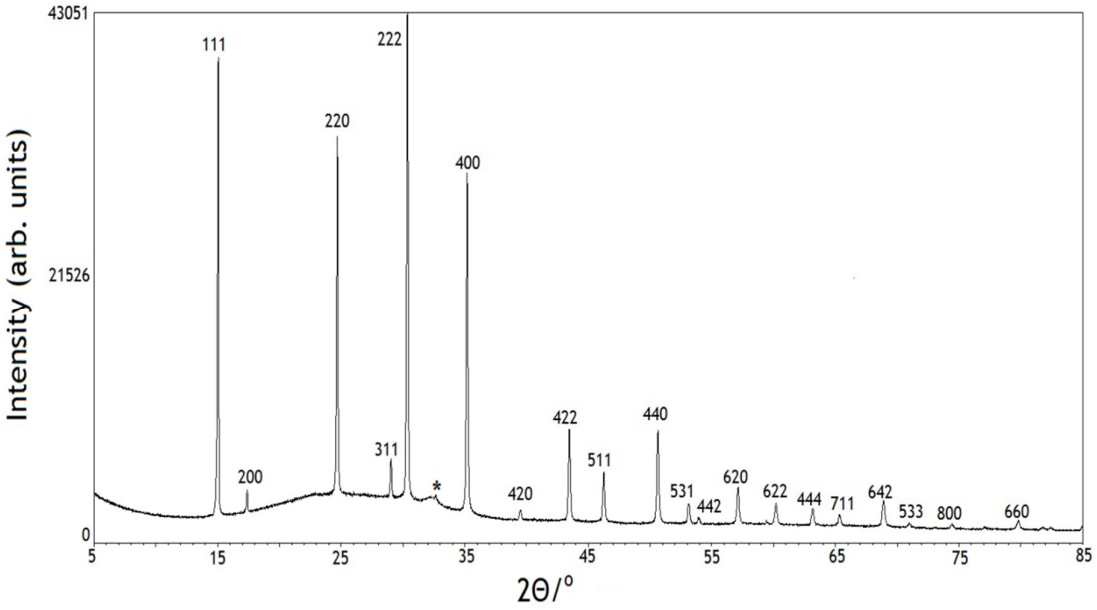

Figure 3.1: PXD pattern of $Mg(NH_3)_6Cl_2$. The NH_4Cl phase is indicted by the asterisk

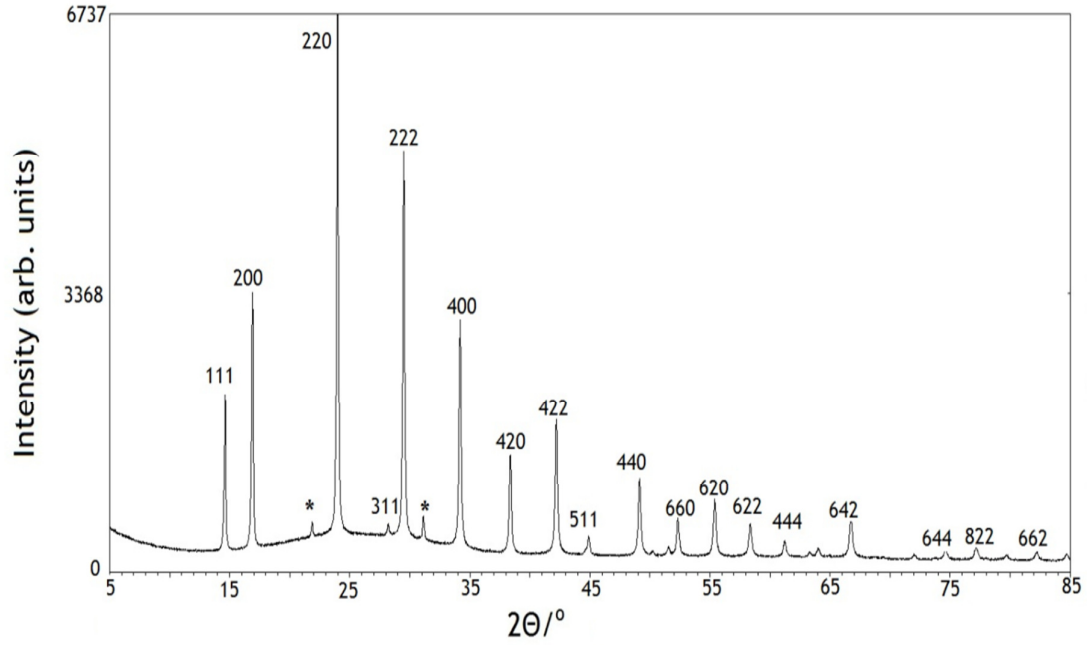

Figure 3.2: PXD pattern of $Mg(NH_3)_6Br_2$ (sample **2**). The NH_4Br phase is indicted by the asterisks

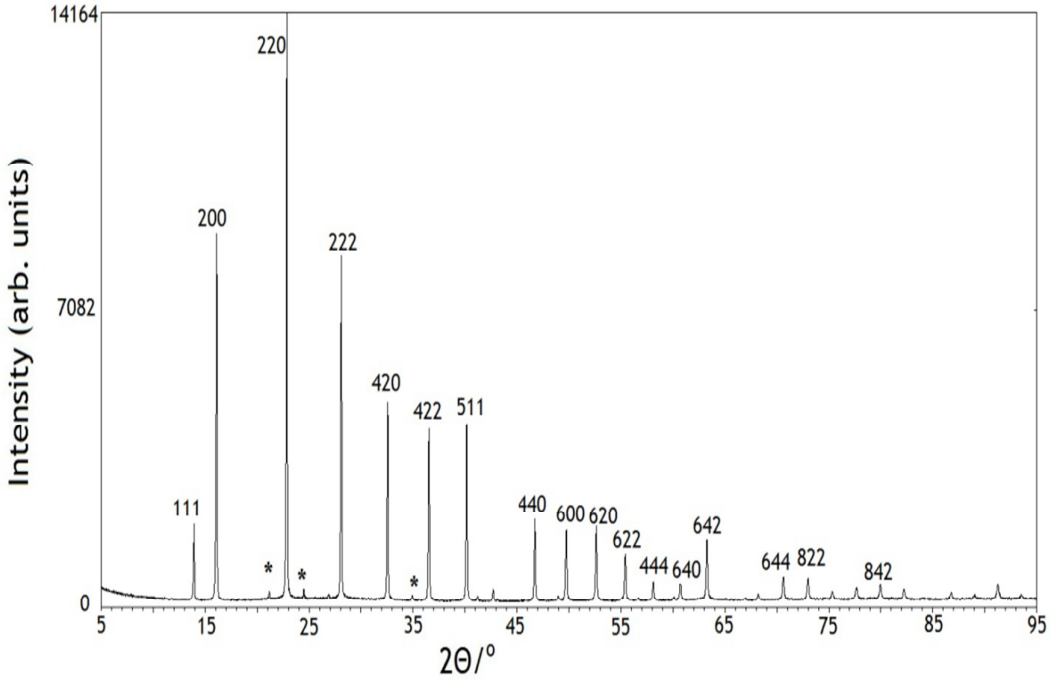

Figure 3.3: PXD pattern of $Mg(NH_3)_6I_2$ (sample **3**). The NH_4I phase is indicted by the asterisks

3.3.1.1 Reitveld Refinement of the Hexaammines

The PXD data of the hexaammines (samples **1-3**) were used in the structural refinement via the Rietveld method as described in section 3.2.4. The crystallographic data from the Refinements are presented in Table 3.3

Table 3.3: Crystallographic data for samples **1-3** from PXD data. Phase fraction 1 refers to the $Mg(NH_3)_6X_2$ phase and phase fraction 2 refers to the NH_4X phase

Sample	1	2	3
Phase Fraction (1)	93.8(3)	98.1(5)	99.0(3)
Phase Fraction (2)	6.2(2)	1.9(7)	1.0(6)
Crystal System	Cubic	Cubic	Cubic
Space Group	$Fm\bar{3}m$	$Fm\bar{3}m$	$Fm\bar{3}m$
a/Å	10.1858(1)	10.4744(1)	10.9906(1)
Volume/Å^3	1056.78(1)	1149.18(2)	1327.6(3)
Z	4	4	4
Formula Weight/g	789.588	1145.196	1521.96
Density, ρ_x/gcm^{-3}	1.241	1.6445	1.903
No of observations	4730	4730	5319
No of variables	33	30	42
R_{wp}	0.0407	0.0830	0.0713
R_p	0.0248	0.0405	0.0547
χ^2	4.083	4.302	3.153

From Table 3.3 it can be seen that the three hexaammines all crystallise in the cubic $Fm\bar{3}m$ group and are isostructural to each other. The unit cell of $Mg(NH_3)_6Cl_2$ obtained is comparable to that in the literature, where a value of 10.1899(4) Å is reported.[3] When Cl is replaced with Br the unit cell expands, which would be expected due to the increased ionic radii of the halide. The ICSD file used for the refinement against the PXD data was that of $Fe(NH_3)_6Br_2$ with a unit cell of 10.442(2) Å.[12] The unit cell of $Mg(NH_3)_6I_2$ is the largest of the three hexaammines and is comparable to the unit cell of $Mn(NH_3)_6I_2$ (10.984(5) Å).[13]

The Observed, Calculated and Difference (OCD) Plot for $Mg(NH_3)_6Cl_2$ (sample **1**) with atomic parameters in Table 3.2. The OCD plot for $Mg(NH_3)_6Br_2$ (sample **2**) and $Mg(NH_3)_6I_2$ (sample **3**) are presented in Figures 3.4 and 3.5. The atomic parameters of sample**1**- **3** are presented in Tables 3.4-3.6 with the bond angles and distances presented in Table 3.7.

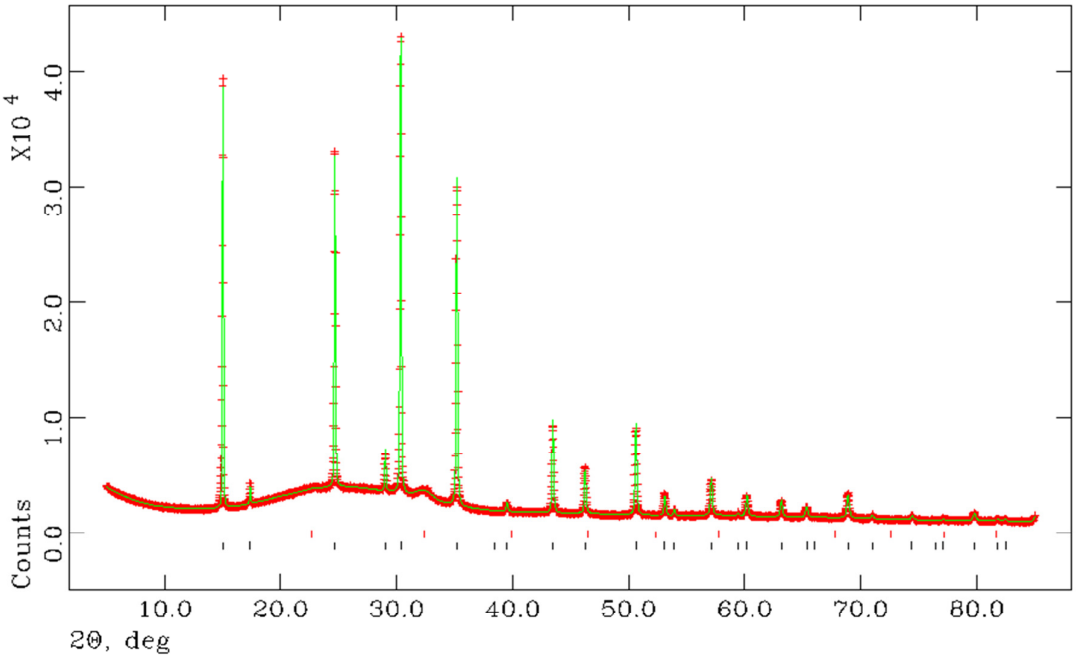

Figure 3.4: Observed, Calculated and Difference (OCD) plot for the structural refinement of sample **1**. The black tick marks indicate reflections the $Mg(NH_3)_6Cl_2$ phase and the red tick marks indicate reflections from the NH_4Cl phase.

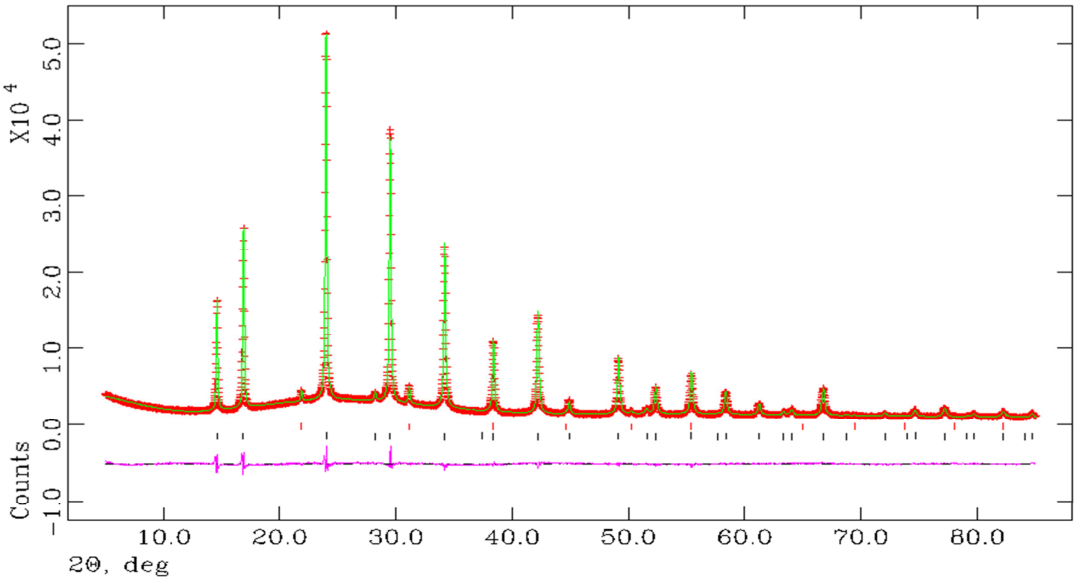

Figure 3.5: Observed, Calculated and difference (OCD) plot for the structural refinement of sample **2.** The black tick marks are reflections from the hexaammine phase and the red tick marks are reflections from NH_4Br.

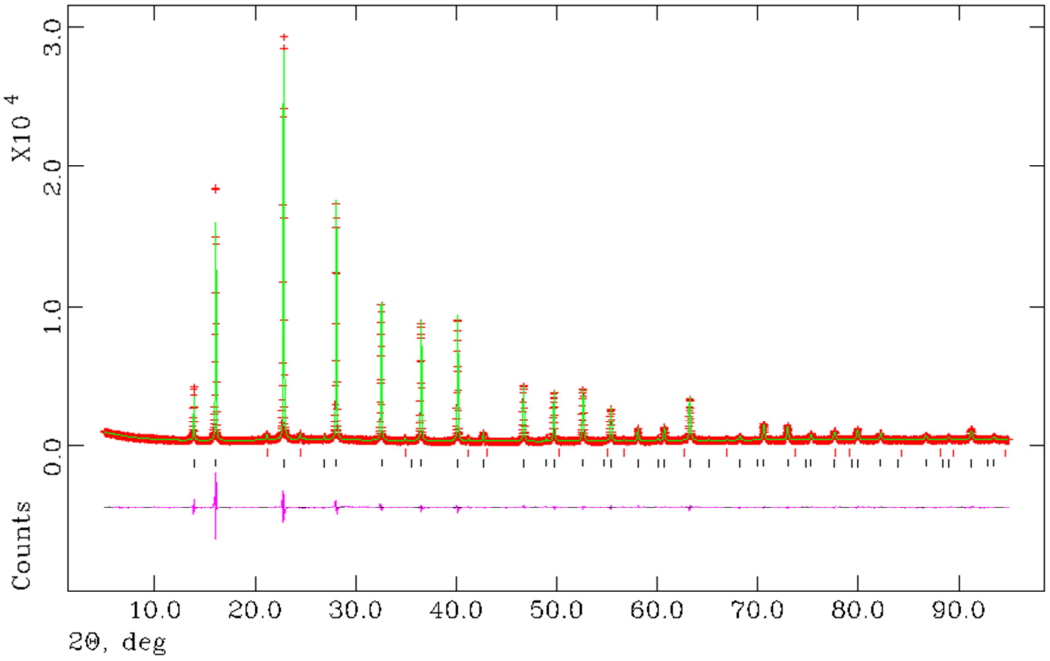

Figure 3.6: Observed, Calculated and difference (OCD) plot for the structural refinement of sample **3**. The black tick marks indicate reflections from $Mg(NH_3)_6I_2$ and the red tick marks indicate reflections from NH_4I.

Table 3.4: Atomic parameters of $Mg(NH_3)_6Cl_2$ (sample **1**)

Atom /Site	x	y	z	Occupancy	U_{iso} x 100/Å^2
Mg /4a	0	0	0	1	4.54(10)
Cl/8c	0.25	0.25	0.25	1	5.93(7)
N/24e	0	0	0.21633(2)	1	6.48(12)
H/ 96k	0.0636(8)	0.0636(8)	0.2552(8)	0.75	6.48

Table 3.5: Atomic parameters of $Mg(NH_3)_6Br_2$ (sample **2**)

Atom /Site	x	y	z	Occupancy	U_{iso} x 100/Å^2
Mg /4a	0	0	0	1	4.47(11)
Br /8c	0.25	0.25	0.25	1	6.21(4)
N/24e	0.20977(34)	0	0	1	6.76(2)
H/96k	0.0570(8)	0.0570(8)	0.2503(12)	0.75	6.76

Table 3.6: Atomic parameters of $Mg(NH_3)_6I_2$ (sample **3**)

Atom /Site	x	y	z	Occupancy	U_{iso} x 100/Å^2
Mg /4a	0	0	0	1	3.19(2)
I /8c	0.25	0.25	0.25	1	4.52(4)
N/24e	0.01991(6)	0	0	1	4.70(3)
H/96j	0	0.2434(22)	0.0733(22)	0.75	4.70

Table 3.7: Bond angles and distances

Atoms	Distance/Å	Angles/ °
Sample **1**		
Mg-N	6x 2.203(3)	
N-H1	5x 0.998(11)	4x 81.0(5), 2x 133.3(13)
H1-H1	2x 1.295(15), 1x 1.83(2)	
Sample **2**:		
Mg-N	6x 2.197(4)	
N-H1	5x 0.945(14)	
H-N-H		4x 78.3(7), 2x 116.7(9)
H1-H1	3x 1.223(16), 1.69(3)	
Sample **3**:		
Mg-N	6x 2.187(6)	
N-H1	4x 0.94(2)	
H-N-H		4x 74.6(16), 118(3)
H1-H1	2x 1.14(3), 1x 1.61(5)	2x 52.8(8)

There are differences within the models with the location of the hydrogen. In $Mg(NH_3)_6Cl_2$ and $Mg(NH_3)_6Br_2$ the hydrogen is located at the 96k Wyckoff site while for $Mg(NH_3)_6I_2$ the hydrogen is located at the 96j Wyckoff sites. In all three cases, the hydrogen has an occupancy of 0.75 which results from the

dynamic disorder of the NH_3 ligands in the octahedral cations. For an accurate position of the hydrogens, powder neutron diffraction (PND) has been carried out and the results presented in Chapter 4.

The Mg-N bond distances in samples **1-3** are comparable to each other and are in good agreement with previous published M-X bonds in the literature, for example for Mg-Cl a bond length of 2.197(15) Å has been reported.[14] No bond angle data for $Mg(NH_3)_6Br_2$ and $Mg(NH_3)_6I_2$ has been published so no direct comparison is available for these two compounds. The N-H bond lengths and bond angles are also acceptable for the ammines. N-H bond length values of 1.020 Å have been reported for calcium amidoborane ammoniates.[15]

3.3.2 Raman of the Hexaammines

Raman spectroscopy has previously been used to study metal ammines including $Mn(NH_3)_6Cl_2$ and $Mn(NH_3)_6Br_2$.[16] In the metal ammines, Raman measures the internal modes of $M(NH_3)_6X_2$ (where M= metal, X= halide) and also the lattice modes connected with the transitional vibrations of the anions in respect of the cations and the torsions of the anions and cations.[17] The stretches from the N-H bonds in the NH_3 species as can the M-N stretches, which confirms with the model from PXD and PND which demonstrates that the metal is bonded to the nitrogen of the ammonia ligands and not to the halide.

$Mg(NH_3)_6Cl_2$ was previously been studied by Raman spectroscopy by Plus.[18] All internal and external vibrations predicted by group theory were seen and there was some splitting of degenerative vibrations leading to the conclusion that the ligands were not in fact, freely rotating.

The three synthesised hexammines (samples **1-3**) have been studied by Raman. The Raman spectrum for these ammines can be seen in Figures 3.7-3.9 with assignments in Table 3.8

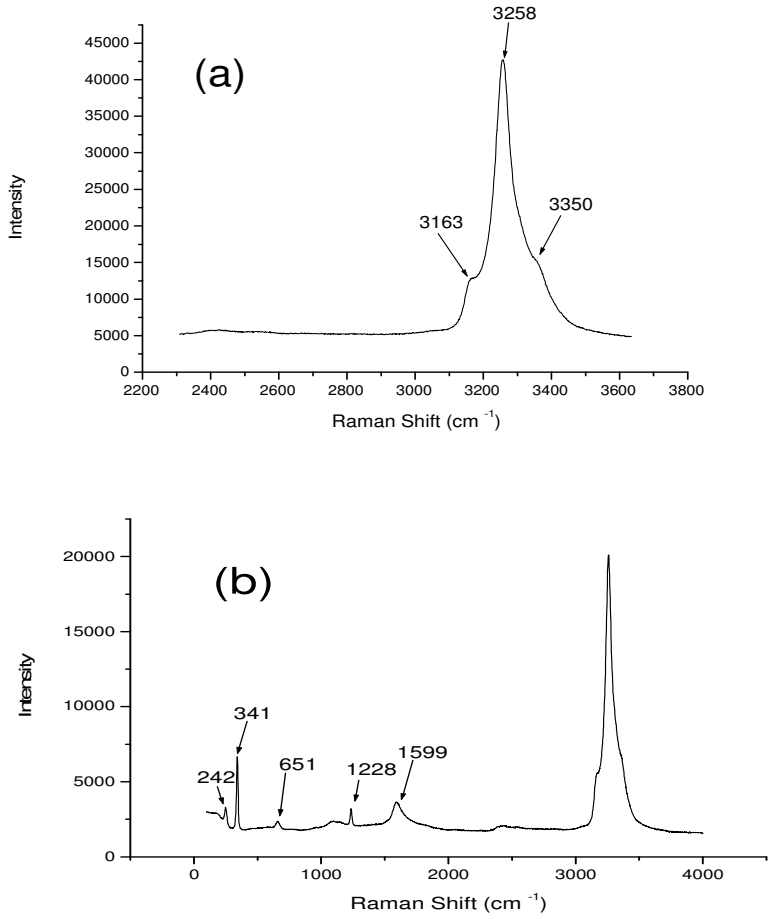

Figure 3.7: Raman spectrum of $Mg(NH_3)_6Cl_2$ (a) is between 2200 cm^{-1} – 3800 cm^{-1} illustrating N-H stretches (b) is a broad range spectrum illustrating all the stretches

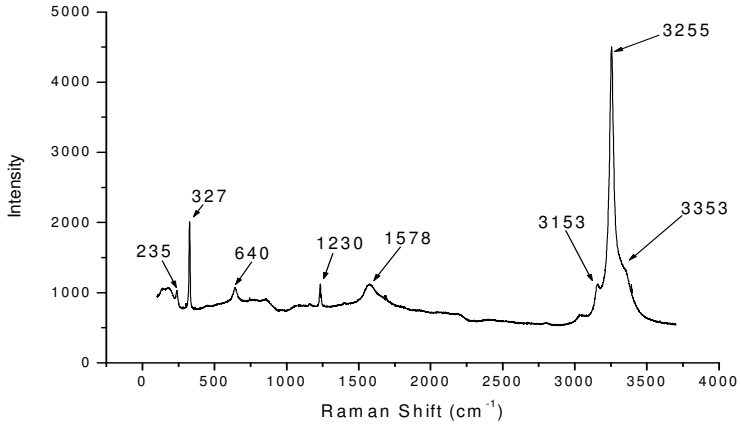

Figure 3.8: Raman spectrum of $Mg(NH_3)_6Br_2$

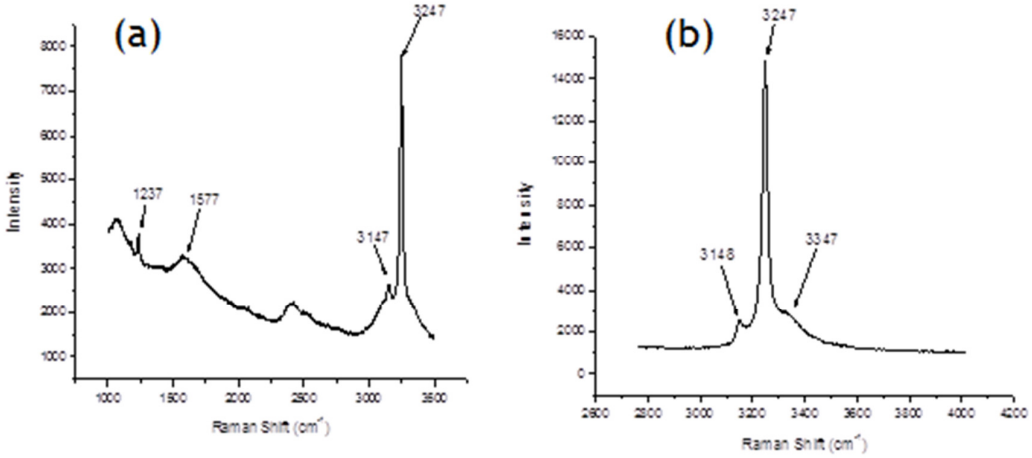

Figure 3.9: Raman spectrum of $Mg(NH_3)_6I_2$ (a) is between 2600 cm^{-1} – 4200 cm^{-1} illustrating N-H stretches (b) is a broad range spectrum illustrating all the stretches

Table 3.8: Raman assignments of $Mg(NH_3)_6X_2$ (X= Cl, Br, I)

	Raman Shift (cm^{-1})						
Sample	**ν_{as}(NH)**	**ν_s(NH)**	**δ_{as}(NH)**	**δ_s(NH)**	**δ_x(NH)**	**ν(MN)**	**ν(NMN)**
1	3350 3258	3163	1599	1228	651	341	242
2	3353 3255	3153	1578	1230	640	327	235
3	3347 3247	3148	1577	1237 1084	619	314	

As can be seen in Table 3.8, the ammines (sample **1-3**) consists of a number of internal modes consistent with previous Raman studies.[18] The stretching vibrations of the N-H, M-N and N-M-N bonds are present for all three samples. The presence of the M-N and N-M-N bonds agree with the PXD/PND data where the magnesium is bonded to the nitrogen from the ammonia and not bound to the halide in the hexaammines. The presence of the asymmetric and symmetric stretches of N-H conclude that NH_3 is present in all three samples and these have been seen in other Raman studies of the ammines and the stretches have been assigned from these. [18,19,]

The rotation degenerative band (δ) of the N-H deformation along the M-X axis is seen at 1599 cm $^{-1}$ for $Mg(NH_3)_6Cl_2$, 1578 cm $^{-1}$ for $Mg(NH_3)_6Br_2$ and 1577 cm $^{-1}$ for $Mg(NH_3)_6I_2$, which is in agreement with $Mn(NH_3)_6I_2$ where this stretch is at 1583 cm $^{-1}$.[20] Pius observed the splitting of the degenerative bands for $Mg(NH_3)_6Cl_2$ but this has not been observed for any of the hexaammines. [18]

The presence of another N-H degenerative band between 1228 -1237 cm^{-1} for the samples also indicates there is likely to be more disorder in the structure particularly in regard to the NH_3. In both the $Mg(NH_3)_6Br_2$ and $Mg(NH_3)_6I_2$ further NH_3 degenerative bands are also seen with the assignments of these in Table 3.8.

3.3.3 Air Sensitivity Studies of the ammines- $Mg(NH_3)_6I_2$

It has been previously reported that the ammine $Al(BH_4)_3.6NH_3$ was relatively inert to air after 10 days of exposure [21] although the exposure of $Ca(NH_3)_8Cl_2$ to air for one week ammine resulted in the formation of NH_4X and an amorphous phase attributed to CaClOH. [22] In order to determine the air sensitivity of the halide ammines, synthesised $Mg(NH_3)_6I_2$ (sample **3**) was exposed to air while on the Powder X-ray Diffractometer (PXD) for a period of 3 hours. PXD scans were sequentially taken each 5 minutes in length between 15^o – 34^o. This area of the PXD pattern was chosen as three of the strongest Bragg reflections (111, 200, 222) are located in this region. The results of the PXD experiment versus time are presented in Figure 3.10.

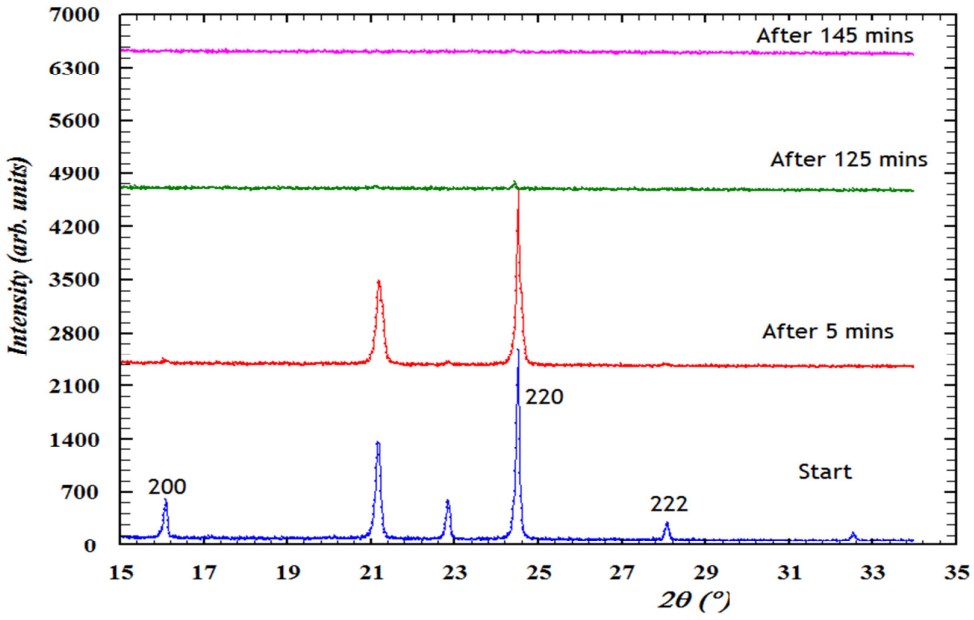

Figure 3.10: Powder X-ray diffraction patterns for $Mg(NH_3)_6I_2$ over a three hour period.

From Figure 3.10 for the start scan it phases from NH_4I are already present at 21° and 23°. After the first scan (after five mins of exposure to air), the intensity of the 200, 220 and 222 bragg reflections for $Mg(NH_3)_6I_2$ have decreased in intensity significantly. The strongest intensity reflections present are those from NH_4I. NH_4I has previously been observed in the PXD of $Mg(NH_3)_6I_2$ (Figure 3.3) when the sample may have been exposed to air during the capillary sealing. The 5 min scan does not agree with the previous air sensitive studies where the ammines have not been affected by air exposure after such a short period. This result shows that the halide ammines are particularly sensitive to air and so their potential as indirect H_2 storage materials would be comprised if the ammine is not stored in an inert atmosphere. An amorphous background may be present after 5 mins (which could be due to the hydroxide amorphous phase (MgIOH) although a significant background could not be seen at this time point.

After 10 minutes of exposure to air, the 200, 220 and 222 reflections from $Mg(NH_3)_6I_2$ are lost, with NH_4I by far dominant phase. From this it can be concluded that the ammine is no longer able to be used as an indirect hydrogen storage material after such a short period of air exposure (in this case a period of ten mins). An amorphous phase is not yet seen in the PXD pattern.

After 15 minutes to 145 mins of air exposure, the reflections attributed to NH_4I gradually decrease in intensity with an increase an amorphous background, which could be from the amorphous MgIOH phase or another unidentified crystalline phase (s). By 145 mins of air exposure, the sample now longer possess any NH_4I reflections and is now amorphous in nature.

As can be seen from this air sensitivity study, the magnesium halide ammines synthesised are very air sensitive and must be handled in inert conditions at all times.

3.4 Deammoniation of the Ammines: TPD studies

3.4.1 Deammoniation of $Mg(NH_3)_6Cl_2$

TPD (TG-DTA-MS) analysis was carried out on $Mg(NH_3)_6Cl_2$ (sample **1**) to investigate its decomposition properties and the products of decomposition. The data are presented in Figures 3.11 and 3.12.

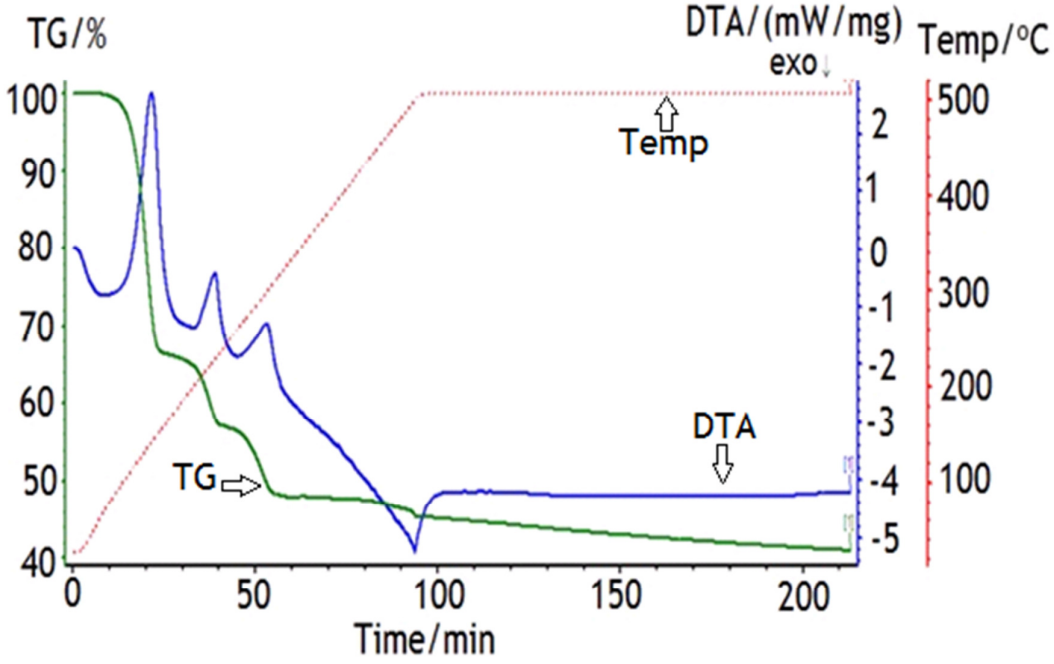

Figure 3.11: TGA-DTA Profile of $Mg(NH_3)_6Cl_2$ (sample **4**)

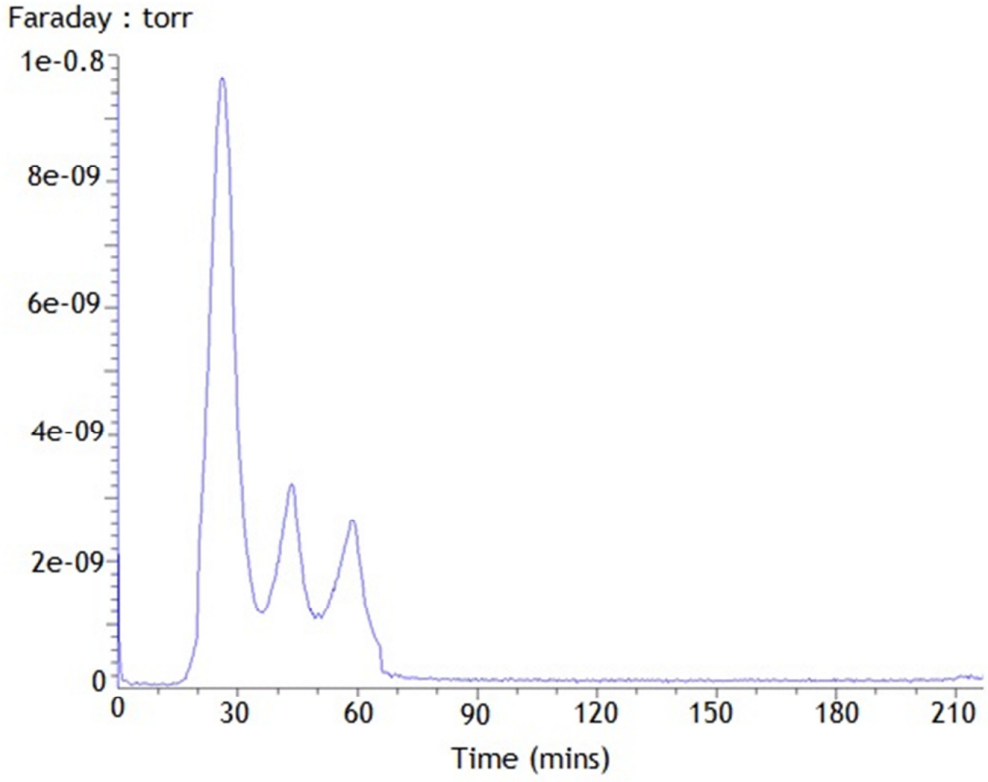

Figure 3.12: MS profile of the decomposition of $Mg(NH_3)_6Cl_2$ showing the release of NH_3 (blue)

For the TPD measurements, sample 1 has been heated. Using different batches of the synthesised $Mg(NH_3)_6Cl_2$ results in the deammoniation temperatures varying by 5-10 ^oC. The samples between the batches are similar in homogeneous nature. From Figure 3.11 there are three endothermic events occurring to three associated weight loss steps. These can be correlated to a three step decomposition process as has been seen in the literature.[8] A summary of the processes seen are summarised in Table 3.9

Table 3.9: Deammoniation temperatures and weight loss of sample **4**

Step	Observed weight loss/%	Theoretical weight loss/%	Onset temperature (° C)	End temperature (° C)
1	32.7	34.5	65	148
2	8.80	8.6	158	230
3	8.72	8.6	234	303

Step 1 of the deammoniation process, which is the onset of reaction occurs at 65 °C. This first weight loss step is complete at 138 °C, with a midpoint temperature of 120 °C. The weight loss of this step is 32.66% which corresponds to a theoretical weight loss of 34.5 % for the loss of 4 equivalent NH_3. The loss of NH_3 can be seen in Figure 3.12 with the first weight loss step evolving the greatest amount of NH_3(g). The first step of the reaction can thus be rationalised by the decomposition of the hexaammine to the diammine:

$$Mg(NH_3)_6Cl_2 \rightarrow Mg(NH_3)_2Cl_2 + 4\ NH_3 \qquad (3.4)$$

Step 2 in Table 3.9 is associated with the second endothermic event in the DTA. This step has a midpoint temperature of 210 °C with an endpoint temperature of 230 °C. The weight loss of this step is 8.8%, with the theoretical weight loss for the loss of 1 equivalent NH_3 being 8.6%. The mass spectrum (Figure 3.12) shows release of NH_3 but to a smaller extent than the first step. This step can thus be associated with the decomposition of the diammine to the monoammine:

$$Mg(NH_3)_6Cl_2 \rightarrow Mg(NH_3)Cl_2 + NH_3 \qquad (3.5)$$

Step 3 has a midpoint of 280 °C and an endpoint of 303 °C. The weight loss for this step is 8.72% compared to the theoretical weight loss of 1 NH_3 being 8.5%. MS (Figure 3.12) shows a small release of NH_3. This step is the final deammoniation step to $MgCl_2$:

$$Mg(NH_3)Cl_2 \rightarrow MgCl_2 + NH_3 \qquad (3.6)$$

The total weight loss of those three weight loss is 50.18 wt. % which is close to the theoretical weight loss for 6 equivalents of NH_3 of $Mg(NH_3)_6Cl_2$ of 51.7 wt.%.

There is a further weight loss to 500 ^{o}C and the sample continues to lose weight during the dwell period.

Ex-situ PXD analysis of the product at 500 ^{o}C was used to determine the post TPD product. The product was a mixture of $MgCl_2$ and MgO (Figure 3.13). The presence of MgO could be explained by some reaction of the chloride with the alumina TG-DTA pan (which may explain the continued weight loss of the TG during the dwell period) for heating as $MgCl_2$ was the final product when using vanadium can in PND analysis as discussed in Chapter 4.

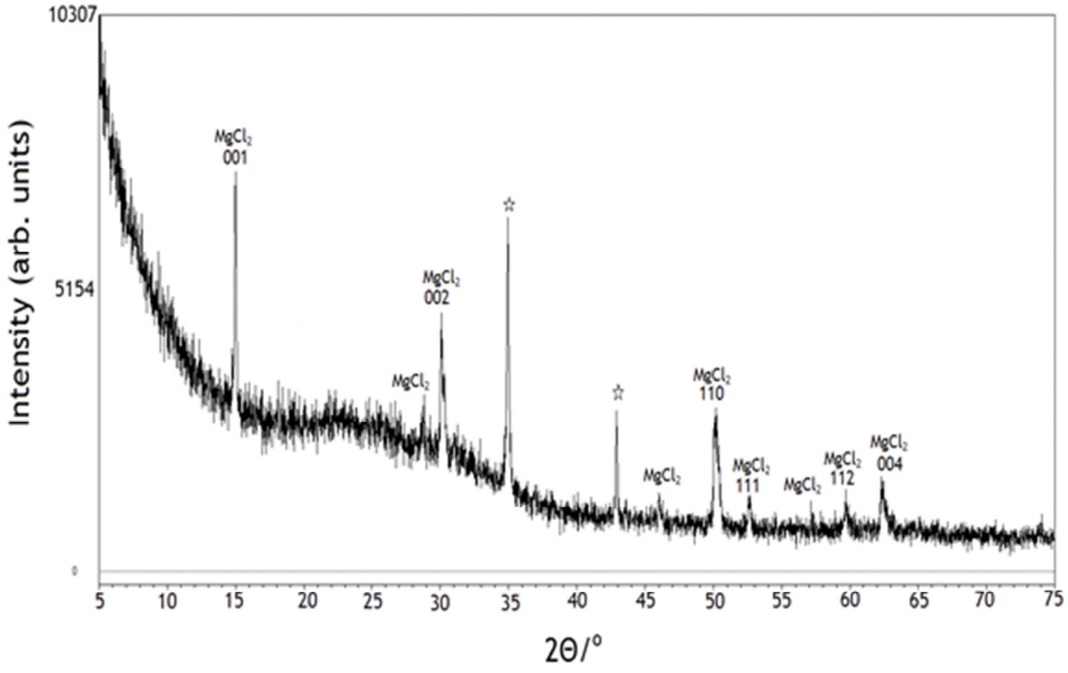

Figure 3.13: PXD of the post TPD product for the complete deammoniation of $Mg(NH_3)_6Cl_2$ (peaks labelled with the stars are MgO)

3.4.2 Deammoniation of $Mg(NH_3)_6Br_2$

The deammoniation properties of $Mg(NH_3)_6Br_2$ were investigated by TPD analysis as seen in Figure 3.14 (TGA-DTA) and Figure 3.15 (MS analysis).

The TPD profile for this ammine is similar to the profile for $Mg(NH_3)_6Cl_2$ (section 3.4.1). In the TG-DTA profile there are three main weight loss and endothermic events respectively which are summarised in Table 3.10.

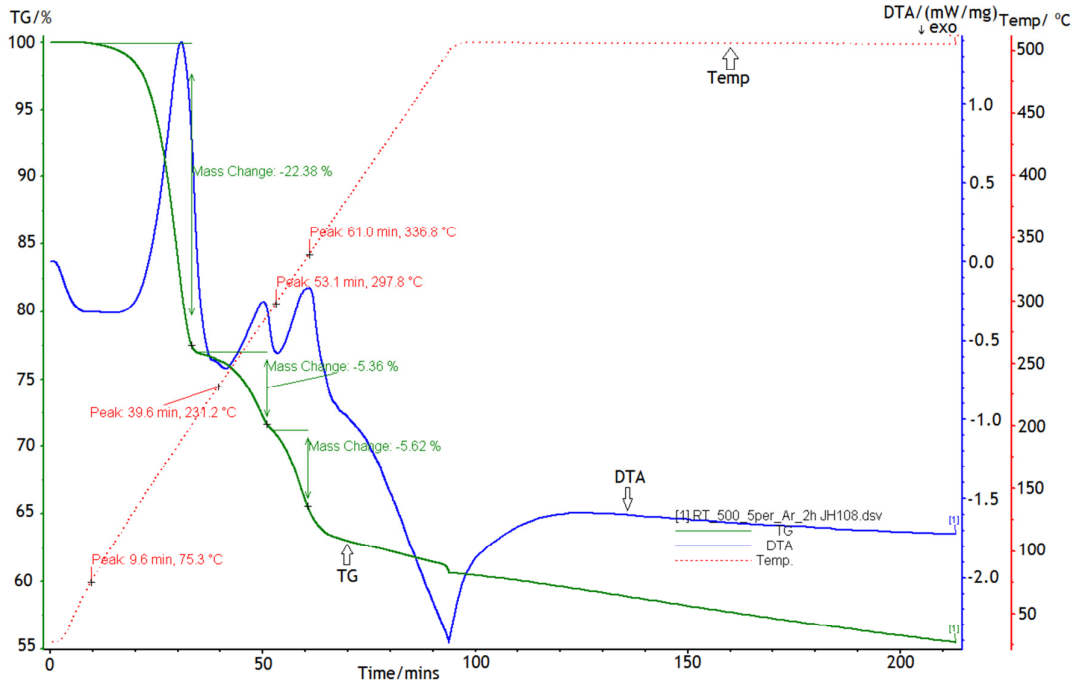

Figure 3.14: TGA-DTA of $Mg(NH_3)_6Br_2$ (sample **5**).

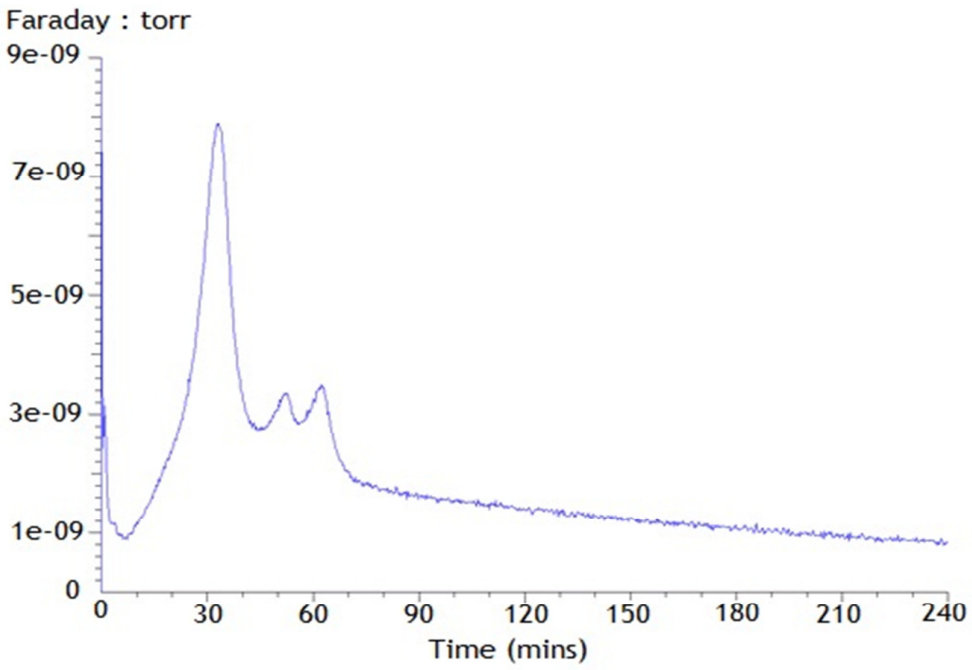

Figure 3.15: MS profile for the decomposition of $Mg(NH_3)_6Br_2$ (sample **5**) showing the release of NH_3 (blue)

Table 3.10: Deammoniation temperatures and weight loss of sample **5**

Step	Observed weight loss/%	Onset temperature (° C)	End temperature (° C)
1	22.38	75	200
2	5.36	224	298
3	5.62	298	337

Step 1 in the deammoniation commences at 75 °C, has a midpoint temperature of 135 °C and finishes at 200 °C and consists of a large endothermic event. The accompanying weight loss for the step is 22.38 %, while the theoretical weight change for the loss 4 NH_3 is 23.8%. This correlates with the mass spec (Figure 3.14) in which a large evolution of NH_3 is observed. This step in the process can thus be identified as the decomposition of the hexaammine to its corresponding diammine:

$$Mg(NH_3)_6Br_2 \rightarrow Mg(NH_3)_2Br_2 + 4\ NH_3 \qquad (3.7)$$

Step 2 in the deammoniation process corresponds to the decomposition of the diammine to the corresponding monoammine:

$$Mg(NH_3)_2Br_2 \rightarrow Mg(NH_3)Br_2 + NH_3 \qquad (3.8)$$

This step has a midpoint temperature of 265 °C and an endpoint of 298 °C. The weight loss of this step is 5.36% while the theoretical weight change for loss of 1 NH_3 from the diammine is 5.95%. Mass spec (Figure 3.15) shows release of NH_3 which can be linked to the endothermic event in the DTA.

The final step (step 3) in the TPD profile is the release of the final NH_3 to $MgBr_2$:

$$Mg(NH_3)Br_2 \rightarrow MgBr_2 + NH_3 \qquad (3.9)$$

This weight loss step has a midpoint temperature of 320 °C and finishes at 337 °C. From the TGA curve, the weight loss of this step is 5.62% while the theoretical weight change for loss of 1 NH_3 from the monoammine is 5.95%. The release of NH_3 is seen on the MS profile for this step. The total weight loss in the

three steps of deammoniation is 33.36 wt. % compared to the theoretical weight change for the release of 6 NH_3 of 35.7 wt. %. As per the equivalent chloride, there is further weight loss after deammoniation is complete, although PXD of the final product, as for the chloride hexaammine sample showed the presence of MgO in addition to the halide ($MgBr_2$).

3.4.3 Deammoniation of $Mg(NH_3)_6I_2$

The TGA-DTA profile and MS profile for the decomposition of $Mg(NH_3)_6I_2$ (sample **6**) can be seen in Figures 3.16 and 3.17. The three step process which is observed are summarised in Table 3.11.

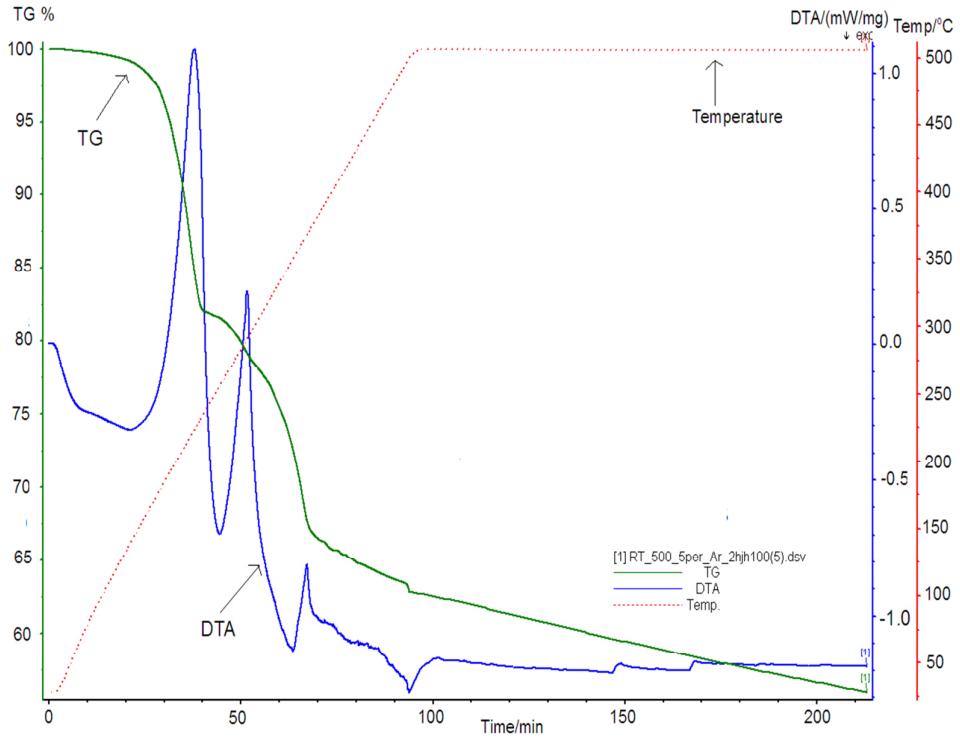

Figure 3.16: TGA-DTA curve of $Mg(NH_3)_6I_2$ (sample **6**)

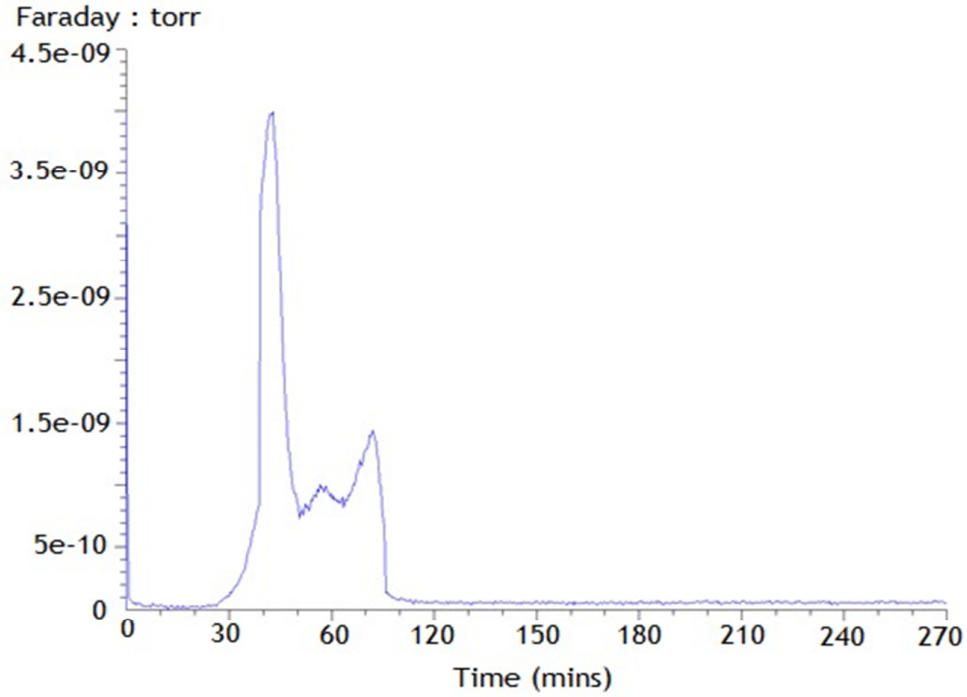

Figure 3.17: MS profile of the decomposition of $Mg(NH_3)_6I_2$ showing the release of NH_3

Table 3.11: Deammoniation temperatures and weight loss of sample **6**

Step	Observed weight loss/%	Onset temperature (° C)	End temperature (° C)
1	18.0	81	231
2	4.41	234	313
3	5.62	314	366

From the TPD profiles, this ammine appears to deammoniate in three steps, like $Mg(NH_3)_6Cl_2$ and $Mg(NH_3)_6Br_2$. In the TGA curve there are two clear weight loss steps and possibly the second weight loss could be integrated as two separate weight losses. The DTA curve shows three endothermic events and the MS profile (Figure 3.17) confirms three separate ammonia release processes.

Step 1 involves the decomposition of $Mg(NH_3)_6I_2$ to $Mg(NH_3)_2I_2$ with the release of NH_3. This step commences at 81 °C and finishes at 231 °C with a midpoint of 200 °C. The weight loss for this step is 18.0 % which is close to the theoretical

weight loss value of 17.3% for the loss of 4 equivalent NH_3. The MS profile shows that this stage releases the most NH_3 in agreement with the weight loss data

Step 2 involves the decomposition of $Mg(NH_3)_2I_2$ to $Mg(NH_3)I_2$. This step commences at 234 ^oC (immediately after deammoniation to the diammine) and finishes at 313 ^oC with a midpoint of 285 ^oC. The weight loss for this step is 4.41 wt.% which matches the theoretical weight change of 4.33 wt. % for the loss of 1 equivalent NH_3 to the corresponding monoammine.

The third step is the final deammoniation step to MgI_2 (step 3).The weight loss for this step is 5.62 wt.% which is above that of the theoretical weight loss value of 4.33 wt.%. After this point, the sample continues to lose weight. PXD of the post TPD product confirmed that the product was MgI_2 while the background would also suggest an amorphous component to the product. (Figure 3.18). The melting point of MgI_2 is 637 ^oC so this amorphous component is not expected.

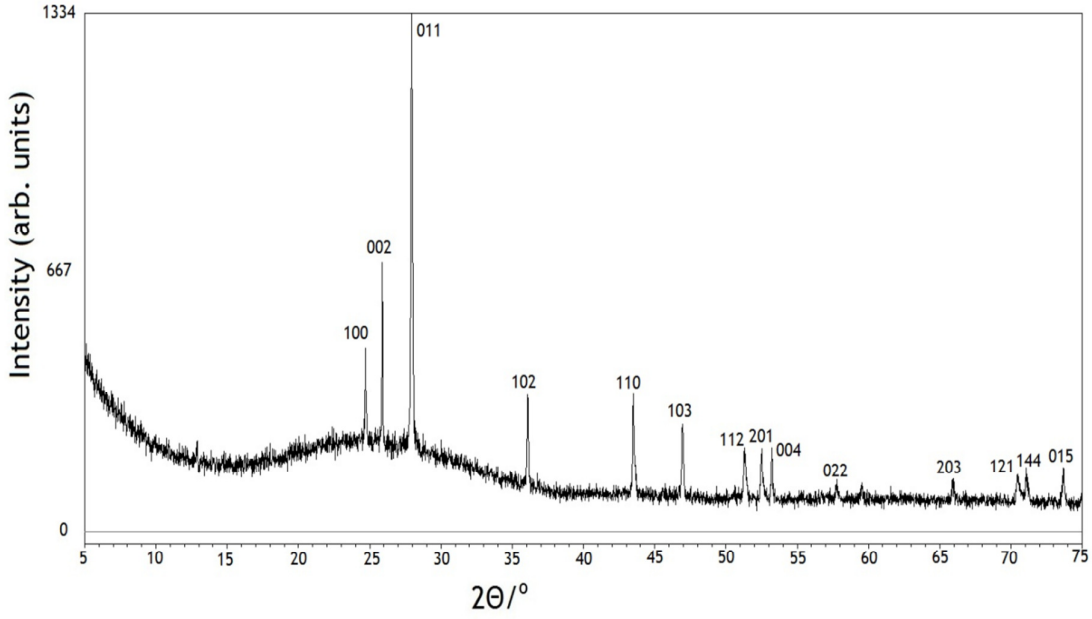

Figure 3.18: PXD of the post TPD product - MgI_2

3.5 Intermediates Of The Deammoniation Process of the ammines

In order to confirm the mechanisms of the deammoniation processes (section 3.4) and the structural changes of the ammines, the 'intermediate' ammines ($Mg(NH_3)_2X_2$ and $Mg(NH_3)X_2$) were isolated using TPD and analysed using PXD and Raman.

3.5.1 PXD and Raman Studies of $Mg(NH_3)_nCl_2$ (n= 2,1)

3.5.1.1 Isolation and Structural Studies of $Mg(NH_3)_2Cl_2$

Initial attempts to isolate $Mg(NH_3)_2Cl_2$ by TPD of $Mg(NH_3)_6Cl_2$ at 160 ^oC proved unsuccessful as the weight loss values were below that of the theoretical weight loss value (34.5%). Heating the sample to 170 ^oC with a hold of 30 minutes proved successful in isolating the diammine and also possess an onset temperature of the reaction was 73 ^oC which is comparable to the heating of $Mg(NH_3)_6Cl_2$ to 500 ^oC. Heating to 500 ^oC resulted in an onset temperature of 65 ^oC (section 3.4.1) for sample **1**. A weight loss of 32.78 wt. % was obtained (Figure 3.19) although the theoretical weight loss of 34.5 wt. % was not successfully achieved The mass spec pofile (Figure 3.20) showed the one step evolution of NH_3 corresponding to the loss of 4 NH_3 from the hexaammmine. PXD confirmed $Mg(NH_3)_2Cl_2$ (PDF no: 01-073-4070) had been formed (Figure 3.21).The sample is contiually losing weight during the dwell period although the DTA curve (consists of one endothermic event) has levelled which could suggest that the next step of deammoniation is close to commencing.

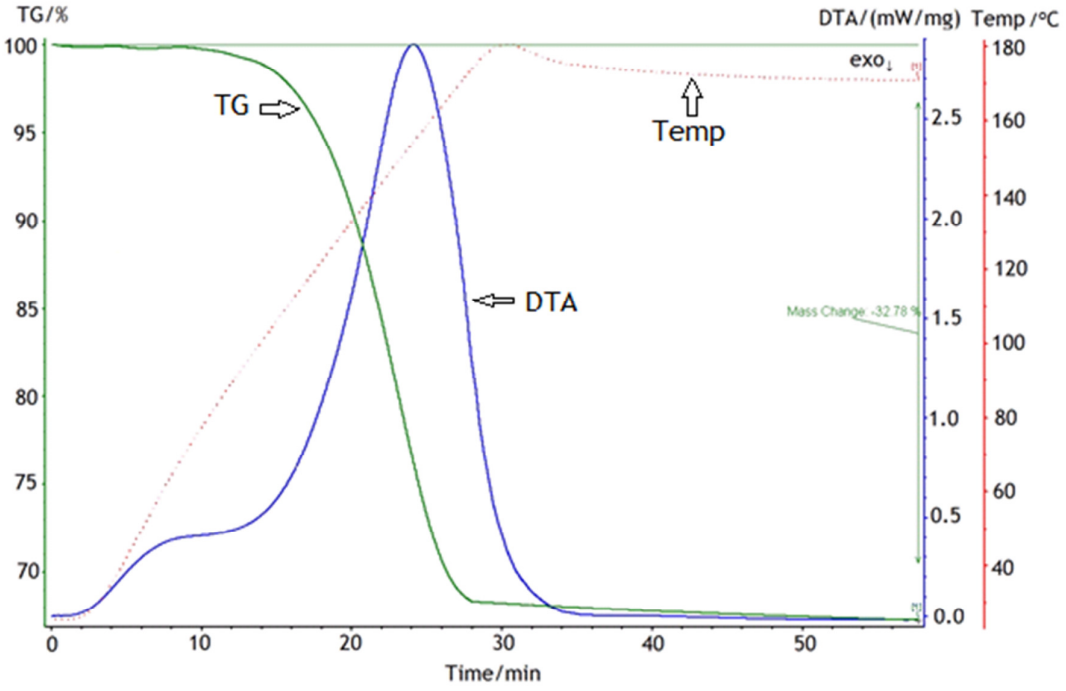

Figure 3.19: TGA-DTA profile for the formation of $Mg(NH_3)_2Cl_2$ (sample **7**)

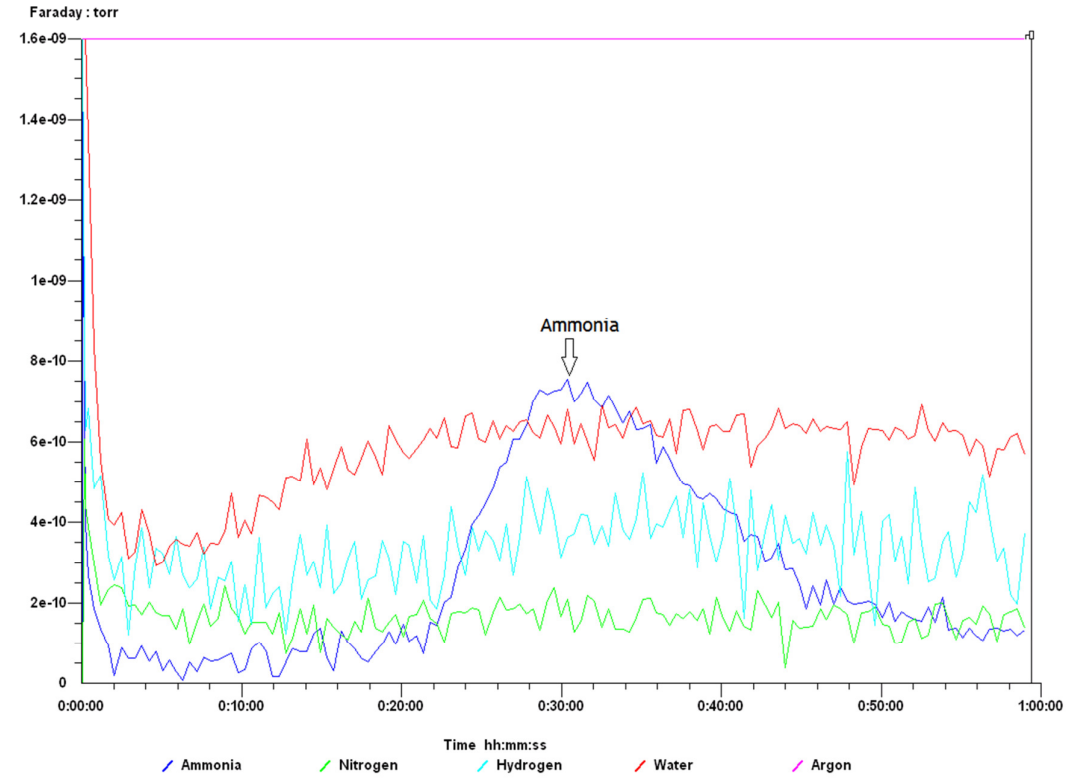

Figure 3.20: MS profile for the formation of $Mg(NH_3)_2Cl_2$ (sample **7**)

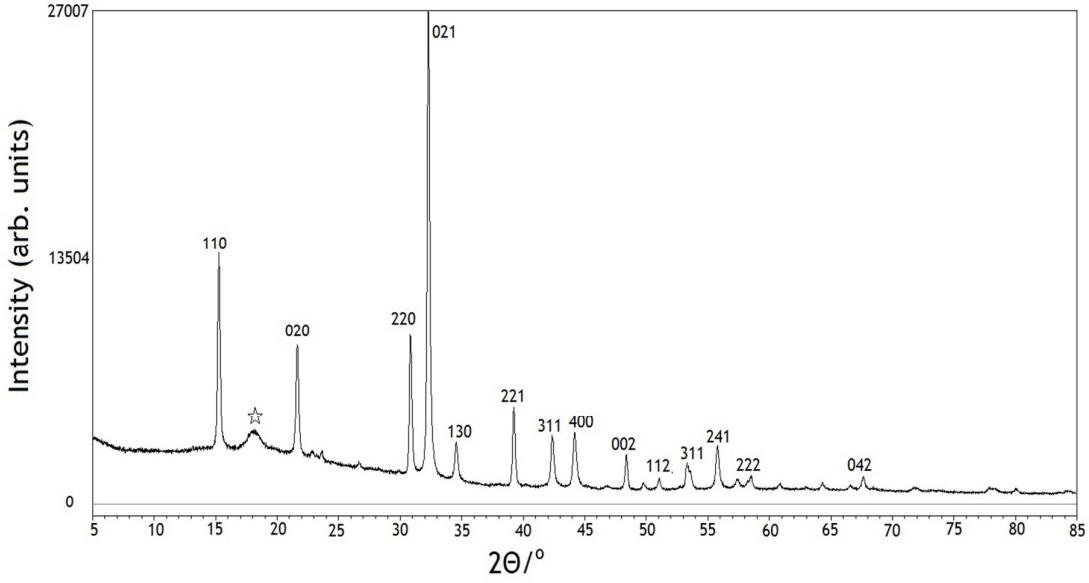

Figure 3.21: PXD pattern of $Mg(NH_3)_2Cl_2$ (sample **7**) after TPD analysis corresponding to $Mg(NH_3)_2Cl_2$ (* is a reflection from the air sensitive bracket)

The structure of $Mg(NH_3)_2Cl_2$ is orthorhombic (*Cmmm)* with lattice parameters of *a*= 8.180(2) Å, *b*= 8.2067(2) Å, *c*= 3.7550(1) Å as determined by single X-ray crystallography.[4] There is a rearrangement of the atoms when compared to the cubic hexaammine as the magnesium is now also bonded to the chloride in addition to the nitrogens from the ammonia ligands. The structure of the diammine which is belongs to the $Cd(NH_3)_2Cl_2$ group can be thought of as edge-sharing octahedra of $[MgCl_{4/2}(NH_3)_2]$ chains with the chloride acting as a linker atom between the chains along the c axis. In the 001 axis the CsCl units are in a "brick" like arrangement.[4] The position of the hydrogen is also now located at the 16r Wyckoff site but possess an occupancy of 0.75 indicating as per the hexaammine that there is disorder of NH_3.

To determine the lattice parameters and the differences in the bond angles and distances in the diammine, refinement against the PXD data for the obtained $Mg(NH_3)_2Cl_2$ produced by deammoniation of $Mg(NH_3)_6Cl_2$ was undertaken. The OCD plot for this refinement can be seen in Figure 3.22 with selected crystallographic data presented in Table 3.12 and the atomic parameters of $Mg(NH_3)_2Cl_2$ are presented in Table 3.13.

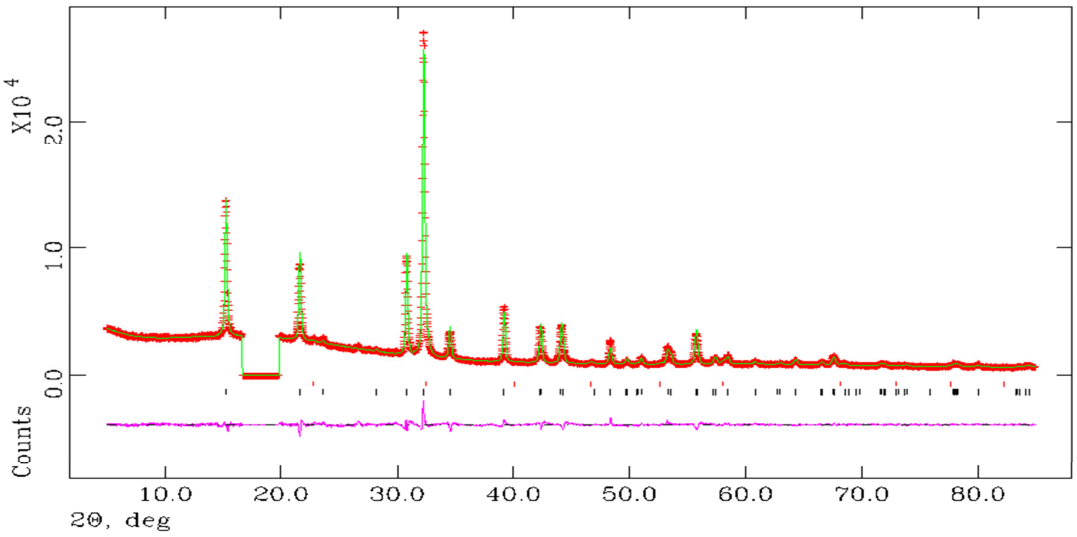

Figure 3.22: Observed, Calculated and Difference (OCD) plot for the Rietveld Refinement of $Mg(NH_3)_2Cl_2$. The black tickmarks are reflections from $Mg(NH_3)_2Cl_2$ and the red tickmarks are relections from NH_4Cl. The excluded region is a reflection from the air sensitive flat plate set-up

Table 3.12: Crystallographic data for sample **7** against PXD data.

Sample	**7**	
Phase	$Mg(NH_3)_2Cl_2$	NH_4Cl
Phase Fraction/wt.%	95.1(2)	4.9(3)
Crystal System	Orthorhombic	Cubic
Space Group	*Cmmm*	$Pm\bar{3}m$
a/Å	8.163(4)	3.880(7)
b/Å	8.192(4)	
c/Å	3.756(2)	
Volume/Å^3	251.31(2)	58.36(1)
Z	2	1
Formula Weight/g	262.578	57.524
Density, ρ_x/gcm^{-3}	1.735	1.634
No of observations	4596	
No of variables	32	
R_{wp}	0.0451	
R_p	0.0605	
χ^2	3.570	

Table 3.13: Atomic parameters of $Mg(NH_3)_2Cl_2$ (sample **7**)

Atom /Site	x	y	z	Occupancy	U_{iso} x 100/Å^2
Mg /2a	0	0	0	1	8.96(17)
Cl /4h	0.2191(18)	0	0.25	1	7.83(11)
N/4i	0	0.2526(4)	0	1	8.31(15)
H/16r	0.045	0.312	0.158	0.75	8.31

From refinement (Table 3.12) it can be determined that the orthorhombic Cmmm structure is a good fit for sample **1(b)** and is comparable to the literature values. A comparison of the bond lengths and angles compared to the published data for $Mg(NH_3)_2Cl_2$ [4] are presented in Table 3.14

Table 3.14: Bond distances and angles of $Mg(NH_3)_2Cl_2$

Distance (Å) or angle(°)	Sample 1(b)	Literature values [4]
Mg-Cl	4 x 2.594(10)	4x 2.563(1)
Mg-N	2x 2.070(3)	2x 2.130(5)
N-H	4x 0.851(2)	0.82(8)
Cl-Mg-Cl	87.24(5)	85.7(4)

As can be seen in Table 3.14 the bond distances of the Mg-Cl and N-H and the Cl-Mg-Cl are comparable with the values in the literature.

3.5.1.2 Isolation and Structural Studies of $Mg(NH_3)Cl_2$

Following on from the isolation of $Mg(NH_3)_2Cl_2$ from $Mg(NH_3)_6Cl_2$ the monoammine $Mg(NH_3)Cl_2$ has been isolated heating $Mg(NH_3)_6Cl_2$ to 245 °C at 5 °C per min (sample **8**).

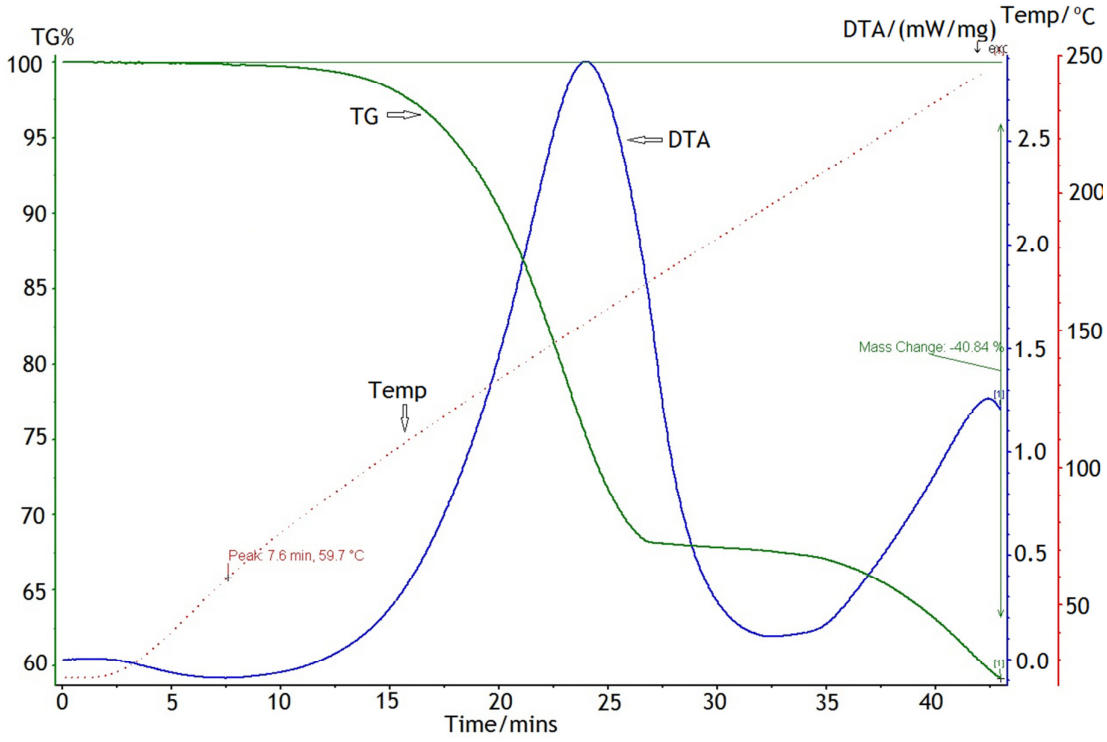

Figure 3.23: TGA- DTA profile of the decomposition of $Mg(NH_3)_6Cl_2$ to $Mg(NH_3)Cl_2$ (sample **8**)

The weight loss of this step is 40.84 wt.% compared to the theoretical weight loss from release of 5 NH_3 of 43.08 wt.%. The DTA curve also shows that the second endothermic event (corresponds to second step of NH_3 release in the mass spectrum). Attempts to reach this theoretical value, including holding at 245 °C for 30 mins or heating to a higher temperature were unsuccessful as the obtained sample was amorphous when analysed by PXD. It has been previously reported that $Mg(NH_3)Cl_2$ could be isostructural with $Ni(NH_3)Cl_2$ (from initial studies), which is monoclinic although no powder pattern or structure has been published. [6] Fitting the data to the known pattern from $Ni(NH_3)Cl_2$ proved unsuccessful and on searching the High Score database, only $Mg(NH_3)_2Cl_2$ was suggested as a solution with peaks matching the experimental data (Figure 3.24)

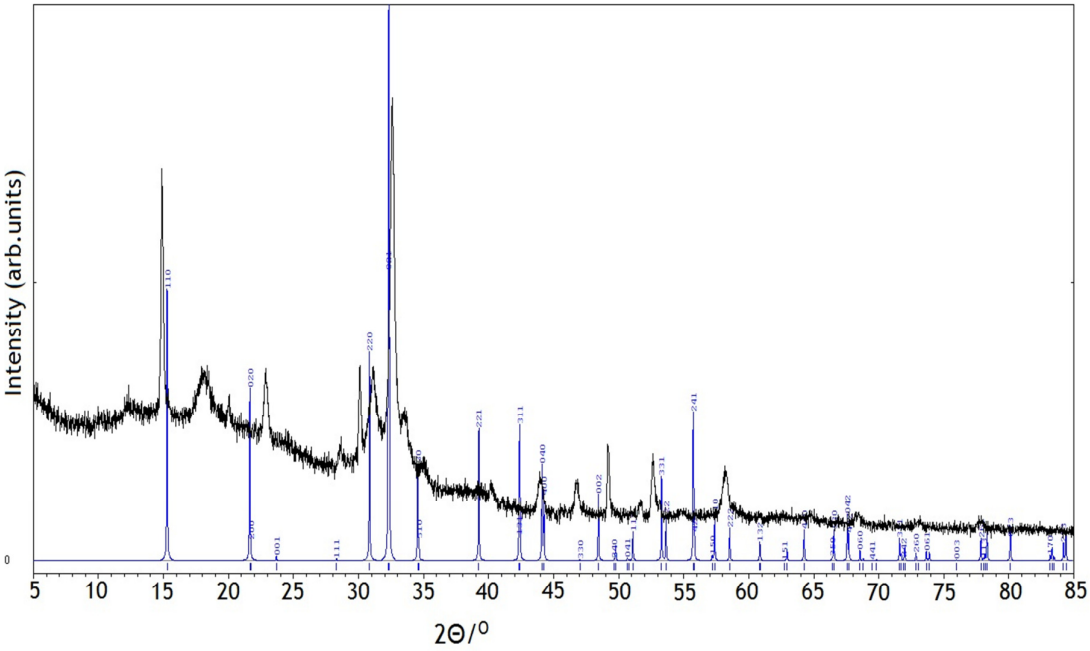

Figure 3.24: PXD pattern of sample **8** compared with the calculated pattern for $Mg(NH_3)_2Cl_2$ (blue)

From Figure 3.24 there is a 2Θ shift from the calculated pattern which is probably due to sample displacement. This concludes that the isolation of only the monoammine has not been achieved although a similar problem has been seen for the monoammines of $MnCl_2$ and $MnBr_2$ where the monoammines were not isolated due to their thermal stabilities.[16] Indexing the peaks from the experimental powder pattern that match against $Mg(NH_3)_2Cl_2$ resulted in unit cell parameters of *a*= 8.1623(19) Å, *b*= 8.2577(6) Å and *c*= 3.6881(8) Å being obtained. These values are different to the literature values of *a*= 8.180(2) Å, *b*= 8.2067(2) Å and *c*= 3.7550(1) Å which could suggest that decomposition of the sample is occuring (PXD is a mixture of phases). The unknown peaks could not be indexed.

3.5.1.3 Raman Spectroscopy of $Mg(NH_3)_nCl_2$ (n= 2,1)

Raman spectroscopy was also performed on sample **7** and sample **8**. The N-H stretching bands are seen as in the spectra of the hexammine. The Raman spectrum for the intermediates is presented in Figure 3.25 and the assignments of the bonds is presented in Table 3.15.

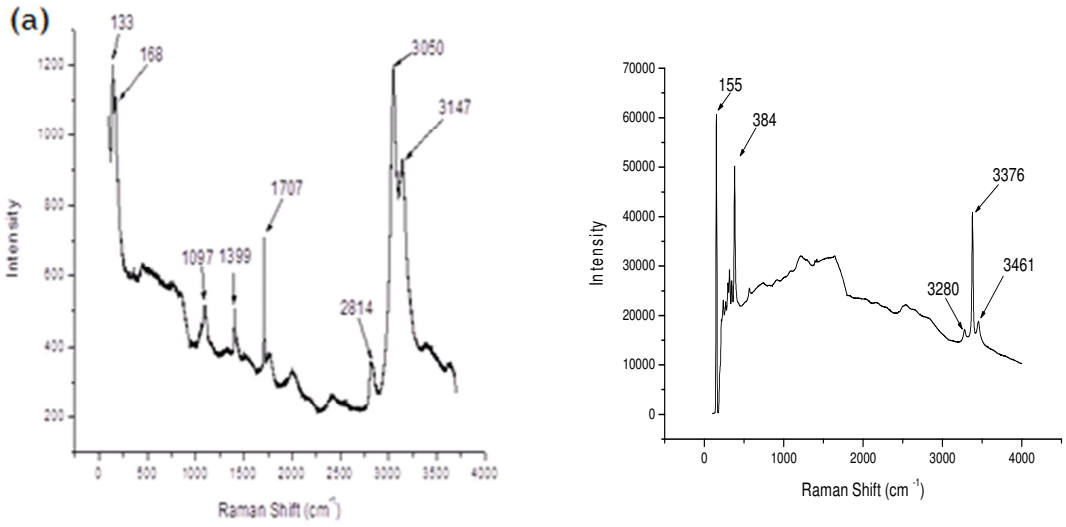

Figure 3.25: Raman Spectroscopy of (a) $Mg(NH_3)_2Cl_2$ (sample **7**) (b) $Mg(NH_3)_2Cl_2$ (sample **8**).

Table 3.15: Raman assignments of $Mg(NH_3)_xCl_2$ (x= 2,1). The peak at 2814 cm^{-1} for sample **8** can be attributed to NH_4Cl [23]

	Raman Shift (cm^{-1})						
Sample	**ν_{as}(NH)**	**ν_s(NH)**	**δ_{as}(NH)**	**δ_s(NH)**	**δ_x(NH)**	**ν(MN)**	**ν(NMN)**
7	3147	3050	1707	1399	1097		168 133
8	3461	3280				384	155

As can be observed in the Raman shifts, the degenerative band of N-H is present at 1707 cm^{-1} only in sample 7 which suggests that dynamic disorder is present for the diammine. The corresponding band was not observed in sample 8 which would be expected as the diammine is still present in the sample. This could indicate that dynamic disorder/rotation of the NH_3 is not present in the monoammine. M-N stretching is seen in both samples confirming that the magnesium is bonded to the nitrogen in both samples. PND has been used to aid in structure determination of the monoammine (Chapter 4).

3.5.2 PXD and Raman Studies of $Mg(NH_3)_nBr_2$ (n= 2,1)

3.5.2.1 Isolation and Structural Studies of $Mg(NH_3)_2Br_2$

To isolate $Mg(NH_3)_2Br_2$, $Mg(NH_3)_6Br_2$ was heated using TPD analysis as per the Cl equivalent. The optimum conditions for the successful isolation of the diammine were heating to 205 °C at 5 °C/min and holding at this temperature for thirty minutes.

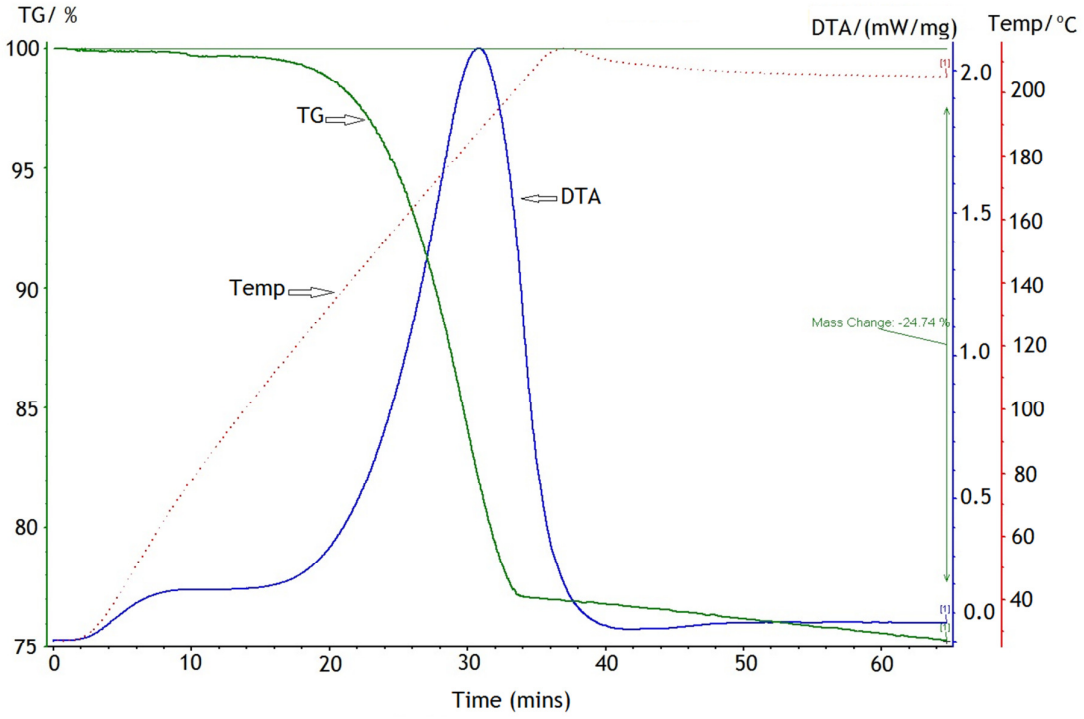

Figure 3.26: TGA-DTA of the formation of $Mg(NH_3)_2Br_2$ from $Mg(NH_3)_6Br_2$ (sample **9**)

The weight loss obtained was 24.74 % compared to the theoretical weight loss value of 23.8%. The TG curve does not plateau as expected and the DTA curve suggests that the next deammoniation step is commencing which agrees with the weight loss value obtained. The mass spec profile showed the release of the corresponding 4 NH_3. PXD analysis confirmed that the obtained sample post TG-DTA is $Mg(NH_3)_2Br_2$ (PDF no: 01-089-6789).[4]

The structure of $Mg(NH_3)_2Br_2$ has been previously studied by single X-ray crystallography and crystallises in the orthorhombic *Pbam* space group.[4] As per its Cl equivalent, the bromide diammine consists of edge-sharing octahedra of $[MgCl_{4/2}(NH_3)_2]$ chains which are arranged as a "herringbone" structure along the 001 axis. The unit cell dimensions of the structure were a = 5.944 (2) Å, b = 11.876(3) Å and c = 3.983(1) Å. Rietveld Refinement was performed using XRD data for sample **2(b)** using the published structure as a starting model. The data obtained by Rietveld Refinement are shown in Figure 3.27 and Tables 3.16-3.17.

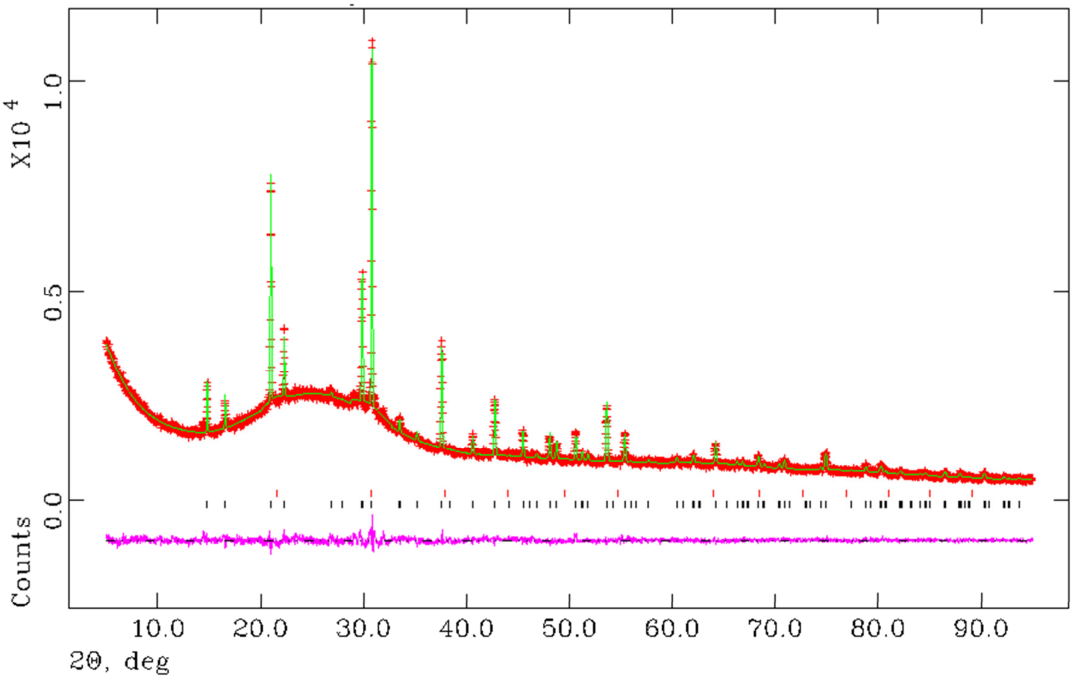

Figure 3.27: Observed, Calculated and Difference (OCD) plot from the PXD refinement of sample **9**. The black tick marks are the reflections from $Mg(NH_3)_2Br_2$ and the red tickmarks are reflections from NH_4Br.

Table 3.16: Crystallographic data for sample **9** against PXD data.

Sample	**9**	
Phase	$Mg(NH_3)_2Br_2$	NH_4Br
Phase Fraction/wt.%	95.7(3)	4.3(4)
Crystal System	Orthorhombic	Cubic
Space Group	*Pbam*	$Pm\bar{3}m$
a/Å	5.979(3)	4.134(5)
b/Å	11.941(6)	
c/Å	3.983(1)	
Volume/Å^3	284.41(2)	70.65(9)
Z	2	1
Formula Weight/g	436.350	101.975
Density, ρ_x/gcm^{-3}	2.548	2.522
No of observations	5323	
No of variables	35	
R_{wp}	0.0346	
R_p	0.0793	
χ^2	1.594	

Table 3.17: Atomic parameters of $Mg(NH_3)_2Br_2$

Atom /Site	**x**	**y**	**z**	**Occupancy**	**U_{iso} x 100/Å^2**
Mg /2a	0	0	0	1	5.0(4)
Br /4h	0.2660(7)	0.3885(20)	0.25	1	4.4(9)
N/4g	0.2774(4)	0.1314(13)	0	1	3.1(4)
H1/8i	0.3509	0.1103	0.2092	0.75	3.1
H2/8i	0.2231	0.185	0.1055	0.75	3.1

The lattice parameters in sample **9** are comparable to the lattice parameters in the literature. The positions of the hydrogen could not be refined using the PXD data so PND is required (Chapter 4). The bond distances and angles compared to the literature data are presented in Table 3.18 and the N-H bond lengths are in

fair agreement with the literature although do not match exactly as the octahedral are axially compressed which has been observed for Mn ammines .[4]

Table 3.18: Bond angles and distances

Distance/Å or Angles/ °	Sample 9
Mg-N	2x 2.283(18) Å
Mg-Br	4 x 2.774(2) Å
N-H1	2x 0.771(18) Å
N-H2	2x 0.831(15) Å
H1-H1	0.725(2) Å
H2-H2	0.841(2) Å
Br-Mg-Br	91.76(9) °

3.5.2.2 Isolation and Structural Studies of $Mg(NH_3)Br_2$

The monoammine, $Mg(NH_3)Br_2$ (sample **10**) has been isolated from TPD experiments of $Mg(NH_3)_6Br_2$ (sample **2**) as per its Cl equivalent. The optimum conditions for the isolation were found to be heating to 300 °C at 5 °C per minute with no hold at this temperature (Figure 3.28). If the temperature was held for any length of time the subsequent product was found to be amorphous by PXD.

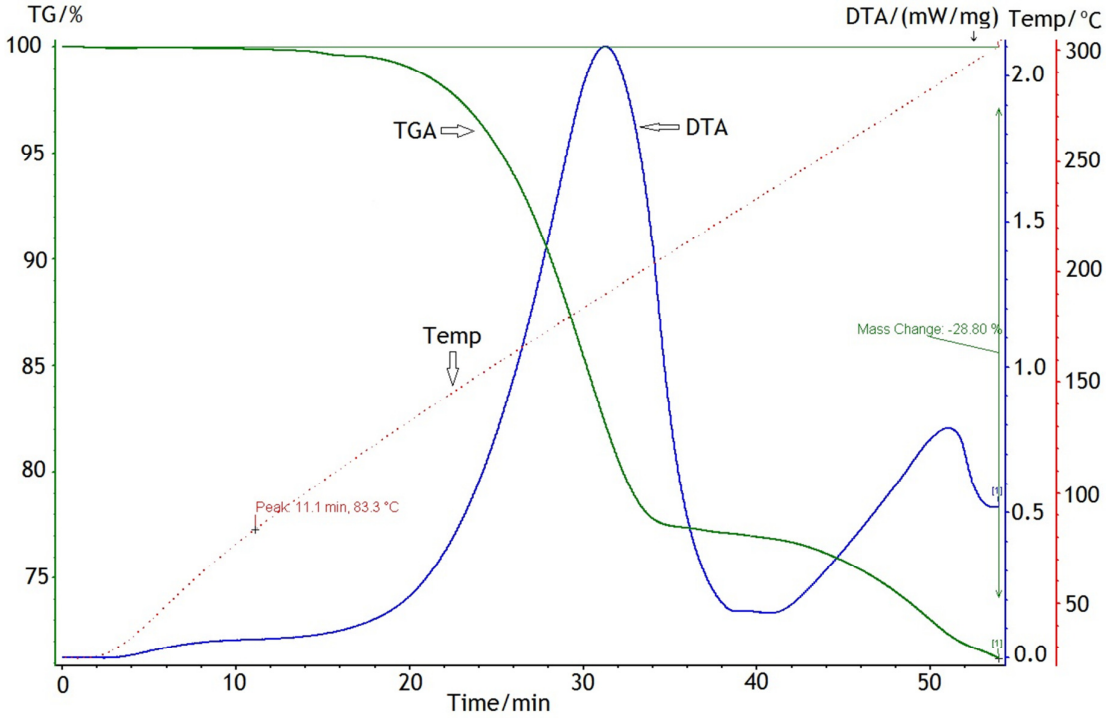

Figure 3.28: TGA-DTA of the isolation of $Mg(NH_3)Br_2$ from $Mg(NH_3)_6Br_2$

The weight loss from the TGA is 28.80 wt.%. The theoretical weight loss of the deammoniation of $Mg(NH_3)_6Br_2$ to $Mg(NH_3)Br_2$ is 29.75 wt.%. From the DTA curve, there are two thermal events corresponding to the loss of 4 NH_3 first followed by a single equivalent NH_3 subsequently.

It has been previously been suggested that the structure of $Mg(NH_3)Br_2$ could be isostructural with the *(C2/m)* monoclinic $Ni(NH_3)Br_2$.[6] The experimental PXD powder pattern did not match the calculated pattern for $Ni(NH_3)Br_2$ in Powdercell (Figure 3.29).

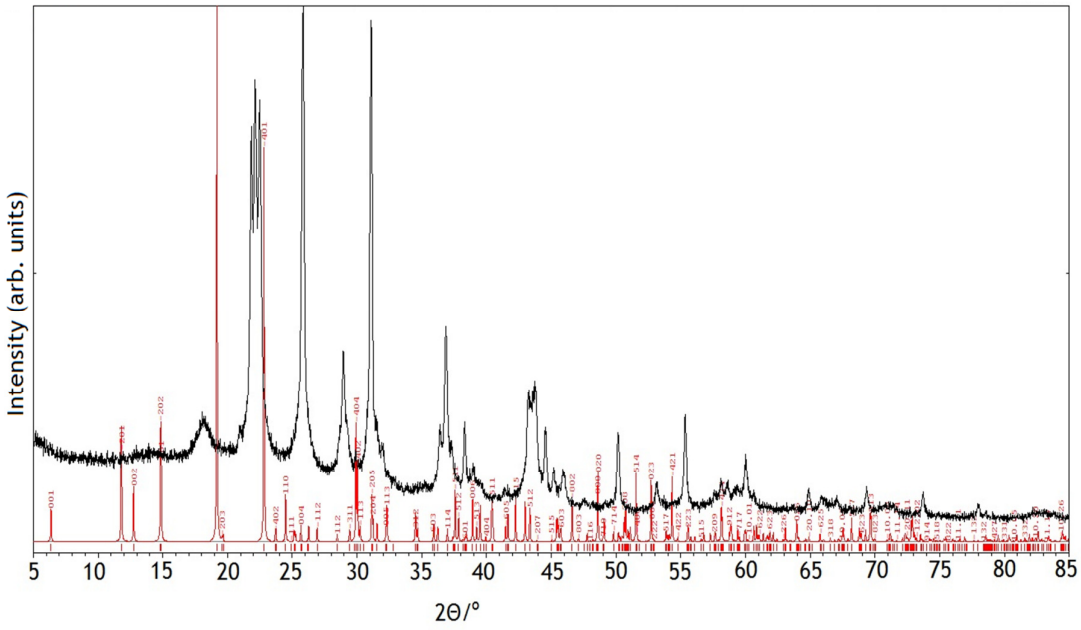

Figure 3.29: PXD pattern of sample compared to the calculated pattern for $Ni(NH_3)Br_2$ (red)

Using the High Score database, orthorhombic $Mg(NH_3)_2Br_2$ has been suggested as a possible match, although only a number of peaks including the strongest reflection at 32 ^{o} (210) as can be seen in Figure 3.29. Indexing these peaks to $Mg(NH_3)_2Br_2$ results in unit cell dimensions of *a*= 5.9172(5) Å, *b*= 11.8760(22) Å and *c*= 3.9830(1) Å. The unit cell of the *a* parameter has only decreased in size when compared to the literature values. In the PXD it can be concluded that $Mg(NH_3)_2Br_2$ is present along with another phase which is likely to be that of the monoammine. The decrease of the a parameter of $Mg(NH_3)_2Br_2$ suggests that a fraction of NH_3 is lost before the conversion to the monoammine.

3.5.2.3 Raman Spectroscopy of $Mg(NH_3)_nBr_2$ (n= 2,1)

Raman spectroscopy has also been carried out on the $Mg(NH_3)_2Br_2$ (Figures 3.30) and $Mg(NH_3)Br_2$. The assignments are presented in Table 3.19

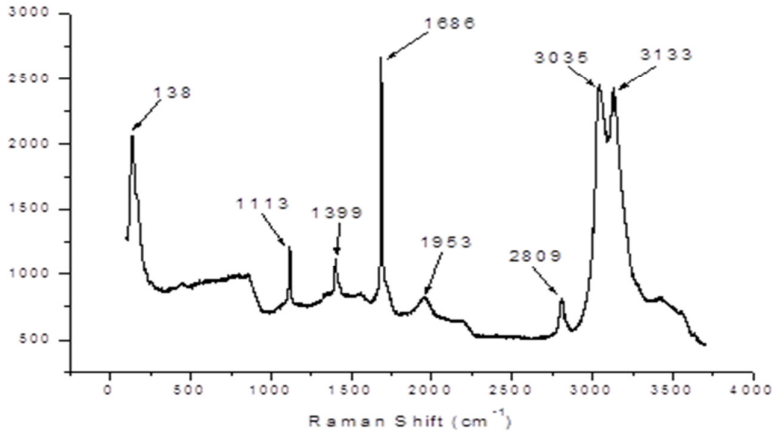

Figure 3.30: Raman of $Mg(NH_3)_2Br_2$ (sample **9**)

Table 3.19: Raman assignments of $Mg(NH_3)_xBr_2$ (X= Cl, Br, I)

	Raman Shift (cm^{-1})						
Sample	**ν_{as}(NH)**	**ν_s(NH)**	**δ_{as}(NH)**	**δ_s(NH)**	**δ_x(NH)**	**ν(MN)**	**ν(NMN)**
9	3133	3053	1686	1399 1113			138
10	3400 3364	3269				306	155

In both samples **9** and **10** the stretches of NH (asymmetric and symmetric stretches) are present indicating the presence of NH_3. The Raman shift at 2809 cm^{-1} in sample **9** can be attributed to the NH_4^+ species in NH_4Br.[23]

The peak at 1686 cm^{-1} in sample 2(b) may be due to the dynamic disorder (rotation) of $Mg(NH_3)_2Br_2$ although the deformation of NH_4^+ has been seen previously at 1690 cm^{-1}. [23] In sample 2(c) there are δ bands are present in this sample which includes the δ NH rotation which would not be expected as there is diammine present.

For both samples **9** and **10** Mg-N bands are present, indicating that the NH_3 is still bonded to the magnesium.

Further investigations involving PND have been performed to analyse the structure (Chapter 4).

3.5.3 PXD and Raman Studies of $Mg(NH_3)_nI_2$ (n= 2,1)

3.5.3.1 Isolation and Structural Studies of $Mg(NH_3)_2I_2$

$Mg(NH_3)_2I_2$ (sample **11**) has been isolated by the partial deammoniation of $Mg(NH_3)_6I_2$ as per its Cl and Br equivalents. The optimum conditions for the isolation were found to be heating to 235 °C at 5 °C per minute with no subsequent hold at this temperature (Figure 3.31). The weight loss was 15.98% compared with a theoretical weight loss of 17.9% for the deammoniation of $Mg(NH_3)_6I_2$ to $Mg(NH_3)_2I_2$ with the loss of 4 NH_3. The TG and DTA curve have not reached a plateau so a heating rate of 1 °C/min could improve this. Ideally, the experimental weight loss could be improved to be closer to the theoretical value however resulted in an amorphous product from the TG-DTA experiment by PXD.

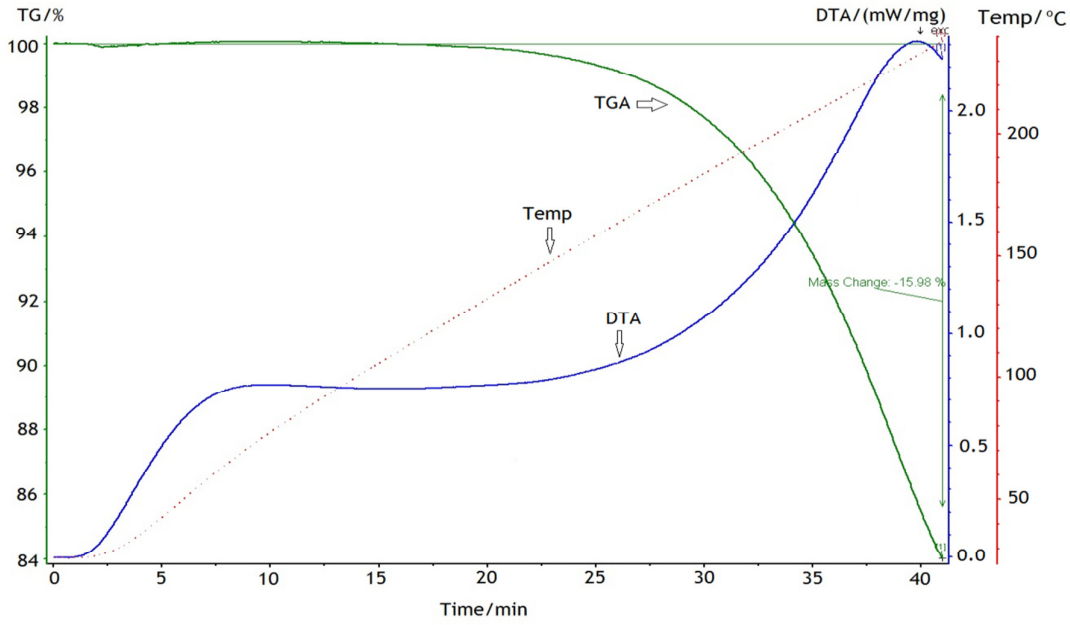

Figure 3.31: TGA-DTA for the formation of $Mg(NH_3)_2I_2$ from $Mg(NH_3)_6I_2$ (sample **11**)

PXD analysis of sample **11** confirmed that the diammine had been formed from the deammoniation of the hexammine (Figure 3.32). The structure of $Mg(NH_3)_2I_2$ (PDF no: 01-089-6790) has previously been reported as crystallising in the orthorhombic *Pbam* group making it isostructural with $Mg(NH_3)_2Br_2$ (section 3.5.2.1) with lattice parameters of *a*= 6.285(1), *b*= 12.559(3) and *c*= 4.302(1) Å.

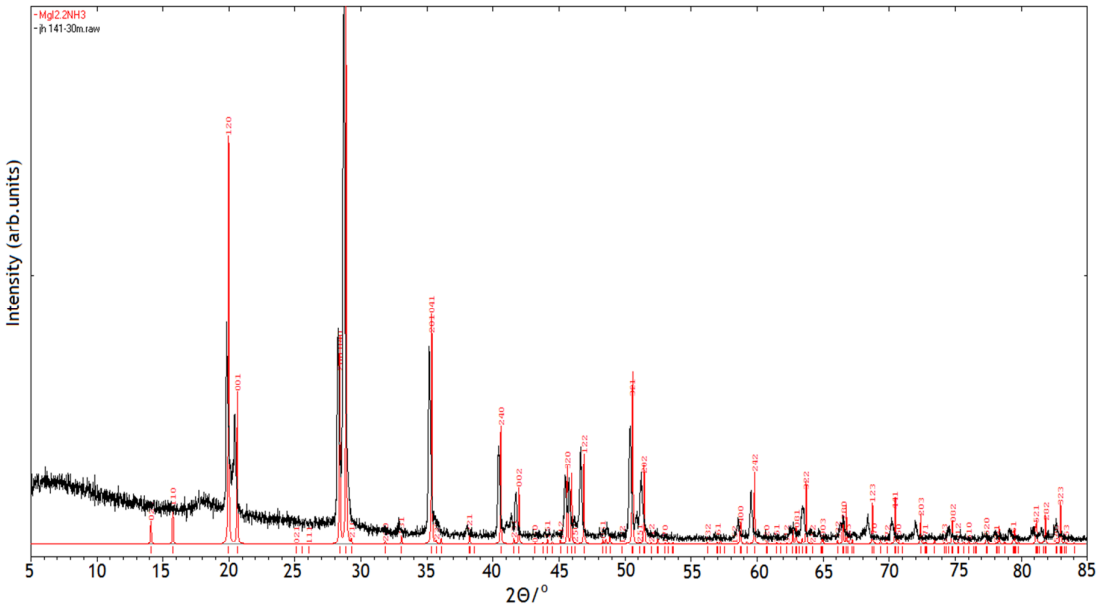

Figure 3.32: PXD powder pattern of sample **11**. The calculated red lines are $Mg(NH_3)_2I_2$

Subsequent refinement against the PXD data resulted in obtained lattice parameters were *a*= 6.237(3) Å, *b*= 12.235(4) Å and *c*= 4.382(1) Å with a χ^2 value of 5.55 obtained.

3.5.3.2 Isolation and Structural Studies of $Mg(NH_3)I_2$

TG-DTA-MS experiments were performed on $Mg(NH_3)_6I_2$ by heating to 320°C at a rate of 5°C per minute to isolate the corresponding monoammine (Figure 3.33).

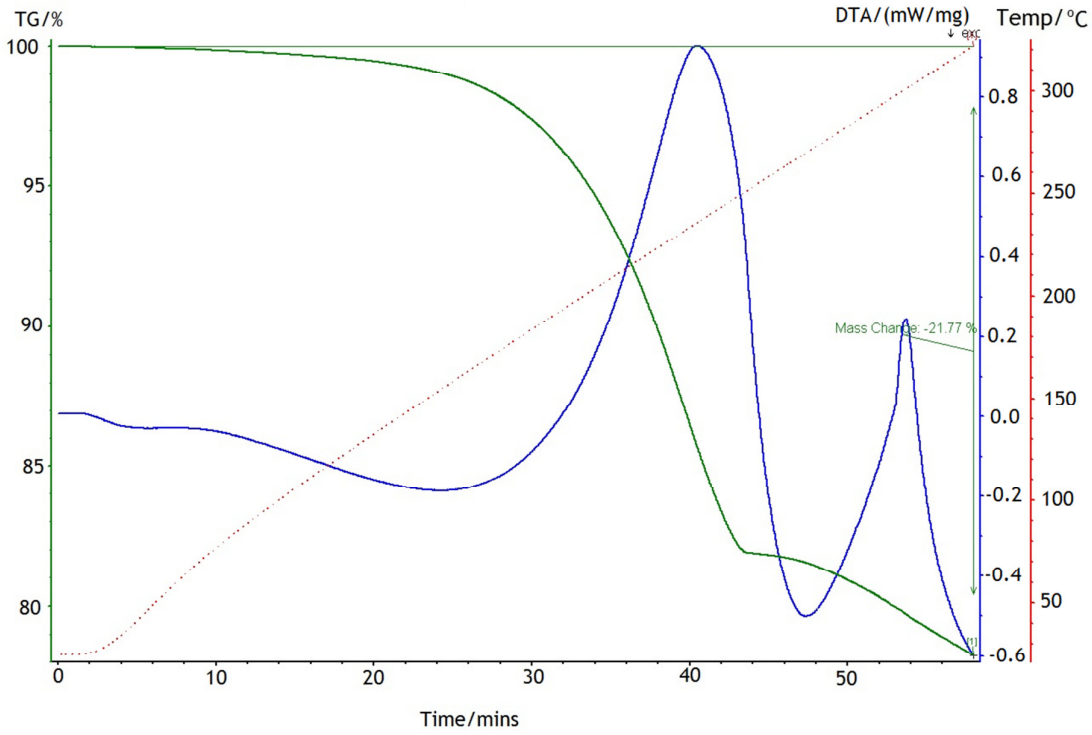

Figure 3.33: TGA-DTA profile for the formation of $Mg(NH_3)I_2$ (sample **12**)

The obtained PXD pattern was amorphous so no structure could be suggested or assigned. Raman spectroscopy (section 3.5.3.3) was carried out to determine what bonding was present.

3.5.3.3 Raman Spectroscopy of $Mg(NH_3)_nI_2$ (n= 2,1)

The Raman spectra obtained for $Mg(NH_3)I_2$ (sample **11**) are presented in Figure 3.34 and the assignments of $Mg(NH_3)_2I_2$ and $Mg(NH_3)I_2$ presented in Table 3.20.

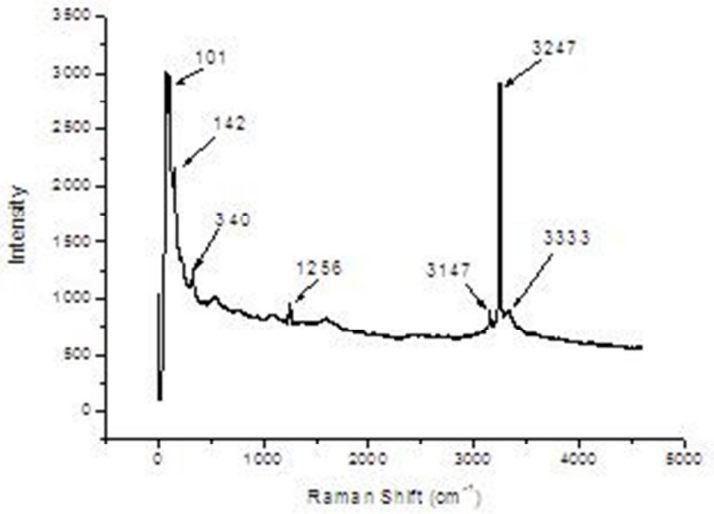

Figure 3.34: Raman spectroscopy of sample **11** ($Mg(NH_3)_2I_2$)

Table 3.20: Raman assignments of $Mg(NH_3)_nI_2$ (n= 2,1)

	Raman Shift (cm^{-1})						
Sample	**ν_{as}(NH)**	**ν_s(NH)**	**δ_{as}(NH)**	**δ_s(NH)**	**δ_x(NH)**	**ν(MN)**	**ν(NMN)**
11	3333	3147	1627	1250 1130	533	333	155
12	3333	3147		1256		340	142 101

In sample **11** the stretches are similar to that seen for $Mg(NH_3)_6I_2$ with the stretches present as expected (see section 3.3.3) although there are differences in the Raman shift with the bonds. For example, the δ_{as}(NH) is at 1577 cm^{-1} in the hexaammine and the δ_x(NH) is at 619 cm^{-1} for the hexaammine **.**

The Raman for sample **2(c)** indicates the presence of NH_3 which confirms that this sample is still an ammine which could not be determined by PND. Mg-N and N-Mg-N bands are also present indicating that the bonding between the Mg and nitrogen from the NH_3 is similar to that of the diammine.

3.6 Conclusions

The magnesium hexaammines have been successfully synthesised at room temperature and are all cubic in structure. Subsequent refinement of the PXD data confirmed that $Mg(NH_3)_6I_2$ is isostructural with $Mn(NH_3)_6I_2$ and $Mg(NH_3)_6Br_2$ is isostructural with $Fe(NH_3)_6Cl_2$. Raman measurements have also probed the bonding of the hexammines . This has confirmed the bonding of the hexammines (nitrogen from NH_3 bonded to Mg whereas the halide is "free" in the unit cell) and also that dynamic disorder (rotation of NH_3 is present).

TPD measurements confirmed that all three hexaammines decompose in a three step process to form the starting material:

$$Mg(NH_3)_6X_2 \rightarrow Mg(NH_3)_2X_2 + 4\ NH_3 \qquad (3.10)$$

$$Mg(NH_3)_2X_2 \rightarrow Mg(NH_3)X_2 + NH_3 \qquad (3.11)$$

$$Mg(NH_3)X_2 \rightarrow MgX_2 + NH_3 \qquad (3.12)$$

In terms of both gravimetric capacities and onset temperatures, $Mg(NH_3)_6Cl_2$ is the most encouraging system of the three halides studied. From equation 10, the diammines of the three magnesium ammines have been isolated. The isolated diammines agree with the structures in the literature, with $Mg(NH_3)_2Cl_2$ crystallising in the *Cmmm* orthorhombic group and the $Mg(NH_3)_2Br_2$ and $Mg(NH_3)_2I_2$ both being isostructural to each other and crystallising in the *Pbam* space group.[4] Attempts to isolate the monoammine proved unsuccessful with PXD analysis showing a mixture of the diammine and an unknown phase for the Cl and Br adduct. The PXD pattern for monoammine for $Mg(NH_3)I_2$ is amorphous so no clues could be derived although Raman confirmed the presence of NH_3 and Mg-N bonding in the sample.

As the mechanisms of the three magnesium ammines have been understood in this chapter, the next stage is to improve the performance of the systems. Deammoniation temperatures will have to be improved for all three systems, even though $Mg(NH_3)_6Cl_2$ commences deammoniation at 64.8 ^oC. Nanopores have been observed previously for the demmoniation of $Mg(NH_3)_6Cl_2$ but were not

observed during the deammoniation process presented in this chapter. This allows for favourable kinetics.[24] Nanostructuring the $Mg(NH_3)_6Cl_2$ is a potential solution to improve the deammoniation , although the ball milling of $Mg(NH_3)_6Cl_2$ on its own could lead to NH_3 decomposition before heating, thus reducing the gravimetric capacity.[25] Ball milling $MgCl_2$ before ammoniation could improve both the uptake/release kinetics. Other nanostructuring approaches, including templating and nanoconfinement could be employed for the ammines to improve their deammoniation temperatures.[26]

For use as a hydrogen storage material, then investigations into lowering the temperature required for the splitting of NH_3 to N_2 and H_2 are required. Current research is focussing on using transition metal nanoparticles (such as Co and Ni) for borohydride ammines .[27] In the case of the three magnesium ammines presented in this chapter limited research involving the splitting of $Mg(NH_3)_6Cl_2$ has been performed.[28]

3.7 References

[1] T. D. Elmøe, R. Z. Sørensen, U. Quaade, C. H. Christensen, J. K. Norskøv and T. Johannessen, *Chem. Eng. Sci*., 2006, **61**, 2618.

[2] C. H. Christensen, R. Z. Sørensen, T. Johannessen, U. J. Quaade, T. D. Elmøe, R. Køhler and J. K. Nørskov, *J. Mater. Chem.,* 2005, **15**, 4106.

[3] M. H. Sørby, O. M. Løvvik, M. Tsuboto, T. Ichikawa, Y. Kojima and B. C. Hauback, *Phys. Chem. Chem. Phys*., 2011, **13**, 7644

[4] A. Leineweber, M. W. Fredriszik and H. Jacobs, *J. Solid. State. Chem.,* 1999, **147**, 229.

[5] A. Leineweber, H. Jacobs, P. Fischer and G. Böttger, *J. Solid. State. Chem,* 2001, **156**, 487.

[6] A. Leineweber, H. Jacobs and H. Ehrenberg, *Z. Anorg. Allg. Chem,* 2000, **626**, 2146.

[7] I. Olovosson, *Acta. Crystallogr*., **1965**, *18*, 889.

[8] R. Z. Sørensen, J. S. Hummelshoj, A. Klerke, J. B. Reves, T. Vegge, J. K. Norskov and C. H. Christensen, *J. Am. Chem. Soc*., 2008, **130**, 8660

[9] G. W. Watt and D .R. Foerster, *J. Inorg. Nucl. Chem*, 1959,**11**, 253.

[10] A. C. Larson, R. B. von Dreele, The General Structure Analysis System, Los Alamos National Laboratories, Report LAUR 086–748, LANL, Los Alamos, NM, 2000

[11] B. H. Toby, *J. Appl. Crystrallogr.,* 2001, **34**, 210.

[12] R. Essmann, G. Kreiner, A. Niemann, D. Rechenbach, A. Schmeiding, T. Sichla, U. Zachweija and H. Jacobs, *Z. Anorg. Allg. Chem*., 1996, **662**, 1161.

[13] H. Jacobs, J. Bock and C. Stove, *J. Less Common Metals*, 1987, **134**, 207.

[14] I. C. Hwang, T. Drews and K. Seppelt, *J. Am. Chem. Soc*., 2000, **122**, 8486.

[15] W. Lu, G. Wu, Y. Chao, Y. P. Feng and P. Chen, *Inorg. Chem*., 2012, **51**, 76.

[16] H. Reardon, J. M. Hanlon, M. Grant, I. Fullbrook and D. H. Gregory, *Crystals*, 2012, **2**, 123.

[17] J. M. Janik, J. A. Janik, G. Pytasz and J. Sokolowki, *J. Raman Spectrosc*., 1975, **4**, 13.

[18] R. Plus, *J. Raman Spectrosc*., 1973, **1**, 551.

[19] T. E. Jenkins and A. R. Bates, *J. Phys. C: Solid St. Phys*., 1981, **14**, 817.

[20] H. Jacobs, J. Brock and C. Stüve, *J. Less-Common Metals,* 1987, **134**, 207.

[21] Y. Gao, X. Yu, W. Sun, D. San and W. Yang, *Angew. Chem. Int. Ed*., 2011, **50**, 1087.

[22] S. Westman, P. E. Werner, T. Schuler and W. Raldow, *Acta Chemica Scand. A*, 1981, **35**, 467.

[23] N. Wen and M. H. Brooker, *J. Phys. Chem*., 1995, **99**, 359.

[24] J. S. Hummelshøj, R. Z. Sørensen, M. Y. Kustova, T. Johannessen, J. K. Norskøv and C. H. Christensen, *J. Am. Chem. Soc*., 2006, **128**, 16

[25] M. Tsuboto, S. Hino, H. Fujii, C. Oomatsu, M. Yamana, T. Ichikawa and Y. Kojima, *Int. J. Hydrogen Energy*, 2010, **35**, 2058.

[26] H. Reardon, J.M. Hanlon, R. W. Hughes, A. G. Jopek, T. K. Mandal and D. H. Gregory, *Energy Environ. Sci.,* 2012, **5**, 5951.

[27] X. Zheng, G. Wu, W. Li, Z. Xiong, T. He, J. Gou, H. Chen and P. Chen, *Energy Environ. Sci*., 2011, **4**, 3593.

[28] A. Klerke, C. H. Christensen, J. K. Norskov and T. Vegge, *J. Mater. Chem*., 2008, **18**, 2304.

4. PND Investigations of the Magnesium Ammines, $Mg(NH_3)_6X_2$ (where X= Cl, Br, I)

4.1 Introduction

As discussed in Chapter 3, the structure of the hexaammines has been proposed as cubic with the Mg bonded to the nitrogen from the NH_3 with the chloride "free" in the unit cell.

This structure has subsequentially been determined experimentally and refined from Powder Neutron Diffraction (PND) data as the PXD can be regarded as being inconsistent with the three fold symmetry of NH_3.[1] Using $Mg(ND_3)_6Cl_2$, Molecular Dynamic calculations (MD) were performed in parallel. The conclusion from this combined experimental/theoretical study, is that the ammonia in the hexammines exhibits the behaviour of free ammonia rather than being constrained as might be expected.[1] In the refined structure, the position of the nitrogen was modified from a fully occupied 24e Wyckoff site to a partially occupied 96j Wyckoff site as the nitrogen is displaced from its average position. Further, in the modified structural model, deuterium (hydrogen) partially occupies two 96-fold positions as this allows two deuterium atoms to be close to its positions in the ordered structure as seen during MD calculations. This arrangement of partly occupied sites is regarded as a weighted superposition of the 4 ND_3 positions and orientations, which can be seen in Figure 4.1.

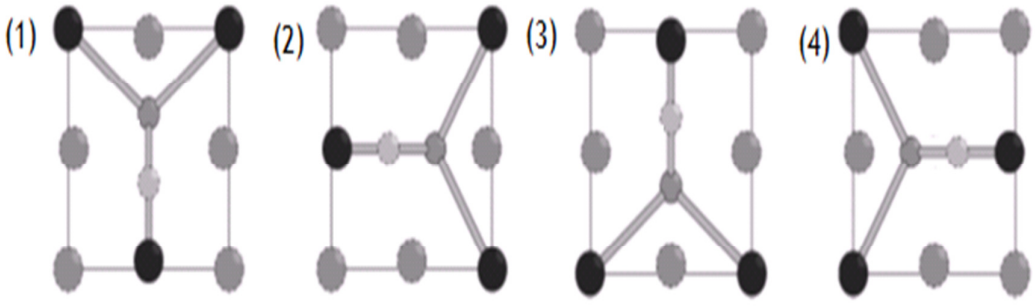

Figure 4.1: Refined ND_3 arrangement in the proposed new model of $Mg(ND_3)_6Cl_2$ as a weighted superposition of the four ND_3 orientations. The small spheres are nitrogen and the large sphere is deuterium. The deuterium atoms at the square corners are D1 and those slightly off the edges are D2. Modified from Ref 1

The N-D bond lengths and angles obtained from the refinement are in good agreement with free ND_3.

This new model could subsequentially be used to produce an improved refined structural model for $Mg(ND_3)_6Br_2$ and $Mg(ND_3)_6I_2$ which has not been performed previously due to the limitations of PXD with regards to hydrogen.

The deammoniation of $Mg(ND_3)_6X_2$ (X= Cl, Br, I) has been reported in Chapter 3 but a fuller picture is required for the ammines to improve the deammoniation kinetics. The only previous in-situ research on the hexammines has been on $Mg(NH_3)_6Cl_2$.[2] In this study, the dynamics of the ammonia was studied by both DFT and neutron scattering with the release of NH_3 limited by bulk diffusion for the three-step deammoniation process. The intermediates between the three ammines were not reported. PND can be exploited to understand the mechanism of the desorption of ammonia in the three magnesium hexaammines as the technique allows the ability to follow phases and structure as each molecule of NH_3 is desorbed from the sample during the deammoniation steps and identify intermediates formed. From the PND data, the systems can then be improved.

The aim of this chapter has been to employ the refined structure of $Mg(ND_3)_6Cl_2$ to successfully refine the structure of the synthesised $Mg(ND_3)_6X_2$ (X= Cl, Br, I) using PND. The deammoniation of $Mg(ND_3)_6X_2$ has also been investigated using in-situ PND to investigate the deammoniation processes in more detail.

4.2 Experimental

4.2.1 Synthesis of $Mg(ND_3)_6X_2$ where X= Cl, Br, I

The deuterated hexaammines were synthesised by the reaction of the starting salt MX_2 (X= Cl (Sigma, 98%), Br (Sigma, 98%), I (Alfa 99%, Sigma 98%)) under a flow of ND_3(Isotec, 99%). The experimental set-up is described in section 2.2.7.

4.2.2 Powder Neutron Diffraction (PND) Experiments

4.2.2.1 Ex-Situ PND

Ex situ PND measurements of the deuterated hexaammines (samples **1-3**) were performed on the high resolution D2B diffractometer at the ILL laboratory in Grenoble as described in section 2.3.3.[3] Experiments were performed at room temperature. 1.5 g-2 g of samples were loaded into large vanadium cans (> 3 cm^3) with indium seals and data collected at each temperature for a period of 4 – 5 hrs as described in section 2.3.3.2

4.2.2.2 In-Situ PND

In situ PND experiments on the deuterated hexaammines (samples **4-6**) were performed on the GEM (General Materials) diffractometer at the ISIS facility at the Rutherford Appleton Lab, Didcot. [4,5] Initially, data were collected at room temperature before heating the samples to 500 °C and collecting data at given temperature points.

Typically 1.5 g – 2g of sample were loaded into 6 mm or 8 mm diameter vanadium cans with a copper seal. The cans were sealed and transferred from the glove box, and attached to a capillary for gas flow in an argon filled glove bag. The experimental set up is described in section 2.3.3.2. Samples were heated under a flow of Ar(g) to temperature points determined by TPD measurements (section 3.4) and data were collected for 1 - 2 hrs at each temperature point depending on the sample quality.

4.2.2.3 Rietveld Refinement against PND data

The structures of the ammines and GEM in-situ measurements were refined using the GSAS program with the EXPGUI interface.[6,7] The backgrounds of the hexaammine samples for the ex-situ ILL measurements were modelled using background function 1, a shifted Chebyschev function. For the GEM in-situ measurements the background was successfully fitted using background function 8, a reciprocal interpolation function. This was then followed by refinement of cell parameters, atomic positions, profile coefficients, peak widths and temperature factors. Peak profiles were successfully modelled using function 2

in GSAS, a Simpson's integration of the Pseudo-Voight function. Other phases were then added and refined as appropriate.

For the GEM in-situ measurements, the Bank 3 data (24.6-45.6^{o}) was refined first followed by the Bank 4 data (50-75^{o}).

4.2.3 Summary of Reactions

Table 4.1: Summary of Reactions presented in this chapter

Reaction	Material	Conditions
1	$Mg(ND_3)_6Cl_2$	Ex-situ PND
2	$Mg(ND_3)_6Br_2$	Ex-situ PND
3	$Mg(ND_3)_6I_2$	Ex-situ PND
4	$Mg(ND_3)_6Cl_2$	In-situ PND
5	$Mg(ND_3)_6Br_2$	In-situ PND
6	$Mg(ND_3)_6I_2$	In-situ PND

4.3 Results and Discussion

4.3.1 Structural Studies of $Mg(ND_3)_6X_2$ where X= Cl,Br,I

4.3.1.1 Room temperature PND of $Mg(ND_3)_6Cl_2$

The new disordered proposed model of $Mg(ND_3)_6Cl_2$ by Sørby *et al.* as discussed in the introduction was used as the basis for the PND refinements.

For sample **1** ($Mg(ND_3)_6Cl_2$), this new structure agrees with the experimental data (Figure 4.2) as the quality of fit is improved compared to the old model for $Mg(ND_3)_6Cl_2$. In the ordered model (used for PXD refinements in chapter 3), the X^2 value obtained for the PND was 8.211 which was greater than the disordered model (see Table 3.3). The R_{wp} value for Bank 3 for the ordered model is 0.0474

compared to the R_{wp} of 0.0437 for the disordered model. The main difference between the ordered and the new disordered model is the symmetry of ND_3. In the ordered model the nitrogen is located at the 24e Wyckoff site and is fully occupied while in the ordered model the nitrogen is located at the 96j Wyckoff site and is partially occupied with occupancy of 0.25. For the H(D) in the ordered model this is located at the 96k Wyckoff site with a partial occupancy of 0.75. In the disordered model the D1(H1) is located at the 96k Wyckoff site with occupancy of 0.5 while D2(H2) is located at the 96j Wyckoff site with a partial occupancy of 0.25.

Crystallographic data is presented in Table 4.2 with the bond angles (for selected converged ND_3 unit) and distances presented in Tables 4.3 and 4.4.

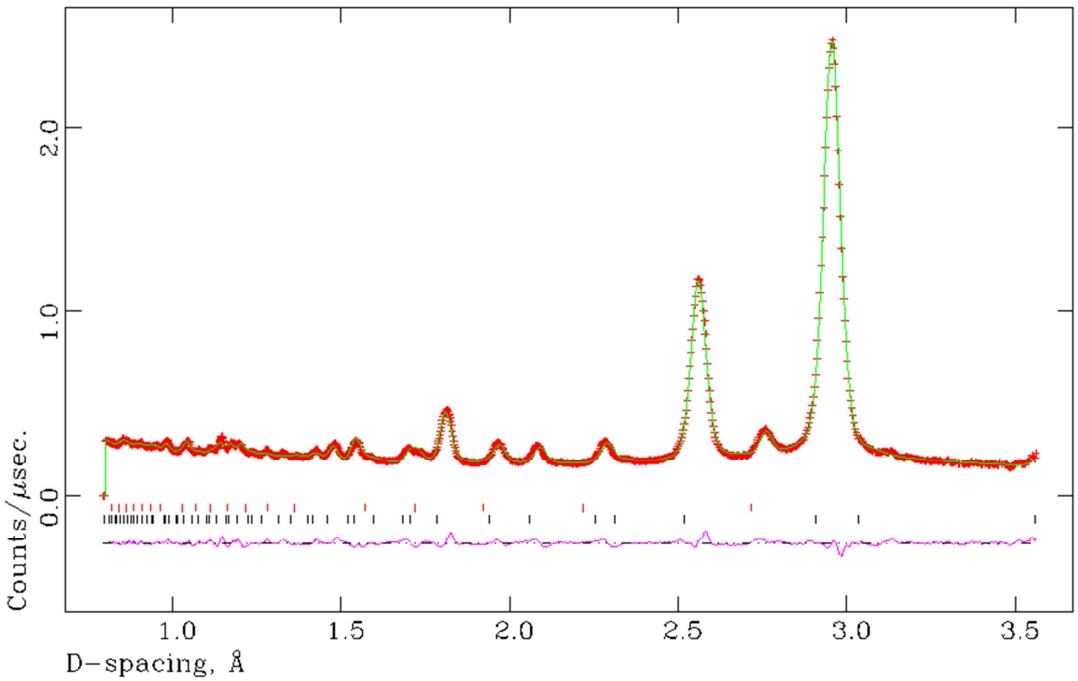

Figure 4.2: Observed, Calculated and difference (OCD) plot for the structural refinement of sample **1** against TOF PND data. The black tick marks indicate reflections from the $Mg(ND_3)_6Cl_2$ phase and the red tick marks indicate reflections from ND_4Cl.

Table 4.2: Crystallographic data for PND for $Mg(ND_3)_2Cl_2$ at 25 ^oC

Phases	$Mg(ND_3)_6Cl_2$	ND_4Cl
Phase Fraction (.wt%)	93.6(3)	6.4(4)
Crystal System	Cubic	Cubic
Space Group	*Fm$\bar{3}$m*	*Pm$\bar{3}$m*
a/Å	10.219(2)	3.895(13)
Volume/Å^3	1067.052(6)	59.112(1)
Z	4	1
Formula Weight/g	862.020	49.460
Density, p_x/gcm^{-3}	1.339	1.388
No of observations	3285	
No of variables	62	
R_{wp}	0.0851	
R_p	0.1605	
χ^2	7.875	

Table 4.3: Atomic positions and temperature factors for $Mg(ND_3)_6Cl_2$ at 25 ^oC.

Atom /Site	**x**	**y**	**z**	**Occupancy**	**U_{iso} x100/Å^2**
Mg /4a	0	0	0	1	2.5
Cl /8c	0.25	0.25	0.25	1	4.1(3)
N/96j	0	0.0209(7)	0.2485(6)	0.25	3.5(2)
D1/96k	0.0649(5)	0.0650(5)	0.2323(9)	0.5	6.5(2)
D2/96j	0	0.0836(14)	0.2054(17)	0.25	6.4(2)

Table 4.4: Bond distances and angles for $Mg(ND_3)_6Cl_2$

Angle/^{o} or Distance/Å	Sample 1
Mg-N	24x 2.266(14)
N-D1	2x 0.818(10), 2x 1.112(6)
N-D2	2x 0.98(2), 1x 1.15(2)
D1-N-D1/^{o}	108.3(10)
D1-N-D2/^{o}	106.3(9)

In the refinement (Table 4.2) the unit cell obtained is 10.219(2) Å which is larger than that obtained for the PXD refinement of 10.158(1) Å. In the PND experiment, the background required a larger number of terms as there was indication of a possible amorphous phase. This could be due to some air exposure during synthesis as a lecture bottle of ND_3 making it difficult to control the flow rate. A large phase of 6.4 wt. % ND_4Cl is seen however this could be explained by the synthesis and also issues encountered during the transfer of the vanadium can to the capillary used for the experiment in an Ar(g) filled glove box. During the transfer of the vanadium can to the capillary used for PND inside the glove bag, the sample was exposed for a short period of time so any oxygen and moisture present in the glove bag would have reacted with the sample. The vanadium can containing the sample may have also not been fully sealed from the atmosphere during the transfer process that could explain the presence of the ND_4Cl.

For the atomic parameters (Table 4.3) the PND data provides a good fit to that of the published disorder structure in the literature.[1] The position of the Nitrogen in the published structure is x= 0.021, y=0 and z=0.2161 while in the experimental data there has been displacement from the y and z position. The positions of the D1 and D2 atoms have also shifted from the literature (D1= x,y-0.0739, z= 0.2427, D2= y= 0.0690 and z= 0.2670). When the refinement of the D atoms are compared to the PXD data the disordered structure provides a better fit to the data as the D are more disordered and behave like the three-fold symmetry of gaseous ND_3. The ordered model only has a D atom with a partial occupancy of 0.75 which takes into account there is disorder but does not account for the full picture and this disorder is inconsistent with the behaviour of ND_3.

The bond distances obtained for the refinement show an increase in the Mg-N bond from 2.195(3) Å to 2.266(14) Å. In the PXD refinement, it is possible to view the Mg-Cl bond distances but is not possible in the PND refinement which would agree that the Mg is not bonded to the halide. The N-D1 bond distance of 1.112(6) Å and 0.818(10) (average is 0.965Å) is comparable to that obtained in the literature of 0.966(6) Å (where only one ND_3 unit distance was reported) and is comparable to the 1.02 Å distance for N-D1 in ND_3. The N-D2 values are also comparable to that in the published disorder structure of 1.06(1) Å and that of free ND_3. The bond angles of D1-N-D1 (108.3(10)^o) and D1-N-D2 (106.3(9)^o) are also in good agreement with those in the literature for the disordered structure and free gaseous ND_3. From PND measurements the proposed disordered structure is favoured. PND has allowed the rotations of the ND_3 to be seen and also allowed accurate refinement of the positions of the partially occupied deuterium atoms.

4.3.1.2 Room Temperature PND of $Mg(ND_3)_6Br_2$

Rietveld Refinement was performed on the RT (25 ^{o}C) scan of $Mg(NH_3)_6Br_2$ on the D2B diffractometer at the ILL. The disorder model proposed by Sørby *et al*. for $Mg(ND_3)_6Cl_2$ has been used in the refinement as the starting phase. The OCD plot can be seen in Figure 4.3. There are three phases presents, the hexammine, the diammine (the suggestion would be that some decomposition had occurred during preparation/transport) and ND_4Br. Crystallographic data for $Mg(ND_3)_6Br_2$ is presented in Table 4.45 although the data is not given for the diammine as this is discussed later (section 4.3.2) and atomic positions can be seen in Table 4.6 with bond distances/angles presented in Table 4.7.

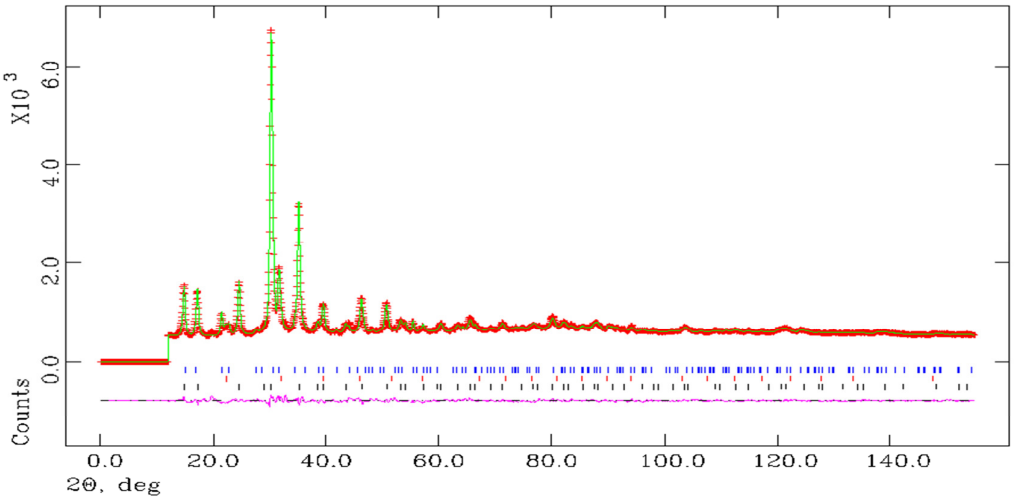

Figure 4.3: Observed, Calculated and difference (OCD) plot for the structural refinement of sample **2**. The blue tick marks indicate reflections the $Mg(ND_3)_6Br_2$ phase, the red tick marks indicate reflections from ND_4Br and the black tick marks indicate reflections from the $Mg(ND_3)_2Br_2$.

Table 4.5: Crystallographic data for PND for $Mg(ND_3)_6Br_2$

Phases:	$Mg(ND_3)_6Br_2$	ND_4Br	$Mg(ND_3)_2Br_2$
Phase Fraction(wt. %):	77.2(2)	5.2(3)	17.6(7)
Crystal System	Cubic	Cubic	Orthorhombic
Space Group	*Fm$\bar{3}$m*	*Pm$\bar{3}$m*	*Pbam*
a/Å	10.480(9)	4.066(2)	5.976(2)
b/ Å			11.951(3)
c/ Å			3.987(1)
Volume/Å^3	1151.15(3)	67.199(1)	284.731(1)
Z	4	1	2
Formula Weight/g	1217.628	101.967	448.442
Density (ρ_x/gcm^{-3})	1.756	2.520	2.615
No of observations	2859		
No of variables	61		
R_{wp}	0.0256		
R_p	0.0503		
χ^2	9.311		

Table 4.6: Atomic positions and temperature factors for $Mg(ND_3)_6Br_2$ at 25 °C.

Atom /Site	x	y	z	Occupancy	U_{iso} x 100/Å^2
Mg /4a	0	0	0	1	3.30(3)
Br /8c	0.25	0.25	0.25	1	2.57(2)
N/96j	0	0.0189(12)	0.2122(3)	0.25	3.65(2)
D1/96k	0.0697(4)	0.0697(4)	0.2371(5)	0.5	6.69(2)
D2/96j	0	0.0760(8)	0.2619(8)	0.25	7.0(5)

Table 4.7: Bond contacts and angles for $Mg(ND_3)_6Br_2$

Angle/° or Distance/Å	$Mg(ND_3)_2Br_2$
Mg-N	24x 2.333(6)
Br-D1	12x 2.676(5)
N-D1	2x 0.941(10), 2x 1.209(11)
N-D2	2x 0.972(8), 1x 1.122(12)
D1-N-D1/°	101.9(112)
D1-N-D2/°	111.9(6)

When the disordered structure is compared to the disordered structure of $Mg(ND_3)_6Cl_2$ it can be seen that the disordered structure is a good fit for the bromide (and appears to be a better fit). The bond distances for both N-D1 and N-D2 are both an improved fit to that of the N-H bond distance in NH_3 and the D1-N-D1 and D1-N-D2 angles are also a reasonable fit to that of 107.6 ° for free NH_3. The Mg-N bond distances are also comparable to those of the transition metal hexaammines.[8] In the atomic parameters, the positions of the nitrogen and the deuterium are closer to the published disorder structure of $Mg(ND_3)_6Br_2$.

As per its equivalent chloride (sample **1**) the disordered structure for the bromide is favoured over the previous ordered structure. Also, as per the PXD data these are also isostructural to each other. Whereas, in the PXD data the H1(D1) was located at different Wyckoff sites (96k and 96j respectively) in the PND model they are located at the same site which allows the demmoniation process to be studied in greater depth and improved.

4.3.1.3 Room temperature PND of $Mg(ND_3)_6I_2$

As per its chloride and bromide hexaammine equivalents, PND has been used to further understand the structure and the position of the deuterium (hydrogen) atoms in $Mg(ND_3)_6I_2$ (sample **3**). The model used for PND experiments is the disordered model used for the refinements of the PND data for $Mg(ND_3)_6Cl_2$ and $Mg(ND_3)_6Br_2$. This model provides the best fit to the PND data of $Mg(ND_3)_6I_2$ as with the ordered model having an R_{wp} value of 0.0455 compared to an R_{wp} value of 0.0360 for the disordered model for Bank 3 data using GEM.

The room temperature structure was further analysed using the high resolution D2B diffractometer at the ILL. The background for this refinement was fitted using background function 1, a shifted Chebyschev function. The OCD plot for sample **3** is presented in Figure 4.4. Two phases are present, with $Mg(ND_3)_6I_2$ being the dominant phase with weaker reflections also, attributable to a minor phase of $Mg(ND_3)_2I_2$ (as seen for the bromide in section 4.3.1.2).

Selected crystallographic data for sample **3** is presented in Table 4.8.

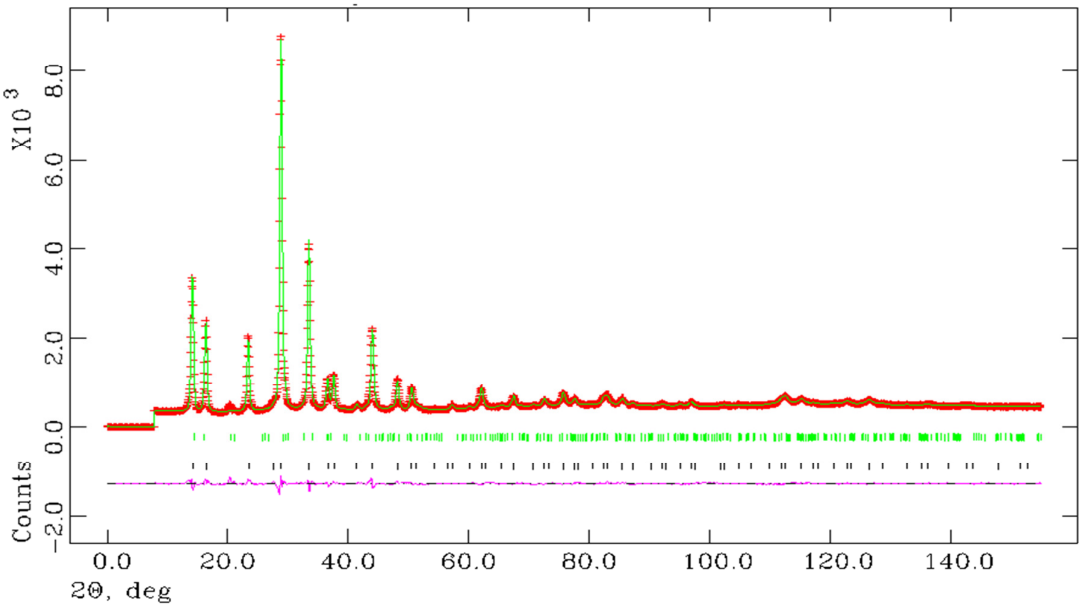

Figure 4.4: Observed, Calculated and difference (OCD) plot for the structural refinement of sample **3**. The green tick marks indicate reflections for the $Mg(ND_3)_6I_2$ phase and the black tick marks indicate reflections from the $Mg(ND_3)_2I_2$ phase.

Table 4.8: Crystallographic data for PXD for sample **3** at 25 °C

Phases	$Mg(ND_3)_6I_2$	$Mg(ND_3)_2I_2$
Phase fraction (wt. %):	86.4(7)	13.6(4)
Crystal System	Cubic	Orthorhombic
Space Group	*Fm$\bar{3}$m*	*Pbam*
a/Å	10.998(5)	6.278(6)
b/Å		12.649(14)
c/Å		4.327(3)
Volume/Å^3	1330.225(2)	343.617(1)
Z	4	2
Formula Weight/g	1593.628	612.254
Density, ρ_x/gcm^{-3}	1.989	2.964
No of observations	2859	
No of variables	46	
R_{wp}	0.0292	
R_p	0.0346	
χ^2	9.822	

The unit cell obtained for sample **3** is in good agreement with the unit cell for the PXD refinement data and also that of $Mn(NH_3)_6I_2$ which was isostructural in the PXD data.[9]

The atomic parameters for the dominant $Mg(ND_3)_6I_2$ phase are presented in Table 4.9 and the bond angles/distances presented in Table 4.10.

Table 4.9: Atomic positions and temperature factors for $Mg(ND_3)_6I_2$ at 25 °C.

Atom /Site	**x**	**y**	**z**	**Occupancy**	**U_{iso} X 100/Å^2**
Mg /4a	0	0	0	1	2.4(2)
I/8c	0.25	0.25	0.25	1	6.0(2)
N/96j	0	0.004(13)	0.2039(22)	0.25	4.2(1)
D1/96k	0.0625(24)	0.0625(24)	0.2330(4)	0.5	5.7(1)
D2/96j	0	0.0672(27)	0.2386(13)	0.25	6.1(3)

Table 4.10: Bond distances of sample **3**

Distance/Å	Sample 3
Mg-N	24x 2.239(2)
N-D1	2x 1.00(3), 2x 1.05(3)
N-D2	1x 0.95(4) 2x 0.990(7), 1x 1.03(4)
D1-N-D1/ °	107.0(17)
D1-N-D2/ °	115.6(15)

The N-D1 bond distance for the selected ND_3 unit compared to the literature is 0.932(10) Å and the N-D2 bond distance is 1.08(3) Å which is in good agreement with the literature values for free ND_3 and $Mg(ND_3)_6Cl_2$. The Mg-N is also smaller in the iodide which was seen in the PXD data where the chloride had the longest M-N bond length. The bond lengths for N-D are comparable to previous values reported as per the Cl and Br adducts. The bond angles for a selected ND_3 unit reported are in fair agreement with the literature value of 107.8° for the gas phase of ND_3. From the PND data, it can be determined that the disordered model is also favourable for $Mg(ND_3)_6I_2$ and that the ND_3 behaviour in all three ammines is the same.

4.4 In-Situ PND Studies of the Ammines

4.4.1 In-Situ Deammoniation of $Mg(ND_3)_6Cl_2$

The structural changes involved when $Mg(ND_3)_6Cl_2$ (sample **4**) was heated can be observed in Figure 4.5. The cubic phase is dominant at 120 °C and at 160 °C the peaks at 5.1 Å and 5.7 Å have decreased in intensity along with the most intense peak from the cubic phase at 2.9 Å which has decreased in relative intensity. It can be seen that the diffraction pattern between 210 °C and 280 °C appears essentially the same. At 400 °C, a new phase ($MgCl_2$) is formed.

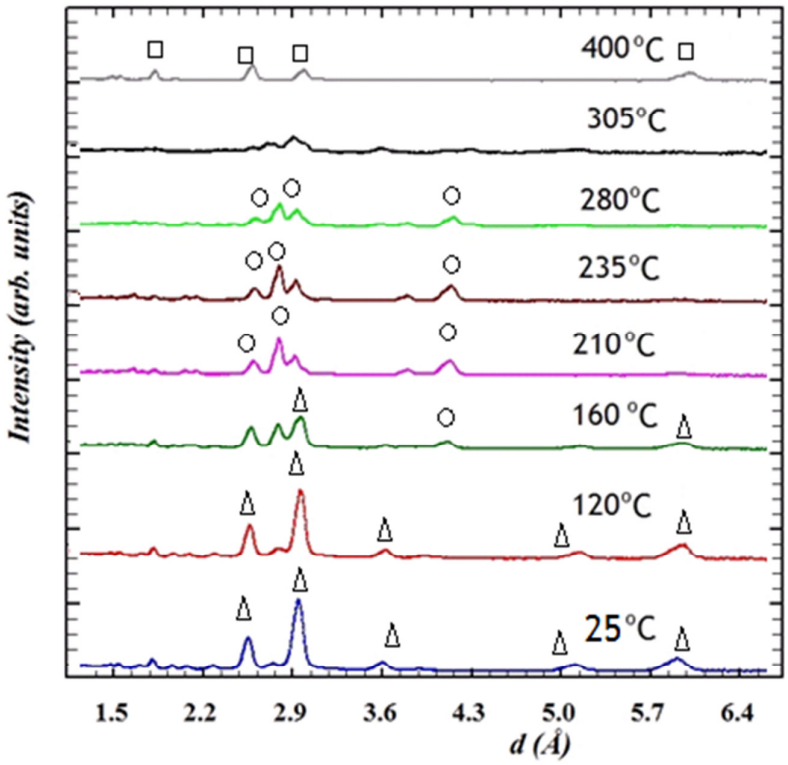

Figure 4.5: Bank 3 data for the deammoniation of $Mg(ND_3)_6Cl_2$. The triangles indicate reflections for $Mg(ND_3)_6Cl_2$, the circles indicate reflections from $Mg(ND_3)_6Cl_2$ and the squares indicate reflections from $MgCl_2$

The 25 °C measurement is discussed in section 4.3.1.1. At 120 °C the cubic hexammine phase remains, while by this temperature the orthorhombic $Mg(ND_3)_2Cl_2$ phase (*Cmmm*)[10] has appeared. The phrase fraction of this diammine phase present at 120 °C is 12.1 wt. % from the refinement for the bank 3 and bank 4 data. This finding corresponds to the TPD measurements (chapter 3) which indicate that at this temperature both $Mg(ND_3)_6Cl_2$ and $Mg(ND_3)_2Cl_2$ are likely to be present. Selected crystallographic data for sample **4** at this temperature point can be seen in Figure 4.6 and Table 4.11.

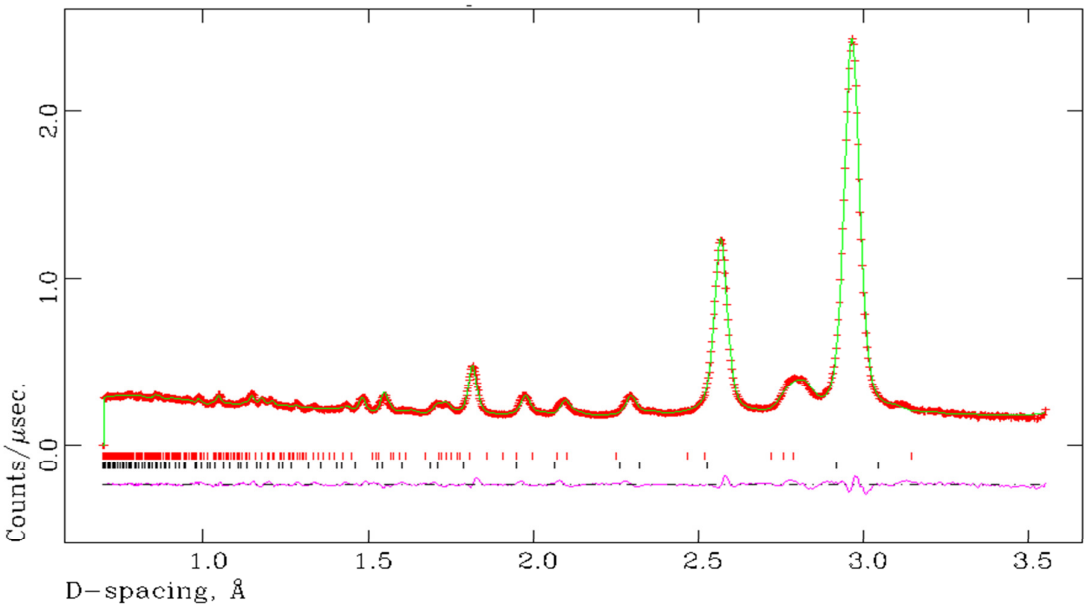

Figure 4.6: Observed, Calculated and Difference (OCD) plot of the bank 4 data at 120 °C. The black tick marks are reflections from $Mg(ND_3)_6Cl_2$ and the red tick marks are the reflections from $Mg(ND_3)_2Cl_2$. The observed data is the red crosses, the calculated data is the green lines and the difference line is the lower lane.

Table 4.11: Crystallographic data for PND for $Mg(ND_3)_6Cl_2$ and $Mg(ND_3)_2Cl_2$ at 120 °C

Phases	$Mg(ND_3)_6Cl_2$	$Mg(ND_3)_2Cl_2$
Phase Fraction (wt%)	88.2(5)	11.8(7)
Crystal System	Cubic	Orthorhombic
Space Group	*Fm$\bar{3}$m*	*Cmmm*
a/Å	10.252(1)	7.880(6)
b/Å		8.098(4)
c/Å		3.879(3)
Volume/Å^3	1077.738(4)	247.537(2)
Z	4	2
Formula Weight/g	862.020	270.618
Density (ρ_x/gcm^{-3})	1.328	1.815
No of observations	3288	
No of variables	62	
R_{wp}	0.1226	
R_p	0.1778	
χ^2	4.946	

As can be seen in Table 4.11 the lattice parameters for $Mg(ND_3)_6Cl_2$ has expanded from 10.223 Å for the room temperature scan to 10.252(1) Å at 125 °C. This lattice parameter would be expected due to thermal expansion. The lattice parameters for the $Mg(ND_3)_2Cl_2$ are smaller than those in the literature which are a= 8.128(6) Å, b= 8.2007(6) Å and c= 3.7543(2) Å.[10] The PND data shows no new phase between $Mg(ND_3)_6Cl_2$ and $Mg(ND_3)_2Cl_2$ (for example $Mg(ND_3)_4Cl_2$) which is consistent with the TPD data and also previous studies.[2]

At an increase of temperature (160 °C), the weighted fraction of the diammine phase has increased to 35.5(1) wt. % which is nearly a factor of 3 compared to 120 °C more of the $Mg(ND_3)_6Cl_2$ is decomposing to its diammine with the release of 4 ND_3. The OCD plot for the refinement is presented in Figure 4.7 with selected crystallographic data presented in Table 4.12.

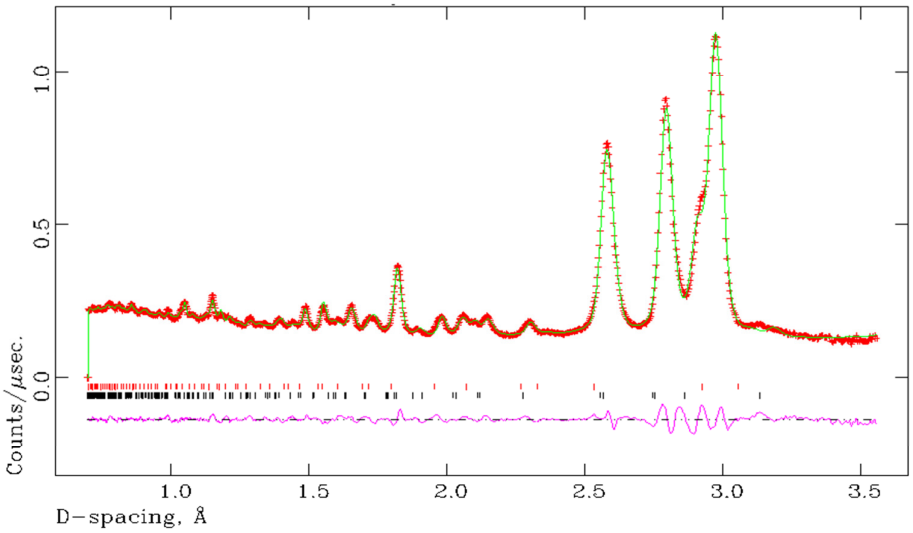

Figure 4.7: Observed, Calculated and Difference (OCD) plot of the bank 4 data at 160 °C. The black tick marks are reflections from $Mg(ND_3)_6Cl_2$ and the red tick marks are the reflections from $Mg(ND_3)_2Cl_2$. The observed data is the red crosses, the calculated data is the green lines and the difference line is the lower lane.

Table 4.12: Crystallographic data for PXD for $Mg(ND_3)_6Cl_2$ and $Mg(ND_3)_2Cl_2$ at 160 ^oC

Phases	$Mg(ND_3)_6Cl_2$	$Mg(ND_3)_2Cl_2$
Phase Fraction (wt. %)	64.9(2)	35.3(1)
Crystal System	Cubic	Orthorhombic
Space Group	$Fm\bar{3}m$	*Cmmm*
a/Å	10.282(2)	8.229(3)
b/Å		8.188(2)
c/Å		3.800(8)
Volume/Å^3	1087.00(5)	256.053(1)
Z	4	2
Formula Weight/g	862.020	270.618
Density (ρ_x/gcm^{-3})	1.316	1.754
No of observations	3403	
No of variables	76	
R_{wp}	0.0673	
R_p	0.1053	
χ^2	5.161	

As can be seen in Table 4.12, the unit cell of the hexaammine has expanded from the 120 ^oC measurement (more ND_3 release) which is also seen for the other hexaammines. The lattice parameters of the diammine are now closer to that of the literature values.

At 210 ^oC, there is no $Mg(ND_3)_6Cl_2$ present, meaning that the first step of the deammoniation is complete. In the PND data, only orthorhombic $Mg(ND_3)Cl_2$ is present although there a new phase which might be tentatively identified as the monoammine begins to appear in the diffraction pattern. This matches the TG-DTA-MS data from chapter 4 where the monoammine is forming between 158-230 ^oC . The OCD plot for the bank 3 data is presented in Figure 4.8. It has been attempted to determine the structure of this at higher temperatures. It has previously been suggested that $Mg(NH_3)Cl_2$ may be isostructural with $Ni(NH_3)Cl_2$ (monoclinic, *C2/m*).[11] This structure has also been used for DFT calculations for $Mg(NH_3)Cl_2$ with lattice parameters of *a*= 19.26 Å, *b*= 3.62 Å and *c*= 6.59 Å

although was not observed experimentally.[2] When the coordinates were refined this resulted in an unstable refinement and when the phase fractions were refined resulted in an unstable refinement. Other possible phases were attempted in the refinement including ND_4Cl and $Mg(ND_2)_2$ with no success. Due to small number of peaks present along with their poor intensity (and possible overlap with the diammine phase at higher temperatures) indexing was not possible to achieve a successful result. To obtain the structure, the monoammine will need to be present as the major phase which may be possible by synthesising the phase directly in an autoclave reaction as per the experimental procedure for $Ni(NH_3)Cl_2$. [11] For the refinement, these unknown peaks have been excluded. Selected crystallographic data from the Bank 3 refinement of $Mg(ND_3)_2Cl_2$ are presented in Tables 4.13-4.15.

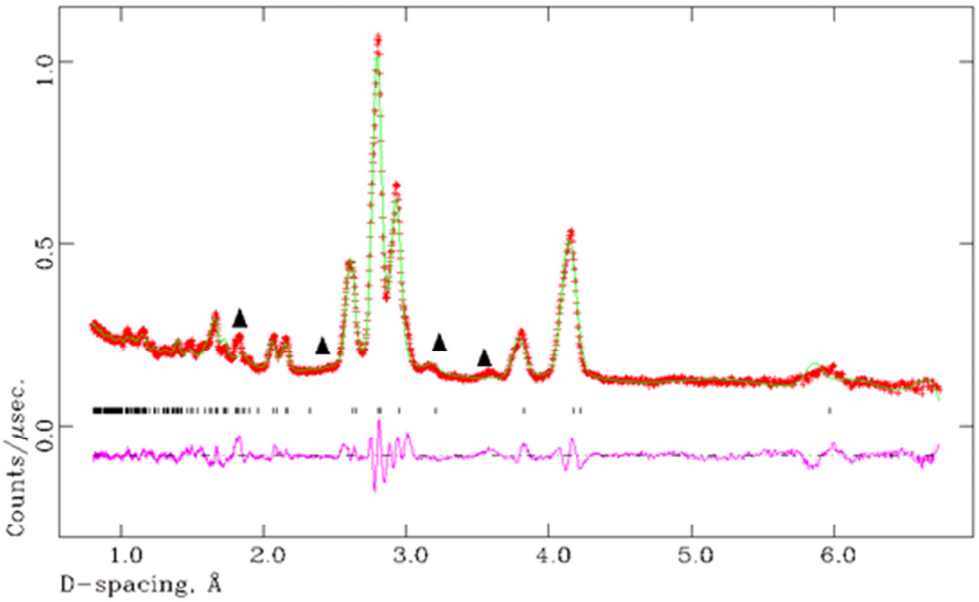

Figure 4.8: Observed, Calculated and Difference (OCD) plot of the bank 3 data at 210 °C showing the presence of a new phase. The black tick marks are the reflections from $Mg(ND_3)_2Cl_2$ and the triangles indicate reflections that might be from $Mg(ND_3)Cl_2$ .The observed data is the red crosses, the calculated data is the green lines and the difference line is the lower lane.

Table 4.13: Crystallographic data for PND for $Mg(ND_3)_2Cl_2$ at 210 ^oC

Phases	$Mg(ND_3)_2Cl_2$
Temperature	210 ^oC
Crystal System	Orthorhombic
Space Group	*Cmmm*
a/Å	8.277(5)
b/Å	8.188(4)
c/Å	3.784(2)
Volume/Å^3	256.452(3)
Z	2
Formula Weight/g	270.618
Density, ρ_x/gcm^{-3}	1.752
No of observations	1929
No of variables	28
R_{wp}	0.0653
R_p	0.1168
χ^2	8.483

Table 4.14: Atomic positions and temperature factors for $Mg(ND_3)_2Cl_2$ at 210 ^oC.

Atom /Site	**x**	**y**	**z**	**Occupancy**	**U_{iso} x 100/Å^2**
Mg /2a	0	0	0	1	2.5
Cl /4h	0.2176(10)	0	0.5	1	2.5
N/4i	0	0.269(13)	0	1	2.5
D1/16r	0.0980(11)	0.307(8)	0.188(13)	0.75	2.5

Table 4.15: Bond distances and angles for $Mg(ND_3)_2Cl_2$ at 210 °C.

	Distance/Å	Angles/ °
Mg-N	2x 2.198(11)	
Mg-Cl	4x 2.612(8)	
N-D1	4x 1.123(11)	
Cl-D1	4x 2.496(10)	
Mg-X-Mg		2x 92.8(3), 2x87.2(3), 180,90

The lattice parameters are slightly larger than those in the literature due to thermal expansion with elongation of the N-D bond also (0.9615 Å).[10]

At 235 °C, the prominent phase in the diffraction patterns is still the orthorhombic diammine, with the reflections from the new phase excluded as can be seen in Figure 4.9. Selected crystallographic data for this temperature point is presented in Table 4.16 for the Bank 3 PND data in which further thermal expansion in the lattice parameters can be seen.

Table 4.16: Crystallographic data for PND for $Mg(ND_3)_2Cl_2$ at 235 °C

Phases	$Mg(ND_3)_2Cl_2$
Temperature	235 °C
Crystal System	Orthorhombic
Space Group	*Cmmm*
a/Å	8.312(5)
b/Å	8.235(3)
c/Å	3.783(2)
Volume/Å^3	259.15(3)
Z	2
Formula Weight/g	270.618
Density, p_x/gcm^{-3}	1.756
No of observations	1768
No of variables	31
R_{wp}	0.0631
R_p	0.2256
χ^2	6.997

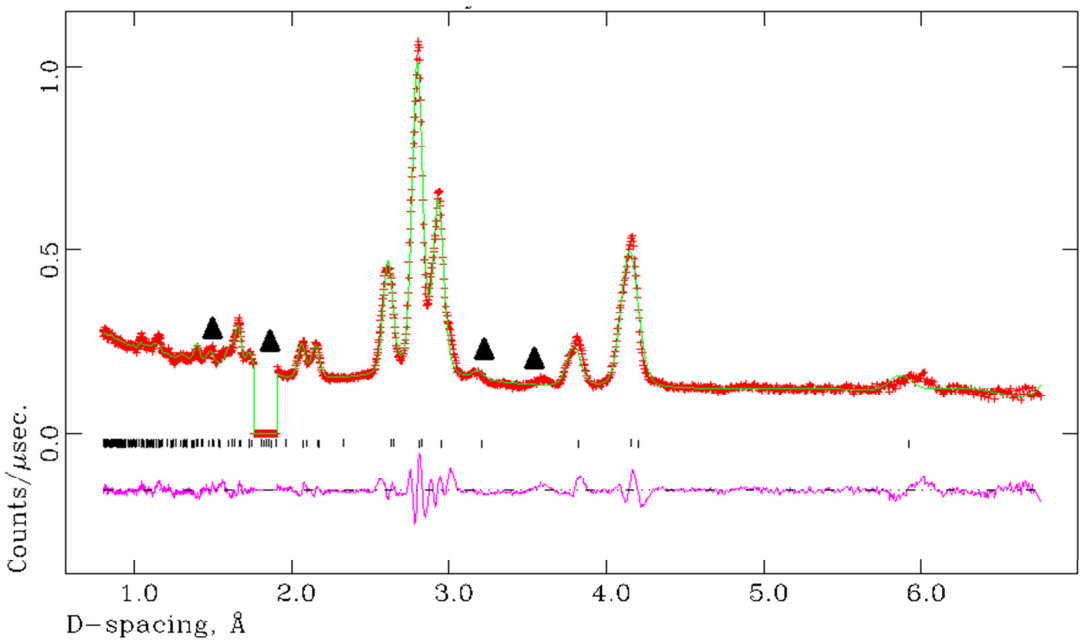

Figure 4.9: Observed, Calculated and Difference (OCD) plot of the bank 3 data at 235 °C showing the presence of the new phase. The black tick marks are the reflections from $Mg(ND_3)_2Cl_2$ and the triangles indicate reflections that might be from $Mg(ND_3)Cl_2$ .The observed data is the red crosses, the calculated data is the green lines and the difference line is the lower lane.

At the next temperature point of 280 °C (Figure 4.9), $MgCl_2$ is present indicating deammoniation to the chloride is starting as per the TPD data The reflections assigned to the possible monoammine are clearer at this point but are few and weak in intensity (see 210 °C results). Selected crystallographic data is presented in Table 4.17, with atomic parameters presented in Table 4.18.

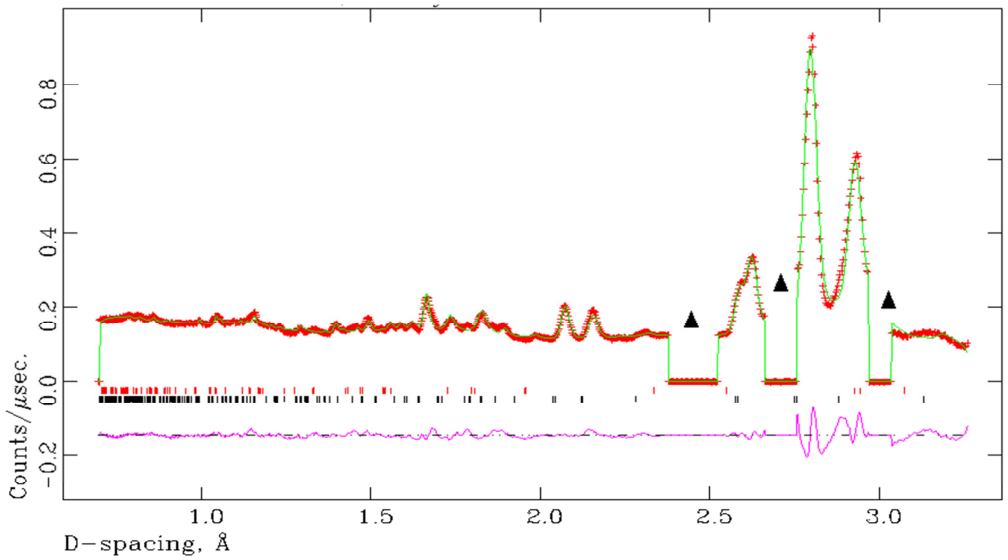

Figure 4.10: Observed, Calculated and Difference (OCD) plot of the bank 4 data at 280 °C. The black tick marks are the reflections from $Mg(ND_3)_2Cl_2$, the red tick marks indicate reflections from $MgCl_2$ and the triangles indicate excluded reflections. The observed data is the red crosses, the calculated data is the green lines and the difference line is the lower lane.

Table 4.17: Crystallographic data for PND (bank 4) for $Mg(ND_3)_2Cl_2$ and $MgCl_2$ at 280 °C

Phases	$Mg(ND_3)_2Cl_2$	$MgCl_2$
Phase Fraction (wt. %)	69.5(3)	30.5(2)
Crystal System	Orthorhombic	Trigonal
Space Group	*Cmmm*	$R\bar{3}m$
a/Å	8.244(5)	3.662(2)
b/Å	8.284(3)	
c/Å	3.784(2)	17.770(13)
Volume/Å^3	258.382(3)	206.338(2)
Z	2	
Formula Weight/g	270.618	285.663
Density, ρ_x/gcm^{-3}	1.739	2.299
No of observations	1271	
No of variables	34	
R_{wp}	0.0631	
R_p	0.4644	
χ^2	7.862	

Table 4.18: Atomic positions and temperature factors for $Mg(ND_3)_2Cl_2$ at 280 ^oC.

Atom /Site	x	y	z	Occupancy	U_{iso} x 100/Å^2
Mg /2a	0	0	0	1	2.5
Cl /4h	0.2141(20)	0	0.5	1	3.5(6)
N/4gi	0	0.2641(3)	0	1	5.7(7)
D1/16r	0.0635(18)	0.2963(15)	0.145(3)	0.75	5.7(7)

At 280 ^oC it can be seen the position of the N and D atoms in the 4g and 16r Wyckoff sites have changed respectively. The N position on the y axis has changed from 0.2176(10) and for D on the x axis has moved from 0.0908(11). The N-D1 bond length at 280 ^oC is 0.804(16) Å which is in respectable agreement with the value published in the literature.

At 305 ^oC, a mixture of the $Mg(ND_3)_2Cl_2$ phase and $MgCl_2$ phase is present, with the weighted phase fraction of $MgCl_2$ increasing to 50 wt. %. At 305 ^oC, the diffraction pattern showed indications of an amorphous phase possible being present which is seen for $Mg(ND_3)_6I_2$ (section 4.43).

At 400 ^oC full deammoniation has taken place to $MgCl_2$ (Figure 4.11). Selected crystallographic data is presented in Table 4.19.

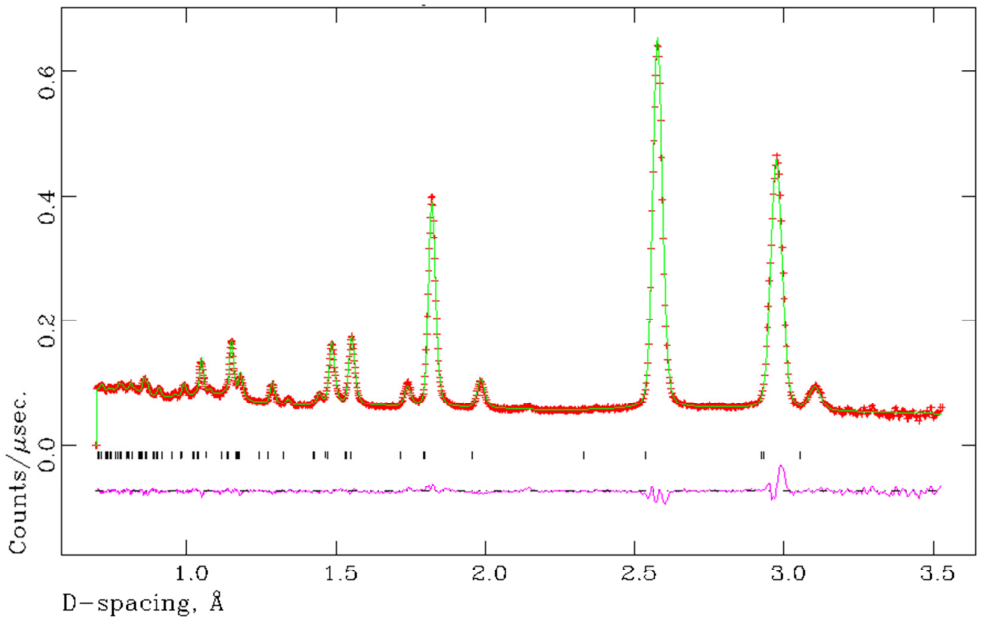

Figure 4.11: Observed, Calculated and Difference (OCD) plot of the Bank 4 data at 400 °C. The black tick marks are the reflections from $MgCl_2$. The observed data is the red crosses, the calculated data is the green lines and the difference line is the lower line.

Table 4.19: Crystallographic data for PND for $MgCl_2$ at 400 °C

Phases	$MgCl_2$
Temperature	400 °C
Crystal System	Trigonal
Space Group	$R\bar{3}m$
a/Å	3.633(3)
c/Å	3.781(1)
Volume/Å^3	17.856(4)
Z	2
Formula Weight/g	285.663
Density, ρ_x/gcm^{-3}	2.324
No of observations	1950
No of variables	33
R_{wp}	0.0663
R_p	0.2107
X^2	2.515

4.4.2 In-Situ Deammoniation of $Mg(ND_3)_6Br_2$

Sample **5** was heated and data collected at temperature points determined previously by TPD measurements (section 3.4). The temperature points selected were room temperature (25 ^oC), 175 ^oC, 210 ^oC, 265 ^oC, 295 ^oC, 320 ^oC, 340 ^oC and 500 ^oC. A measurement point at 235 ^oC was set but due to experimental error the data was not been used as the sample was heated to 265 ^oC beforehand. Data were collected at each temperature for one hour and Rietveld Refinements were then performed.

4.4.2.1 In Situ Results of the Deammoniation of $Mg(ND_3)_6Br_2$

At room temperature, cubic $Mg(ND_3)_6Br_2$ was the only phase present in the GEM in-situ data. For the D2B ex-situ data a unit cell parameter of a=10.480(9) Å was obtained (see section 4.3.1.2)

The structural changes involved when $Mg(ND_3)_6Br_2$ was heated can be observed in Figure 4.12. The cubic phase is dominant at 175 ^oC with reflections from a new phase appearing at 4.3 Å and the diffraction patterns between 210 ^oC and 295 ^oC are very similar and different from the starting phase. This data indicate the formation of the diammine phase.

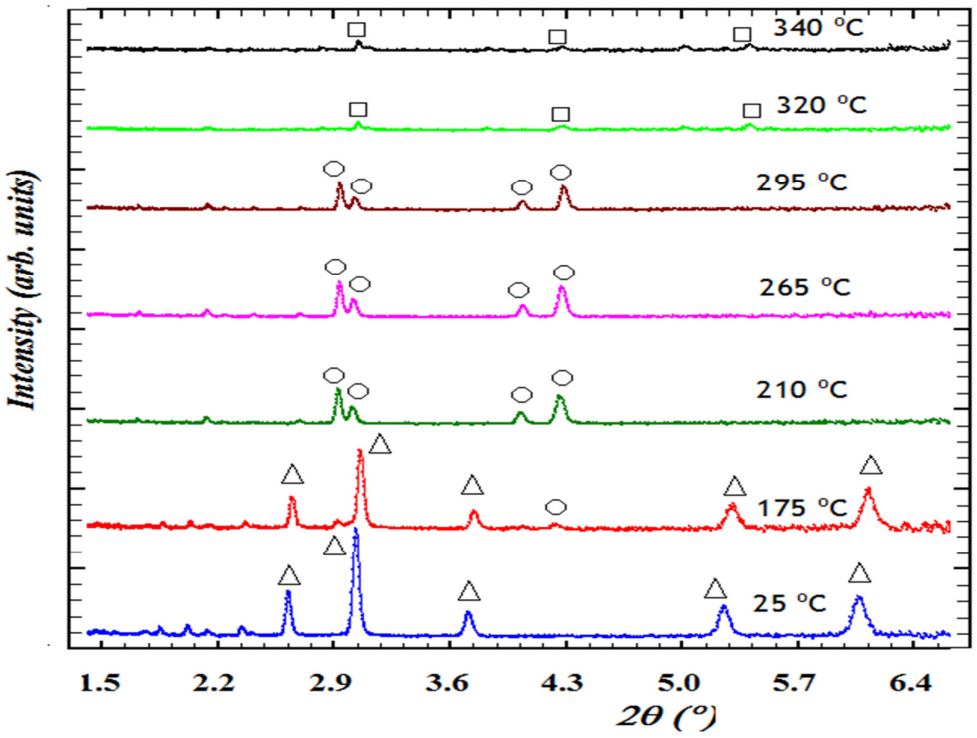

Figure 4.12 Bank 3 data for the deammoniation of $Mg(ND_3)_6Br_2$ with increasing temperature. The triangles indicate reflections from $Mg(ND_3)_6Br_2$, the circles indicate reflections from $Mg(ND_3)_2Br_2$ and the circles indicate reflections from $MgBr_2$

As can be seen in Figure 4.13, at 175 °C which is an intermediate temperature for the deammoniation of $Mg(ND_3)_6Br_2$ to $Mg(ND_3)_6Br_2$, the cubic hexammine phase is present with a lattice parameter of a= 10.564(1) Å.[10] However, at this temperature point the orthorhombic diammine is also present with a weighted fraction of 16.3(4) wt. %. The lattice parameters for the diammine are a= 5.965(1) Å, b= 11.999(4) Å and c= 4.025(1) Å which are larger the values obtained by *Leineweber et al.* of a= 5.971(2) Å, b= 11.918(3) Å and c= 3.985(8) Å. The differences in the parameters can be explained by thermal expansion since Leineweber *et al.* determined the structure of $Mg(ND_3)_2Br_2$ at room temperature. Selected crystallographic data is presented in Table 4.20.

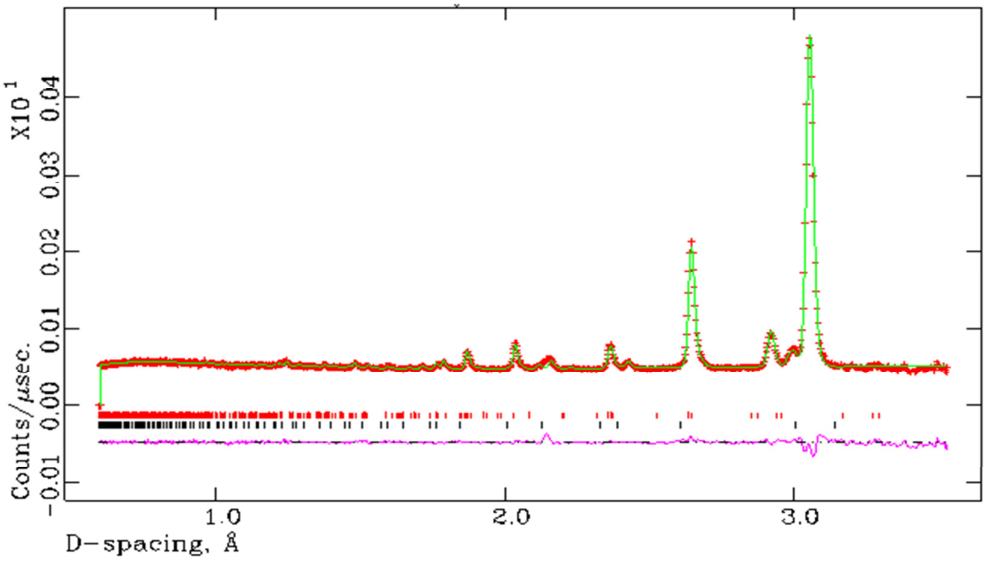

Figure 4.13: Observed, Calculated and Difference (OCD) plot of the bank 4 data at 175 °C showing the small fraction of $Mg(ND_3)_2Br_2$ (red tick marks) along with the dominant $Mg(ND_3)_6Br_2$ phase (black tick marks).

Table 4.20: Crystallographic data for PXD for $Mg(ND_3)_6Br_2$ and $Mg(ND_3)_2Br_2$ at 175 °C

Phases	$Mg(ND_3)_6Br_2$	$Mg(ND_3)_2Br_2$
Phase Fraction (wt. %)	83.7(2)	16.3(5)
Temperature:	175 °C	
Crystal System	Cubic	Orthorhombic
Space Group	*Fm$\bar{3}$m*	*Pbam*
a/Å	10.564(1)	5.965(2)
b/Å		11.999(4)
c/Å		3.985(8)
Volume/Å^3	1178.979(3)	288.082(1)
Z	4	2
Formula Weight/g	1217.628	448.442
Density (ρ_x/gcm^{-3})	1.715	2.585
No of observations	3543	
No of variables	52	
R_{wp}	0.0673	
R_p	0.2734	
χ^2	1.136	

At 210 °C, $Mg(ND_3)_6Br_2$ has fully deammoniated to $Mg(ND_3)_2Br_2$ in agreement with the TPD measurements. The OCD plot for data at this temperature is presented in Figure 4.14. Atomic parameters are presented in Table 4.21, crystallographic data is presented in Table 4.22 and bond distances and angles presented in Table 4.23.

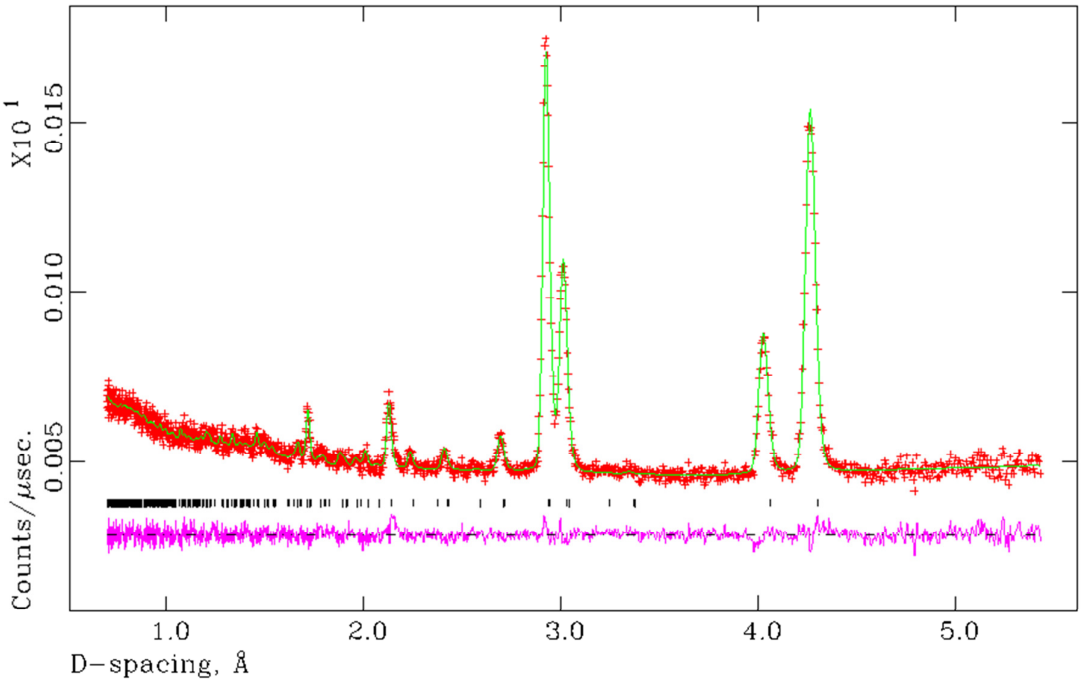

Figure 4.14: Observed, Calculated and Difference (OCD) plot of the bank 3 data at 210 °C. The black tick marks indicate reflections from $Mg(ND_3)_2Br_2$. The observed data is the red crosses, the calculated data is the green lines and the difference line is the lower line.

Table 4.21: Atomic positions and temperature factors for $Mg(ND_3)_2Br_2$ at 210 °C.

Atom /Site	x	y	z	Occupancy	U_{iso} x 100/Å^2
Mg /2a	0	0	0	1	2.5
Br /4h	0.2620(2)	0.3834(1)	0.5	1	2.5
N/4g	0.1935(2)	0.1498(1)	0	1	2.5
D1/8i	0.3246(2)	0.0974(1)	0.0972(3)	0.75	2.5
D2/8i	0.2729(3)	0.1696(1)	0.1797(2)	0.75	2.5

Table 4.22: Crystallographic data for PND for $Mg(ND_3)_2Br_2$ at 210 ^oC

Phases	$Mg(ND_3)_2Br_2$
Temperature	210 ^oC
Crystal System	Orthorhombic
Space Group	*Pbam*
a/Å	6.010(10)
b/Å	12.068(19)
c/Å	4.020(6)
Volume/Å^3	291.65(8)
Z	2
Formula Weight/g	448.422
Density, ρ_x/gcm^{-3}	2.554
No of observations	3220
No of variables	46
R_{wp}	0.0571
R_p	0.7006
χ^2	1.096

Table 4.23: Bond distances and angles for $Mg(ND_3)_2Br_2$ at 210 ^oC.

Distance/Å or Angles/Å	**$Mg(ND_3)_2Br_2$**
Mg-Br	4x 2.841(9) Å
Mg-N	2x 2.150(13) Å
N-D1	2x 1.084(10) Å
N-D2	2x 0.898(13) Å
D1-D2	0.983(17), 1.447(16) Å
Mg-Br-Mg	92.4(3)^o Å

The bond distances of the N-D1 and N-D2 are in good agreement with known N-D bonds and the Mg-Br-Mg bond angle is similar to the literature[10] Thermal expansion of the lattice parameters have also occurred which is expected.

At 265 °C, as apparent from the pattern presented in Figure 4.15, the only phase present is the orthorhombic $Mg(ND_3)_2Br_2$ phase. This is unexpected, as at this point it was expected from TG-DTA-MS that the monoammine phase would be presented. Atomic parameters are presented in Table 4.24, selected crystallographic data is presented in Table 4.25 with bond distances reported in Table 4.26.

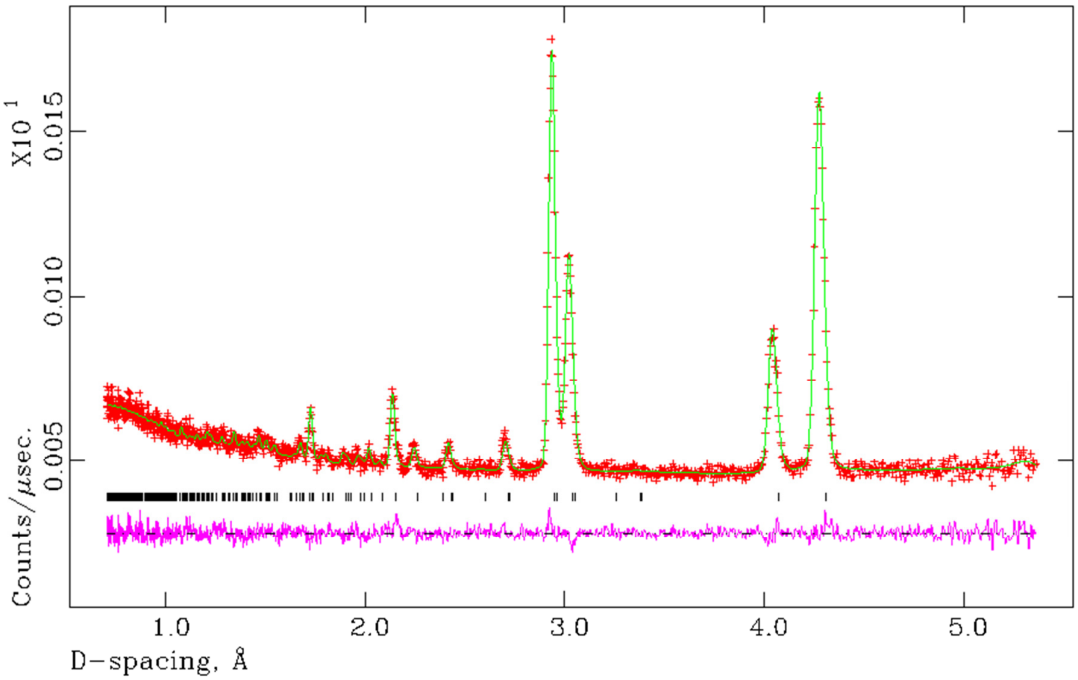

Figure 4.15: Observed, Calculated and Difference (OCD) plot of the bank 3 data at 265 °C. The black tick marks indicate reflections from $Mg(ND_3)_2Br_2$.

Table 4.24: Atomic positions and temperature factors for $Mg(ND_3)_2Br_2$ at 265 °C.

Atom /Site	x	y	z	Occupancy	U_{iso} x 100/Å^2
Mg /2a	0	0	0	1	2.5
Br /4h	0.2640(2)	0.3814(1)	0.5	1	2.5
N/4g	0.2007(2)	0.1589(2)	0	1	2.5
D1/8i	0.3244(2)	0.0964(1)	0.0928(3)	0.75	2.5
D2/8i	0.2691(3)	0.157(11)	0.1768(2)	0.75	2.5

Table 4.25: Crystallographic data for PND for $Mg(ND_3)_2Br_2$ at 265 ^oC

Phases	$Mg(ND_3)_2Br_2$
Temperature	265 ^oC
Crystal System	Orthorhombic
Space Group	*Pbam*
a/Å	6.021(8)
b/Å	12.095(18)
c/Å	4.020(5)
Volume/Å^3	293.720(1)
Z	2
Formula Weight/g	448.422
Density, ρ_x/gcm^{-3}	2.554
No of observations	3258
No of variables	49
R_{wp}	0.0540
R_p	0.7814
χ^2	1.016

Table 4.26: Bond distances and angles for $Mg(ND_3)_2Br_2$ at 265 ^oC.

Distance/Å or Angles/Å	**$Mg(ND_3)_2Br_2$**
Mg-Br	4x 2.853(3) Å
Mg-N	2x 2.269(13) Å
N-D1	2x 0.966(19) Å
N-D2	2x 0.823(12) Å
D1-D2	0.875(18), 1.354(17) Å
Mg-Br-Mg	89.9(3)^o Å

When the refined cell parameters are compared with those at 210 ^{o}C, there has been an increase in the cell parameters and the cell volume which would be expected as a result of thermal expansion with an increase in data collection temperature.

At 295 ^{o}C, the phase present is still the orthorhombic $Mg(ND_3)_2Br_2$ phase (Figure 4.16). Selected crystallographic data is presented in Table 4.27.

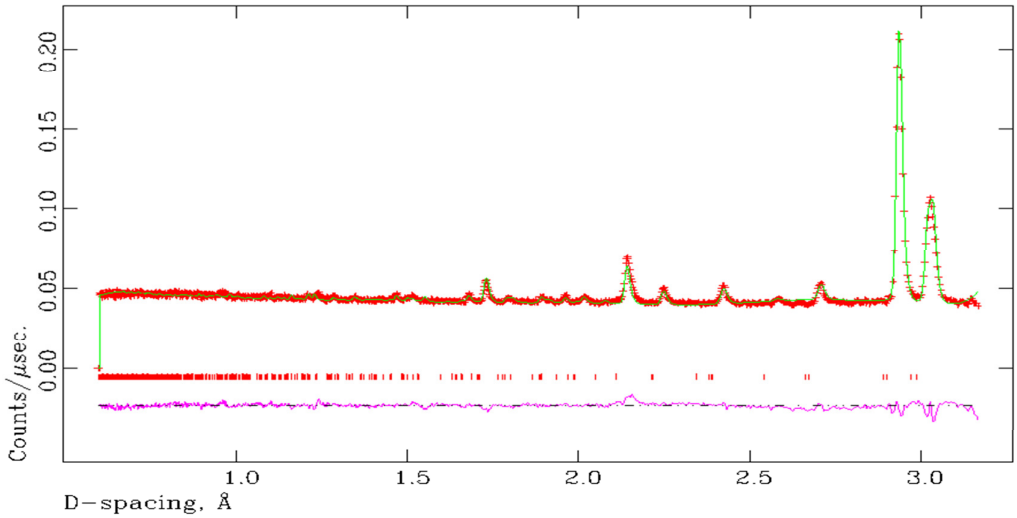

Figure 4.16: Observed, Calculated and Difference (OCD) plot of the Bank 4 data at 295 ^{o}C. The black tick marks indicate reflections from $Mg(ND_3)_2Br_2$. The observed data is the red crosses, the calculated data is the green lines and the difference line is the lower line.

Table 4.27: Crystallographic data for PXD for $Mg(ND_3)_2Br_2$ at 295 ^oC

Phases	$Mg(ND_3)_2Br_2$
Temperature:	295 ^oC
Crystal System	Orthorhombic
Space Group	*Pbam*
a/Å	6.065(2)
b/Å	12.066(1)
c/Å	4.029(1)
Volume/Å^3	294.840(1)
Z	2
Formula Weight/g	448.442
Density, ρ_x/gcm^{-3}	2.525
No of observations	3108
No of variables	41
R_{wp}	0.0580
R_p	0.863
χ^2	1.200

At 320 ^oC onwards $MgBr_2$ (trigonal, *P3m1*)[12] is present although due to the small sample volume (at 320 ^oC $Mg(ND_3)_2Br_2$ is present) satisfactory fits were not obtained. From the PND data it can be concluded that full deammoniation of the hexaammine has occurred.

4.4.3 In-Situ Deammoniation of $Mg(ND_3)_6I_2$

Scans were performed on the deammoniation of $Mg(ND_3)_6I_2$ (sample **6**) at 25 ^oC, 120 ^oC, 160 ^oC, 210 ^oC, 235 ^oC, 285 ^oC, 325 ^oC, 350 ^oC, 380 ^oC, 450 ^oC and 500 ^oC. The aim of selecting these temperatures was to study the structural changes during the three step deammoniation process to MgI_2. Data were collected at each of the temperature points for one hour and Rietveld Refinement performed with the obtained data. PND refinement has also been performed at room temperature (298 K) at the ILL (section 4.3.1.3). The disordered model proposed for $Mg(ND_3)_6Cl_2$ (section 4.1) has been used as a basis for the refinement of $Mg(ND_3)_6I_2$.

4.3.1.1 In- Situ Results $Mg(ND_3)_6I_2$

The structural changes observed during the in situ deammoniation can be seen in Figure 4.15. After 285 °C the lack of Bragg reflections in the pattern over this temperature range suggested that the sample had become amorphous. It was observed after the experiment that the obtained sample had melted inside the vanadium can (in the equivalent TPD measurements the sample solidified after heating). As can be seen in Figure 4.17, the dominant phase present up to 235 °C is $Mg(ND_3)_6I_2$. No evidence for the monoammine, $Mg(ND_3)_2I_2$ was seen which corresponds with the TPD data where no monoammine structure could be isolated.

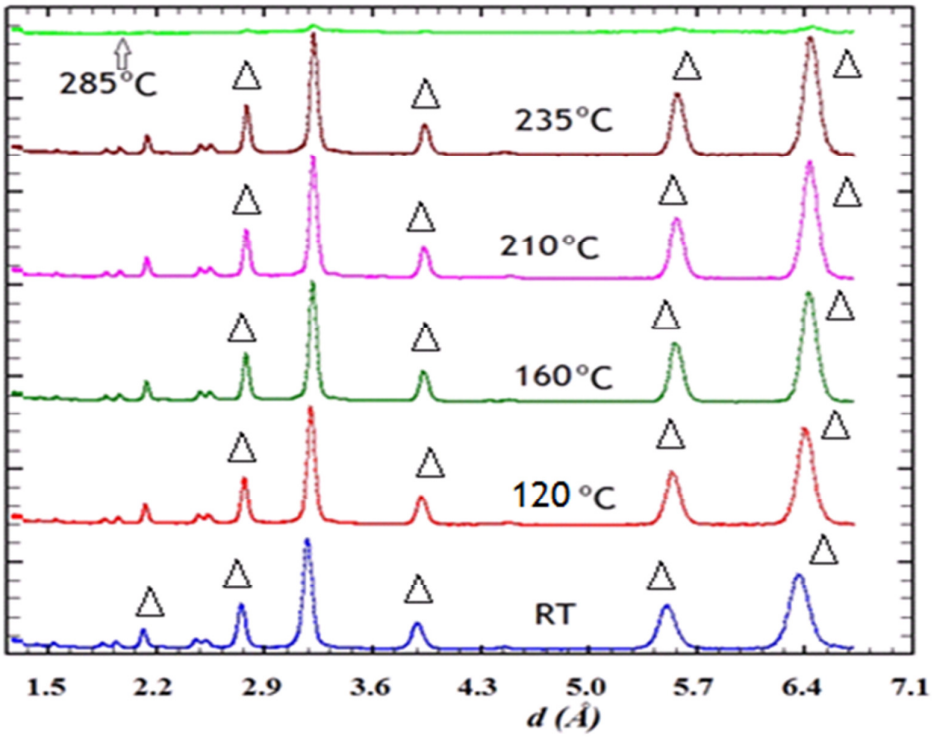

Figure 4.17: In situ Bank 3 PND data for the deammoniation of $Mg(ND_3)_6I_2$ (sample **6**) at variable temperature. The triangles indicate reflections from the hexaammine phase

The weighted fraction present at room temperature for the GEM measurements was 92.2 % for $Mg(ND_3)_6I_2$ and 7.8 % for the $Mg(ND_3)_2I_2$ phase. More structural information for the room temperature measurement of $Mg(ND_3)_6I_2$ can be seen in section 4.3.1.1

At 135 °C (Figure 4.18), both the hexaammine and orthorhombic diammine phase (*Pbam*) phase are present. The weighted fraction (6.6(3) %) of the diammine phase is similar to the room temperature. This would be expected as from the TG-DTA-MS deammoniation to the diammine commences at 81 °C and is complete at 230 °C.

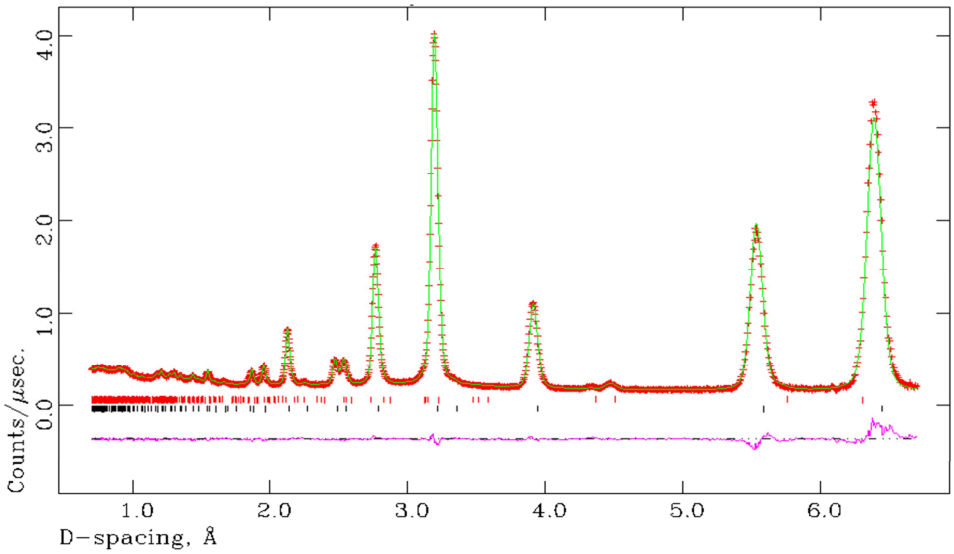

Figure 4.18: Observed, Calculated and Difference (OCD) plot of the Bank 3 data at 135 °C. The red tick marks indicate reflections from $Mg(ND_3)_6I_2$ and black tick marks indicate reflections from $Mg(ND_3)_2Cl_2$. The observed data is the red crosses, the calculated data is the green lines and the difference line is the lower line.

The unit cell of the hexammine at this temperature point has increased from 10.97(5) Å at 25 °C to 11.043(4) Å. This would be expected as a result of thermal expansion.

At 200 °C (Figure 4.19), the weighted fraction of $Mg(ND_3)_2I_2$ has increased to 10.6(3) % indicating that deammoniation of the $Mg(ND_3)_6I_2$ is well underway which corresponds to the TG-DTA-MS data. Selected crystallographic data is presented in Table 4.28 with the atomic parameters of the hexaammine phase presented in Table 4.29.

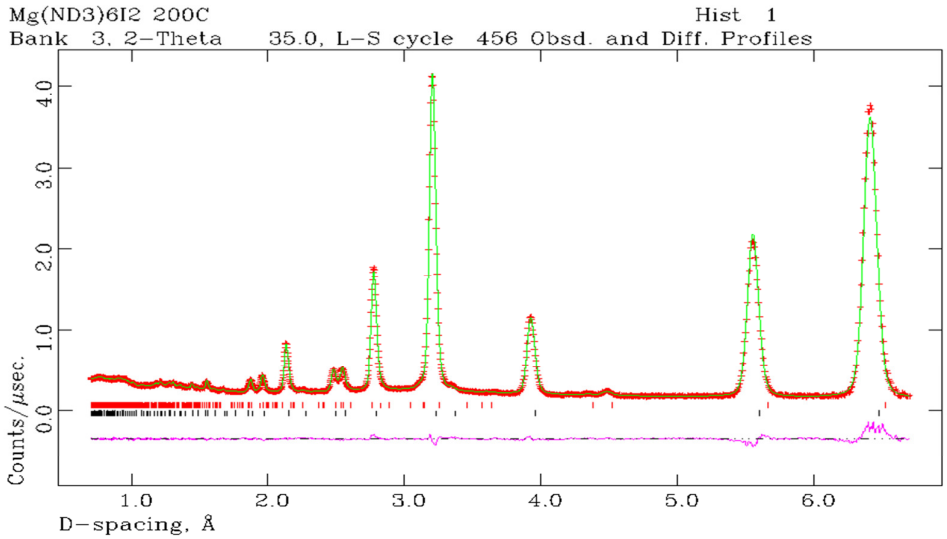

Figure 4.19: Observed, Calculated and Difference (OCD) plot of the Bank 3 data at 200 °C. The red tick marks indicate reflections from $Mg(ND_3)_6I_2$ and black tick marks indicate reflections from $Mg(ND_3)_2I_2$. The observed data is the red crosses, the calculated data is the green lines and the difference line is the lower line.

Table 4.28: Crystallographic data for PXD for $Mg(ND_3)_6I_2$ at 200 °C

Phases	$Mg(ND_3)_6I_2$	$Mg(ND_3)_2I_2$
Phase Fraction (wt. %)	89.4(1)	10.6(3)
Temperature:	200 °C	
Crystal System	Cubic	Orthorhombic
Space Group	*Fm$\bar{3}$m*	*Pbam*
a/Å	11.082(3)	6.212(5)
b/Å		12.894(10)
c/Å		4.388(3)
Volume/Å^3	1360.978(1)	347.705(2)
Z	4	2
Formula Weight/g	1593.628	612.254
Density (ρ_x/gcm^{-3})	1.944	2.924
No of observations	3404	
No of variables	75	
R_{wp}	0.0444	
R_p	0.1543	
X^2	2.444	

Table 4.29: Atomic positions and temperature factors for $Mg(ND_3)_6I_2$ at 200 °C.

Atom /Site	x	y	z	Occupancy	U_{iso} X 100/Å^2
Mg /4a	0	0	0	1	4.0(2)
I/8c	0.25	0.25	0.25	1	4.6(2)
N/96j	0	0.0317(3)	0.1986(2)	0.25	2.5
D1/96k	0.0641(3)	0.0641(3)	0.2272(4)	0.5	9.1(2)
D2/96j	0	0.0694(4)	0.2509(4)	0.25	3.1(2)

As can be seen in Table 4.28, the unit cell continues to expand due to thermal expansion with an increase in temperature. The disordered structure for the hexammine is also providing a good fit for the data during the demmoniation process. At 235 °C (Figure 4.20), the weighted fraction of the diammine continues to increase to 17.2(8) wt. %. At this point in the TGA-DTA-MS deammoniation to the diammine is complete however a larger volume of sample has been used for the PND measurements. Selected crystallographic data is presented in Table 4.30.

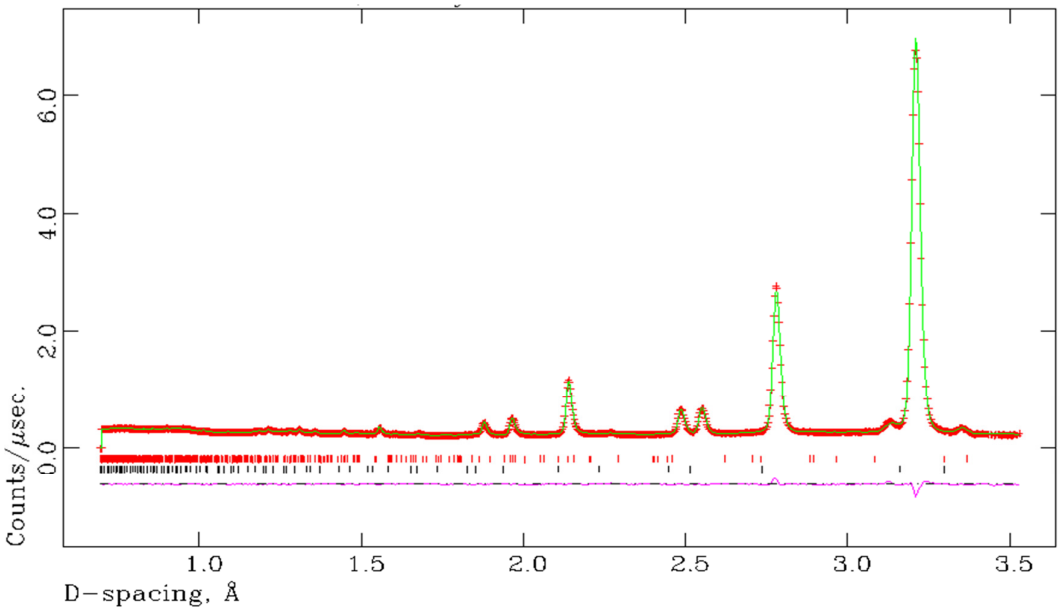

Figure 4.20: Observed, Calculated and Difference (OCD) plot of the Bank 4 data at 200 °C. The red tick marks indicate reflections from $Mg(ND_3)_6I_2$ and black tick marks indicate reflections from $Mg(ND_3)_2I_2$.

Table 4.30: Crystallographic data for PXD for $Mg(ND_3)_6I_2$ at 235 ^oC

Phases	$Mg(ND_3)_6I_2$	$Mg(ND_3)_2I_2$
Phase Fraction (wt. %)	82.8(9)	17.2(8)
Temperature:	235 ^oC	
Crystal System	Cubic	Orthorhombic
Space Group	*Fm$\bar{3}$m*	*Pbam*
a/Å	11.104(4)	6.020(4)
b/Å		13.391(3)
c/Å		4.373(2)
Volume/Å^3	1369.072(2)	352.504(2)
Z	4	2
Formula Weight/g	1593.628	612.254
Density (ρ_x/gcm^{-3})	1.933	2.884
No of observations	3404	
No of variables	71	
R_{wp}	0.0444	
R_p	0.1912	
χ^2	2.870	

As per previous temperature points, the lattice parameters of both the hexaammine and diammine phase continue to expand due to thermal expansion as expected. Selected bond distances for the hexammine phase are presented in Table 4.31.

Table 4.31: Bond distances for $Mg(ND_3)_6I_2$ at 235 ^oC

Distance/Å	
Mg-N	24x 2.212(2)
N-D1	2x 0.873(6), 2x 1.399(7)
N-D2	0.715(5), 1.051(4), 1.303(4)

At 285 ^oC, no $Mg(ND_3)_2I_2$ is observed (Figure 4.21) with only the hexaammine observed. The lattice parameter of this phase has again expanded due to

thermal expansion and is now a= 11.114(3) Å. An amorphous phase has also appeared which dominates at temperatures above 285 °C which could be associated with the monoammine phase. In the PND data only one crystalline phase transition is seen.

From the PND data along with the TG-DTA-MS data it can be concluded that the monoammine phase becomes amorphous at an elevated temperature which could be as a result of a melting transition.

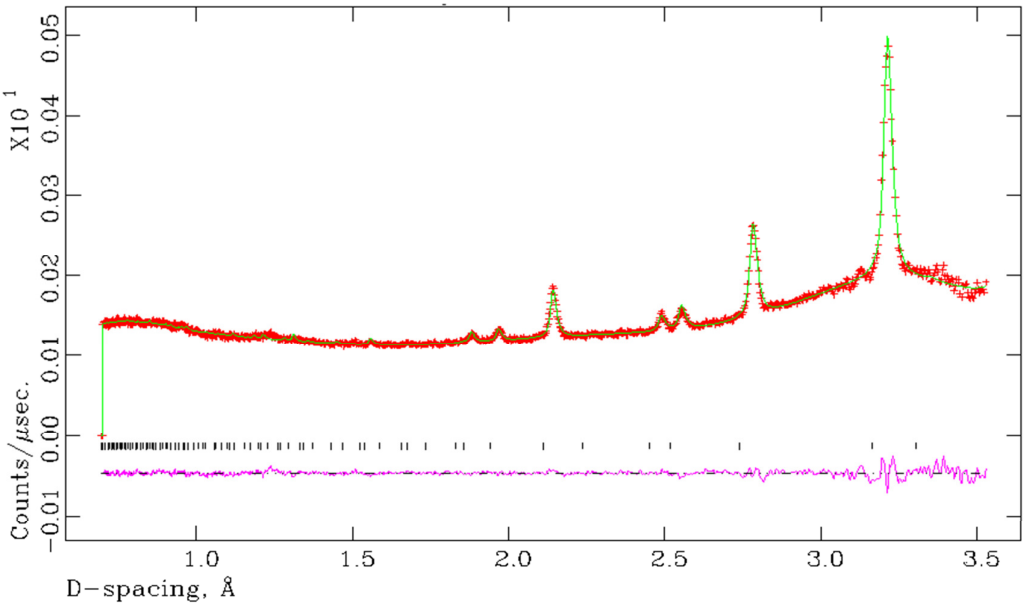

Figure 4.21: Observed, Calculated and Difference (OCD) plot of the Bank 4 data at 285 °C. The red tick marks indicate reflections from $Mg(ND_3)_6I_2$ and black tick marks indicate reflections from $Mg(ND_3)_2I_2$. The observed data is the red crosses, the calculated data is the green lines and the difference line is the lower line.

4.5 Conclusions

PND structural investigations of the hexaammines have successfully refined the structure. The disordered model proposed by Sørby *et al.*[1] for $Mg(ND_3)_6Cl_2$ has been successfully refined for $Mg(ND_3)_6Cl_2$, $Mg(ND_3)_6Br_2$ and $Mg(ND_3)_6I_2$ with the refined data (including bond distances and angles) agreeing with those published particularly for N-D when compared to "free" gaseous ND_3.

PND investigations of the ammines have also been carried out to probe the structural changes involved when the ammines are heated. For the refinements of the hexxammine phases the disordered model has been used which refined satisfactory to the PND data which indicates that the ND_3 is disorded when heated. The known ordered model (occupancy of 0.75 for D) used for the diammines.[10] For both known phases thermal expansion was also viewed.

For the deammoniation of $Mg(ND_3)_6Cl_2$ it has been confirmed that this decomposes in three clear stages. The intermediate stages between the deammoniation of the hexaammine to the diammine confirmed that the sample contained a mixture of two ammines (for example 120 ^oC showed that $Mg(ND_3)_6Cl_2$ and $Mg(ND_3)_2Cl_2$ were present). Reflections of an unknown phase were seen from 210 ^oC to 285 ^oC which may possibly be assigned to the monoammine. These reflections were few and of low intensity so indexing was not possible. For structure determination of the monoammine then the phase will need to be isolated on its own. One possible way is synthesis in the autoclave like that of the $NiCl_2$ and $NiBr_2$ monoammines.[11] The end product of the deammoniation was $MgCl_2$ which allows the system to be recycled.

For the deammoniation of $Mg(ND_3)_6Br_2$, demmoniation occurred in two steps (for the TGA-DTA-MS three steps were seen). The phases seen were $Mg(ND_3)_6Br_2$, $Mg(ND_3)_2Br_2$ and $MgBr_2$. During the intermediate stage of n=6 -> 2, only the hexaammine and diammine phases were seen. No monoammine phase was observed which concludes that to characterise this stage then the same procedure as for the Cl_2 equivalent will need to be followed.

For $Mg(ND_3)_6I_2$ the sample deammoniated to $Mg(ND_3)_2I_2$ with increasing weighted fractions of the diammine seen with increasing temperature, with no other

phases observed. As had been found from ex-situ measurements the structure of the iodide monoammine could not be resolved and at elevated temperatures appears to be amorphous possibly due to a melting point transition.

In the case of three all hexaammines PND when coupled with the TGA-DTA-MS (Chapter 3) deammoniation data has allowed the mechanism of deammoniation to be better understood although further work is required for the monoammines.

4.6 References

[1] M. H. Sørby, O. M. Løvvik, M. Tsuboto, T. Ichikawa, Y. Kojima and B. C. Hauback, *Phys. Chem. Chem. Phys.*, 2011, **13**, 7644.

[2] A. Tekin, J. S. Hummelshøj, H. S. Jacobsen, D. Sveinbjőrnsson, D. Blanchard, J. K. Nørskov and T. Vegge, *Energy Environ. Sci.*, 2010, **3**, 448.

[3] E. Suard and A. Hewitt, *Neutron News*, 2001, **4**, 350.

[4] W. G. Williams, R. M. Ibberson, P. Day and J. E. Enderby*, Physica B*, 1998, **234**, 241.

[5] A. C. Hannon, *Nucl. Instrum. Methods Phys. Res. A*, 2005, **551**, 81.

[6] A. C. Larson and R. B. von Dreele, The General Structure Analysis System, Los Alamos National Laboratories, Report LAUR 086–748, LANL, Los Alamos, NM, 2000.

[7] B. H. Toby, *J. Appl. Crystallogr.*, 2001, **34**, 210.

[8] R. Eßmann, G. Kreiner, A. Niemann, D. Rechenbacj, A. Schmieding, T. Sichla, U. Zachwieja and H. Jacobs, *Z. Anorg. Allg. Chem.*, 1996, **622**, 1161.

[9] H. Jacobs, J. Brock and C. Stüve, *J. Less Common Metals,* 1987, **134**, 207.

[10] A. Leineweber, H. Jacobs, P. Fischer and G. Boettger, *J. Solid State Chem.*, 1999, **156**, 487.

[11] A. Leineweber, H. Jacobs and H. Ehrenberg, *Z. Anorg. Allg. Chem,* 2000, **626**, 2146.

[12] C. M. Widdifield and D. L. Bryce, *Phys. Chem. Chem. Phys.*, 2009, **11**, 7120.

5. Ammines as a Component of a '*H_2 release*' system

5.1 Introduction

'*H_2 release systems*' could provide a suitable alternative to the H_2 storage problem as presented in section 1.4. These systems involve using a mixture of two components, a hydride and another suitable material and heating the mixture to release H_2 (g).

One component of the '*H_2 release*' system along with a hydride could be the metal ammines, especially $Mg(NH_3)_6Cl_2$ due to its high H_2 gravimetric capacity and its good desorption properties (in terms of NH_3). $Mg(NH_3)_6Cl_2$ can indirectly store 9.7 wt. % H_2 although a catalyst is typically required to split the NH_3 to N_2 and H_2. This ammine could be mixed with a suitable hydride (in terms of gravimetric capacity) and used as a '*H_2 release*' system.

One possible system is $Mg(NH_3)_6Cl_2$ with LiH. This system can theoretically release 4.9 wt. % H_2:

$$Mg(NH_3)_6Cl_2 + 6\ LiH \rightarrow MgCl_2 + 6\ LiNH_2 + 6\ H_2 \quad \Delta H = -21.2\ KJ\ mol^{-1}\ H_2 \quad (5.1)$$

The $MgCl_2$ produced as an end product can then be reammoniated to reproduce $Mg(NH_3)_6Cl_2$.[1] LiH can be regenerated from $LiNH_2$ by heating with H_2 in a H_2(g) flow with the release of NH_3.[2]

The system involving equation 1 has been studied by Tsubota *et al*. [3] The components of the system, $Mg(NH_3)_6Cl_2$ and LiH were milled together at -40 ^oC to avoid decomposition of the $Mg(NH_3)_6Cl_2$. This temperature would be unsuitable for fuel cell use (as per MOFs) so a higher temperature for mixing such as room temperature would need to be investigated. Using ball milled $Mg(NH_3)_6Cl_2$ and LiH mixed at -40 ^oC, three mass spec events were observed. The first mass spectroscopy (MS) event (also corresponds with the first weight loss in the TGA curve) is the release of NH_3 (indicating decomposition of the $Mg(NH_3)_6Cl_2$). However, there are two MS events beginning at 230 ^oC which corresponds to the release of H_2(weight loss of approximately 6% on the TG curve). The total weight

loss of the reaction was approximately 16 wt. % which is above that of the theoretical weight loss indicating that the mixing time may have been insufficient and also some decomposition of the ammine had occurred during the mixing process. The authors also investigated using catalysed LiH (milled LiH with $LiNH_2$ and $TiCl_3$) as it was previously been found by Isobe *et al*. that $LiNH_2$ with a small amount of $TiCl_3$ has a catalytic effect on the $LiNH_2$-LiH reaction.[4] During ball milling $Mg(NH_3)_6Cl_2$ decomposed with $LiNH_2$ being formed. When the mixture was heated this led to an increased in the wt. % of H_2 released which could be due to the reaction of $LiNH_2$ and LiH. The TGA and MS data for these reactions can be seen in Figure 5.1:

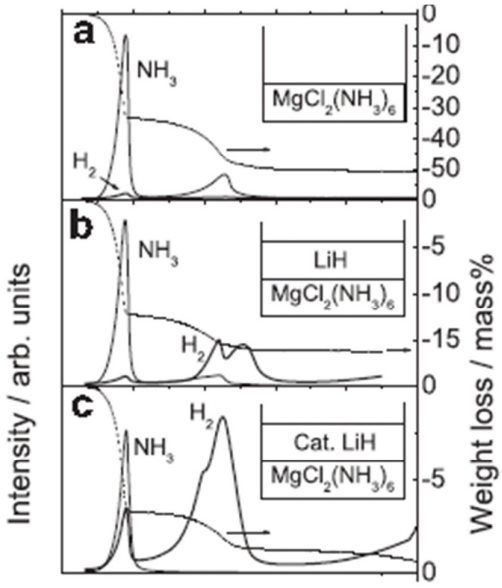

Figure 5.1: TGA and MS data for (a) $Mg(NH_3)_6Cl_2$ only (b) $Mg(NH_3)_6Cl_2$ with LiH and (c) $Mg(NH_3)_6Cl_2$ with milled LiH/0.1 $LiNH_2$ and 0.05 $TiCl_3$. Reprinted from *Int. J. Hydrogen Energy*, 2010, **35**, 2058. Reaction between magnesium ammine complex compound and lithium hydride. M. Tsubota, S. Hino, H. Fujii, C. Oomatsu, M. Yamana, T. Ichikawa and Y. Kojima. Copyright 2010, with permission from International Association for Hydrogen Energy.

Another potential '*H_2 release*' system involving a metal ammine as an integral component of the system is the $Mg(NH_3)_6Cl_2$ and MgH_2 system:

$$Mg(NH_3)_6Cl_2 + 3\ MgH_2 \rightarrow MgCl_2 + 3\ Mg(NH_2)_2 + 6\ H_2 \qquad (5.2)$$

This system can theoretically release 4.5 wt. % H_2 with the $MgCl_2$ being able to be recycled to produce the $Mg(NH_3)_6Cl_2$. There are currently no reports of this system presently in the literature.

In this chapter, $Mg(NH_3)_6Cl_2$ has been hand mixed with both LiH and MgH_2 at room temperature and investigated by TPD (by TGA-DTA-MS). The results of these systems are discussed. In-situ PND measurements of these systems using GEM at ISIS are also discussed in this chapter.

5.2 Experimental

5.2.1 Synthesis of $Mg(NH_3)_6Cl_2$ and $Mg(ND_3)_6Cl_2$

$Mg(NH_3)_6Cl_2$ was synthesised as described in sections 2.2.7 and 3.2.1 and $Mg(ND_3)_6Cl_2$ was synthesised as described in section 2.2.7.

5.2.2 Powder X-ray Diffraction (PXD) Experiments

Compounds were characterised by PXD, as described in section 2.3.1.2. For the hexaammines capillaries were prepared and collected from 5 – 75 ^{o} for 1 hour with a step size of 1.3 ^{o}/min and 5 - 95 ^{o} for 12 hrs with a step size of 0.14 ^{o}/min for refinement purposes using the Brucker D8. For the pre and post TPD data, characterisation was performed using the air sensitive flat plate between 5-85 ^{o} for 20-30 mins using the PANalytical X'pert Pro.

5.2.3 Thermal Programmed Desorption (by TGA-DTA-MS) analysis of the 'H_2 release' systems

Measurements of the '*H_2 release systems*' were performed using a Netzsch STA 409 analyser which was interfaced to a Hiden HPR 20 Mass Spectrometer (section 2.6). Measurements were performed in an Ar(g) recirculating glove box, with 30-40 mg of samples typically used.

$Mg(NH_3)_6Cl_2$ were hand mixed with LiH (Sigma, 95%) or MgH_2 (Alfa, 98%) in a N_2 (g) recirculating glove box using a mortar and pestle. The mixtures were then heated to 400 ^{o}C with a heating rate of 5 ^{o}C per min and held at 400 ^{o}C for 1 hr. Mass spec (m/z) data were collected for NH_3, N_2, H_2 and H_2O. The intermediates of the reactions were isolated by heating to the appropriate temperature.

5.2.4 In-Situ Powder Neutron Diffraction (PND) Experiments

In situ PND experiments were carried out on the GEM (General Materials) diffractometer at the ISIS facility at Didcot. [5,6] Initially, data was collected at room temperature before heating the samples to 400 ^{o}C and collecting data at various temperature points.

Typically 1-5 g – 2 g of the prepared mixture was loaded into 6 mm or 8 mm vanadium cans with a copper seal. The mixtures used were $Mg(ND_3)_6Cl_2$ (as synthesised in Chapter 4) + 6 LiD (Sigma, 98%) and $Mg(ND_3)_6Cl_2$ + 3 MgH_2 (Alfa 98%). These mixtures were prepared by hand mixing in a Ar(g) recirculating glove box immediately before PND analysis. The sealed cans containing the mixtures were transferred outside the glove box, and attached to a capillary stick for gas flow in an argon filled glove bag. The experimental set up is described in section 2.3.3.2. Samples were heated under a flow of Ar(g) to temperature points determined by TPD measurements (section 5.2.3 and 5.4.1) and data were collected for 1 - 2 hrs at each temperature point depending on the sample quality. For the LiD system the temperatures measured were: 25 ^{o}C, 125 ^{o}C, 150 ^{o}C, 160 ^{o}C, 215 ^{o}C, 235 ^{o}C, 270 ^{o}C, 295 ^{o}C, 350 ^{o}C and 400 ^{o}C. For the MgH_2 system the temperatures measured were: 25 ^{o}C 125 ^{o}C, 150 ^{o}C, 160 ^{o}C, 210 ^{o}C, 230 ^{o}C, 275 ^{o}C, 305 ^{o}C and 400 ^{o}C

5.2.4.1 Rietveld Refinement of the PND data

The in-situ and measurements were refined using the GSAS program with the EXPGUI interface. [7,8] The background of the ammines was successfully fitted using background function 1, a Chebyschev polynominal function. In some cases, the background was fitted manually. This is achieved by selecting background points manually and then fitting the background using the Chebyschev polynominal function until a good background fit is achieved.

Background fitting was then followed by refinement of cell parameters, atomic positions, profile coefficients, peak widths and temperature factors. Peak profiles were successfully modelled using function 2 in GSAS, a Simpson's integration of the Pseudo-Voight function. Other phases were then added (for example LiD and MgH_2) and refined as appropriate.

For the GEM in-situ measurements, Bank 3 (24.6-45.6^{o}) were used first in refinements followed by the data from Bank 4 (50-75^{o}).

5.2.5 Summary of Reactions

Table 5.1: Summary of Reactions

Sample	Materials	Experiment
1	$Mg(NH_3)_6Cl_2$ +LiH	Heated to 400 ^{o}C
2	$Mg(NH_3)_6Cl_2$ +LiH	Heated to 160 ^{o}C
3	$Mg(ND_3)_6Cl_2$ +LiD	Heated to 400 ^{o}C- PND
4	$Mg(NH_3)_6Cl_2$ +MgH_2	Heated to 400 ^{o}C
5	$Mg(NH_3)_6Cl_2$ +MgH_2	Heated to 170 ^{o}C
6	$Mg(ND_3)_6Cl_2$ +MgH_2	Heated to 400 ^{o}C- PND

5.3 Results and Discussion

5.3.1 Synthesis of $Mg(NX_3)_6Cl_2$, where X= H,D

Results of the synthesis of $Mg(NH_3)_6Cl_2$ are presented in section 3.3.1 and sections 4.3.1.1 for the preparation of $Mg(ND_3)_6Cl_2$

5.3.2 Thermal Programmed Desorption (TPD) analysis of the $Mg(NH_3)_6Cl_2$ and LiH system

Sample **1** was prepared as per section 5.2.4

The TGA-DTA curve produced by heating the $Mg(NH_3)_6Cl_2$ and 6 LiH mixture (sample **1**) can be seen in Figure 5.2:

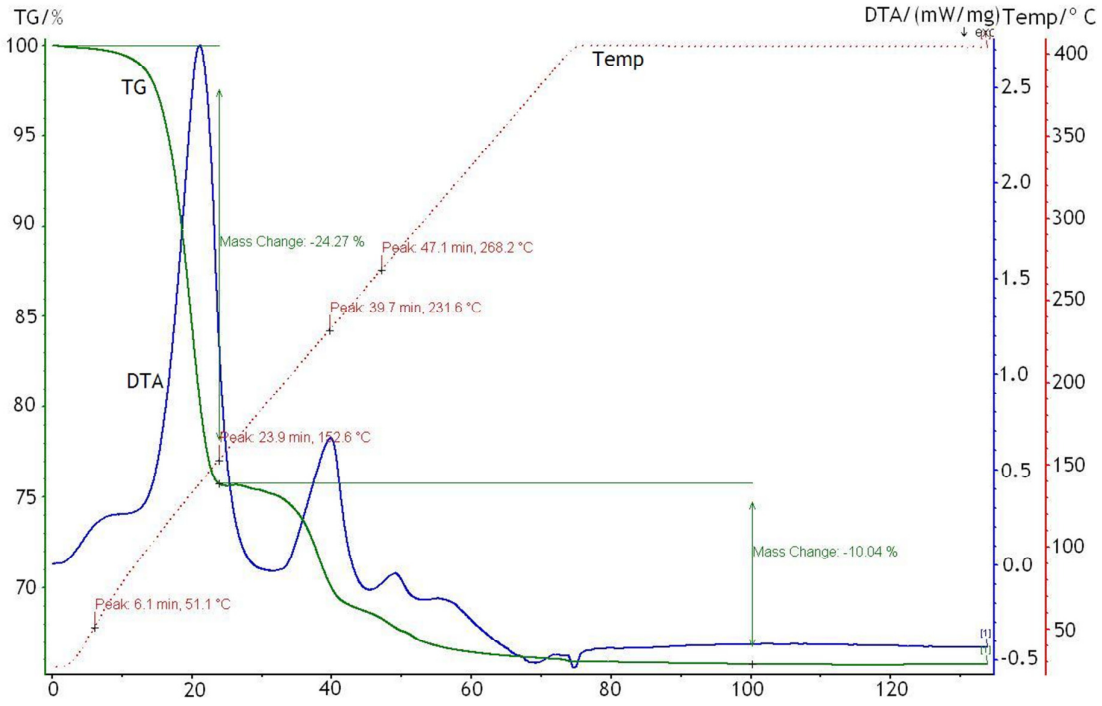

Figure 5.2: TGA-DTA curve for the $Mg(NH_3)_6Cl_2$ + 6 LiH mixture (sample **1**)

As can be seen, the total weight loss of the reaction is 24.27 wt. % which is considerably higher than the theoretical weight loss value of 4.9 wt. % H_2. The first weight loss step of 24.14 wt. % corresponds with a large endothermic event occurring in the DTA curve. This weight loss step commences at 51 °C and is complete at 153 °C with NH_3 released from the ammine as can be seen in Figure 5.2. This could be as a consequence of the decomposition of $Mg(NH_3)_6Cl_2$:

$$Mg(NH_3)_6Cl_2 \rightarrow Mg(NH_3)_2Cl_2 + 4\ NH_3 \qquad (5.3)$$

This intermediate stage has been isolated (section 5.3.3) confirming the presence of $Mg(NH_3)_2Cl_2$ at 160 °C.

As can be seen in Figure 5.2, the next two thermal events involve a large endothermic event followed by a small endothermic event which occurs at 232 °C and finishes at 300 °C. These thermal events corresponds to the release of the H_2 which has been observed on the MS data (Figure 5.3) although a small peak of NH_3 is seen before the H_2 which is likely to be associated with some decomposition of the diammine to its monoammine. The onset temperature of H_2 release is similar to the seen by Tsubota who observed H_2 release

commencing at 230 °C.[3] From the onset H_2 release temperature it can be seen that mixing at room temperature appears to slightly improve the onset temperature compared to mixing at -40 °C although there are other possible factors including the possibility of decomposition of the hexaamine during mixing and also the possibility of the LiH acting as a catalyst (as per the LiH-NH_3 reaction).[9]

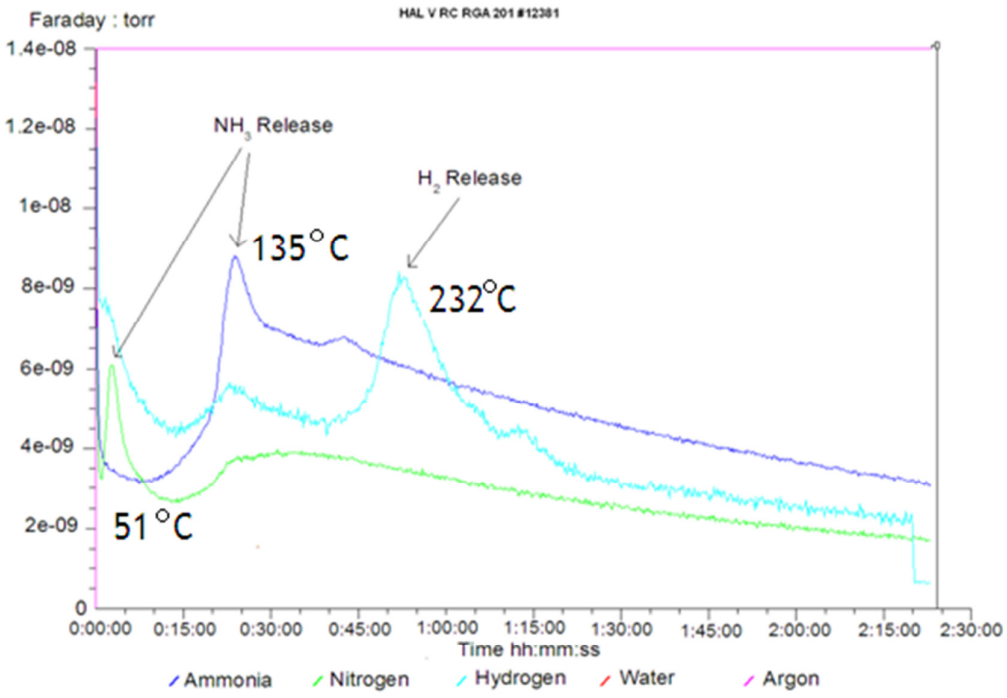

Figure 5.3: MS profile for sample **2** showing the NH_3 and H_2 release

As can be seen in Figure 5.2, during the hold period at 400 °C the TGA curve is levelled indicating that the reaction has gone to completion. PXD analysis (Figure 5.4) showed that $MgCl_2$ is present Li_2NH which is a better fit for the data than $LiNH_2$ (using Powder Cell).

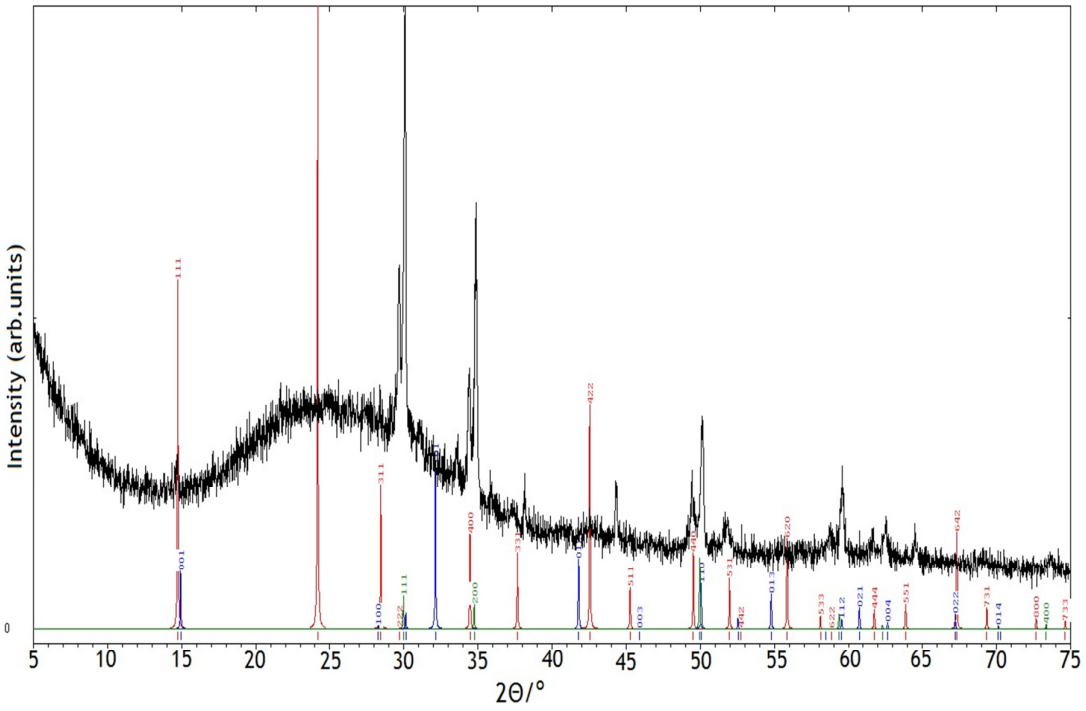

Figure 5.4: PXD of sample **1** post TPD. The blue lines indicate the calculated reflections for $MgCl_2$, the green lines indicate the calculated reflections for Li_2NH and the red lines indicate the calculated reflections for $LiNH_2$.

5.3.3 Intermediate Study of the $Mg(NH_3)_6Cl_2$ + LiH system at 160 °C

In order to determine the intermediate products after the first weight loss and thermal event, a mixture of $Mg(NH_3)_6Cl_2$ and LiH were heated to 160 °C at a heating rate of 5 °C per minute and held at 160 °C for 30 minutes. The TG-DTA profile for sample **2** can be seen in Figure 5.5:

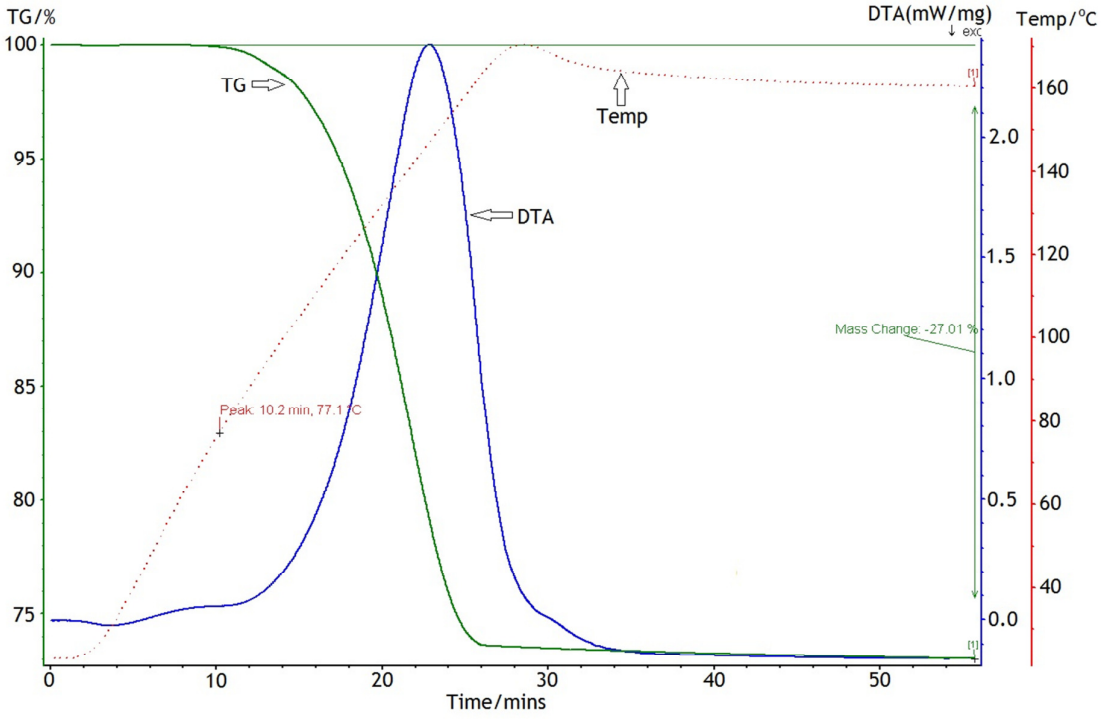

Figure 5.5: TG-DTA profile for sample **2** heated to 160 °C

As can be seen in Figure 5.5, the onset of reaction is 77 °C which is comparable to sample **1** heated to 400 °C. There is also one thermal endothermic event which corresponds to the DTA curve seen for the first weight loss step of $Mg(NH_3)_6Cl_2$ only (section 3.4.1). During the hold period, the TG and DTA curve level off indicating that the reaction is complete at 160 °C. The MS profile (Figure 5.6) also indicates that NH_3 is released during heating:

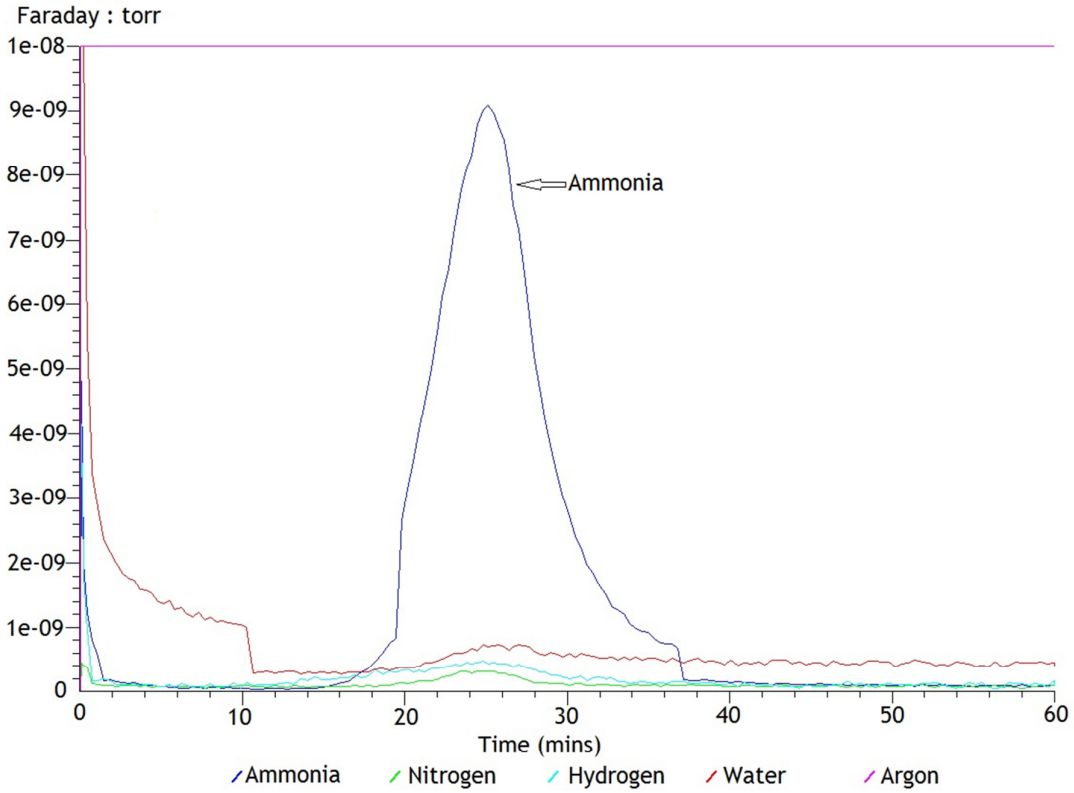

Figure 5.6: MS profile of sample **2** heated to 160 ^{o}C

PXD analysis (Figure 5.7) confirms the TPD results that only the decomposition of $Mg(NH_3)_6Cl_2$ to $Mg(NH_3)_2Cl_2$ (PDF no: 01-073-4070) has occurred in the first step of the reaction and that LiH is present alongside the diammine:

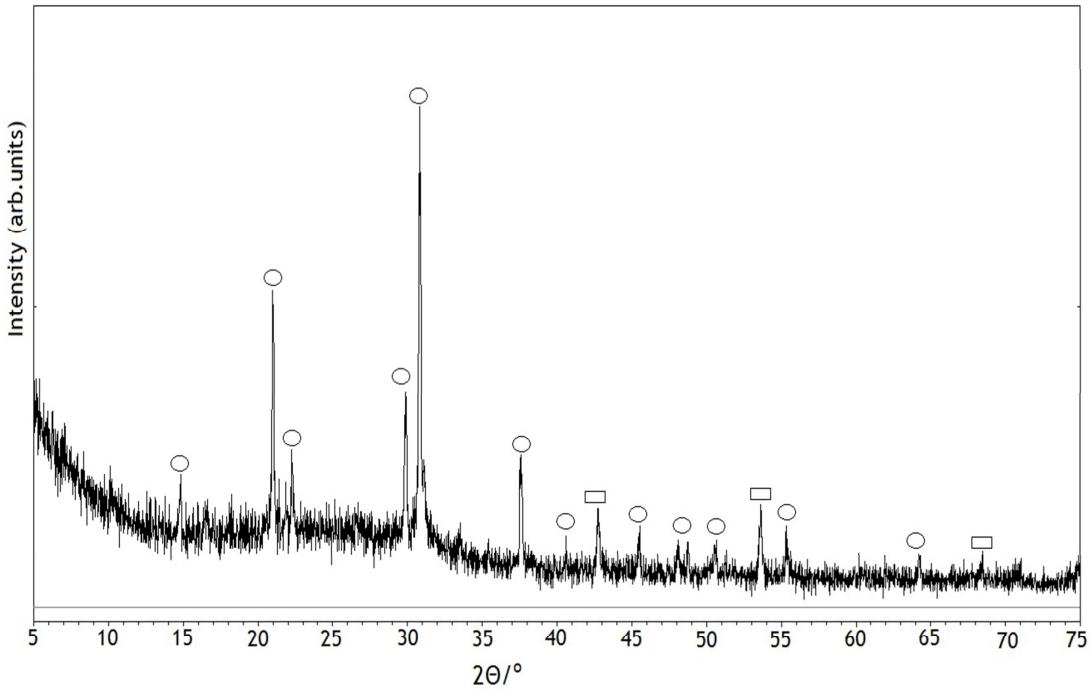

Figure 5.7: PXD of the post TPD product of sample **2**. The circles represent reflections from the $Mg(NH_3)_2Cl_2$ and the rectangles represent reflections from the LiH phase

Hence, from the TPD and PXD data it can be determined that the first step of the reaction between $Mg(NH_3)_6Cl_2$ and LiH is the decomposition of $Mg(NH_3)_6Cl_2$. The theoretical weight loss for the decomposition of $Mg(NH_3)_6Cl_2$ to $Mg(NH_3)_6Cl_2$ is 34.7 wt. % while the weight loss seen from the intermediate study was 27.1 wt. %. The difference in the weight loss could indicate that there is a reaction occurring between $Mg(NH_3)_6Cl_2$ and LiH although there is no evidence in the PXD (Figure 5.7) or the difference could be due to decomposition of $Mg(NH_3)_6Cl_2$ during mixing. PND studies (section 5.3.4) have been used to examine the intermediate processes.

$$Mg(NH_3)_6Cl_2 + 6\ LiH \rightarrow Mg(NH_3)_2Cl_2 + 6\ LiH + 4\ NH_3 \qquad (5.4)$$

5.3.4 Powder Neutron Diffraction (PND) Study of the $Mg(ND_3)_6Cl_2$ + LiD 'D$_2$ Release' System

The PND experiment for the $Mg(ND_3)_6Cl_2$ and LiD was carried out as per section 5.2.4

5.3.4.1 PND In-Situ Results

The reactions which occurred when sample **3** ($Mg(ND_3)_6Cl_2$ + LiD) during heating can be seen in Figure 5.8.

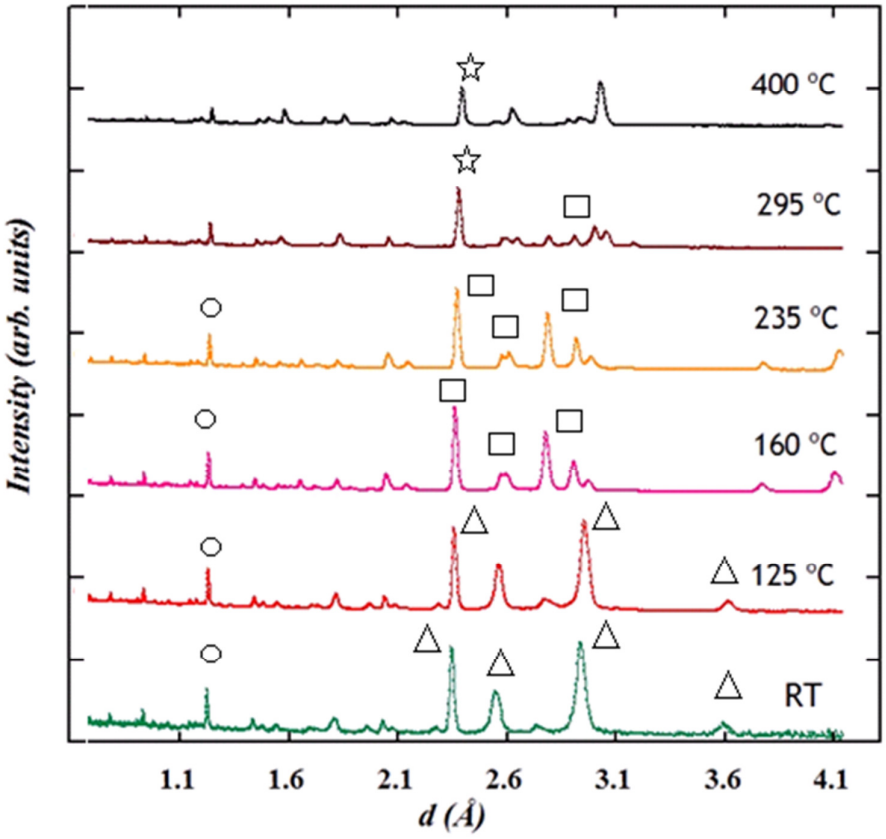

Figure 5.8 Data collected from Bank 4 showing the reaction changes for the $Mg(ND_3)_6Cl_2$ + LiD system. The triangles represent reflections from $Mg(ND_3)_6Cl_2$, the squares represent reflections from $Mg(ND_3)_2Cl_2$, the stars represent $MgCl_2$ and the circles represent reflections from LiD.

After mixing at room temperature, three phases are present. These phases are $Mg(ND_3)_6Cl_2$ [10], LiD [11] and $Mg(ND_3)_2Cl_2$.[12] The presence of the orthorhombic $Mg(ND_3)_2Cl_2$ phase indicates that some decomposition of $Mg(ND_3)_6Cl_2$ has occurred during mixing at room temperature. This was also observed by Tsuboto *et al*. for

$Mg(NH_3)_6Cl_2$ during mixing with LiH. [3] There is also a small quantity of ND_4Cl in the sample (which was also observed for $Mg(ND_3)_6Cl_2$ only at room temperature (section 3.3.4). The ND_4Cl was present as made and not generated during mixing. Selected Rietveld Refinement data for the room temperature experiment is presented in Table 5.2 and Figure 5.9.

Table 5.2: Crystallographic data for the 25 °C mixture

Phases	$Mg(ND_3)_6Cl_2$	$Mg(ND_3)_2Cl_2$	LiD	ND_4Cl
Phase Fraction	62.2(1)%	11.2(5)%	20.0(6)%	6.6(4)%
Temperature:		25 °C		
Crystal System	Cubic	Orthorhombic	Cubic	Cubic
Space Group	*Fm$\bar{3}$m*	*Cmmm*	*Fm$\bar{3}$m*	*Pm$\bar{3}$m*
a/Å	10.170(15)	8.393(7)	4.059(4)	3.892(22)
b/Å		8.069(4)		
c/Å		3.617(25)		
Volume/Å^3	1051.84(16)	244.92(29)	66.81(1)	58.97(3)
Z	4	2	4	1
Formula Weight/g	862.020	270.168	35.820	53.492
Density ,p_x/gcm^{-3}	1.361	1.832	0.90	1.506
No of observations	1886			
No of variables	47			
R_{wp}	0.0320			
R_p	0.0792			
χ^2	5.216			

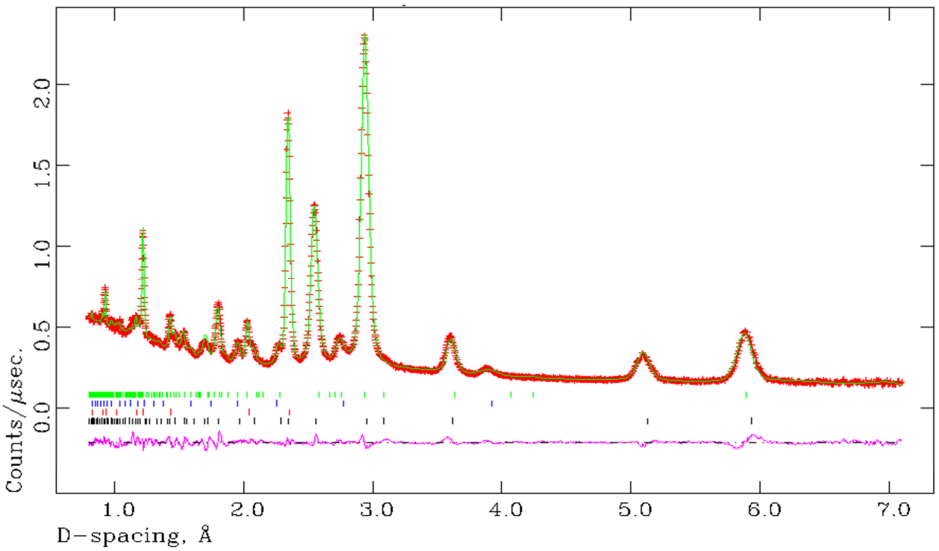

Figure 5.9: Observed, Calculated and difference (OCD) plot for the structural refinement of sample **3** using bank 3. The black tick marks indicate reflections from the $Mg(ND_3)_6Cl_2$ phase, the blue tick marks indicate reflections from the LiD phase, the red tick marks indicate reflections from the $Mg(ND_3)_2Cl_2$ phase and the green tick marks indicate reflections from the ND_4Cl phase.

The next measured temperature point was 125 °C, which is a midpoint temperature for the decomposition of $Mg(ND_3)_6Cl_2$ to $Mg(ND_3)_6Cl_2$ and also an appropriate midpoint temperature for the $Mg(NH_3)_6Cl_2$ and LiH system based on TPD measurements. At 125 °C, there are five phases present. Three phases from the RT measurement are present: $Mg(ND_3)_6Cl_2$, $Mg(ND_3)_2Cl_2$, LiD and ND_4Cl. However, the fourth phase is significant at this temperature as the phase is $MgCl_2$ which is the one of the end products of the reaction. As $Mg(ND_3)_2Cl_2$ is present at room temperature it can be concluded that some of this has fully deammoniated at 125 °C. The phase fractions, based on bank 3 data (which allows the high d spacing reflections from the cubic $Mg(ND_3)_6Cl_2$) are: 40.2 wt. % for $Mg(ND_3)_6Cl_2$, 9.6 wt. % for $Mg(ND_3)_2Cl_2$, 20.8 wt. % for LiD, 26.5 wt. % for $MgCl_2$ and 2.9 % for ND_4Cl.

When compared to the phase functions at room temperature, the wt. % of $Mg(ND_3)_6Cl_2$ is decreasing although there is no increase in $Mg(ND_3)_2Cl_2$ (this could be due to the decomposition to $MgCl_2$). The decrease in $Mg(ND_3)_6Cl_2$ is expected based on the TPD study at 160 °C (Section 5.3.2) which concluded that the first stage of the reaction is the decomposition of $Mg(NH_3)_6Cl_2$. The OCD plot for this

temperature point is presented in Figure 5.10 and selected crystallographic data presented in Table 5.3. Atomic parameters data are presented in Tables 5.1A in the appendix:

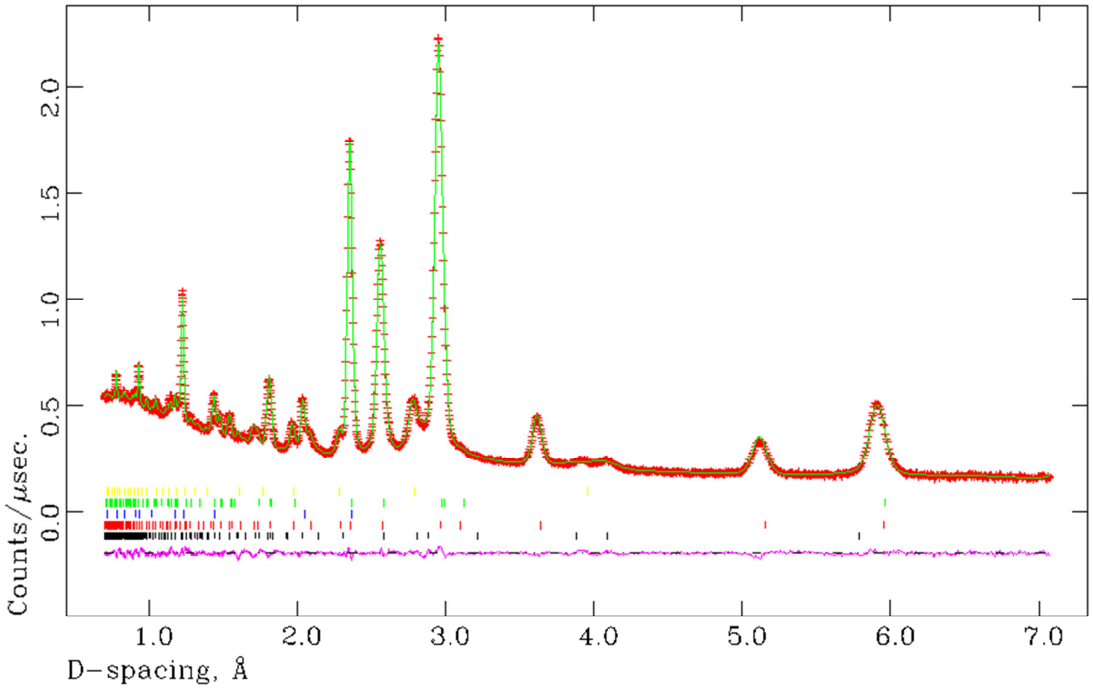

Figure 5.10: Observed, Calculated and difference (OCD) plot for the structural refinement of sample **4** using bank 3 at 125 °C. The green tick marks indicate reflections the $Mg(ND_3)_6Cl_2$ phase, the blue tick marks indicate reflections from the LiD phase, the red tick marks indicate reflections from the $Mg(ND_3)_2Cl_2$ phase the black tick marks indicate reflections from the $MgCl_2$ phase and the yellow tickmarks indicate reflections from the ND_4Cl phase.

The lattice parameters for $Mg(ND_3)_6Cl_2$ in Table 5.3 are similar to that in the literature [12] (a= 8.1828(6) Å, b= 8.2007(6) Å and c= 3.7543(2) Å). The lattice parameter of the LiD shows thermal expansion from the literature value of 4.065(10) Å.[11]

Table 5.3: Selected Crystallographic data of the $Mg(ND_3)_6Cl_2$ and LiD system at 125 °C from Bank 3. The ND_4Cl phase with a phase fraction of 2.9(3) % is not shown for clarity

Phases	$Mg(ND_3)_6Cl_2$	$Mg(ND_3)_2Cl_2$	LiD	$MgCl_2$
Phase Fraction	40.2(4)%	9.6(4)%	20.8(2)%	26.5(6)%
Temperature:		125 °C		
Crystal System	Cubic	Orthorhombic	Cubic	Trigonal
Space Group	$Fm\bar{3}m$	$Cmmm$	$Fm\bar{3}m$	$R\bar{3}m$
a/Å	10.210(12)	8.073(15)	4.075(3)	3.640(10)
b/Å		8.114(9)		
c/Å		3.837(3)		17.715(8)
Volume/Å^3	1064.30(3)	250.31(6)	67.65(1)	203.376(1)
Z	4	2	4	3
Formula Weight/g	862.020	270.168	35.820	285.633
Density,ρ_x/gcm^{-3}	1.345	1.788	0.879	2.334
No of observations		2002		
No of variables		54		
R_{wp}		0.0197		
R_p		0.0718		
χ^2		2.160		

At 150 °C, a mixture of the five phases observed at 125 °C are present (Figure 5.11). The phase fractions, based on bank 3 data (which allow the high d spacing reflections from the cubic $Mg(ND_3)_6Cl_2$ to be included) are: 9.0 wt. % for $Mg(ND_3)_6Cl_2$, 39.7 wt. % for $Mg(ND_3)_2Cl_2$, 23.8 wt. % for LiD, 26.6 wt. % for $MgCl_2$ and 0.9% for ND_4Cl. When compared to the 125 °C data, the fraction of $Mg(ND_3)_6Cl_2$ has decreased significantly (the unit cell has also expanded to 10.226(8) Å) while the fraction of $Mg(ND_3)_2Cl_2$ has increased significantly and can conclude that the first step of the reaction is close to completion (eqn 5.5). The fraction of LiD is also largely unchanged from lower temperatures which supports the premise that the reaction of ammine and hydride is not occurring at the low temperatures as seen in the TG-DTA-MS data:

$$Mg(ND_3)_6Cl_2 + 6\ LiD \rightarrow Mg(ND_3)_2Cl_2 + 6\ LiD + 4ND_3 \qquad (5.5)$$

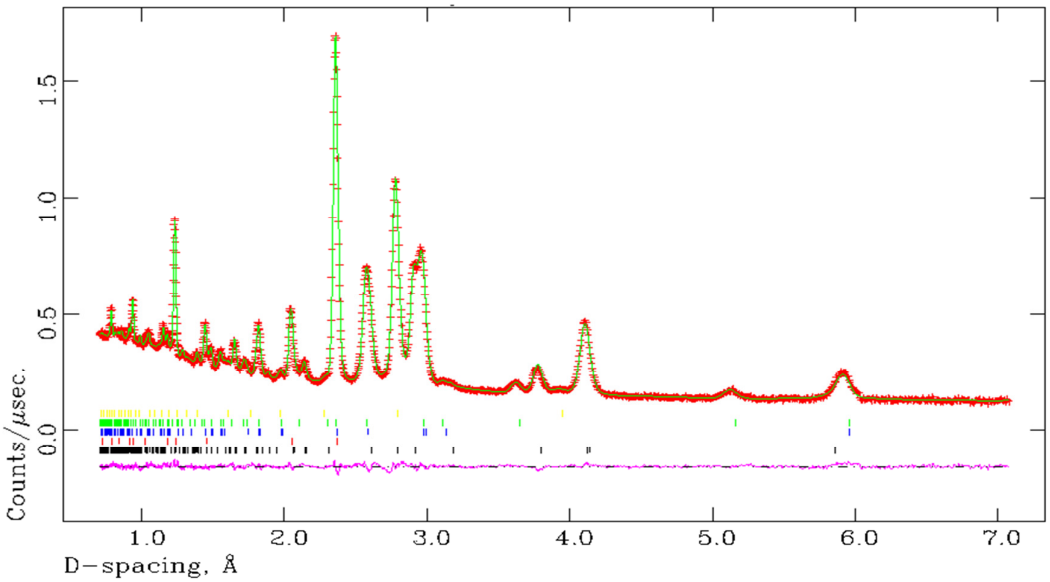

Figure 5.11: Observed, Calculated and difference (OCD) plot for the structural refinement of sample **4** using bank 3 data at 150 ^{o}C. The green tick marks indicate reflections the $Mg(ND_3)_6Cl_2$ phase, the blue tick marks indicate reflections from the LiD phase, the red tick marks indicate reflections from the $MgCl_2$ phase the black tick marks indicate reflections from the $Mg(ND_3)_2Cl_2$ phase and the yellow tick marks indicate reflections from the ND_4Cl phase.

At 160 ^{o}C, there is no $Mg(ND_3)_6Cl_2$ present. This corresponds to the mechanism presented in equations 5.4 and 5.6. The OCD plot for the refinement are presented in Figure 5.12, Selected crystallographic data are presented in Table 5.4 and bond distances are reported in Tables 5.2A and 5.3A in the appendix . From this data it can be seen that there has been in an expansion in the lattice parameters of $Mg(ND_3)_2Cl_2$ and LiD from 150 ^{o}C and the lattice parameters of the $MgCl_2$ have also slightly increased:

Table 5.4: Crystallographic of the $Mg(ND_3)_6Cl_2$ and LiD system at 160 °C.

Phases	$Mg(ND_3)_2Cl_2$	LiD	$MgCl_2$
Phase Fractions	47.8(5)	24.8(3)	27.4(4)
Temperature:		160 °C	
Crystal System	Orthorhombic	Cubic	Trigonal
Space Group	*Cmmm*	$Fm\bar{3}m$	$R\bar{3}m$
a/Å	8.020(8)	4.083(1)	3.644(3)
b/Å	8.226(5)		
c/Å	3.767(3)		17.721(3)
Volume/Å^3	253.869(3)	68.088(2)	203.841(1)
Z	4	4	2
Formula Weight/g	270.618	35.820	285.633
Density, ρ_x/gcm^{-3}	1.770	0.874	2.327
No of observations		3730	
No of variables		67	
R_{wp}		0.1321	
R_p		0.2016	
χ^2		4.560	

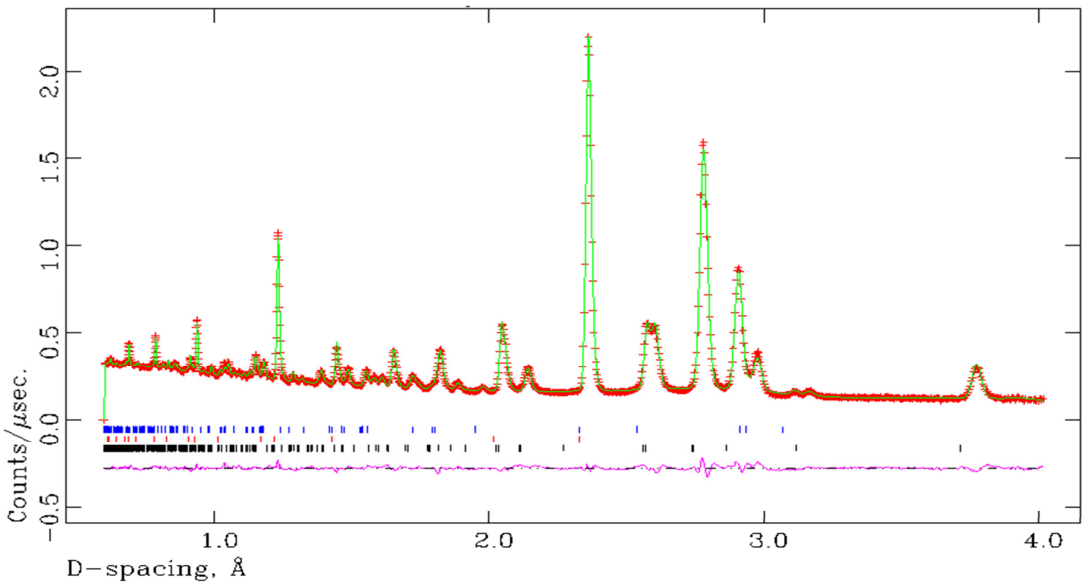

Figure 5.12: Observed, Calculated and difference (OCD) plot for the structural refinement of sample **4** using bank 4 data at 160 °C. The blue tick marks indicate reflections from the $Mg(ND_3)_2Cl_2$ phase, the red tick marks indicate

reflections from the LiD phase and the black tick marks indicate reflections from the $MgCl_2$ phase.

The peak at 3.2 Å in Figure 5.12 is possibly the monoammine phase (Chapter 3). The phase fraction of the LiD is also relatively unchanged from 150 ^oC indicating that the reaction of the ammine and hydride has yet to occur.

As at 215 ^oC the $Mg(ND_3)_2Cl_2$, LiD and $MgCl_2$ phases are present (Figure 5.13). The phase fractions for each phase are as follows: 44.2 wt. % for $Mg(ND_3)_2Cl_2$, 24.0 wt. % for LiD and 31.8 wt. % for $MgCl_2$. When compared to the phase functions at 160 ^oC deammoniation of $Mg(ND_3)_2Cl_2$ to Mg $(ND_3)Cl_2$ has occurred which corresponds to the DTA data where a small endothermic event is seen finishing at 232 ^oC which corresponds with the formation of the monoammine. For LiD, the weighted fraction has also decreased slightly at 215 ^oC indicating that some D_2 release from the reaction between the ammine and LiD may have occurred. Crystallographic data is presented in Tables 5.3A- 5.5A in the appendix.

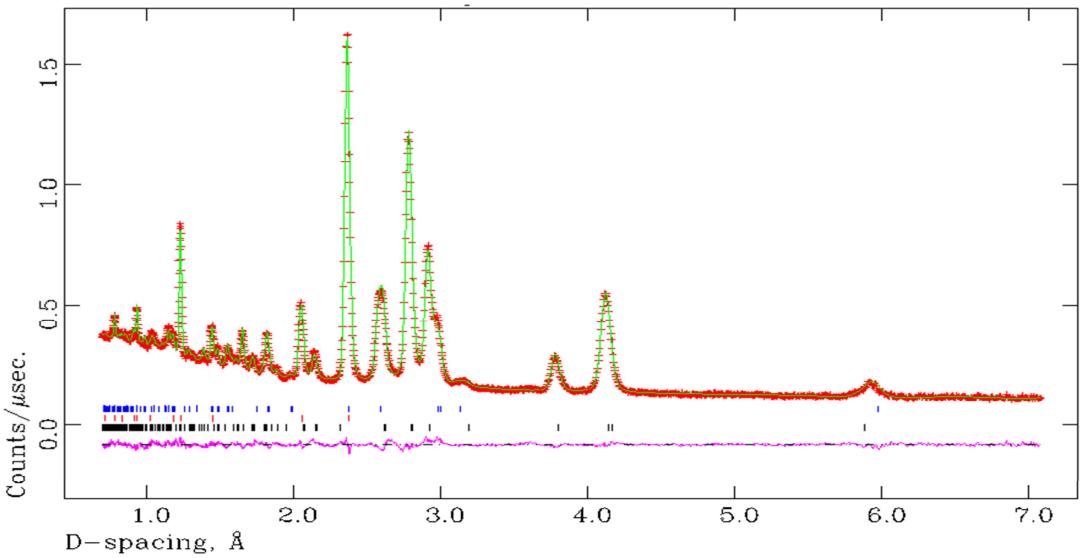

Figure 5.13: Observed, Calculated and difference (OCD) plot for the structural refinement of sample **4** using bank 3 data at 215 ^oC. The blue tick marks indicate reflections the $Mg(ND_3)_2Cl_2$ phase, the red tick marks indicate reflections from the LiD phase, the blue tick marks indicate reflections from the $MgCl_2$ phase

At the next temperature point of 235 °C, three phases ($Mg(ND_3)_2Cl_2$, LiD and $MgCl_2$) are present as per 215 °C indicating that H_2 release has not yet occurred. The weighted fraction of $MgCl_2$ has increased from 31.8 wt. % at 215 °C which will be due to the further formation of the monoammine and the resulted decomposition to $MgCl_2$. The weighted fraction of LiD has decreased from 215 °C which shows that the reaction between the ammine and hydride has commenced at a similar temperature seen in the TPD (section 5.3.2) although addition of the expected product, $LiND_2$ resulted in an unstable refinement indicating that the reaction has possibly just started to commence as the weighted fraction difference between 215 °C and 235 °C is 3.2 wt. %. The Li-D bond length has lengthened from 2.041(7) Å at 135 °C to 2.049(13) Å at 235 °C. Thermal expansion has also occurred in both the $Mg(ND_3)_2Cl_2$ and LiD.

Selected crystallographic data this temperature is presented in Table 5.5 and Figure 5.14. Atomic parameters and bond lengths/angles are presented in Tables 5.6A-5.8A in the appendix

Table 5.5: Crystallographic data of the $Mg(ND_3)_6Cl_2$ and LiD system at 235 °C.

Phases	$Mg(ND_3)_2Cl_2$	LiD	$MgCl_2$
Fractions (wt. %)	36.7(5)	20.5(3)	42.8(9)
Crystal System	Orthorhombic	Cubic	Trigonal
Space Group	*Cmmm*	$Fm\bar{3}m$	$R\bar{3}m$
a/Å	8.224(10)	4.099(2)	3.653(4)
b/Å	8.259(7)		
c/Å	3.773(3)		17.780(6)
Volume/Å^3	256.203(4)	68.852(1)	205.630(1)
Z	2	4	3
Formula Weight/g	270.618	35.820	285.633
Density, ρ_x/gcm^{-3}	1.753	0.864	2.307
No of observations		3711	
No of variables		75	
R_{wp}		0.0947	
R_p		0.1438	
χ^2		5.937	

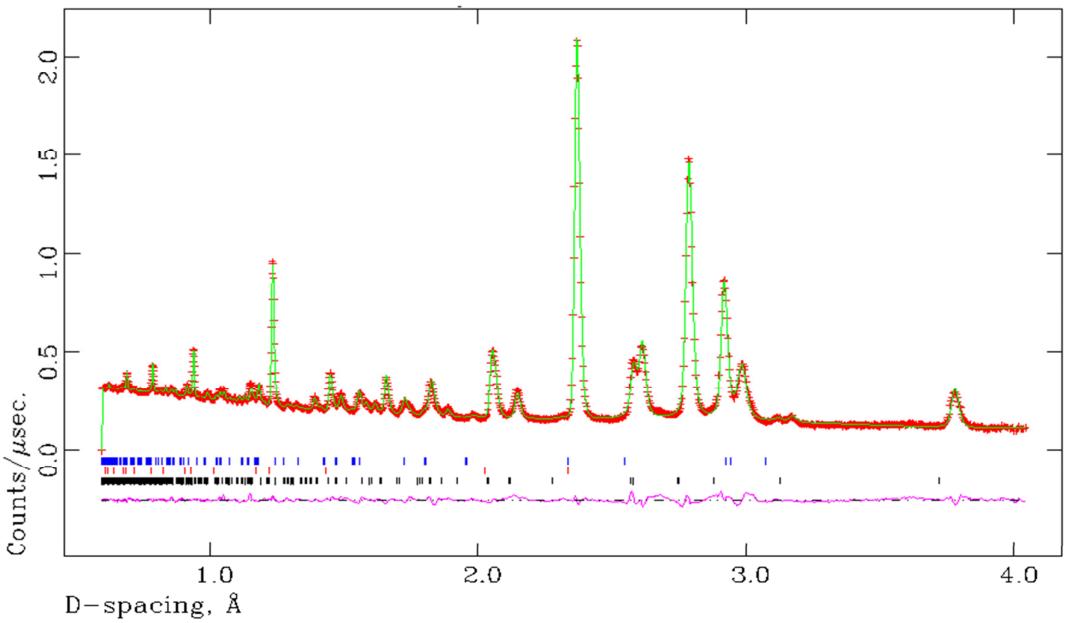

Figure 5.14: Observed, Calculated and difference (OCD) plot for the structural refinement of sample **3** using bank 4 at 235 °C. The blue tick marks indicate reflections the $Mg(ND_3)_2Cl_2$ phase, the red tick marks indicate reflections from the LiD phase and the black tick marks indicate reflections from the $MgCl_2$ phase.

At 270 °C (Figure 5.15), a new phase that can be attributed to $LiND_2$ (*I4*)[13] is present along with $Mg(ND_3)_2Cl_2$, $MgCl_2$ and LiD. The weighted fraction of the amide phase present is 13.1 wt. %. There is also a reflection that has been removed which could be associated with the monoammine (Chapter 4). The presence of $LiND_2$ indicates that D_2 is occurring, and the reaction may be similar to that of LiH and NH_3 where LiH reacted with NH_3 to produce $LiNH_2$ with the release of H_2.[14] The release of D_2 at this temperature indicates that direct reaction of LiD with the ammine may not occur.

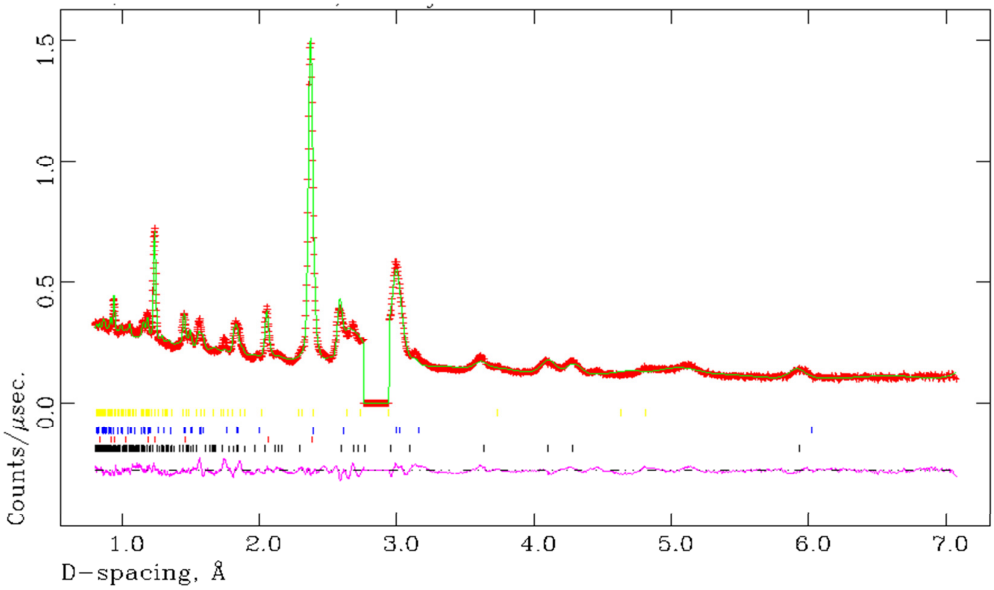

Figure 5.15: Observed, Calculated and difference (OCD) plot for the structural refinement of sample **3** using bank 4 at 270 °C. The blue tick marks indicate reflections the $Mg(ND_3)_2Cl_2$ phase, the red tick marks indicate reflections from the LiD phase, the black tick marks indicate reflections from the $MgCl_2$ phase and the yellow tickmarks indicate reflections from $LiND_2$. The excluded region may be a reflection from the unknown monoammine phase.

At 350 °C, LiD could not be successfully modelled was indicating that the H_2 release step was now complete which also corresponds to the PND data.

At 400 °C ex-situ PXD confirmed that $MgCl_2$ and $LiND_2$ were both present. No Li_2ND was seen in the diffraction pattern.

From the PND experiment, it can be determined that for improvements to the H_2 release system then improvements in the components must be investigated as the $Mg(ND_3)_6Cl_2$ releases the majority of its ND_3 before the LiD reacts which appears to be independent to the ND_3 release (LiD appears to react with the ND_3 from the diammine/monoammine). Tsuboto *et al.*[3] observed $LiNH_2$ formation when ball milling $Mg(NH_3)_6Cl_2$ so improved mixing would affect the wt. % of H_2 released by the system. Other methods will have to be employed.

5.4 $Mg(NH_3)_6Cl_2$ - MgH_2 'H_2 release' system

Following on from section 5.1 another H_2 release system involving the ammines is the $Mg(NH_3)_6Cl_2$-MgH_2 system that can theoretically release 4.5 wt. % H_2:

$$Mg(NH_3)_6Cl_2 + 3\ MgH_2 \rightarrow MgCl_2 + 3\ Mg(NH_2)_2 + 6\ H_2 \qquad (5.6)$$

This system has been studied by thermal programmed desorption (TPD) and Powder Neutron Diffraction (PND).

5.4.1 Thermal Programmed Desorption (TPD) analysis of the $Mg(NH_3)_6Cl_2$ and MgH_2 system

The $Mg(NH_3)_6Cl_2$-MgH_2 was prepared as per section 5.2.3. The TGA-DTA curve produced by heating the $Mg(NH_3)_6Cl_2$ - MgH_2 mixture (sample **5**) can be seen in Figure 5.16:

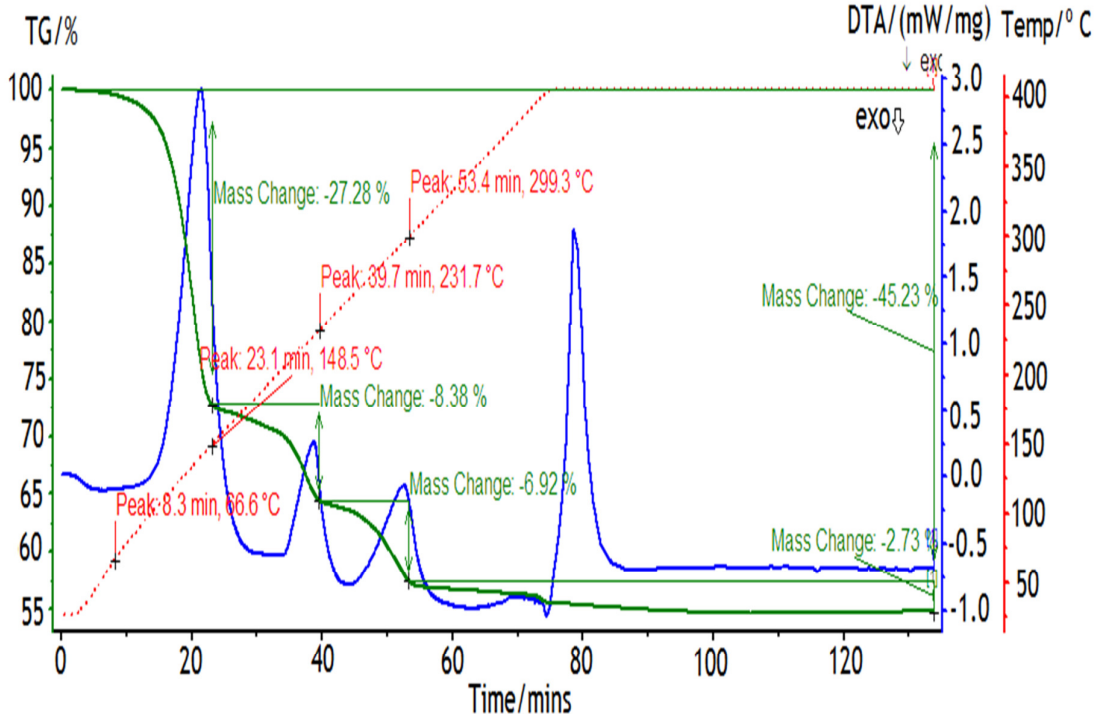

Figure 5.16: TGA-DTA curve for the $Mg(NH_3)_6Cl_2$ + MgH_2 mixture (sample **5**)

As can be seen in Figure 5.16 there are four weight loss steps. The first weight loss step of 27.42 wt. % occurs between 67 °C and 149 °C. This weight loss step is similar to that one of the $Mg(NH_3)_6Cl_2$ + LiH system which involved the

decomposition of $Mg(NH_3)_6Cl_2$ to $Mg(NH_3)_6Cl_2$ (theoretical weight loss of 34.4 wt. % on its own). The DTA trace shows that this weight loss corresponds to large endothermic event which would indicate the loss of 4 NH_3.

The second weight loss step commences between 149 ^oC and 232 ^oC with a weight loss of 8.38 wt. %. This weight loss is similar to that of the decomposition of $Mg(NH_3)_2Cl_2$ to $Mg(NH_3)Cl_2$, which has a theoretical weight loss value of 8.6 wt. %. In the DTA trace this weight loss corresponds to an endothermic event

There is then a further weight loss value of 6.92 wt. % between 232 ^oC and 299 ^oC. This could be due to the further deammoniation of $Mg(NH_3)Cl_2$ to $MgCl_2$ although the weight loss value is 1.7 wt. % less than the theoretical weight loss value. MS data (Figure 5.17) shows a constant evolution of NH_3 throughout heating so NH_3 continues to be released during this step. The DTA curves (three endothermic events) are similar to that seen for the decomposition of $Mg(NH_3)_6Cl_2$ only.

The final weight loss step commences at 300 ^oC and is complete at 400 ^oC with a weight loss of 2.73 wt. % which corresponds with a large endothermic event in the DTA data commencing at 375 ^oC. MS data (Figure 5.19) shows at this stage the evolution of H_2. After this weight loss, there is no further weight loss concluding that the reaction has gone to completion during the hold period at 400 ^oC.

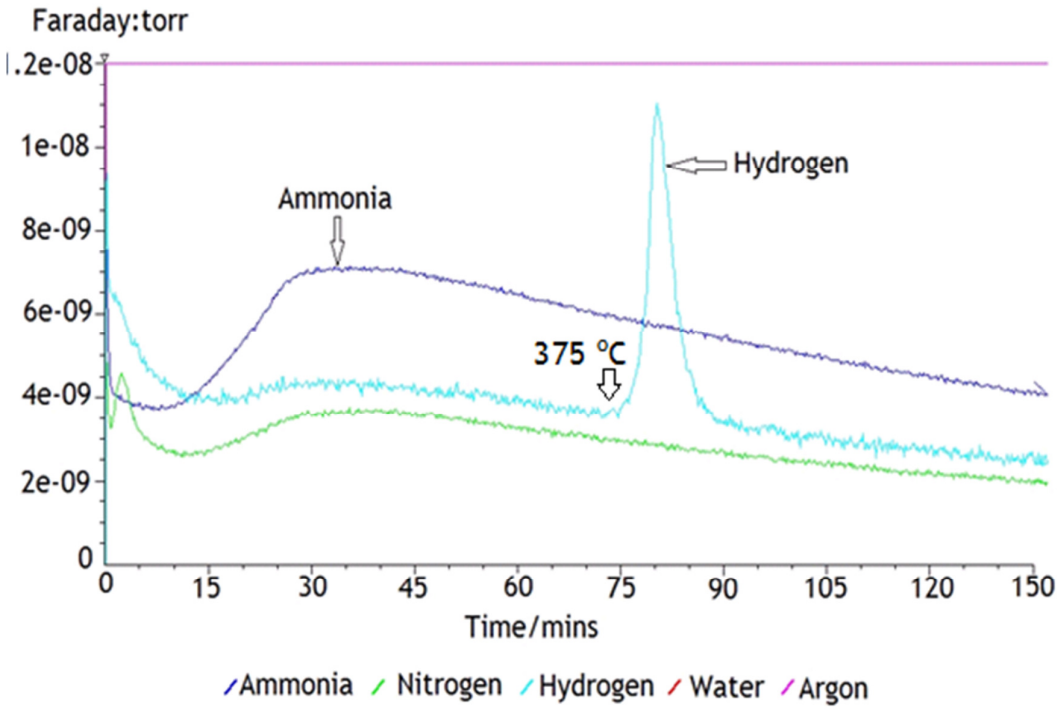

Figure 5.17: MS profile for sample **5** showing the NH_3 and H_2 release

PXD analysis (Figure 5.18) has been carried out on the post TPD product. $MgCl_2$ is present along with $Mg(NH_2)_2$ which are the expected end products of the reaction of equation 7. There are unidentifiable phases (particularly at $2\Theta = 37^{o}$) which could be assigned to MgO which could be due to the sample being exposed to air during the transfer between glove boxes or during the sealing of the capillary.

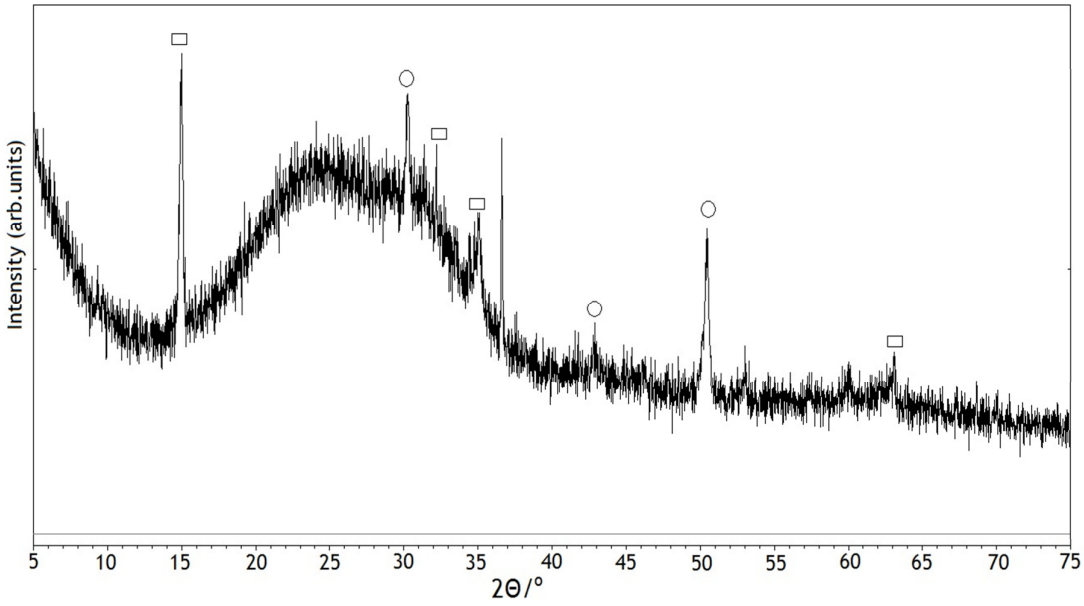

Figure 5.18: PXD of sample **5** post TPD. The rectangles indicate reflections from $MgCl_2$ and the circles indicate the reflections from $Mg(NH_2)_2$. The phase at 37° is Mg

5.4.2 Intermediate Study of the $Mg(NH_3)_6Cl_2$ + MgH_2 system at 160 °C

In order to determine the intermediate products after the first weight loss and thermal event, a mixture of $Mg(NH_3)_6Cl_2$ and LiH was heated to 170 °C at a heating rate of 5 °C per minute and held at 170 °C for 30 minutes. This temperature was the optimum temperature to isolate the intermediates. The TG-DTA profile for sample **6** can be seen in Figure 5.19:

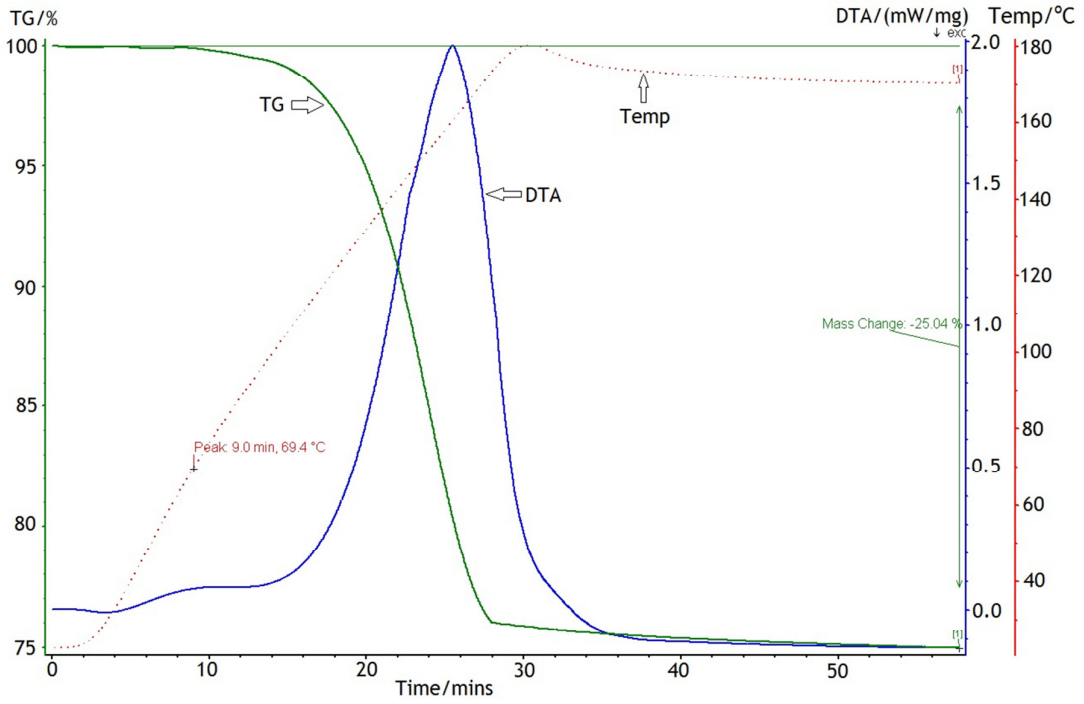

Figure 5.19: TGA-DTA profile for sample **5** heated to 170 °C

As can be seen in Figure 5.19, the onset of reaction is 69 °C which is comparable to that of the mixture heated to 400 °C. There is one coincident endothermic event which corresponds to the DTA curve for the first weight loss step of $Mg(NH_3)_6Cl_2$ only (section 3.4.1). The weight loss of 25.04 wt. % is below than that expected for the loss of 4 NH_3 (32.8 wt. %). This could be due to some decomposition of $Mg(NH_3)_6Cl_2$ prior to the TPD experiment during the mixing process. The MS profile (Figure 5.20) also shows that NH_3 is evolved.

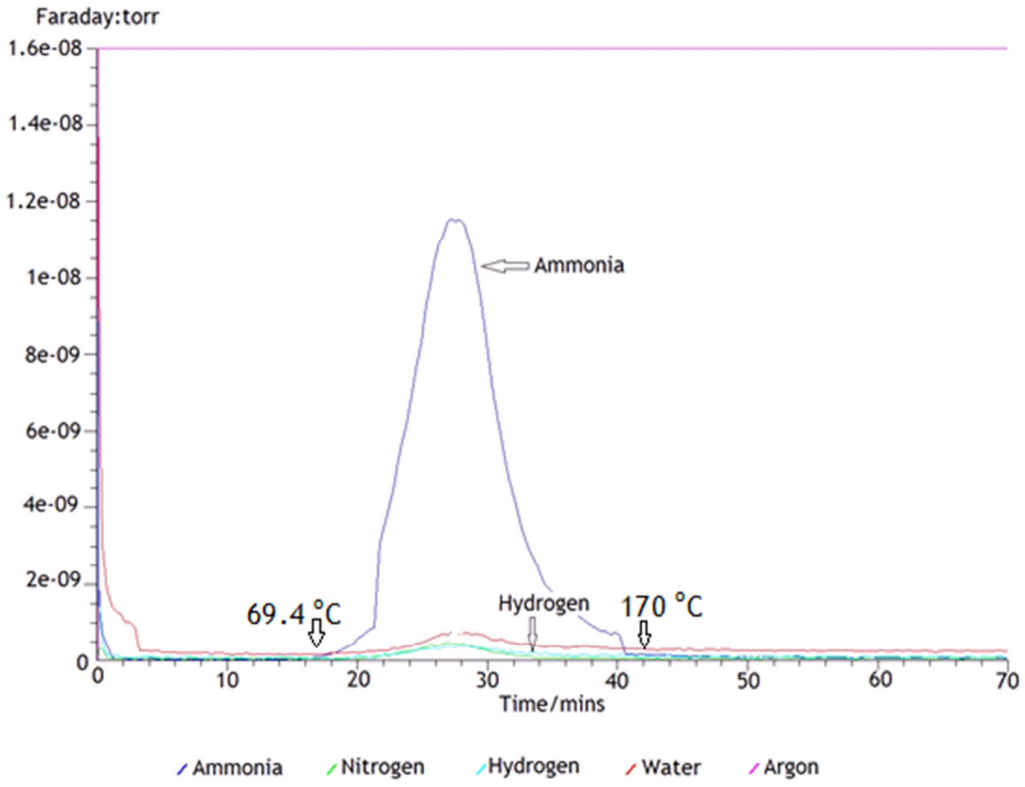

Figure 5.20: MS profile for sample **6** heated to 170 °C

The post TPD sample was then analysed using PXD with $Mg(NH_3)_2Cl_2$ and MgH_2 both present (Figure 5.21).

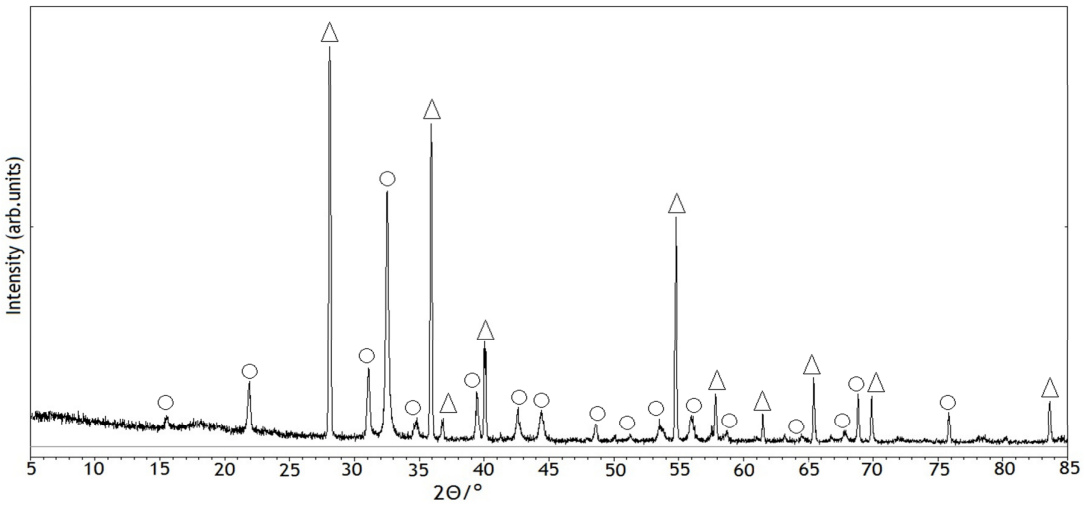

Figure 5.21: PXD of the post TPD product of sample **6**. The circles indicate reflections from the $Mg(NH_3)_2Cl_2$ phase and the triangles indicate the reflections from the MgH_2 phase

From the TPD and PXD data it can be determined that the first stage of the reaction for the $Mg(NH_3)_6Cl_2$ and MgH_2 system is analogous to the situation in the $Mg(NH_3)_6Cl_2$ and LiH system, through the decomposition of $Mg(NH_3)_6Cl_2$:

$$Mg(NH_3)_6Cl_2 + 3\ MgH_2 \rightarrow Mg(NH_3)_2Cl_2 + 3\ MgH_2 + 4\ NH_3 \quad (5.7)$$

5.4.3 PND study of the $Mg(ND_3)_6Cl_2$ + MgH_2 system

In order to study the mechanisms involved in the H_2 release in the $Mg(NH_3)_6Cl_2$ and MgH_2 system, an in-situ PND experiment was carried out on GEM at ISIS.

As per the $Mg(NH_3)_6Cl_2$ and LiH system, $Mg(ND_3)_6Cl_2$ was used in place of $Mg(NH_3)_6Cl_2$. MgD_2 was unsuccessfully synthesised in the lab prior to the experiment so MgH_2 was used. This is not ideal due to the large incoherent scattering of hydrogen but the experiment did allow a greater understanding of the system to be evolved. Stoichiometric amounts of $Mg(ND_3)_6Cl_2$ (as synthesised in section 3.3.4) and MgH_2 (Alfa, 98%) were hand mixed by mortar and pestle on the day of measurement at ISIS according to the proposed reaction (based on the hydrogen containing system):

$$Mg(ND_3)_6Cl_2 + 3\ MgH_2 \rightarrow MgCl_2 + 3\ Mg(ND_2)_2 + 6\ HD \quad (5.8)$$

The temperature points measured were: 25 ^oC, 125 ^oC, 150 ^oC, 160 ^oC, 210 ^oC, 230 ^oC, 275 ^oC, 305 ^oC and 400 ^oC

5.4.3.1 In Situ PND results for the $Mg(ND_3)_6Cl_2$ and MgH_2 system

The reaction changes associated with heating the $Mg(ND_3)_6Cl_2$ and MgH_2 system can be seen in Figure 5.22 (sample **7**).

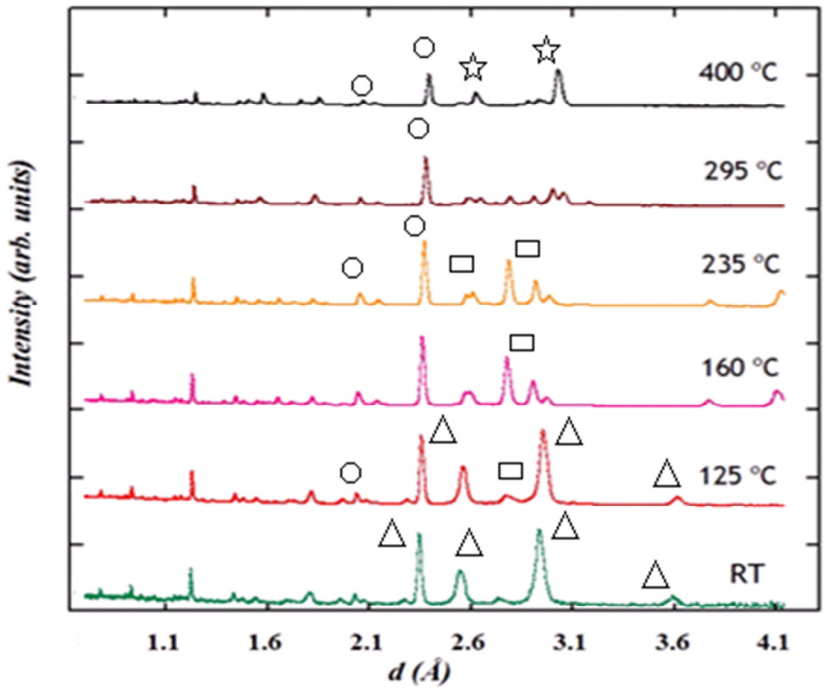

Figure 5.22: Effect of heating on the $Mg(ND_3)_6Cl_2$ and MgH_2 with respect of the Bank 4 data. RT refers to room temperature (25 ^oC). The triangles represent reflections from $Mg(ND_3)_6Cl_2$, the squares represent reflections from $Mg(ND_3)_2Cl_2$, the stars represent $MgCl_2$ and the circles represent reflections from MgH_2.

At room temperature, there are three phases present in the sample. These phases are $Mg(ND_3)_6Cl_2$, MgH_2 and $Mg(ND_3)_2Cl_2$. The orthorhombic $Mg(ND_3)_2Cl_2$ phase has also been seen for the $Mg(ND_3)_6Cl_2$ + LiD system and is likely due to decomposition of the $Mg(ND_3)_6Cl_2$ during mixing. Selected crystallographic data are presented in Table 5.6 and Figure 5.23.

Table 5.6: Crystallographic data for the $Mg(ND_3)_6Cl_2$ and MgH_2 system at 25 °C

Phases	$Mg(ND_3)_6Cl_2$	MgH_2	$Mg(ND_3)_2Cl_2$
Fractions (% .wt):	50.2(8)	29.7(8)	20.1(6)
Crystal System	Cubic	Tetragonal	Orthorhombic
Space Group	$Fm\bar{3}m$	$P4_2/mnm$	$Cmmm$
a/Å	10.184(14)	4.150(5)	7.670(4)
b/Å			8.196(3)
c/Å		3.0174(4)	3.912(15)
Volume/Å^3	1056.335(5)	61.353(1)	246.530(2)
Z	4	2	2
Formula Weight/g	862.020	52.642	270.618
Density, p_x/gcm^{-3}	1.355	1.424	1.823
No of observations		3730	
No of variables		69	
R_{wp}		0.0947	
R_p		0.3252	
χ^2		4.720	

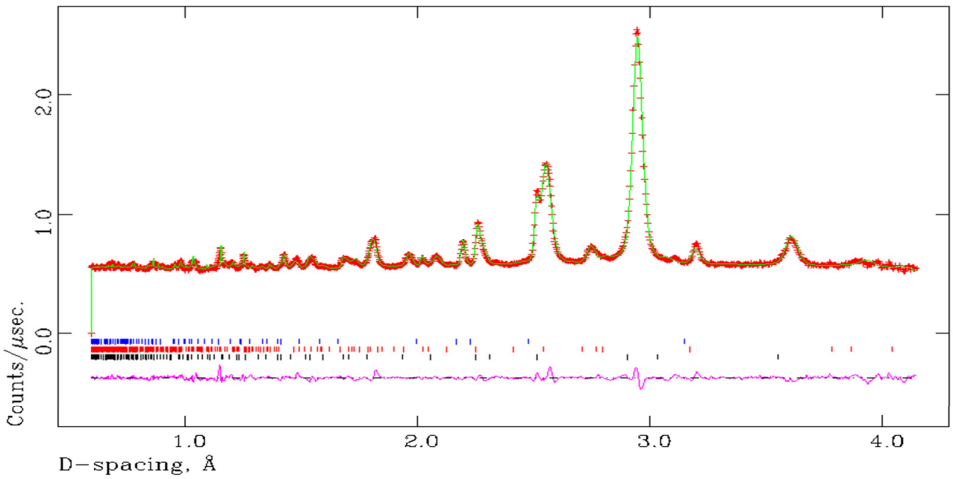

Figure 5.23: Observed, Calculated and difference (OCD) plot for the structural refinement of sample **6** using bank 4 data at 25 °C. The blue tick marks indicate reflections the $Mg(ND_3)_6Cl_2$ phase, the red tick marks indicate reflections from the $Mg(ND_3)_2Cl_2$ phase, and the black tick marks indicate reflections from the MgH_2 phase.

At 125 °C, $MgCl_2$ is also seen in addition to the three phases seen at RT. As per the $Mg(ND_3)_6Cl_2$ and LiD system this is due to the decomposition of $Mg(ND_3)_6Cl_2$ (which may be during mixing and the sample has lost ND_3 after synthesis during storage). The fraction of $Mg(ND_3)_2Cl_2$ is less than at 25 °C indicating that decomposition of the $Mg(ND_3)_6Cl_2$ is not yet fully under way. Selected crystallographic data for this temperature point, with phrase fractions can be seen in Table 5.7 and Figures 5.24 and 5.25.

Table 5.7: Crystallographic data for the $Mg(ND_3)_6Cl_2$ and MgH_2 system at 125 °C

Phases	$Mg(ND_3)_2Cl_2$	MgH_2	$Mg(ND_3)_6Cl_2$	$MgCl_2$
Phrase Fractions (% .wt):	6.5(2)	25.2(1)	42.2(2)	26.1(3)
Crystal System	Orthorhombic	Tetragonal	Cubic	Trigonal
Space Group	*Cmmm*	$P4_2/mnm$	$Fm\bar{3}m$	$R\bar{3}m$
a/Å	7.862(3)	4.508(3)	10.212(8)	3.639(4)
b/Å	8.045(2)			
c/Å	3.887(1)	3.016(2)		17.726(4)
Volume/Å^3	245.85(2)	61.285(1)	1065.08(8)	203.24(5)
Z	2	2	4	3
Formula Weight/g	270.618	52.642	862.020	285.633
Density ,p_x/gcm^{-3}	1.828	1.426	1.344	2.334
No of observations		3730		
No of variables		80		
R_{wp}		0.0947		
R_p		0.1474		
χ^2		1.298		

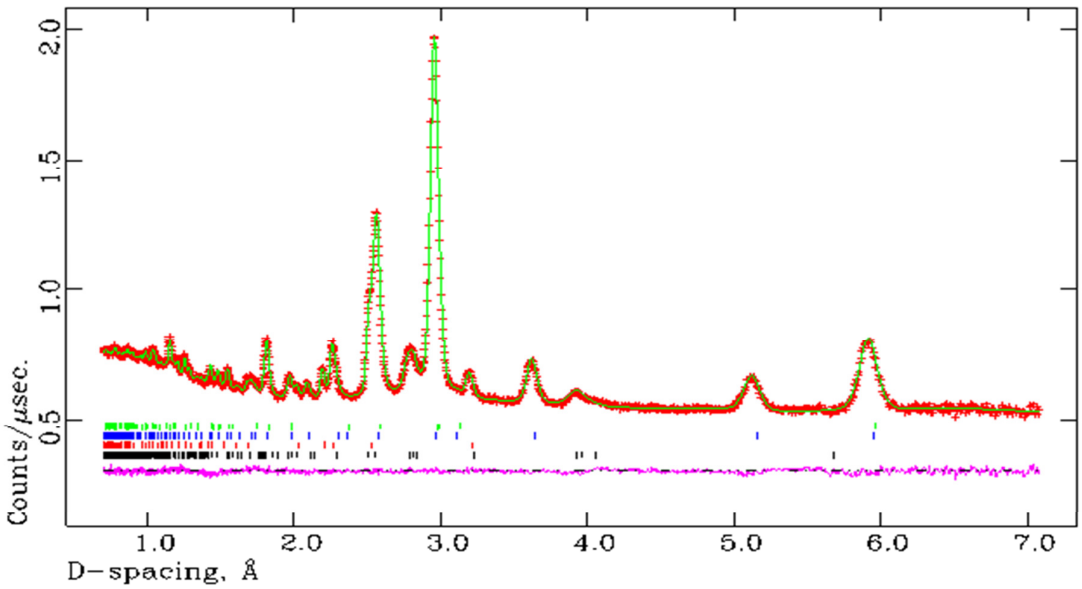

Figure 5.24: Observed, Calculated and difference (OCD) plot for the structural refinement of sample **6** using bank 3 at 125 °C. The green tick marks indicate reflections the $Mg(ND_3)_2Cl_2$ phase, the blue tick marks indicate reflections from the MgH_2 phase, the red tick marks indicate reflections from the $Mg(ND_3)_6Cl_2$ phase and the black tick marks indicate reflections from the $MgCl_2$ phase.

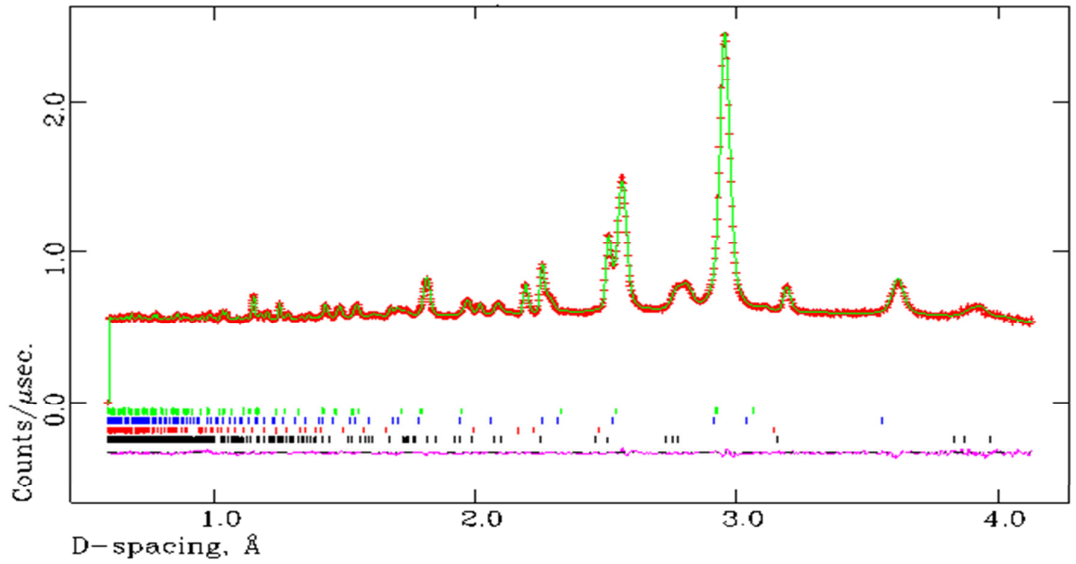

Figure 5.25: Observed, Calculated and difference (OCD) plot for the structural refinement of sample **6** using bank 3 at 125 °C. The green tick marks indicate reflections the $Mg(ND_3)_2Cl_2$ phase, the blue tick marks indicate reflections from the MgH_2 phase, the red tick marks indicate reflections from the $Mg(ND_3)_6Cl_2$ phase and the black tick marks indicate reflections from the $MgCl_2$ phase.

At 150 °C, the same four phases as per 125 °C are present indicating the first stage of the reaction seen in the TPD experiments involving the deammoniation of $Mg(ND_3)_6Cl_2 \rightarrow Mg(ND_3)_2Cl_2$ has yet to have gone to completion. The unit cell of the hexaammine continues to expand, with the unit cell now at 10.263(14) Å due to thermal expansion. At 160 °C, three phases are now only present compared to four phases at the previous temperature measured. The phases present are $Mg(ND_3)_2Cl_2$, MgH_2 and $MgCl_2$. From this data it is concluded that full decomposition to $Mg(ND_3)_2Cl_2$ from $Mg(ND_3)_6Cl_2$ had occurred in accordance with the TPD data and the first step of the reaction is:

$$Mg(ND_3)_6Cl_2 + 3\ MgH_2 \rightarrow Mg(ND_3)_2Cl_2 + 3\ MgH_2 + 4\ ND_3 \qquad (5.9)$$

Selected crystallographic or the160 °C sample are presented in Tables 5.8 and Figures 5.26 and 5.27. Atomic parameters are presented in the appendix

Table 5.8: Crystallographic data for the $Mg(ND_3)_6Cl_2$ and MgH_2 system at 160 °C

Phases	$Mg(ND_3)_2Cl_2$	MgH_2	$MgCl_2$
Phrase Fractions (% .wt)	52.4(4)	29.7(2)	17.9(2)
Crystal System	Orthorhombic	Tetragonal	Trigonal
Space Group	*Cmmm*	*P42/mnm*	$R\bar{3}m$
a/Å	8.171(12)	4.510(4)	3.643(4)
b/Å	8.209(8)		
c/Å	3.775(4)	3.018(3)	17.712(4)
Volume/Å^3	253.253(7)	61.369(1)	203.569(5)
Z	2	2	3
Formula Weight/g	270.618	52.642	285.633
Density, ρ/gcm^{-3}	1.774	1.424	2.330
No of observations	3582		
No of variables	73		
R_{wp}	0.0255		
R_p	0.2574		
χ^2	2.255		

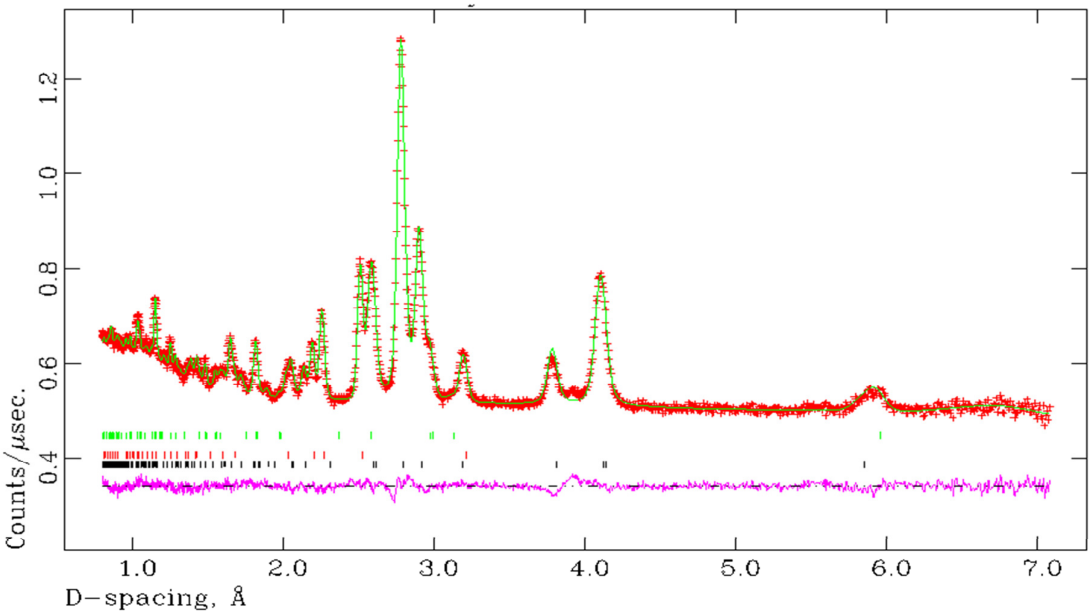

Figure 5.26: Observed, Calculated and difference (OCD) plot for the structural refinement of sample **6** using bank 3 at 160 °C. The green tick marks indicate reflections the $Mg(ND_3)_2Cl_2$ phase, the red tick marks indicate reflections from the MgH_2 phase and the black tick marks indicate reflections from the $MgCl_2$ phase.

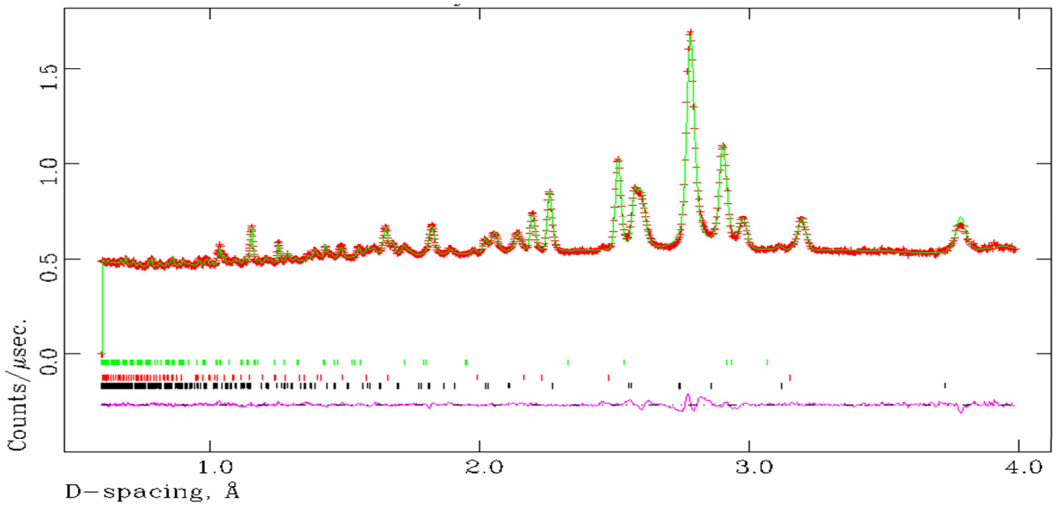

Figure 5.27: Observed, Calculated and difference (OCD) plot for the structural refinement of sample **6** using bank 4 at 160 °C. The green tick marks indicate reflections the $Mg(ND_3)_2Cl_2$ phase, the red tick marks indicate reflections from the MgH_2 phase and the black tick marks indicate reflections from the $MgCl_2$ phase.

From Table 5.8, it can be seen that there is thermal expansion of the lattice parameters. At this temperature, there is no indicating of a decrease in the weighted fraction of MgH_2 indicating that H_2 release is not yet occurring. The reflection at approximately 3.9 Å could not be assigned and may be a reflection from the monoammine phase (see Chapter 4).

At 210 ^oC, the same three phases are present as per 160 ^oC, $Mg(ND_3)_2Cl_2$, MgH_2 and $MgCl_2$. The phase fractions have altered slightly, with 48.7 wt. % $Mg(ND_3)_2Cl_2$, 30.1 wt. % MgH_2 and 21.2 wt.% with respect to $MgCl_2$. The biggest difference between this temperature point is the small increase in $MgCl_2$ indicating further deammoniation (although no reflections from a monoammine phase were seen). Compared to 160 ^oC, the reaction is at a similar stage at 210 ^oC and there is no significant structural or phase changes. The OCD plot of the refined data for this point is presented in the Appendix.

At 230 ^oC, the same phases are present as per 160 ^oC and 210 ^oC which leads to the conclusion from H_2 release from MgH_2 has not yet occurred. Selected crystallographic data with atomic parameters and bond lengths and angles are presented in the Appendix. The N-D bond distance in the diammine is similar to that in the literature (0.9615 Å).[12] The Mg-H bond distance in the MgH_2 is however elongated compared to the literature value of 1.13 Å which would be expected during heating.[15]

At 275 ^oC, the same three phases are present. Refinement at this temperature point proved especially difficult due to the background in this data set, likely due to the scattering of hydrogen in the hydride. Only Bank 3 data were successfully used for refinement. This also proved to be true for the 305 ^oC temperature point where the same phases were present ($Mg(ND_3)_2Cl_2$, MgH_2 and $MgCl_2$). At the 305 ^oC temperature point the refinement proved especially tricky, so a true understanding of what was occurring could not be obtained. Due to the high background, it could be associated with H_2 from the MgH_2 (the high background is typically associated with H containing compounds in PND). The lattice parameters of the three phases, $MgCl_2$, MgH_2 and $Mg(ND_3)_2Cl_2$ are presented in Table 5.9:

Table 5.9: Lattice parameters at 305 °C

Phase	a (Å)	b (Å)	c (Å)	Fraction (wt. %)
$MgCl_2$	3.635(3)		16.822(3)	16.4(5)
MgH_2	4.429(4)		3.271(4)	30.2(8)
$Mg(ND_3)_2Cl_2$	8.260(11)	8.775(12)	4.073(3)	53.4(7)

As can be seen in Table 5.10 the weighted fraction of the diammine phase has decreased from 51.7 % to 16.4% indicting further deammoniation as the $MgCl_2$ fraction has also increased from 16.6 % at 230 °C while the weighted fraction of MgH_2 is relatively unchanged. Due to the background, any evidence of the possible monoammine phase could be seen. From this data set and previous data sets at lower temperatures it can be concluded that H_2 releasing is not occurring between 25 °C and 305 °C (as per the TPD data).

At 400 °C, the background had appeared to return to a reasonable level for high d spacing (>2 Å). From the PND data, both $MgCl_2$ and $Mg(ND_2)_2$ (*$I4_1/acd$*)[13] could be matched and $MgCl_2$, $Mg(ND_2)_2$ and Mg matched the reflections when the ex-situ PXD was run through the High Score database. The PND suggest that, correspond with TG-DTA-MS that H_2 is occurring at the end step of deammoniation (MgH_2 decomposes at 400 °C independently [16]).

From the PND data it can be concluded that the $Mg(NH_3)_6Cl_2$ –MgH_2 needs considerable improvement as mixing at 25 °C is insufficient for favourable H_2 release.

5.5 Conclusion

Two possible '*H_2 release*' systems involving $Mg(NH_3)_6Cl_2$ and a metal hydride (LiH, MgH_2) have been investigated. Hand mixing was performed at room temperature in order to minimise decomposition of the $Mg(NH_3)_6Cl_2$ during mixing. For both systems, using TPD measurements H_2 release has been seen from the MS data, although this occurred after NH_3 release from the ammine. In terms of onset temperature for the release of H_2, the $Mg(NH_3)_6Cl_2$ and LiH is favoured. Although, in the case of both systems the theoretical weight loss values were well exceeded suggesting that the mixing process would have to be improved. However, the drawback of improved mixing (for example ball milling) could be decreased H_2 content in the system due to the decomposition of $Mg(NH_3)_6Cl_2$ when mixed with the appropriate hydride.[3]

In situ PND experiments have been carried out for the $Mg(ND_3)_6Cl_2$ –LiD system and the $Mg(ND_3)_6Cl_2$ –MgH_2. MgH_2 has been used due to the difficulties encountered attempting to synthesise MgD_2 in time for the PND experiment. For both systems, hand mixing at room temperature results in some decomposition of $Mg(ND_3)_6Cl_2$ to $Mg(ND_3)_2Cl_2$. In both systems the first step in the reaction is the decomposition of $Mg(ND_3)_6Cl_2$ to $Mg(ND_3)_2Cl_2$. $MgCl_2$ is also present at low temperatures (150 ^oC) but this is likely due to the decomposition of the $Mg(ND_3)_6Cl_2$ produced during mixing (as the ammonia starts to release at low temperatures) and sample quality.

For the $Mg(ND_3)_6Cl_2$ –LiD reaction at 270 ^oC $LiND_2$ has been assigned in the PND data along with $MgCl_2$ and its diammine. This indicates that H_2 release occurs at this temperature corresponding with the TG-DTA-MS data which could be similar to the LiH + NH_3 reaction.[9] The weighted fraction of LiD was also seen to be decreasing at 230 ^oC which could suggest the beginning of the reaction with the ammine. For this system LiD is not involved during the main deammoniation step of the hexaammine and diammine. From the PND data coupled with the TG-DTA-MS to improve the H_2 release temperature (and minimising NH_3 release) then steps must be undertaken improve the system so that the hydride will react with the ammine at the lower temperature required. This could include ball milling [17] and other nanostructuring techniques.

The in-situ PND data for the $Mg(ND_3)_6Cl_2$ –MgH_2 that at low temperatures MgH_2 is not involved in the reaction with only deammoniation of the ammine occurring with no reaction of the ND_3 with the MgH_2. $H_2(D_2)$ only occurs at towards the end of the deammoniation process at elevated temperatures (~400 ^oC). There was no evidence of any H_2 before this point as the weighted fraction of MgH_2 remains relatively constant. Improvements to this system are needed as the MgH_2 decomposition temperature is too high for reaction with the ammine so similar approaches to the corresponding LiH(D) system could be employed.

5.6 References

[1] R. Z. Sørensen, J. S. Hummelshoj, A. Klerke, J. B. Reves, T. Vegge, J. K. Norskov and C. H. Christensen, *J. Am. Chem. Soc*., 2008, **130**, 8660.

[2] H. Y. Leng, T. Ichikawa, S. Hino and H. Fujii, *J. Alloys Compd*., 2008, **463**, 462.

[3] M. Tsuboto, S. Hino, H. Fujii, C. Oomatsu, M. Yamana, T. Ichikawa and Y. Kojima, *Int. J. Hydrogen Energy*., 2010, **35**, 2058.

[4] S. Isobe, T. Ichikawa, Y. Kojima and H. Fujii, *J. Alloys Compd*., 2007, **446**, 360.

[5] W. G. Williams, R. M. Ibberson, P. Day and J. E. Enderby*, Physica B*, 1998, **234**, 241.

[6] A. C. Hannon, *Nucl. Instrum. Methods Phys. Res. A*, 2005, **551**, 81.

[7] A. C. Larson and R. B. von Dreele, The General Structure Analysis System, Los Alamos National Laboratories, Report LAUR 086–748, LANL, Los Alamos, NM, 2000

[8] B.H. Toby, *J. Appl. Crystallogr.,* 2001, **34**, 210.

[9] Y. H. Hu and E. Ruckenstein, *J. Phys. Chem. A*, 2003, **107**, 9337.

[10] M. H. Sørby, O. M. Løvvik, M. Tsuboto, T. Ichikawa, Y. Kojima and B. C. Hauback, *Phys. Chem. Chem. Phys.,* 2011, **13**, 7644.

[11] J. P. Vidal and G. Vidal-Valet, *Acta. Crystallogr. B*., 1986, **42**, 131.

[12] A. Leinweber, M. W. Fredriszik and H.Jacobs, *J. Solid. State. Chem.,* 1999, **147**, 229.

[13] M. H.Sørby, Y. Nakamaura, H. W. Brinks, T. Ichikawa, H. Fujii and B. C. Hauback, *J. Alloys Compd*., 2007, **428**, 297

[14] Y. H. Hu and E. Ruckenstein, *J. Phys. Chem. A*, 2003, **107**, 9337.

[15] I. E. Malka, A. Blachowski, K. Ruebenbauer, J. Przewoznik, J. Zukrowski, T. Czujko and J. Bystrzycki, *J. Alloys Compd*., 2011, **209**, 5368.

[16] J. F. Fernandez and C. R. Sanchez, *J. Alloys Compd*., 2003, **356**, 348.

[17] R. Ren, A. Ortiz, T. Markmaitree, W. Osborn and L. Shaw, *J. Phys. Chem. B*., 2006, **100**, 10567.

6. Microstructured Hydroxide- Hydride H_2 Release Systems

6.1 Introduction

Following on from Chapter 5, '*one shot*' H_2 release systems (ammines with hydrides) are a possible alternative to the hydrogen storage issue in principal. Hydroxides could be used in such a system.

$Mg(OH)_2$, which crystallises in the hexagonal $P\bar{3}m1$ space group could be a suitable such hydroxide as it can indirectly store 4.83 wt. % H_2 in the form of H_2O. $Mg(OH)_2$ decomposes to its oxide with the release of H_2O when heated:

$$Mg(OH)_2 \rightarrow MgO + H_2O \qquad (6.1)$$

$Mg(OH)_2$ has previously been investigated as an integral component of a H_2 release system. The $Mg(OH)_2 + MgH_2$ system, which can theoretically release 4.5 wt. % H_2 has been investigated with three H_2 release steps observed between 150 ^oC and 450 ^oC.[1] The $Mg(OH)_2$- $NaBH_4$ system has also been investigated. PXD and Raman measurement suggest that this reaction occurs in two steps with the first step proceeding through the decomposition of $Mg(OH)_2$ as per equation 6.1, with the second step involving the reaction of $NaBH_4$ and the H_2O produced through the decomposition of $Mg(OH)_2$ (equation 6.2). No direct evidence for the reaction of $NaBH_4$ and H_2O were seen and no mass spectroscopy data was given which could show the evolution of H_2O and the subsequent H_2 release:[2]

$$NaBH_4 + 2\ H_2O \rightarrow NaBO_2 + 4\ H_2 \qquad (6.2)$$

One '*H_2 release*' system that has not been previously investigated is the $Mg(OH)_2$- LiH system. As a single component system, LiH can store 12.7 wt. % H_2 although the hydride requires a high temperature (> 680 ^oC) for decomposition.[3] By combining LiH with $Mg(OH)_2$ this system can theoretically release 5.44 wt. % H_2:[4,5]

$$Mg(OH)_2 + 2\ LiH \rightarrow MgO + Li_2O + 2\ H_2 \qquad (6.3)$$

Microstructuring both components of a '*H_2 release*' system has also not been previously reported. Increasing the surface area of both reactants of the system could improve the kinetics of hydrogen release.

In terms of its light weight and therefore gravimetric capacity, LiOH is an ideal component for a '*H_2 release*' system. LiOH crystallises in the tetragonal P4/nmm space group and can indirectly store 4.2 wt. % H_2.[6] Its hydrated form, $LiOH.H_2O$ which crystallises in the monoclinic *C2/m* space group can indirectly store 7.2 wt. % H_2. [7] Decomposition of both these materials leads to the formation of Li_2O with the release of H_2O.

LiOH and $LiOH.H_2O$ have been investigated in binary component systems with LiH by Lu *et al*. The theoretical storage capacity of these systems is 6.3 wt. % H_2 and 8.8 wt. % H_2 respectively :[8]

$$LiOH + LiH \rightarrow Li_2O + H_2 \quad (6.4)$$

$$LiOH.H_2O + 3\ LiH \rightarrow 2\ Li_2O + 3\ H_2 \quad (6.5)$$

Using bulk reactants, the onset temperature for equation 6.4 is around 150 ^oC with a final dehydrogenation temperature of 350 ^oC. In equation 6.5, the first step of the reaction occurs between room temperature and 70 ^oC, which corresponds to the formation of LiOH from $LiOH.H_2O$ and LiH with the release of H_2. The second higher temperature step is the formation of Li_2O from LiOH with the release of H_2 (equation 6.4). One possible solution to improve the kinetics of these systems, particularly the dehydrogenation reaction of the dehydrated hydroxide is to use nanostructured LiOH. The drawback to this is that no successful synthesis of nanostructured LiOH has been previously reported. This is likely in part due to the air sensitive nature of LiOH as it readily absorbs CO_2 in an ambient atmosphere.

Synthetic approaches to microstructured $Mg(OH)_2$ using conventional and microwave heating are described in this chapter. Synthetic approaches to produce nanostructured LiOH are also described in this chapter. Each hydroxide was subsequentially used as a component in a '*H_2 release*' system with ball milled hydrides.

Each '*H_2 release*' system is described and compared with the individual bulk components and bulk composite systems.

6.2 Experimental

6.2.1 Synthesis of $Mg(OH)_2$

6.2.1.1 Solvothermal Synthesis using Conventional Heating

Nanostructured $Mg(OH)_2$ has previously been synthesised by both solvothermal and hydrothermal synthesis.[9,10]

The hydothermal method used is that employed by Ding *et al*.[9] 0.033 moles of Mg powder (Alfa Aeser 98%) and 15ml of a solution of ethylenediamine (Acros, 99%) and deionised water (typically 8:1) were placed in a 23 ml Teflon-lined autoclave. Ethylenediamine is employed in the synthesis as plays a vital role in the nucleation and growth of the nanostructured $Mg(OH)_2$.[11] The ethylenediamine could act as a bidentate ligand to form an Mg^{2+} complex with the Mg and as the temperature increases, the stability decreases. This leads to hydroxyl groups coordinating to the complex which leads to gradual loss of the ethylenediamine (en) ligands. In the liquid phase the hydroxyl group attacks the Mg- N bonds (from the ethylenediamine) leading to the formation of Mg-O bonds with the Mg-N eventually being lost which in turn leads to the formation of $Mg(OH)_2$.[12] The autoclave was then heated in an oven at 180 ^oC for 20 hours with the reaction proceeding through equation 6.6.

$$Mg + 2\ H_2O + en \rightarrow Mg(OH)_2 + H_2 + en \qquad (6.6)$$

The obtained precipitate was then washed using water and ethanol, centrifuged and dried.

6.2.1.2 Synthesis Using Microwave heating

This synthesis is based on the MgO and H_2O reaction using conventional heating methods in that the same reactants (and quantities) are used.[13] 0.4 g of MgO (Sigma Aldrich, 98%) and 16 ml of deionised water were placed inside a 23 ml Teflon-lined autoclave suitable for microwave synthesis. The autoclave was

then heated inside a domestic microwave oven for six minutes. The reaction that occurs is described in equation 6.7. The product was dried in air overnight.

$$MgO + H_2O \rightarrow Mg(OH)_2 \qquad (6.7)$$

The reaction was scaled up using 0.8 g of MgO and 32 ml of deionised water and a 45ml Teflon-lined autoclave. Heating in a domestic microwave oven for 6 minutes results in ~1g product.

6.2.3 Synthesis of LiOH

In order to guarantee an inert atmosphere, inside an Ar filled recirculating glove box (Saffron), a molten Na pool was heated. The oxide layer in the Na pool, once molten was then skimmed off using a spoon leaving a shiny surface. (The surface of the Na pool becomes cloudy in the presence of oxygen and formation of oxide). A piece of Li metal (Alfa, 99.9%) was cleaned using a file before weighing in the glove box.

The weighed Li metal was quickly removed from the glove box and placed in a 23 ml Teflon-lined autoclave to which an 8:1 solution of ethylenediamine and water was added and heated at 180 ^{o}C for 20 hrs. Exposure of the cleaned Li metal was kept to a minimum by transferring the Li outside the glove box in a sealed vial prior to adding the H_2O:en solution.

6.2.4 Ball milling of LiH

Approximately 1 g of LiH (Sigma, 95%) were loaded into a 50 ml stainless steel jar with 10 stainless steel grinding balls in a N_2(g) atmosphere. The jar was then sealed using an air sensitive clamp and a rubber O-ring before removal from the glove box. The jar was then placed in a Retszch PM100 planetary ball mill. The LiH was then ball milled at 450 rpm for four hours. A rest time of 1 min per every 15 minutes of ball milling was used.

6.3 Characterisation

6.3.1 Powder X-ray diffraction (PXD)

The compounds synthesised were analysed using PXD as described in Section 2.3.3. Measurements were carried out either using capillaries on the Brucker D8 or using the flat plate on the PANalytical X'pert Pro for the synthesised $Mg(OH)_2$. For capillary measurements, data were collected between 5^o -75^o for one hour. For measurements on the X'pert, data were collected between 5^o- 85^o for a period of 20-25 minutes.

The obtained data were compared to known powder diffraction files using the ICSD database in PowderCell [14] or the ICDD database in the PANalytical HighScore program.

6.3.2 Lattice Parameters Refinement

The refinement of the unit cell parameters of the synthesised $Mg(OH)_2$ were performed using the CELLREF program.[15] In the CELLREF program, the raw PXD file was loaded into the program and the selection of peaks performed. The space group and unit cell parameters were then entered using a known structure in the literature.[16] Peak selection was then undertaken and then refinements of the cell parameters were performed by least squares fitting.

6.3.3 Rietveld Refinement against PXD data

Structures are refined using the GSAS program with an EXPGUI interface.[17,18]

The background was successfully fitted using background function 8 in GSAS, a reciprocal interpolation function. The cell parameters were then refined followed by the atomic positions. The peak profile coefficients, the zero point correction and isotropic temperature were then refined. Finally, all the refined parameters were then allowed to refine freely until convergence was achieved. Peak shape modelling was performed using function 2, which is a multi-term Simpson's integration of the Pseudo-Voight function

6.3.4 Scanning Electron Microscopy (SEM)

SEM samples were prepared as per section 2.7.3. A small amount of sample would be deposited onto a carbon tab attached to an aluminium stub. Preparation of SEM samples for air sensitive products was carried out inside a glove box. Exposure to air for the air sensitive samples was kept to a minimum by transferring the samples in sealed glass vials.

The sample was then transferred to the SEM sample chamber and the SEM chamber evacuated. Some samples were also gold plated in an Ar (g) atmosphere to minimise the charging of the sample. All Measurements were performed on a Phillips XL30 ESEM with a working distance of either 5 mm (for imaging) or 10 mm (for EDX analysis).

Samples requiring further SEM analysis, were then analysed on a Hitachi S4700 cold field SEM by Dr. Saleem Denholme at the James Watt Nanofabrication Centre, University of Glasgow or on a Zeiss Sigma field-emission analytical SEM by Peter Chung at the School of Geographical and Earth Sciences, University of Glasgow.

6.3.5 Microstructured $Mg(OH)_2$ – LiH "Hydrogen Release System"

Microstructured $Mg(OH)_2$ as synthesised in the MW (section 5.4.2) was hand mixed with LiH ball milled for four hours (Figure 5.6) for set periods of time (5, 10 and 15 minutes).

6.3.6 $Mg(OH)_2$ + LiH Mixing Times Results

Bulk $Mg(OH)_2$ + LiH and microstructured $Mg(OH)_2$ + LiH were hand mixed for 5, 10 and 15 minutes and then heated to 450 ^oC at 10 ^oC per minute and held at 450 ^oC for thirty minutes on the STA.

6.3.7 Summary of Reactions

Table 6.1: Summary of Reactions

Sample No	Material	Reaction Conditions
1	$Mg(OH)_2$	180 ^oC for 20 hrs
2	$Mg(OH)_2$	180 ^oC for 20 hrs
3	$Mg(OH)_2$	180 ^oC for 20 hrs
4	$Mg(OH)_2$	DMO for 6 mins
5	LiH	Ball milled for 4 hrs
6	Bulk $Mg(OH)_2$ + LiH	Mixed for 5 mins/heated to 450 ^oC
7	Micro $Mg(OH)_2$ + LiH	Mixed for 5 mins/heated to 450 ^oC
8	Bulk $Mg(OH)_2$ + LiH	Mixed for 10 mins/heated to 450 ^oC
9	Micro $Mg(OH)_2$ + LiH	Mixed for 10 mins/heated to 450 ^oC
10	Bulk $Mg(OH)_2$ + LiH	Mixed for 15 mins/heated to 450 ^oC
11	Micro $Mg(OH)_2$ + LiH	Mixed for 15 mins/heated to 450 ^oC
12	Micro $Mg(OH)_2$ + LiH	Mixed for 10 mins/heated to 240 ^oC
13	Bulk $Mg(OH)_2$ + LiH	Mixed for 10 mins/heated to 500 ^oC

6.4 Results and Discussion

6.4.1 Synthesis of $Mg(OH)_2$ by Conventional Heating Results

The lab synthesised $Mg(OH)_2$ was a white, fine powder (sample **1**). Comparing the experimental PXD pattern (Figure 6.1) with the theoretical pattern (PDF file: 01-083-0144) resulted in a good agreement that $Mg(OH)_2$ had been successfully synthesised by solvothermal synthesis .

6.4.1.1 Powder X-ray Diffraction

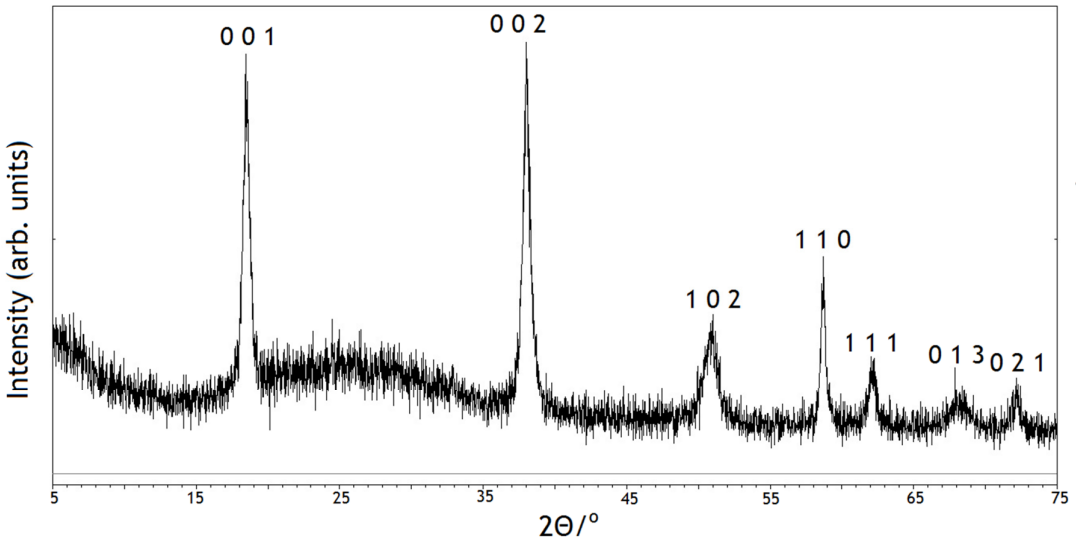

Figure 6.1: PXD of Sample **1.** Reflections are from the synthesised $Mg(OH)_2$

Reducing the concentration mass of Mg used for the synthesis resulted in the synthesis of $Mg(OH)_2$ but also a broadening of the Bragg peaks indicating a reduced particle size. Indexing of the samples was performed using CELLREF and the comparison of the lattice parameters can be seen in Table 6.2

Table 6.2: Lattice parameters of solvothermal synthesised $Mg(OH)_2$

Sample	Mg used (moles)	a($Å^3$)	c($Å^3$)	Volume
1	0.033	3.1419 (7)	4.7787 (8)	40.85 (1)
2	0.025	3.1418 (9)	4.7659 (11)	40.79 (2)
3	0.020	3.1418 (7)	4.7745 (8)	40.81 (1)

In table 6.2, it can be seen that sample **1** that has the highest concentration of Mg used during the synthesis has the largest unit cell and volume. Sample **2** and **3** have comparable unit cell sizes and volume although when comparing all three samples there is no significant difference when altering the concentration of Mg used in the synthesis. PXD analysis of the three samples showed a broadening of the peaks as the concentration of Mg used was decreased which indicates a smaller particle size.

Due to the en template used, $Mg(OH)_2$ synthesised by this method are not ideally suited for use in the '*H_2 release system*' as there is a small amount of template present in the final product as confirmed by TPD and C, H, N microanalysis where 2-3 wt. % carbon was present in the samples . TPD data confirms the presence of nitrogen in the sample. Furthermore the synthesis is time-consuming and the end product yield is small, so a new faster synthesis route which yields a greater wt. % of $Mg(OH)_2$ would be preferred.

6.4.1.2 Scanning Electron Microscopy of $Mg(OH)_2$

Initial SEM micrographs using the Phillips XL SEM showed agglomeration of the particles in the sample. The morphology of the samples was hexagonal microplates as confirmed by subsequent analysis using high resolution SEM as shown in Figure 6.2 (sample **3**). The obtained hexagonal microplates were typically 300-500 nm in diameter and uniform in shape. The thickness of the plates are typically 50-75 nm.

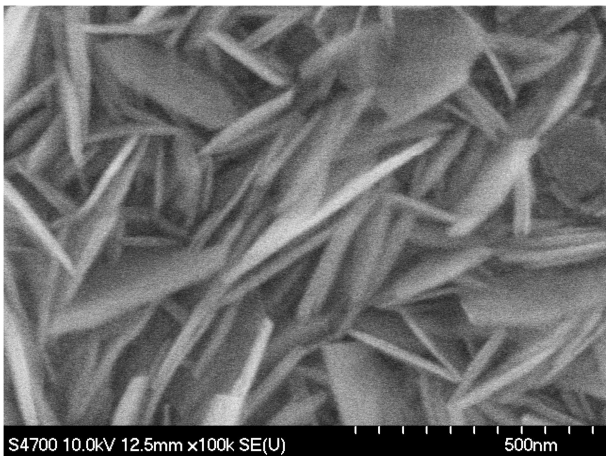

Figure 6.2: High resolution SEM image showing the morphology of sample **3** ($Mg(OH)_2$).

6.4.2 Microwave Preparations of $Mg(OH)_2$

In order to speed up the reaction time for the preparation from hours to a matter of minutes, MW heating was employed. The preparation was as per section 6.2.1.2. The starting MgO is a non-uniformed powder which contains lumps. During heating in the MW special attention is needed to ensure the pressure in the autoclave does not exceed its limits causing rupture of the autoclave to occur. To combat this, the microwave heating can be stopped and recommenced. After heating, the autoclave was allowed to cool to room temperature. The obtained product after drying was a white fine powder.

6.4.2.1 Powder X-ray Diffraction

Comparing the experimental pattern (sample **4**) with the calculated pattern (PDF no: 01-083-011) resulted in full conversion of the MgO to $Mg(OH)_2$ (Figure 6.3) by scaling up the reaction.

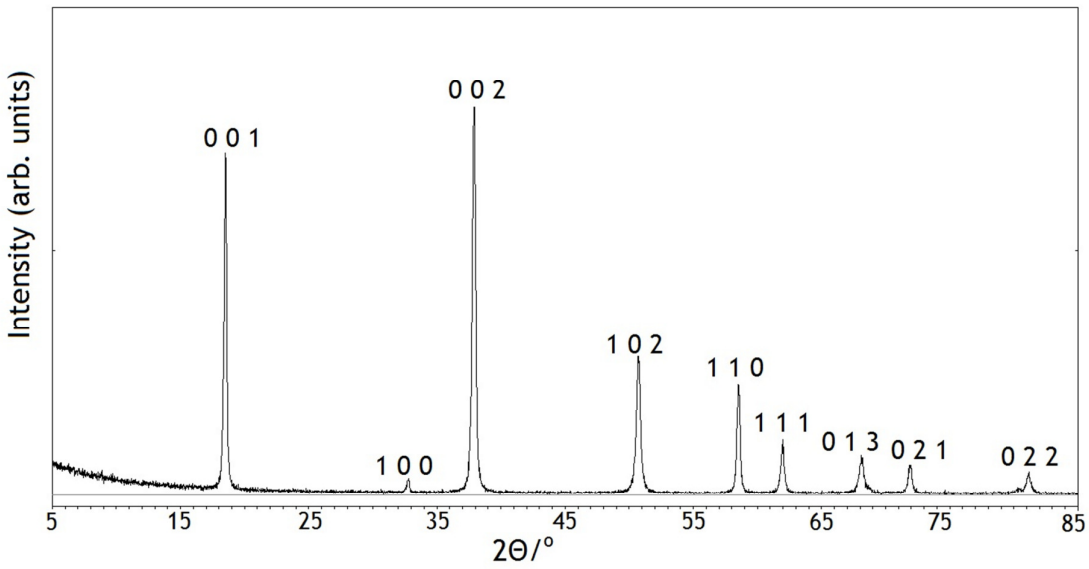

Figure 6.3: PXD of the MW synthesised sample **4**

Refinement resulted in cell parameters of a= 3.1486 (2) $Å^3$ and c= 4.7837 (2) $Å^3$ and a unit cell volume of 41.06 (1) which is in good agreement with the literature values.[16]

6.4.2.2 Rietveld Refinement of $Mg(OH)_2$

Rietveld Refinement were then performed for the MW synthesised $Mg(OH)_2$ (Figure 6.4) in order to accurately determine the cell parameters and the positions of the atoms in the unit cell using known data from the literature.[16] The Rietveld refinement was performed as per section 6.3.3 with the background fitted with 14 terms. The $Mg(OH)_2$ pattern used in the refinement was that by Kazimirov *et al.*[16] The Rietveld refinement data is presented in Table 6.3 and the positions of the atoms and isotropic temperature factors are presented in Table 6.4.

The unit cell parameters obtained are comparable with that in literature. Chizmeshya *et al.*[19] obtained cell parameters of a= 3.149 Å and c= 4.752 Å and a cell volume of 40.81 which are very similar to the values obtained.

Table 6.3: Crystallographic data for the PXD refinement for $Mg(OH)_2$

Formula	$Mg(OH)_2$
Crystal System	Hexagonal
Space Group	$P\bar{3}m1$
a/ Å^3	a= 3.1483 (1)
c/ Å^3	4.722 (3)
Volume/Å^3	40.963
Z	1
Formula Weight/g	58.319
Density (p_x/gcm^{-3})	2.364
No of observations	4787
No of variables	25
R_{wp}	0.0723
R_p	0.1636
X^2	1.645

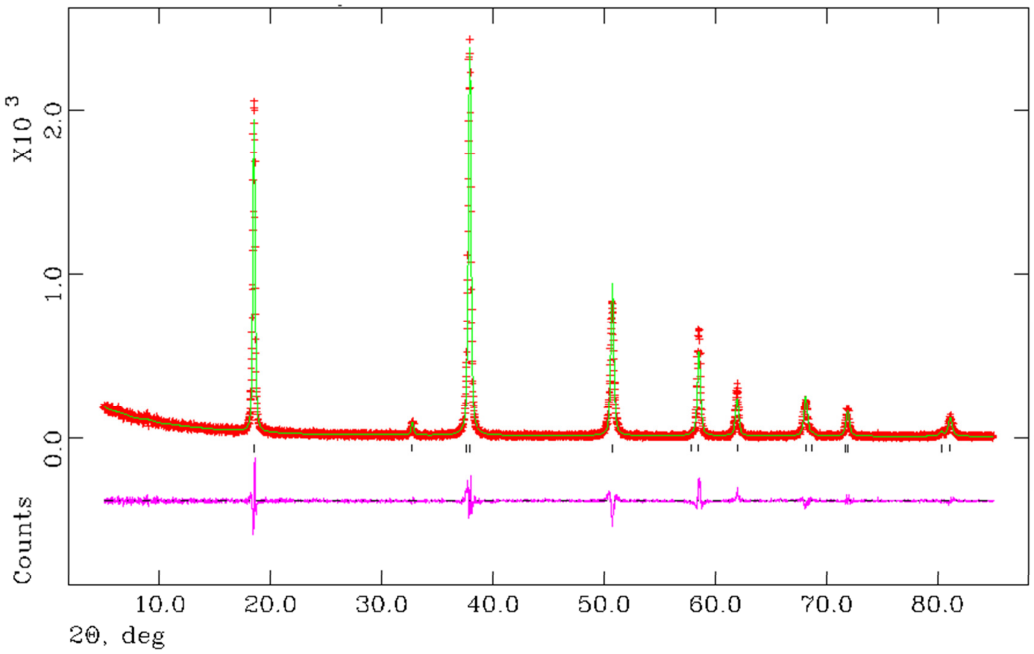

Figure 6.4: Rietveld Refinement OCD (observed (green), calculated (red tickmarks) and difference (purple line) plot of sample **4**. Black tick marks indicate reflections from $Mg(OH)_2$

Table 6.4: Atomic parameters of the MW synthesis of $Mg(OH)_2$

Atom /Site	x	y	z	Occupancy	100/Å^2 x U_{iso}
Mg /1a	0	0	0	1	2.67(1)
O /2d	0.3333	0.667	0.2200(5)	1	3.10(2)
H/2d	0.3333	0.6667	0.4211	1	2.5

6.4.2.3 Scanning Electron Microscopy of MW synthesis of $Mg(OH)_2$

High resolution SEM micrographs for sample show that the obtained morphology was that of hexagonal sub-micron microplates (Figures 6.5). These microplates have an average diameter of 400-600 nm.

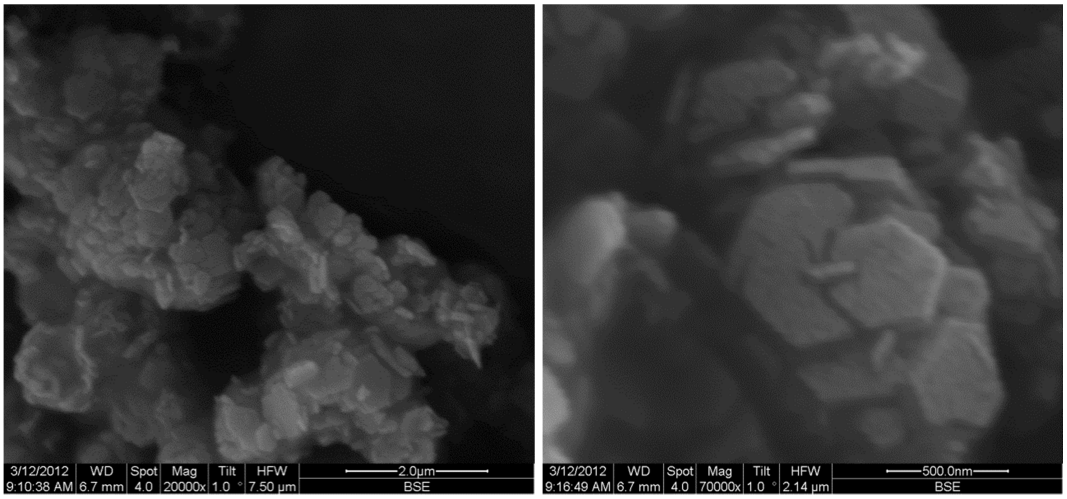

Figures 6.5 (a) and (b): SEM micrographs showing the hexagonal microplate morphology of the MW prep of sample **4**

6.4.3 Preparation of LiOH Results: Oven based Synthesis

The preparation of LiOH is described in section 5.2.3. Unfortunately, attempts to synthesise nanostructured LiOH proved unsuccessful. Transparent needle-like crystals were produced when ethylenediamine was removed from the preparation. This resulted in a phase of $LiOH.H_2O$ but the sample was not pure phase lithium monohydrate. SEM analysis concluded that the sample was not nanostructured but consisted of irregular particles that were micron sized.

Further investigation is needed to obtain nanostructured LiOH for use in a '*H_2 release*' system

6.5 LiH Ball milling Results

Ball milling for four hours (Figure 6.6) resulted in uniform particles with sizes of 1 μm – 3 μm in diameter. Ball milling for longer periods resulted in agglomeration of particles in the sample.

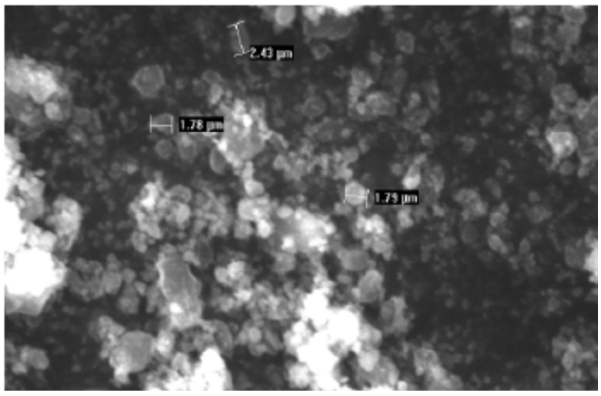

Figure 6.6: Ball milled LiH after four hours ball milling [4,5] (sample **5**)

6.6. *$Mg(OH)_2$ + LiH Mixing Times Results*

The results of the TG-DTA-MS experiments are presented in Table 6.5

Table 6.5: Data from TG-DTA-MS showing a comparison of mixing time on the H_2 release properties

Sample	Mixing time (mins)	Onset temperature (°C)	Weight loss (%)
Bulk (**6**)	5	142	5.28
Micro (**7**)	5	111	4.52
Bulk (**8**)	10	147	5.17
Micro(**9**)	10	79	4.86
Bulk (**10**)	15	132	4.90
Micro (**11**)	15	82	5.30

As can be seen in Table 6.5, using microstructured starting materials results in an improvement in the onset temperature of H_2 release when compared to using bulk starting materials. Hand mixing for 5 minutes results in a high onset temperature (142 ^oC) for bulk materials although the weight loss of 5.28 wt. % is the closer to the theoretical weight loss of 5.44 wt. %. The microstructured mixture mixed for 5 minutes has an improved onset temperature by 31 ^oC although the compromise of this is that the H_2 release content is decreased by 0.76 wt. %.

Mixing the microstructured materials for 10 mins results in the best onset temperature (79 ^oC) for all the mixtures. The microstructured mixture, which has been mixed for 15 minutes is the most encouraging mixture in terms of combining the onset temperature of the reaction and also the weight loss. The weight loss is the closest to that of the theoretical weight loss of the reaction (0.14 wt. % difference). Comparing the bulk and micro mixtures for a 15 minute mixing time shows that using microstructured materials improves the kinetics and the weight loss (% wt. H_2) of the reaction.

The 10 minute and 15 minute mixing times are the most encouraging in terms of performance and will be discussed in more detail in the forthcoming sections.

6.6.1 Ten Minute Mixing Time Results

The pre TPD mixture for the bulk mixture contained both LiH (cubic, $Fm\bar{3}m$) and $Mg(OH)_2$ (Figure 6.7) as expected.

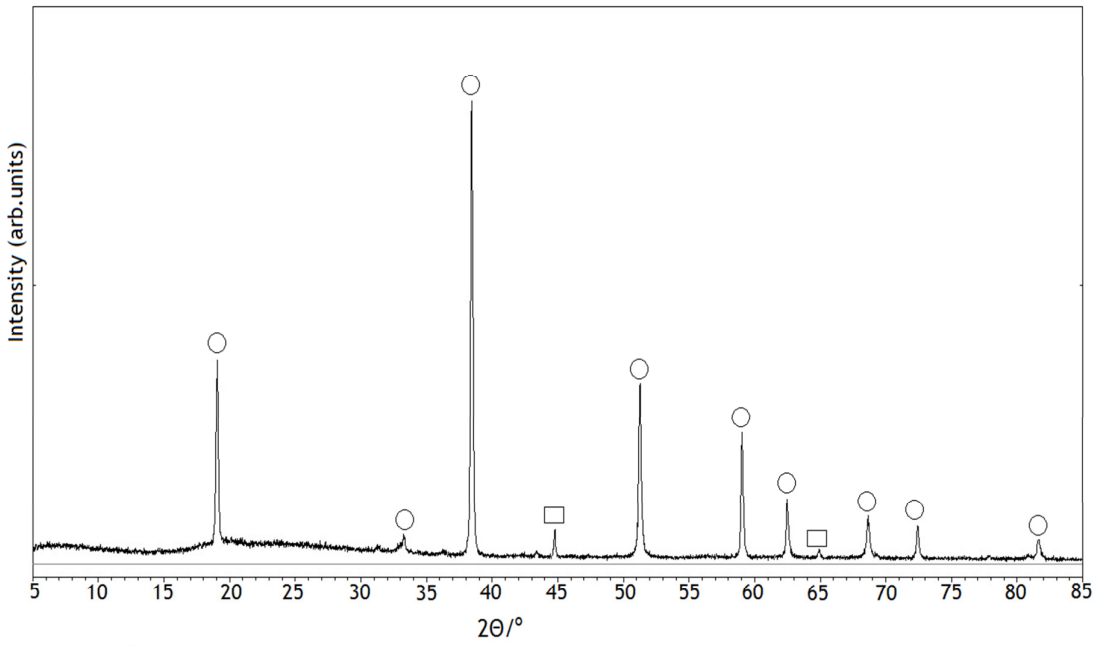

Figure 6.7: PXD of the pre heating products of the hand mixed for 10 min bulk mixture (sample **8**). Circles indicate $Mg(OH)_2$ and the rectangles indicate LiH

The TG-DTA profile of the bulk mixture can be seen in Figure 6.7. The reaction commences at 147 ^{o}C and is still losing weight at 450 ^{o}C as the TG curve does not level off suggesting that the reaction has not completed. MS analysis (Figure 6.8) shows release of H_2 commencing at approximately 155 ^{o}C and finishing at 330 ^{o}C. PXD analysis (Figure 6.9) shows that the sample contains both MgO (cubic, $Fm\bar{3}m$) and Li_2O (cubic, $Fm\bar{3}m$) which is expected as these are the two end products of the reaction, although the presence of LiOH indicates that the reaction had not gone to completion. The LiOH is the product of the hydrolysis of LiH.

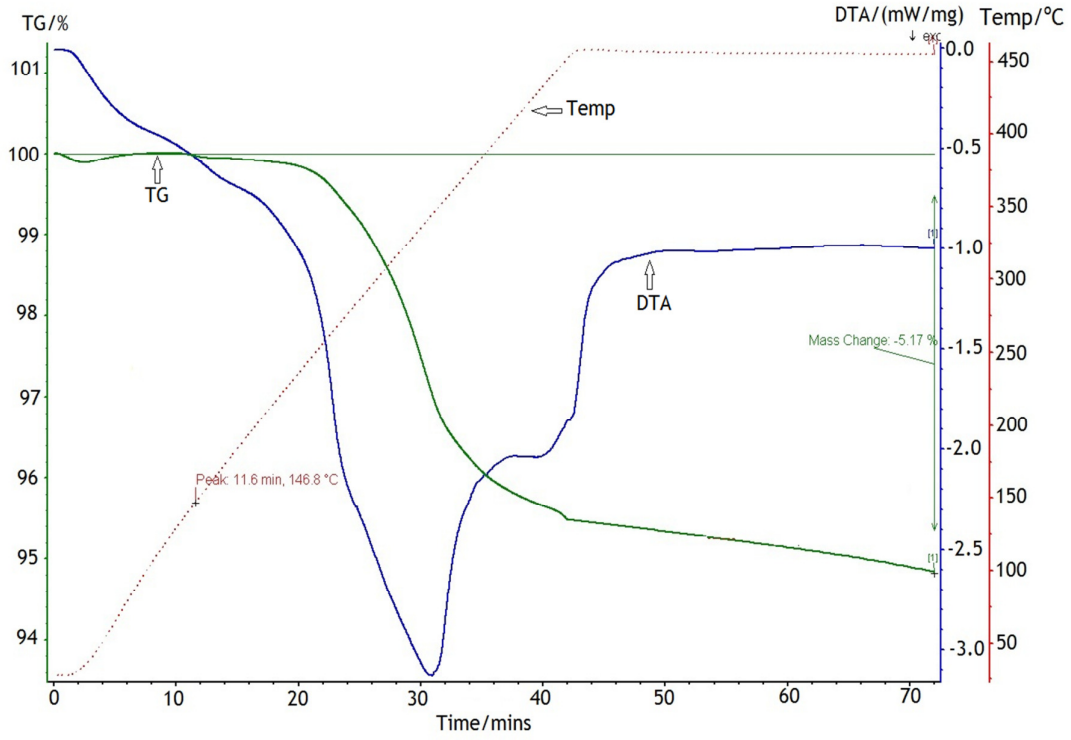

Figure 6.8: TGA-DTA of the bulk mixture after 10 minutes mixing (sample **8**)

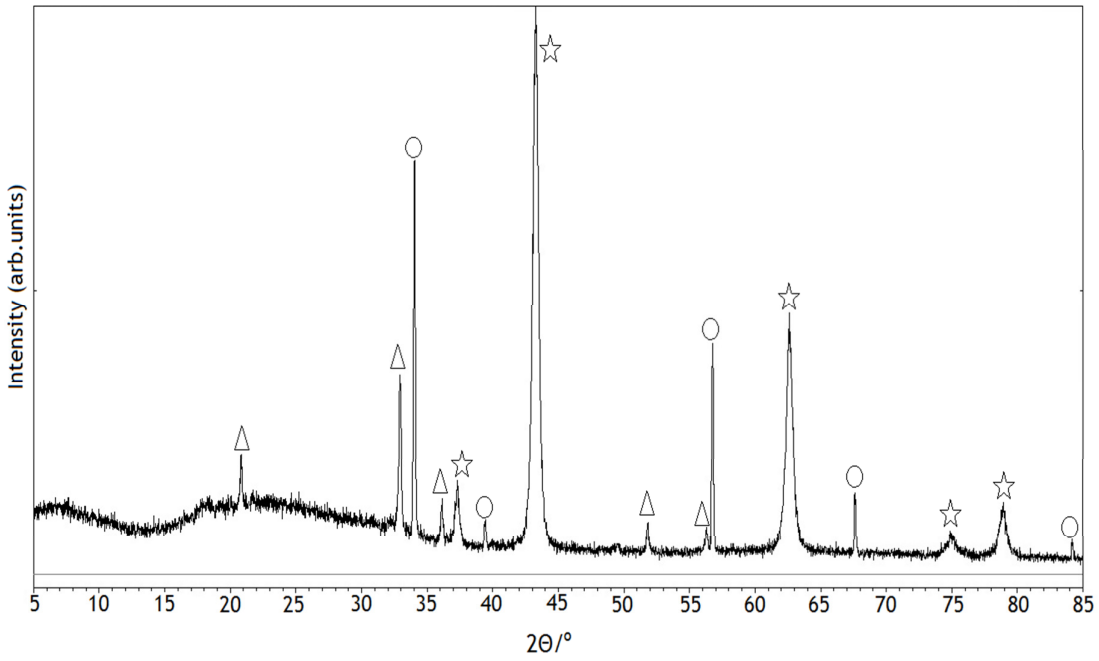

Figure 6.9: PXD of the TG-DTA products from sample **8**. The triangles indicate LiOH phase, the stars are MgO and the circles Li_2O.

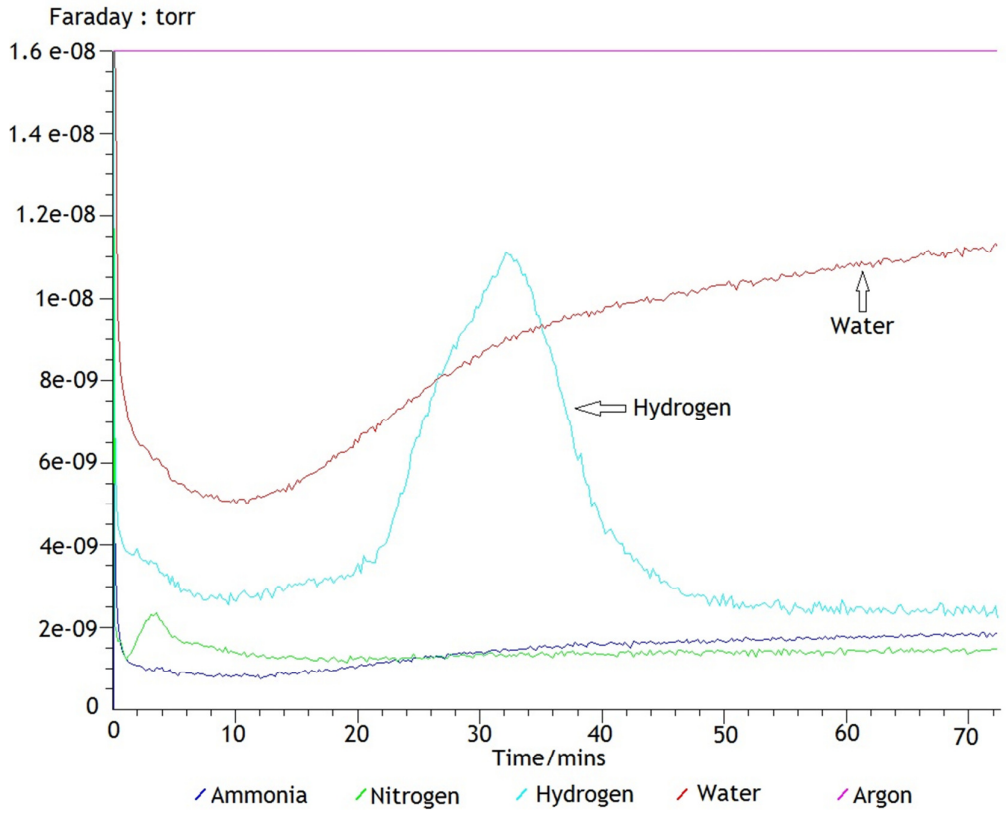

Figure 6.10: MS profile from the TG-DTA experiment of sample **8**

The TG-DTA plot (Figure 6.11) of the reaction of the microstructured mixture (sample **9**) is similar to that of the bulk mixture however two clear thermal events are seen. The onset of reaction occurs at 79 ^{o}C, with an endothermic process seen on the DTA commencing soon after heating with a negative exothermic peak peaking at approximately 230 ^{o}C which is at a lower temperature than for the corresponding bulk mixture. The TG curve also indicates the possibility of a two-step weight loss when the derivate is used in the software.

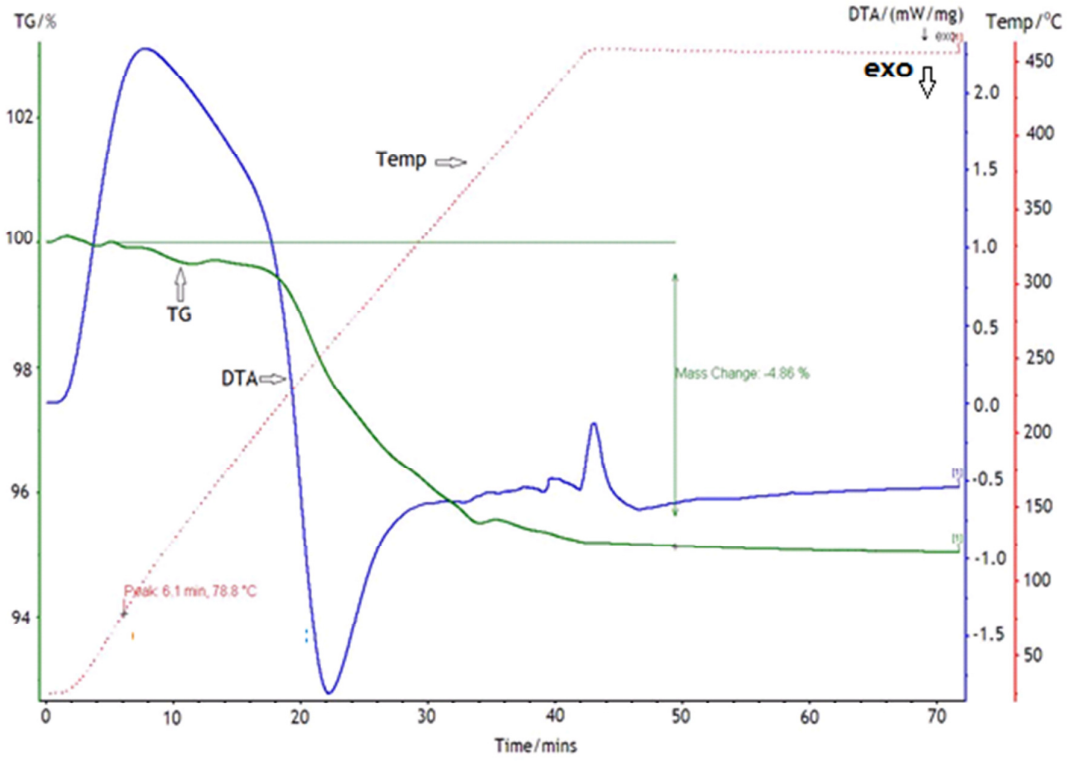

Figure 6.11: TG-DTA profile of sample **9** (10 mins micro mix)

From the two stage thermal event process a possible mechanism of reaction explaining this could be the thermal decomposition of $Mg(OH)_2$ followed by the hydrolysis of LiH (see intermediates section 6.6.4):

$$Mg(OH)_2 \rightarrow MgO + H_2O \qquad \Delta H = 84 \text{ KJ mol}^{-1} \qquad (6.8)$$

The negative DTA peak commencing at approximately 180 °C could correspond to the hydrolysis of the LiH, with the H_2O pre-evolved from equation 6.8

$$2\ LiH + H_2O \rightarrow Li_2O + 2\ H_2 \qquad \Delta H = -178 \text{ KJ mol}^{-1} \qquad (6.9)$$

The post TG-DTA PXD (see bulk PXD- Figure 6.9) shows that there is Li starting material (LiOH) but no magnesium starting material present after heating. This could lead to the suggestion that $Mg(OH)_2$ decomposition (equation 8) is the first step of the reaction as proposed by Drozd et al.[2] for the $NaBH_4$ and $Mg(OH)_2$ system and would then not be reliant on the quality of the mixing as LiH is not involved in the decomposition of $Mg(OH)_2$. Equations 8 and 9 can be linked to the LiH-NH_3 reaction in the Li-Mg-N system. Hu and Ruckenstein [20] found that

LiH would react very fast (matter of seconds) with NH_3 produced by the decomposition of $LiNH_2$ (equation 6.10) with the production of H_2 (equation 6.11):

$$2\ LiNH_2 \rightarrow Li_2NH + NH_3 \qquad (6.10)$$

$$NH_3 + LiH \rightarrow LiNH_2 + H_2 \qquad \Delta H = -42\ KJ\ mol^{-1}\ [21] \qquad (6.11)$$

If equation 6.8 is the first step of the reaction, then it could be that the reaction between LiH and H_2O from the $Mg(OH)_2$ decomposition occurs at a very fast rate similar to that of the LiH and NH_3 reaction as there is no H_2O evolution that can be easily seen on the mass spec profile (Figure 6.10). The fact that no H_2O evolution can be seen in the MS profile and there is only an exponential rise in the H_2O level may also lead to the proposed reaction mechanism involving $H^{\delta+}$ and $H^{\delta-}$ combining from the hydroxide and hydride similar to that seen in the Li-N-H system [22]. This would involve the direct reaction of $Mg(OH)_2$ with one mole of LiH followed by the hydrolysis of the second mole of LiH. In the Li-N-H system there is a combining of the $H^{\delta+}$ from $LiNH_2$ and the $H^{\delta-}$ in the solid state during decomposition (equation 6.12):

$$LiNH_2 + LiH \rightarrow Li_2NH + H_2 \qquad \Delta H = 45\ KJ\ mol\ l^{-1}\ [23] \qquad (6.12)$$

If reaction 6.12 is involved in the $Mg(OH)_2$ and LiH system, then another reaction mechanism can be proposed involving the direct reaction of $Mg(OH)_2$ with one mole of LiH resulting in MgO and LiOH (then further reaction with LiH). H_2 release will be as a result of the combination of $H^{\delta+}$ from the hydroxide (lithium intermediate) and $H^{\delta-}$ from the hydride. This was seen by Lu *et al.*[8] when heating a mixture of monohydrated lithium hydroxide and lithium hydride. The reaction commenced with the dehydrogenation of $LiOH.H_2O$ to LiOH and the subsequent reaction of LiOH and LiH with the release of H_2. Proposed reaction mechanisms are discussed in more detail in section 6.6.3.

The MS profile (Figure 6.12) shows the release of H_2 commencing at 150 ^oC and finishing at 450 ^oC and is compared in the Figure with its bulk equivalent. The main difference between the microstructured mixture and the bulk material is that the weight loss is greater from the bulk material.

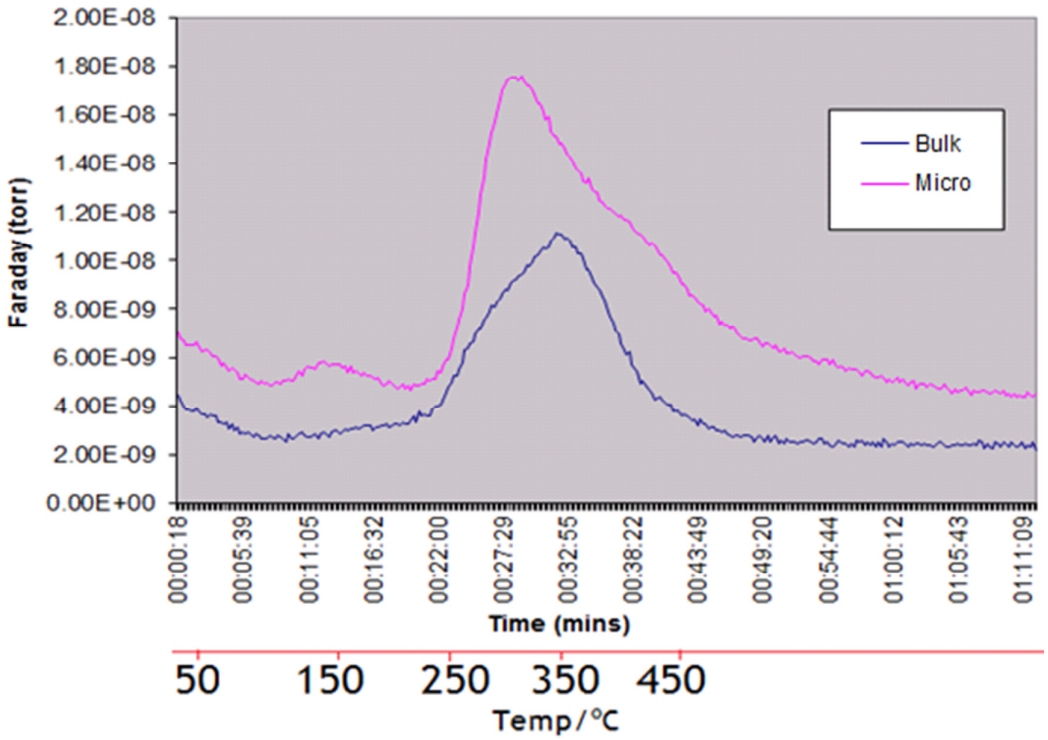

Figure 6.12: MS profiles comparing the H_2 release from the bulk and micro mixture in the TG-DTA experiments

6.6.1.2 SEM of Pre and Post STA products

SEM micrographs (Figures 6.13 and 6.14) were taken for the 10 minute mixed sample of $Mg(OH)_2$ and LiH prior to the TG-DTA experiment. The hexagonal microplates of $Mg(OH)_2$ are present. LiH, which were small particles before mixing may also be observed as deposits on the microplates as seen in Figure 6.13.

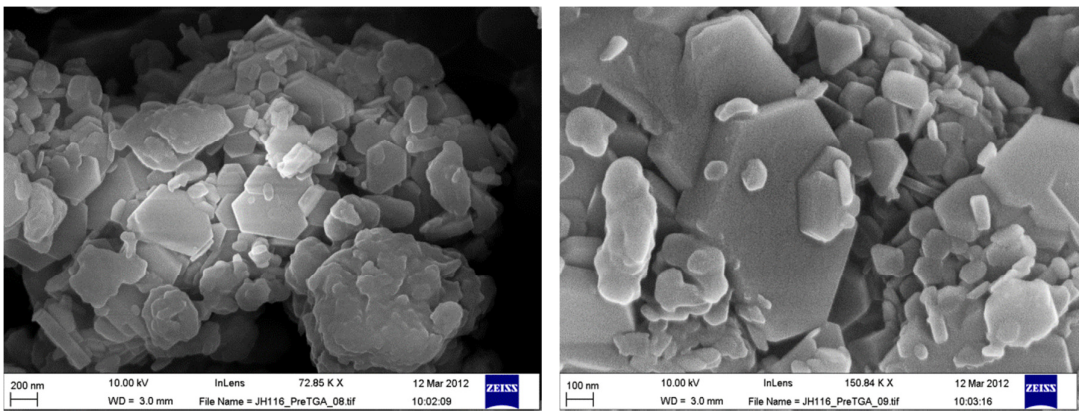

Figures 6.13: Pre TPD SEM of sample **6.9**

After heating, the sample does not retain all of its original morphology (Figures 6.14). Small microplates can be seen in the micrographs. These could be microstructured MgO as seen with the pseudomorphic synthesis of nanostructured MgO from $Mg(OH)_2$ in the literature.[24] The sample may contain lithium phases however due to the limitations of EDX this could not be measured, however post TG-DTA PXD indicate the presence of LiOH. The morphology of the LiH (Figure 6.6) is not observed in the micrographs.

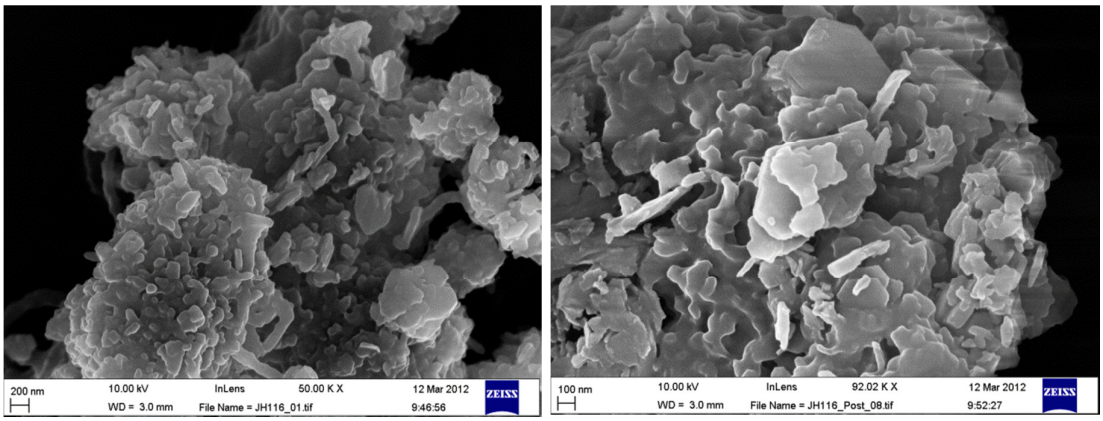

Figures 6.14: Post STA SEM of sample **9**

6.6.2 Fifteen Minute Mixing Time Results

The TG-DTA profile for the fifteen minute bulk mixture (Figure 6.15) is similar to that of the ten minute mixtures for the micro mix (Figure 6.10). The bulk mixture has an onset temperature of 132 ^{o}C and a total weight loss of 4.90 wt. %. In the DTA curve, there is an endothermic event occurring, peaking with the inset of the weight loss at 132 ^{o}C. This is then followed by an exothermic peak peaking at around 270 ^{o}C. The TG curve has flattened after 50 mins after heating suggesting the reaction has gone to completion. This suggests that mixing for fifteen minutes gives better mixing and sample homogeneity as what would be expected for a longer mixing time.

PXD analysis (Figure 6.16) shows no trace of $Mg(OH)_2$ with Li_2O and MgO present however there is a very small phase of LiOH is present which concludes the reaction may not have gone to full completion. Interestingly, in the PXD (Figure 6.16) the crystallinity of the Li_2O and MgO peaks are very different. The Li_2O peaks are very narrow with the MgO peaks being very broad which suggests a

smaller particle size of MgO which corresponds with the post STA SEM (Figure 6.14)

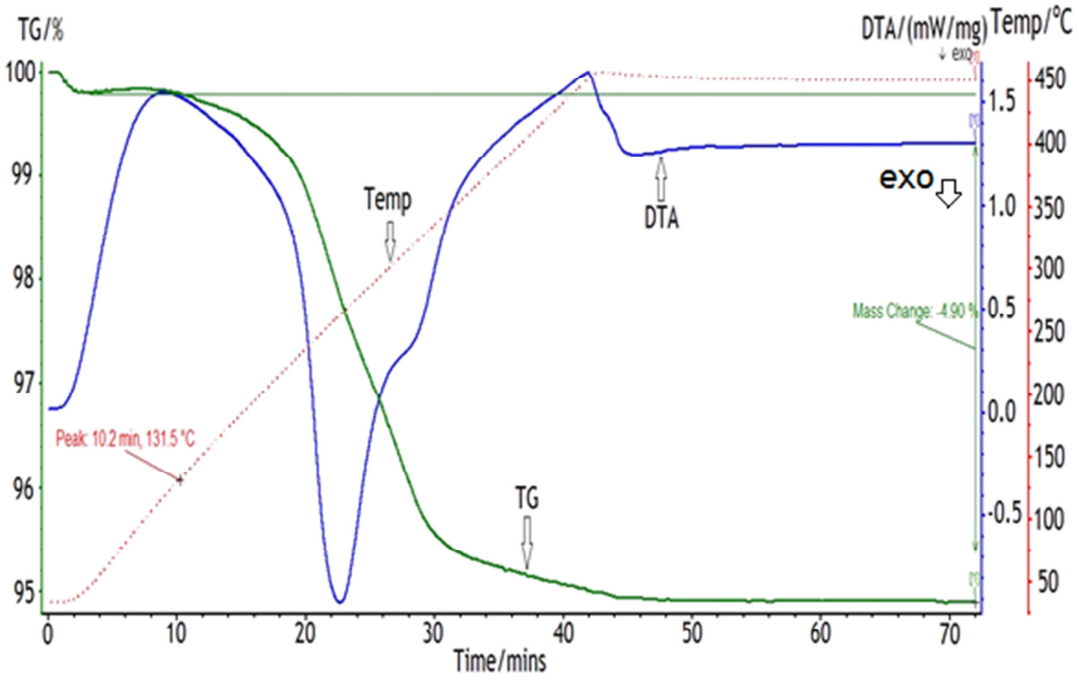

Figure 6.15: TGA-DTA profile of the 15 minute bulk mix (sample **10**)

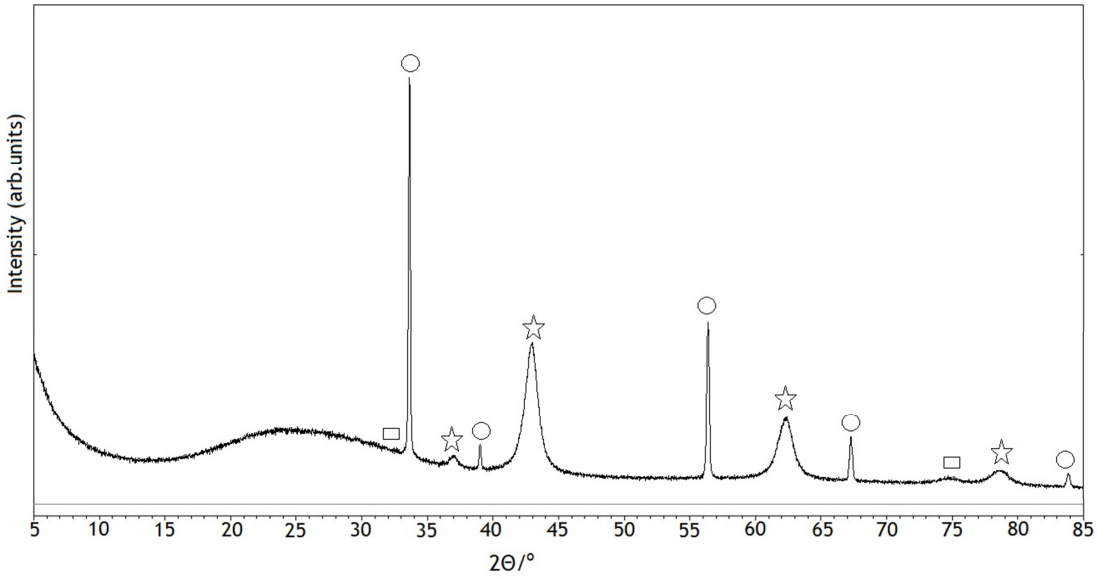

Figure 6.16: PXD of the post TPD product of the 15 minute bulk mixture. Stars indicate MgO, the circles indicate Li_2O and the rectangles represent LiOH

The microstructured 15 minute mixture is the closest mix (Figure 6.17) to the theoretical weight loss. The onset temperature of the reaction is also low, 82 ^{o}C. This temperature is only 4 ^{o}C higher than that of the microstructured 10 minute mixture. The TG plot has not levelled out and is still losing weight at 450 ^{o}C, meaning the reaction has not gone to completion. PXD confirms this as LiOH is present in the end product (Figure 6.18) The DTA curve shows two clear processes with associated weight loss. As per previous TG-DTA there is an endothermic event commencing at 82 ^{o}C with an associated weight loss of approximately 3.7 wt. %. There is then another thermal event which corresponds with the TG curve not being smooth as per the previous weight loss with a weight loss of approximately 2.2 wt. %. This could indicate that H_2 release is a two-step process proceeding through the decomposition of $Mg(OH)_2$ ($Mg(OH)_2$ on its own decomposes at approximately 300 ^{o}C) although it is not clear if it reacts with a mole of LiH as per the second proposed mechanism at the beginning of the reaction (as the weight loss is greater with increased mixing).

In the Post TPD PXD (Figure 6.18) there is no $Mg(OH)_2$ present. There is no evidence of LiH in the PXD however LiOH is present. However, LiOH decomposes to Li_2O above 800 K [25] so the presence of LiOH could be expected and suggests a higher temperature is required for full H_2 release from the system.

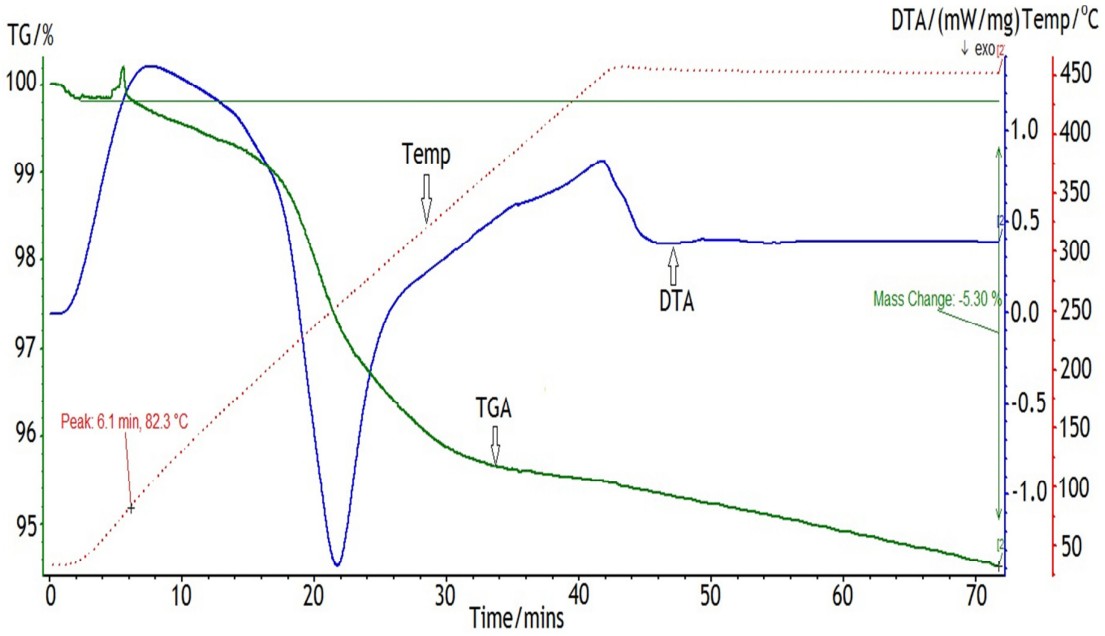

Figure 6.17: TG-DTA plot of the 15 minute micro mix (sample **11**)

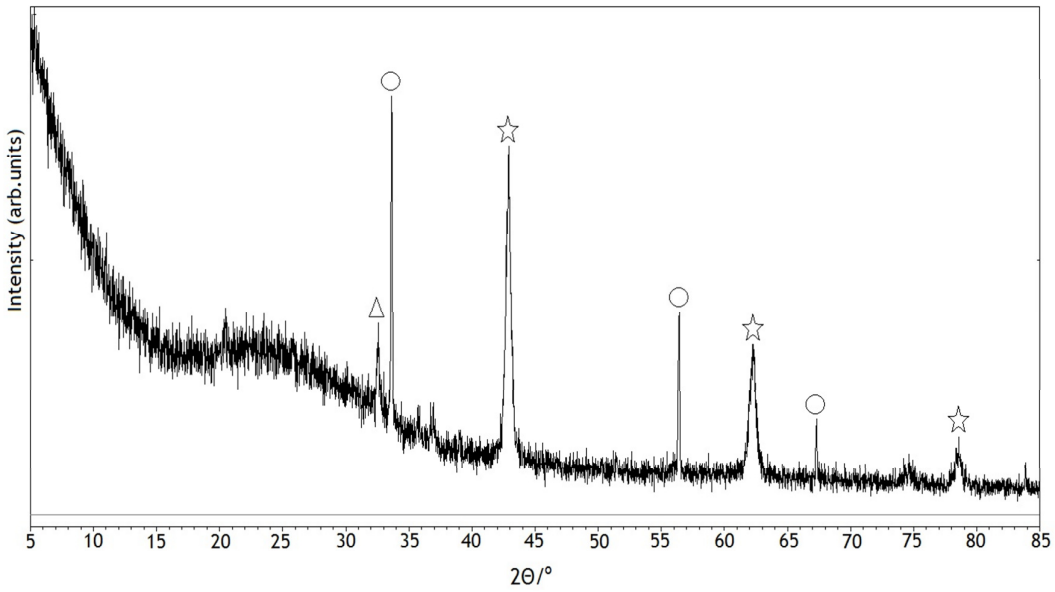

Figure 6.18: PXD of the post TPD mix (**11**). The triangle indicates LiOH, the circles indicate Li_2O and the stars indicate MgO

The MS data (Figure 6.19) shows that a greater amount of % H_2 is evolved from the microtructured mixture than the bulk mixture.

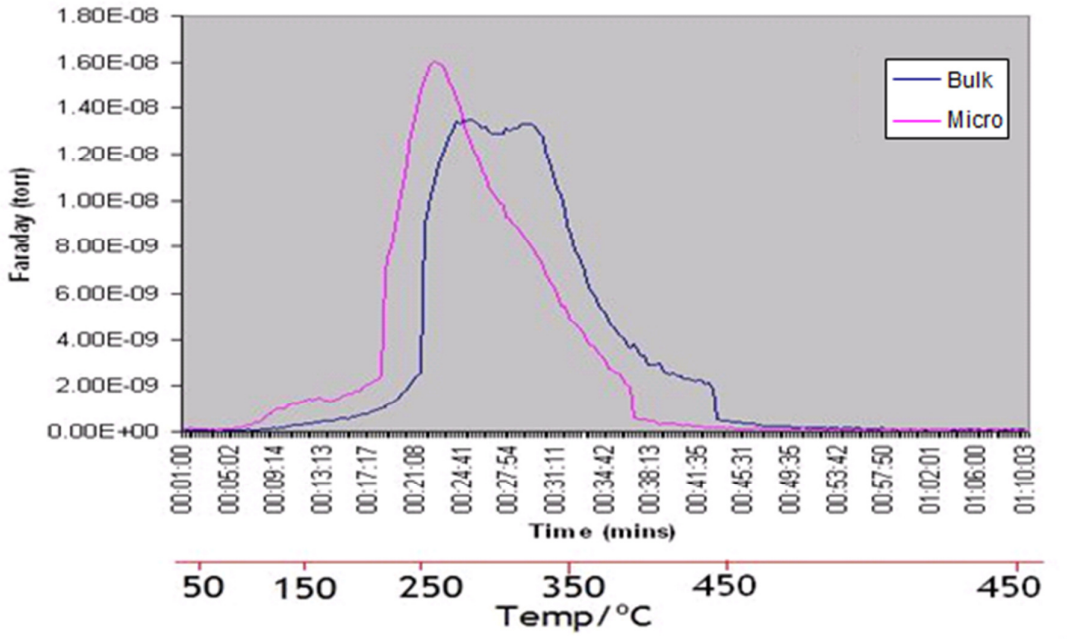

Figure 6.19: MS data showing the release of H_2 from the microstructured and bulk mixtures

6.6.3 Proposed Mechanisms: Intermediate Studies

Two reaction mechanisms can be hypothesised for the H_2 release reaction as discussed. One of the reaction mechanisms proceeds via the decomposition of the hydroxide. The water produced from the decomposition then reacts with one mole of LiH (with a very fast reaction rate as seen for the LiH and NH_3 reaction [21]) with the formation of LiOH. The LiOH then reacts with the second mole of LiH resulting in the release of H_2 and the formation of Li_2O the LiOH decomposes as per the $Mg(OH)_2$ with the H_2O produced reacting with the LiH (equation 6.13):

$$Mg(OH)_2 + 2\ LiH \rightarrow MgO + H_2O + 2\ LiH \rightarrow LiOH + LiH + MgO + H_2 \rightarrow Li_2O + MgO + 2\ H_2 \quad (6.12)$$

or

$$LiOH + LiH + MgO + H_2 \rightarrow \tfrac{1}{2}\ Li_2O + \tfrac{1}{2}\ H_2O + LiH + MgO + H_2 \rightarrow Li_2O + MgO + 2\ H_2 \quad (6.13)$$

Mechanism 1

A similar reaction mechanism, has been suggested by Drozd *et al.* [2] involving H_2 release from a $NaBH_4$ and $Mg(OH)_2$ mixture. Using in-situ PXD and Raman the mechanism is proposed to go via the decomposition of $Mg(OH)_2$ and the release of water.

The second reaction mechanism which can be proposed involves the direct solid state reaction of one mole of LiH with $Mg(OH)_2$ with the products being MgO and LiOH with the release of one mole of H_2. The LiOH then reacts with the second mole of LiH with the release of a further mole of H_2:

$$Mg(OH)_2 + 2\ LiH \rightarrow MgO + LiOH + H_2 + LiH \rightarrow MgO + Li_2O + 2\ H_2 \quad (6.14)$$

Mechanism 2

In order to determine the intermediate products which in turn can be used to determine the favoured mechanism, TPD and PXD analysis has been carried out.

For the intermediates to be isolated, a 10 minute mix of microstructured $Mg(OH)_2$ + LiH was heated to 240 ^oC under Ar(g) with a heating rate of 2 ^oC per minute. From the TGA-DTA data (Figure 6.20) the TG curve has not levelled out although the DTA curve is stable at the end of the measurement. This suggests that the reaction is a simple stepwise reaction and that the next step in the

reaction has already commenced before the previous reaction step has stopped. Various TG-DTA experiments were attempted to successfully the intermediates but none of these resulted in the TG curve being levelled at the end of experiments and that the TG-DTA experiment presented provided the best results both in the TG-DTA data and also PXD.

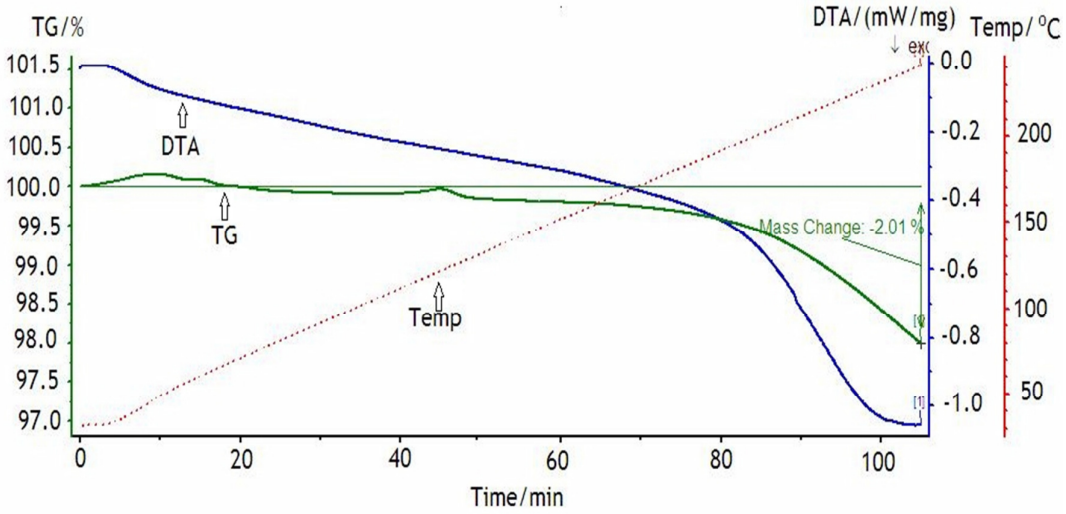

Figure 6.20: TGA-DTA for the isolation of the reaction intermediates (sample **12**)

PXD data (Figure 6.21) of the products produced at this temperature indicated that $Mg(OH)_2$, MgO,LiH and LiOH were present with no Li_2O present. For determining the reaction mechanism the PXD data is inconclusive. If reaction mechanism 1 was favoured then it would be expected that no $Mg(OH)_2$ would be present and that it could be possible to isolate MgO and LiH before LiOH present although as discussed previously the LiH and H_2O could be fast reaction. The PXD data could suggest that mechanism 2 is favoured as this involves the formation of H_2 from the solid state dehydrogenation of $Mg(OH)_2$ and LiH and the presence of three intermediates proposed in equation 6.14. The Mass spec for the intermediate is inconclusive for determining if mechanism 1 is favoured as there is no rise in H_2O (generated by the solid state decomposition of H_2O)

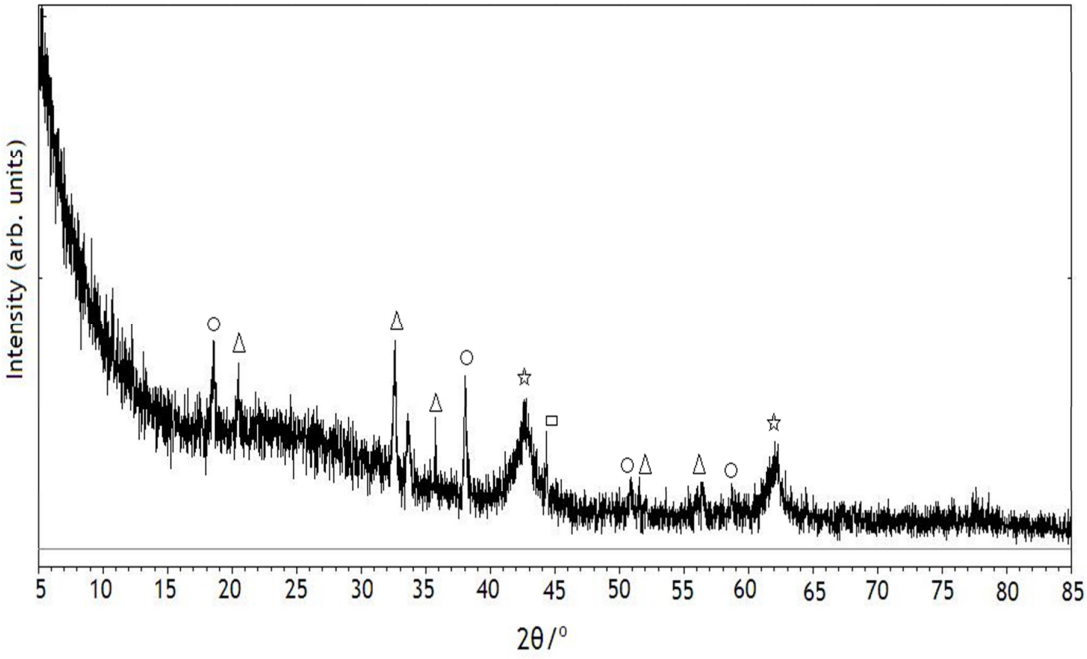

Figure 6.21: PXD of the reaction intermediates (sample **12**). Circle is $Mg(OH)_2$, triangle is LiOH, star is MgO and the rectangle is LiH

The Mass spec for the intermediate is inconclusive for determining if mechanism 1 is favoured as there is no exponential rise in H_2O (generated by the solid state decomposition of H_2O).

6.6.4 TG-DTA at Higher Temperature

The thermal programmed desorption (TPD) method was modified to allow the reaction to go to completion and the theoretical weight loss value to be achieved. The 10 minute mix has been heated to both 500 ^oC and 650 ^oC and held at this temperature. The post TPD PXD contains both MgO and Li_2O with no trace of LiOH concluding that the reaction has gone to completion. However, the TG weight loss was always above the theoretical weight loss value, for example heating a 10 minute bulk mixture to 500 ^oC (sample **14**) and holding at 500 ^oC for two hours resulted in a weight loss of 6.93 wt. % (Figure 6.22). In the TG curve at 500 ^oC at the start of the hold period there is a sudden drop (and weight loss) that may indicate a reaction event but this could not be proved. No clues can be gained from the TG-DTA data or the MS data into why the weight loss is higher than expected as heating to 650 ^oC resulted in a similar weight loss although at this higher temperature the TG does commence to plateau.

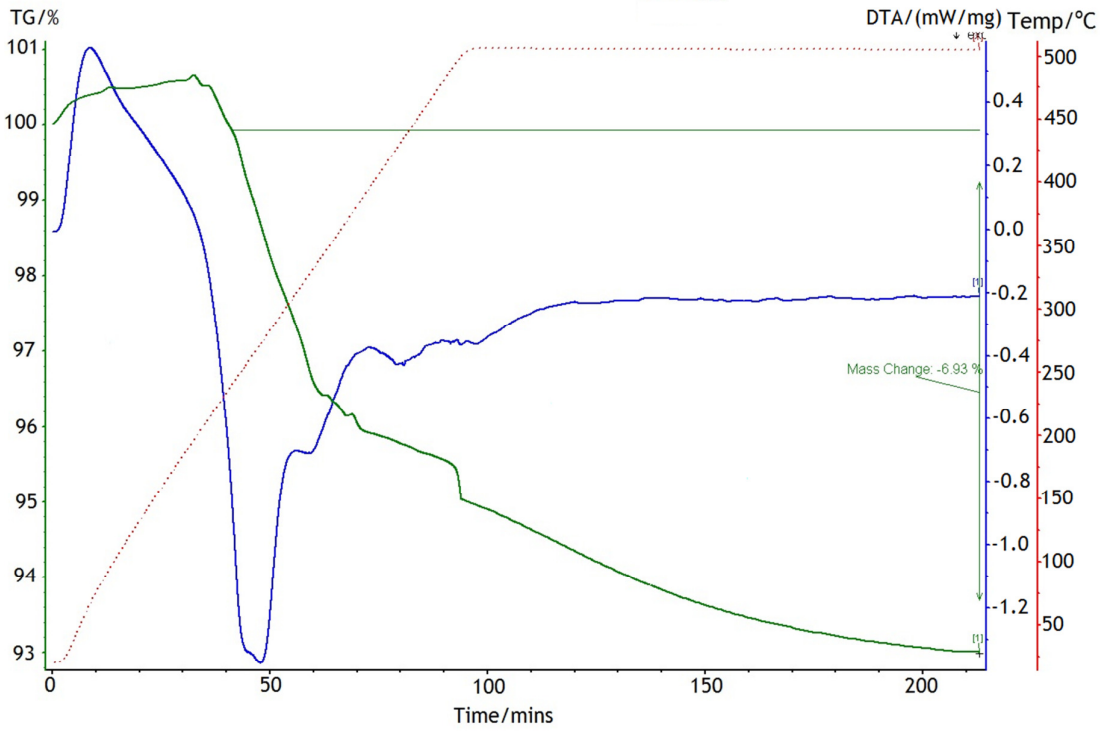

Fig 6.22: TG-DTA profile of sample **14** heated to 500 ^{o}C.

6.7 Conclusions

Microstructured $Mg(OH)_2$ has been successfully synthesised by using conventional heating and microwave heating. Using an oven based hydrothermal synthesis method has resulted in microplates between 300-500 nm in diameter being produced in 20 hrs. The use of a microwave oven has resulted in successful synthesis of $Mg(OH)_2$ in only six minutes. Using a microwave oven, 1g of microplates of $Mg(OH)_2$ can be obtained.

The $Mg(OH)_2$- LiH '*H_2 release system*' has been studied comparing the bulk system and microstructured system. Using microstructured reactants has resulted in the onset of the temperature of H_2 release decreasing by nearly half (79 ^{o}C from 147 ^{o}C) when the mixing time for the system is 10 minutes.

After 15 minutes mixing, the microstructured mixture has a lower onset reaction temperature than the bulk mixture and the mixture loses the greatest weight loss suggesting that longer mixing time results in improved mixing and sample homogeneity. Overall, microstructuring the materials improves the

dehydrogenation temperature of the system. For both the bulk and microstructured system, the theoretical H_2 release value of 5.44 wt. % was not achieved when heated to 450 ^oC. This suggests that heating to a higher temperature may be need although this resulted in a greater weight loss than expected.

Two mechanisms have also been proposed for the '*H_2 release*' system, with the first mechanism involving an initial step of dehydration of $Mg(OH)_2$ to MgO with the H_2O reacting with one of the moles of LiH. This is similar to the reaction of $LiH\text{-}NH_3$ in the Li-N-H system.[12] It could be in this system that the LiH is reacting fast with the H_2O produced from the dehydrogenation of $Mg(OH)_2$ although intermediate studies proved inconclusive. Post STA PXD data of the mixture at 450 ^oC still showed the presence of LiOH but no $Mg(OH)_2$ which could show that the $Mg(OH)_2$ dehydrogenation is the first step. As discussed, previous studies of similar systems involving hydroxides suggest that the reaction proceeds through the dehydrogenation of $Mg(OH)_2$ and the subsequent reaction of the hydride and water.[2]

The second mechanism involves the direct reaction of the $Mg(OH)_2$ with one mole of the LiH. This involves the combination of H_2 in the solid state from LiOH and LiH. This reaction is similar to that of the solid state dehydrogenation of $LiNH_2$ and LiH in the Li-N-H system involving H_2 combination.[22] Lu suggest a similar reaction for the $LiOH.H_2O$ and LiH system which proceeds through the initial dehydrogenation of $LiOH.H_2O$ followed by the reaction of LiOH and LiH.[8] Evidence for this mechanism can be seen in the mixing time results. As the mixing times increases, the weight loss increases that suggests the homogeneity of the mixture is important. This suggests that both starting materials are important in the reaction, as if mechanism 1 is favoured mixing time would not be a factor in the weight loss of the reaction.

To determine which mechanism is favoured, further work is required. In-situ PND is one method that could be exploited. For this, $Mg(OD)_2$ and LiD are required. The mixture would be hand mixed as per the $Mg(OH)_2$- LiH system and heated as per the ammine-hydride system presented in Chapter 5 and measurements would be obtained at selected temperature points. By studying

the reaction at a number of temperature points, the intermediates involved could be observed.

6.8 References

[1] F. Leardini, J. R. Ares, J. Bodega, J.F. Fernandez, I. J. Ferrer and C. Sanchez, *Phys. Chem. Chem. Phys*., 2010, **12**, 572.

[2] V. Drozd, S. Saxena, S. V. Garimella and A. Durygin, *Int. J. Hydrogen Energy*, 2007, **32**, 3370.

[3] R. Ren, A. Ortiz, T. Markmaitree, W. Osborn and L. Shaw, *J. Phys. Chem. B*., 2006, **100**, 10567.

[4] B. A . Stobbs, MSci. Thesis, University of Glasgow, 2010.

[5] J. M. Hanlon, B. A. Stobbs, G. Balducci, L. MacDonald and D. H. Gregory, In Preparation

[6] L. S. Mair, *Acta. Crystallogr. B*, 1978, **34**, 542.

[7] L. Ojamaee, K. Hermansson, C. Pisani, M. Causa and C. Roetti, *Acta Crystallogr. B*., 1994, **50**, 268.

[8] J. Lu, Z. Z Fang and H. Y. Song, *J. Power Sources*, 2007, **172**, 853.

[9] Y. Ding, G. Zhang, H. Wu, B. Hai, L. Wang and Y. Qian, *Chem.Mater*., 2001, **13**, 435.

[10] L. Zhuo, J. Ge and B. Tang, *Crys. Growth Des*., 2009, **9**, 1.

[11] Y. D. Li, H. W. Liao, Y. Ding, Y. T. Qian, L. Yang and G. E. Zhou, *Chem. Mater*, 1998, **10**, 2301.

[12] Y. Li, M. Sui, Y. Ding, G. Zhang, J. Zhuang and C. Wang, *Adv. Mater*., 2000, **22**, 818.

[13] J. C. Yu, A. Xu, L. Zhang, R. Song and L. Wu, J. *Phys. Chem. B*., 2004, **108**, 64.

[14] A. Belsky, M. Hellenbrandt, V.L. Karen and P. Luksch, *Acta. Crystallogr. B*, 2002, **B58**, 364.

[15] J. Laugier and B. Bochu, "CELREF Unit-Cell Refinement Software on a Multiphase System", Laboratoire des Materiaux et du Genie Physique Ecole Nationale Suprieure de Physique de Grenoble**.**

[16] V. Kazimirov, M. B, Smirnov, L. Bourgeios, L. Guerlou Demourgues, L. Servant, A. M. Balagurov, I. Natkaneic, N. R. Khasanova and E. V. Antipov, *Solid State Ionics*, 2010, **181**, 1764.

[17] B.H. Toby, *J. Appl. Crystrallogr,* 2001, **34**, 210.

[18] A. C. Larson and R. B. von Dreele, The General Structure Analysis System, Los Alamos National Laboratories, Report LAUR 086–748, LANL, Los Alamos, NM, 2000

[19] A. V. G.Chizmeshya, M. J. McKelvy, R. Sharma, R. W. Carpenter and H. Bearat, *Mater. Chem. Phys*., 2002, **77**, 416.

[20] Y. H. Hu and E. Ruckenstein, *J. Phys. Chem. A*, 2003, **107**, 9337.

[21] T. Ichikawa, N. Hanada, S. Isobe, H. Leng and H. Fujii, *J. Phys. Chem. B*, 2004, **108**, 7887.

[22] S. Isobe, T. Ichikawa, S. Hino and H. Fujii, *J. Phys. Chem. B,* 2005, **109**, 14855.

[23] P. Chen, Z. Xiong, J. Luo, J. Lin and K. L. Tan, *J. Phys. Chem B*, 2003 **107**, 10967.

[24] L. Yan, J. Zhaung, X. M. Sun, Z. X. Deng and Y. D. Li, *Mater. Chem. Phys*., 2002, **76**, 119.

[25] J. M. Kiat, G. Boemare, B, Rieu and D. Aymes, *Solid State Comm*., 1998, **108**, 241.

7. Conclusions and Future Work

This thesis describes the synthesis and characterisation of direct and indirect H_2 storage materials. The main characterisation techniques employed were Powder X-ray Diffraction (PXD), Powder Neutron Diffraction (PND) and Temperature Programmed Desorption (by TG-DTA-MS).

The ammines, $Mg(NH_3)_6X_2$, where X= Cl, Br and I hold great promise as indirect H_2 storage materials and also as solid state NH_3 storage materials. Research in the literature has focussed on the Cl ammine, due to its high gravimetric H_2 capacity of 9.1 wt.%.[1] The structure has previously been determined to be cubic ($Fm\bar{3}m$).[2]

From the TPD data it can be concluded that the deammoniation of $Mg(NH_3)_6Cl_2$ is a three step process commencing at 65 ^oC and concluding at 302 ^oC:

$$Mg(NH_3)_6Cl_2 \rightarrow Mg(NH_3)_2Cl_2 + 4NH_3 \rightarrow Mg(NH_3)Cl_2 + NH_3 \rightarrow MgCl_2 \qquad (7.1)$$

The intermediate diammine has been successfully isolated and refined against PXD and is orthorhombic (*Cmmm*).[3] The monoammine was unsuccessfully isolated so its structure could not be resolved

$Mg(NH_3)_6Br_2$ which can theoretically store 6.3 wt. %H_2 has been synthesised and from refinement against the PXD data is isostructural with $Fe(NH_3)_6Br_2$ ($Fm\bar{3}m$).[4] TPD investigations of the deammoniation of this system show the process is the same as its Cl equivalent (equation 7.1). The onset temperature of deammoniation had increased to 75 ^oC and the end temperature is now 337 ^oC. The intermediate diammine has been successfully isolated and crystallises in the orthorhombic *Pbam* group.[3] As per its Cl equivalent, the monoammine could not be successfully isolated.

$Mg(NH_3)_6I_2$ (store 4.6 wt.% H_2 indirectly) has been found from refinement against the PXD data to be isostructural with $Mn(NH_3)_6I_2$ ($Fm\bar{3}m$).[5] The deammoniation occurs in three steps similar to its Cl and Br equivalents although the deammoniation temperatures are the highest of the three hexammines (81 ^oC-366 ^oC). The intermediate diammine has been successfully isolated and is

isostructural to its Br equivalent. The monoammine phase was not successfully isolated with an amorphous diffraction pattern obtained although Raman spectroscopy indicated the presence of N-H bonds. The deammoniation properties of all three hexaammines could be improved by nanostructuring and using mixed halides.

Ex-situ and in-situ PND has been used to further characterise the structure and deammoniation process. A new disordered model of ND_3 in the hexaammines has been proposed for $Mg(ND_3)_6Cl_2$.[6] This model has been used as a starting structure for the refinement of the PND data. All three hexaammines have been successfully modelled to the new disordered model with the refined fit being of better quality than when the ordered model was used with bond angles and distances in reasonable agreement with that of free ND_3. From these results, ND_3 is disordered in all three ammines.

In-situ PND has been employed to study the deammoniation process. In all three ammines, the first deammoniation step contained both the cubic disordered phase (which was successfully refined) and the diammine phase. The phase fractions showed an increase in the diammine phase as the temperature was increased. No new phases were observed indicating that deammoniation only involves one structural change. Thermal expansion was also observed in the lattice parameters. In the case of Cl and Br, the diammine orthorhombic phase was successfully isolated and refined with thermal expansion seen with rises in temperature. In the case of the iodide ammine, the diammine phase was always present along with the hexaammine phase. Weak reflections were observed for the $Mg(ND_3)_6Cl_2$ deammoniation from 210 ^oC which could be the appearance of the monoamine phase but these could not be successfully indexed. It has previously been suggested that the monoammine phase may be isostructural with its Ni counterpart but no structure for the monoammine of the chloride has been published. For identification of the monoammine phase the successful isolation of the monoammine phase only is required.[7] This could be achieved by synthesising $MgCl_2$ with NH_4Cl in an autoclave as isolating the monoammine phase was unsuccessful by TPD. Reflections from a possible monoammine Br phase were not observed suggesting that more temperature points could have been measured between the diammine phase and the completion of the deammoniation. In the case of the iodide as per the TPD/PXD an amorphous

phase was observed at higher temperatures of 285 ^{o}C indicating a possible melting point transition.

$Mg(NH_3)_6Cl_2$ has been studied with LiH or MgH_2 as part of an 'H_2 release system'. Mixing the components was performed at 25 ^{o}C by hand to avoid the decomposition of the ammine.[8] From TPD data, the LiH system is favoured as H_2 release is observed at 232 ^{o}C after release of NH_3 from the hexaammine to diammine. In the case of the MgH_2, H_2 release was observed towards the end of reaction (400 ^{o}C) indicating that hand mixing may not be suitable. In the post TPD PXD, $Mg(NH_2)_2$ was present indicating that the reaction of MgH_2 with the NH_3 from the ammine had occurred.

In-situ PND was performed on these two systems. For the $Mg(ND_3)_6Cl_2$ – LiD system up to 230 ^{o}C only deammoniation of the ammine was observed (with associated thermal expansion). LiD is not involved in the major deammoniation step which limits the wt.% of H_2 that can be released from the system while minimising NH_3 release. At 270 ^{o}C, $LiND_2$ was observed so D_2 release from the LiD was occurring through the reaction of LiD and ND_3 [9] from the decomposition of the diammine. For the MgH_2- $Mg(ND_3)_6Cl_2$ system the only structural changes up to 400 ^{o}C were that of the ammine through deammoniation, although at 400 ^{o}C H_2/D_2 release was observed concluding that the MgH_2 is not reacting with $Mg(ND_3)_6Cl_2$ but only towards the end of the deammoniation process as confirmed by the TPD measurements.

For both systems, improvements are needed in order for the hydride to take advantage of the low stability of $Mg(NH_3)_6Cl_2$ so that H_2 release is maximised. This could include nanostructuring the hydride (i.e. through ball milling) or an improved mixing process which keeps NH_3 loss to a minimum.

$Mg(OH)_2$ as a component of a 'H_2 release' system has been studied with LiH. $Mg(OH)_2$ has traditionally been synthesised by conventional heating methods although a new synthesis has been employed using MW heating decreasing the reaction time from 20 hrs to 6 mins. Bulk mixtures of $Mg(OH)_2$-LiH and microstructured mixtures of $Mg(OH)_2$-LiH (prepared by ball milling) were hand mixed for 5, 10 and 15 mins and heated. The 10 min mixtures had the earliest onset temperature. The microstructured mixture reaction commenced at 79 ^{o}C

compared to 147 ^{o}C for the bulk mixture after a 10 min mixing time. From the TPD and post PXD data two possible reactions have been suggested based on the Li-N-H system.[10] The first mechanism involves the decomposition of $Mg(OH)_2$ as the first step of the reaction followed by fast hydrolysis of the LiH. The second mechanism involves the first step of the reaction being the reaction of $Mg(OH)_2$ with one mole of LiH. An intermediate study of the system by TPD and PXD was unsuccessful in determining the mechanism of H_2 release. Further investigation using in-situ PND is required.

7.1 References

[1] C. H. Christensen, R. Z. Sørensen, T. Johannessen, U. J. Quaade, T. D. Elmøe, R. Køhler and J. K. Nørskov, *J. Mater. Chem.,* 2005, **15**, 4106.

[2] I. C. Hwang, T. Drews and K. Seppelt, *J. Am. Chem. Soc*., 2000, **122**, 8486

[3] A. Leineweber, M. W. Fredriszik and H. Jacobs, *J. Solid. State. Chem.,* 1999, **147**, 229

[4] R. Essmann, G. Kreiner, A. Niemann, D. Rechenbach, A. Schmeiding, T. Sichla, U. Zachweija and H. Jacobs, *Z. Anorg. Allg. Chem*., 1996, **662**, 1161.

[5] H. Jacobs, J. Bock and C. Stove, *J. Less Common Metals*, 1987, **134**, 207.

[6] M. H. Sørby, O. M. Løvvik, M. Tsuboto, T. Ichikawa, Y. Kojima and B. C. Hauback, *Phys. Chem. Chem. Phys*., 2011, **13**, 7644

[7] A. Leineweber, H. Jacobs and H. Ehrenberg, *Z. Anorg. Allg. Chem,* 2000, **626**, 2146.

[8] M. Tsuboto, S. Hino, H. Fujii, C. Oomatsu, M. Yamana, T. Ichikawa and Y. Kojima, *Int. J. Hydrogen Energy*., 2010, **35**, 2058.

[9] Y. H. Hu and E. Ruckenstein, *J. Phys. Chem. A*, 2003, **107**, 9337.

[10] T. Ichikawa, N. Hanada, S. Isobe, H. Leng and H. Fujii, *J. Phys. Chem. B.*, 2004, **108**, 7887.

8. Appendix

8.1 Chapter 5

8.1.1 Powder Neutron Diffraction (PND) Study of the $Mg(ND_3)_6Cl_2$ + LiD 'D$_2$ Release' System at 125 °C

Table 5.1A: Atomic positions and temperature factors for $Mg(ND_3)_6Cl_2$ at 125 °C

Atom /Site	x	y	z	Occupancy	100/Å^2 x U_{iso}
Mg /4a	0	0	0	1	2.5
Cl /8c	0.25	0.25	0.25	1	2.5
N/96j	0	0.0197(12)	0.2241(7)	0.25	2.5
D1/96k	0.0710(4)	0.0710(4)	0.2308(7)	0.5	2.5
D2/96j	0	0.0747(10)	0.2737(11)	0.25	2.5

8.1.2 Powder Neutron Diffraction (PND) Study of the $Mg(ND_3)_6Cl_2$ + LiD 'D$_2$ Release' System at 160 °C

Table 5.2A: Bond distances and angles for $Mg(ND_3)_2Cl_2$ at 160 °C.

Atoms	Distance/Å	Angles/Å
Mg-N	2x 2.095(5)	4x 115.3 (5)
Mg-Cl	4x 2.576(3)	2x 93.96(16), 2x 86.04(16)
N-D1	4x 0.949(6)	2x 77.0(3), 2x 81.9(7), 2x 129.4(11)

Table 5.3A: Bond distances for LiD at 160 °C.

Atoms	Distance/Å	
Li-Li	8x 2.877(4)	8x 2.877(10)
Li-D	12x 2.041(7)	

8.1.3 Powder Neutron Diffraction (PND) Study of the $Mg(ND_3)_6Cl_2$ + LiD 'D$_2$ Release' System at 215 °C

Table 5.4A: Selected Crystallographic data for the $Mg(ND_3)_6Cl_2$ and LiD system at 215 °C.

Phases	$Mg(ND_3)_2Cl_2$	LiD	$MgCl_2$
Phrase Fractions	44.2(6)	24.0(3)	31.8(5)
Crystal System	Orthorhombic	Cubic	Trigonal
Space Group	*Cmmm*	*Fm$\bar{3}$m*	*R$\bar{3}$m*
a/Å	8.214(8)	4.095(2)	3.651(4)
b/Å	8.252(5)		
c/Å	3.773(2)		17.764(39)
Volume/Å^3	255.727(4)	68.666(1)	205.087(3)
Z	2	4	3
Formula Weight/g	270.618	35.820	285.633
Density (ρ_x/gcm^{-3})	1.757	0.866	2.313
No of observations		3709	
No of variables		77	
R_{wp}		0.0552	
R_p		0.3052	
χ^2		4.744	

Table 5.5A Atomic Positions and temperature factors for $Mg(ND_3)_2Cl_2$ at 215 °C

Atom /Site	**x**	**y**	**z**	**Occupancy**	**100/Å^2 x U_{iso}**
Mg /2a	0	0	0	1	1.9(3)
Cl /4h	0.216(6)	0	0.5	1	2.0(2)
N/4i	0	0.261(9)	0	1	6.5(3)
D/16r	0.072(8)	0.300(6)	0.155(10)	0.75	8.8(3)

Table 5.6A: Atomic positions and temperature factors for LiD at 215 °C

Atom /Site	x	y	z	Occupancy	100/Å^2 x U_{iso}
Li /4a	0	0	0	1	1.9(6)
D /4b	0.5	0.5	0.5	1	2.3(4)

8.1.4 Powder Neutron Diffraction (PND) Study of the $Mg(ND_3)_6Cl_2$ + LiD 'D$_2$ Release'System at 235 °C

Table 5.7A: Atomic positions and temperature factors for $Mg(ND_3)_6Cl_2$ at 235 °C.

Atom /Site	x	y	z	Occupancy	100/Å^2 x U_{iso}
Mg /2a	0	0	0	1	2.4(4)
Cl /4h	0.2117(8)	0	0.5	1	2.5
N/4i	0	0.261(10)	0	1	6.3(3)
D/16r	0.0701(11)	0.298(7)	0.154(13)	0.75	8.9(4)

Table 5.8A: Atomic positions and temperature factors for LiD at 235 °C

Atom /Site	x	y	z	Occupancy	100/Å^2 x U_{iso}
Li /4a	0	0	0	1	1.9(7)
D /4b	0.5	0.5	0.5	1	2.6(5)

Table 5.9A: Bond distances for LiD at 235 °C

Atoms	Distance/Å
Li-Li	8x 2.898 (10)
	4x 2.898 (14)
Li-D	6x 2.049 (10)

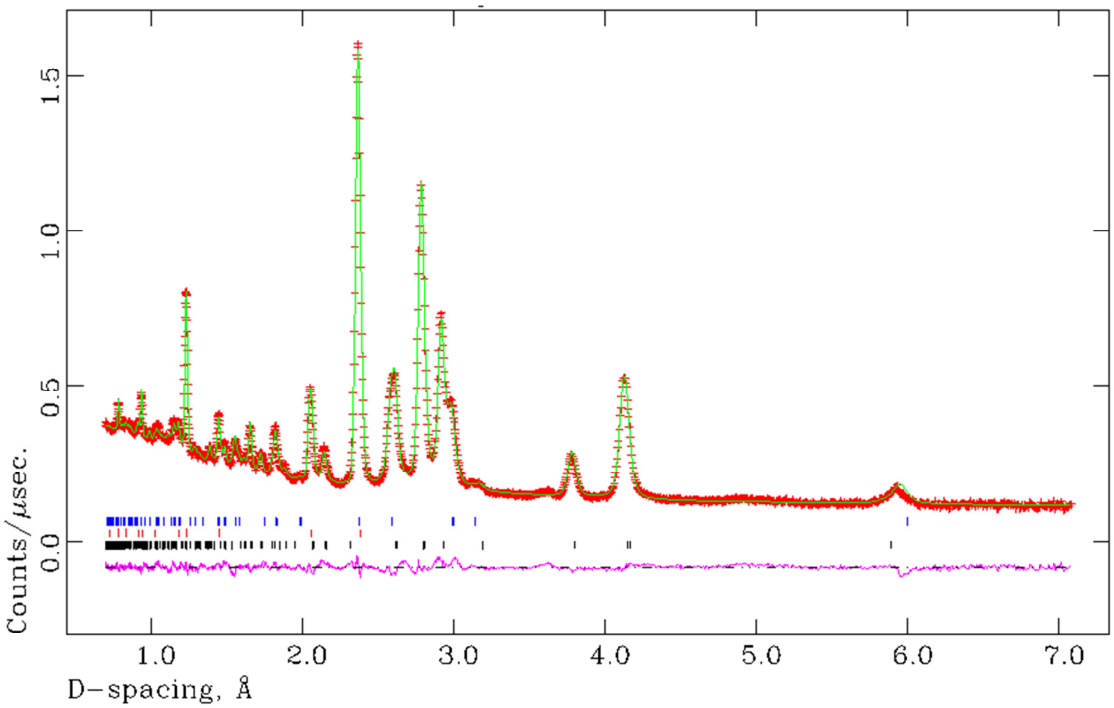

Figure 5.1A: Observed, Calculated and difference (OCD) plot for the structural refinement of sample **4** using bank 3 data at 235 °C. The blue tick marks indicate reflections the $Mg(ND_3)_2Cl_2$ phase, the red tick marks indicate reflections from the LiD phase and the black tick marks indicate reflections from the $Mg(ND_3)_2Cl_2$ phase.

8.2.1 PND study of the $Mg(ND_3)_6Cl_2 + MgH_2$ system

8.2.2 Powder Neutron Diffraction (PND) Study of the $Mg(ND_3)_6Cl_2 + MgH_2$ 'D$_2$ Release' System at 160 °C

Table 5.10A: Atomic positions and temperature factors for $Mg(ND_3)_2Cl_2$ at 160 °C.

Atom /Site	x	y	z	Occupancy	100/Å^2 x U_{iso}
Mg /2a	0	0	0	1	4.1(4)
Cl /4h	0.219(7)	0	0.5	1	1.5(1)
N/4i	0	0.262(10)	0	1	6.8(3)
D/16r	0.0880(8)	0.304(6)	0.163(13)	0.75	9.7(4)

Table 5.11A: Atomic positions and temperature factors for MgH_2 at 160 °C

Atom /Site	x	y	z	Occupancy	100/Å^2 x U_{iso}
Mg /2a	0	0	0	1	0.8(1)
H /4f	0.307(3)	0.307(3)	0	1	2.0(1)

8.2.3. Powder Neutron Diffraction (PND) Study of the $Mg(ND_3)_6Cl_2 + MgH_2$ 'D$_2$ release' system at 210 °C

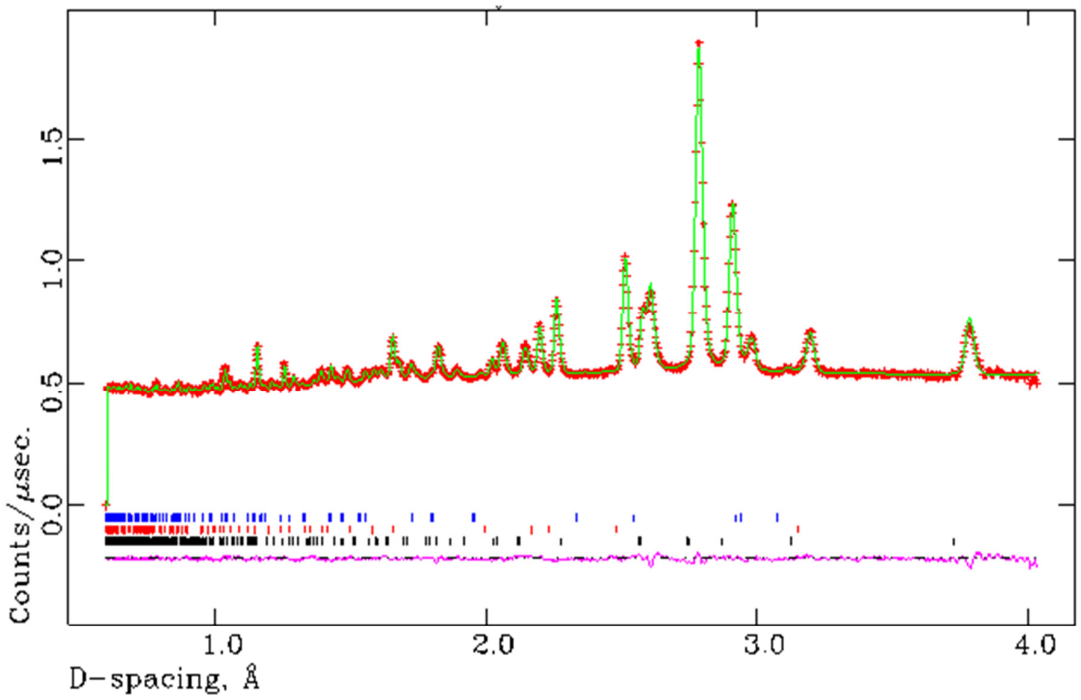

Figure 5.2A: Observed, Calculated and difference (OCD) plot for the structural refinement of sample **6** using bank 4 at 210 °C. The blue tick marks indicate reflections the $Mg(ND_3)_2Cl_2$ phase, the red tick marks indicate reflections from the MgH_2 phase and the black tick marks indicate reflections from the $MgCl_2$ phase.

8.2.4 Powder Neutron Diffraction (PND) Study of the $Mg(ND_3)_6Cl_2 + MgH_2$ 'D$_2$ Release' System at 230 °C

Table 5.12A: Crystallographic data for the $Mg(ND_3)_6Cl_2$ and MgH_2 system at 230 ^oC

Phases	$Mg(ND_3)_2Cl_2$	MgH_2	$MgCl_2$
Phrase Fractions (% .wt):			
	47.2(7)	34.7(5)	18.1(4)
Crystal System	Orthorhombic	Tetragonal	Trigonal
Space Group	*Cmmm*	$P4_2/mnm$	$R\bar{3}m$
a/Å	8.204(9)	4.512(3)	3.649(4)
b/Å	8.247(6)		
c/Å	3.778(3)	3.020(2)	17.760(4)
Volume/Å^3	225.523(6)	61.472(1)	204.736(4)
Z	2	2	3
Formula Weight/g	270.618	52.642	285.633
Density (p_x/gcm^{-3})	1.758	1.421	2.316
No of observations		3705	
No of variables		67	
R_{wp}		0.0227	
R_p		0.2311	
χ^2		1.692	

Table 5.13A: Atomic positions and temperature factors for $Mg(ND_3)_2Cl_2$ at 230 ^oC.

Atom /Site	**x**	**y**	**z**	**Occupancy**	**100/Å^2 x U_{iso}**
Mg /2a	0	0	0	1	3.5(3)
Cl /4h	0.218(7)	0	0.5	1	2.0(2)
N/4i	0	0.260(7)	0	1	4.5(2)
D/16r	0.0734(6)	0.302(4)	0.153(8)	0.75	4.6

Table 5.14A: Atomic positions and temperature factors for MgH_2 at 230 ^oC.

Atom /Site	**x**	**y**	**z**	**Occupancy**	**100/Å^2 x U_{iso}**
Mg /2a	0	0	0	1	1.0(1)
H /4f	0.307(3)	0.307(3)	0	1	2.6(1)

Table 5.15A: Bond distances and angles for $Mg(ND_3)_2Cl_2$ at 230 ^oC.

Atoms	Distance/Å	Angles/Å
Mg-N	2x 2.142(6)	
Mg-Cl	4x 2.600(4)	2x 86.82(18), 2x 93.18(18)
Mg-D1	8x 2.625(3)	
N-D1	4x 0.903(5)	
D1-D1	1x 1.154(6)	
	1x 1.204(11)	
	1x 1.667(11)	

Table 5.16A: Bond distance and angles for MgH_2 at 230 ^oC

Atoms	Distance/Å	Angles/Å
Mg-Mg	2x 3.020(23)	
	8x 3.530(2)	
Mg-H1	4x 1.9494(11)	
	2x 1.9573(18)	
Mg-H1-Mg		2x 101.52(9)

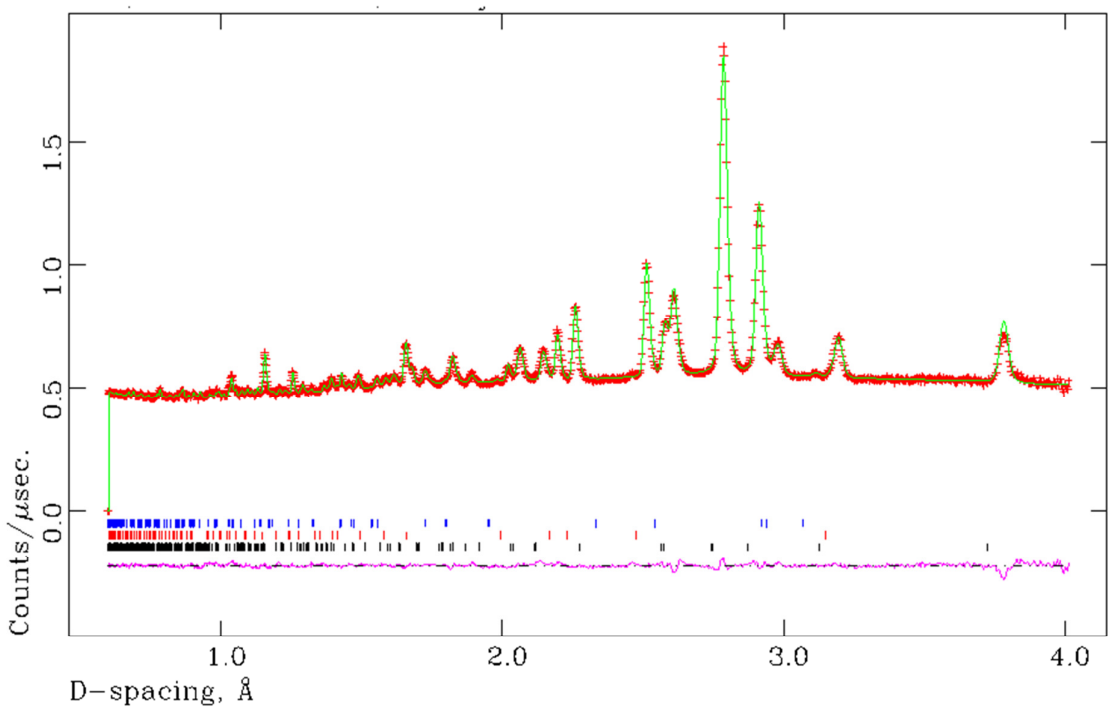

Figure 5.3A: Observed, Calculated and difference (OCD) plot for the structural refinement of sample **6** using bank 4 at 230 °C. The blue tick marks indicate reflections the $Mg(ND_3)_2Cl_2$ phase, the red tick marks indicate reflections from the MgH_2 phase and the black tick marks indicate reflections from the $MgCl_2$ phase.

9. Glossary of Common Terms Used

Ball milling: Technique used for reducing the particle size of a sample.

D2B: PND instrument for ex-situ PND in Chapter 4.

Deammoniation: Refers to the process of the release of ammonia when the metal ammines are heated.

Differential Thermal Analysis: Measures the thermal events when a sample is heated.

Ex-situ PND: Refers to a Powder Neutron Diffraction (PND) experiment where measurements are performed at room temperature, so no structural changes will occur during the measurement.

Fuel Cells: Produce electricity from a fuel via a chemical reaction with an oxidising agent

GEM: PND instrument used for In-situ PND in Chapter 4 and 5.

Glove box: A glove box with an inert atmosphere (either Ar(g) or N_2(g) is used for the handling and storage of air sensitive samples.

Gravimetric Weight: Refers to the wt. % a sample has of an element of compound, for example refers to the wt.% of ammonia contained in the metal ammines.

'Hydrogen Release' Systems: Refers to a system where there are two components containing hydrogen. When the sample is heated, hydrogen is released. The system is typically non-reversible under standard conditions.

In-Situ PND: Refers to a PND experiment where the sample is heated and PND is used to follow the reaction and the associated changes.

Mass Spectrometry: Measures the gases evolved when a sample is heated.

Metal ammines: Metal salts that contain ammonia.

Microstructured: Refers to reducing the particle size of a sample on the micron scale.

Nanostructured: Refers to reducing the particle size of a sample on the nanoscale.

PND (Powder Neutron Diffraction): Complimentary technique used in conjugation with PXD. In PND, the neutrons interact with the nucleus of an element so PND can be used in the refinement of samples containing lighter elements.

PXD (Powder X-ray Diffraction): PXD is a technique that gives information about the phase or phases present in a sample while longer PXD scans allow Rietveld refinement to be carried.

Rietveld Refinement: Technique used to determine the crystal structure and quantative phase composition of a sample.

Scanning Electron Microscopy (SEM): Technique used for determining the morphology and particle size of a sample.

Temperature Programmed Desorption (TPD): Technique used for measuring the changes in a sample when it is heated. The three components are: Thermogravemetric Analysis , Differential Thermal Analysis and Mass Spectrometry.

Thermogravemetric analysis (TGA): Measures the weight loss when a sample is heated.